The Role of the Laminar Separation Bubble in Wind Turbine Aeroacoustics and Dynamic Stall

by

Alison Zilstra

A thesis
presented to the University of Waterloo
in fulfillment of the
thesis requirement for the degree of
Doctor of Philosophy
in
Mechanical Engineering

Waterloo, Ontario, Canada, 2024

© Alison Zilstra 2024

Examining Committee Membership

The following served on the Examining Committee for this thesis. The decision of the Examining Committee is by majority vote.

External Examiner:	Pierre E. Sullivan Professor, Dept. of Mechanical & Industrial Engineering, University of Toronto
Supervisor:	David A. Johnson Professor, Dept. of Mechanical & Mechatronics Engineering, University of Waterloo
Internal Member:	Fue-Sang Lien Professor, Dept. of Mechanical & Mechatronics Engineering, University of Waterloo
Internal Member:	Xianguo Li Professor, Dept. of Mechanical & Mechatronics Engineering, University of Waterloo
Internal-External Member:	Francis Poulin Professor, Dept. of Applied Mathematics University of Waterloo

Author's Declaration

I hereby declare that I am the sole author of this thesis. This is a true copy of the thesis, including any required final revisions, as accepted by my examiners.

I understand that my thesis may be made electronically available to the public.

Abstract

The implementation of airfoils in low Reynolds number (Re) conditions requires careful consideration of the natural boundary layer (BL) transition as it covers a significant portion of the airfoil surface and often includes the formation of a laminar separation bubble (LSB). This study focuses on the role of the LSB in two design challenges facing low Re applications including small wind turbines (SWT): the generation of tonal airfoil self-noise and the blade loading fluctuations that occur during dynamic stall. Computational fluid dynamic (CFD) and computational aeroacoustic (CAA) methods were applied to two low Re airfoils to first validate the ability of the chosen methods to predict the complex LSB behaviour and second investigate the role of the LSB in these processes. Multiple detailed experimental data sets were combined to form a comprehensive validation of the simulated aerodynamic and aeroacoustic behaviours.

The investigation of tonal airfoil self-noise was completed using the SD 7037 airfoil at a modest Re of 4.1×10^4. The numerical methods of incompressible wall-resolved large eddy simulation (LES) and the Ffowcs-Williams and Hawkings (FW-H) acoustic analogy correctly predicted the tonal aeroacoustic noise and the Kelvin-Helmholtz (K-H) rolls that form in the LSB were identified as the acoustic source. Analysis of the transient BL development showed that the K-H rolls were amplified through a LSB pressure feedback process that altered the development of the laminar BL upstream of the LSB.

Later, the analysis of the deep dynamic stall process was completed using unsteady Reynolds-Averaged Navier-Stokes (URANS) simulations of the SD 7037 airfoil at $Re = 4.1 \times 10^4$ and a pitching reduced frequency of $k = 0.08$, and the S833 airfoil at $Re = 1.7 \times 10^5$ and $k = 0.06$. The simulated timing of the dynamic stall agreed with experimental data for both airfoils which is an advancement from the early prediction of stall seen consistently in previous numerical studies. The accurate prediction of dynamic stall was found to be dependent on the correct simulation of the bursting of the LSB, which initiated the complete separation of the boundary layer and the formation of a leading edge vortex.

The airfoil self-noise and dynamic stall simulations both proved the important role the LSB plays in these behaviours for low Re airfoils. All simulation methods also required strict grid refinement at the leading edge of the airfoil to correctly develop the transient BL transition behaviours for the tonal noise prediction and to capture the bursting of the LSB in the dynamic stall simulations. Grid refinements offset from the airfoil surface were also required to capture the BL transition that occurs in the separated region of the LSB. The successful application of LES and FW-H for tonal noise prediction and URANS for dynamic stall prediction opens the possibility of incorporating these methods into the aerodynamic and aeroacoustic design of airfoils for low Re applications including SWTs.

Acknowledgements

My journey through my PhD program would not have been possible without the help and guidance from many people along the way.

First and foremost, I would like to thank my supervisor, Professor David A. Johnson, who provided invaluable guidance and support during my research. He allowed me to explore my own path and created a research environment where I felt safe to try new ideas and learn from the failures and successes that come with the research process. In recognizing my passion for teaching, he mentored me through the ups and downs of university course instruction, including the Covid years. I truly feel prepared for whatever my future academic career will throw at me, and I have him to thank for that.

I would like to say thank you to my committee members, Professors Pierre Sullivan, Fue-Sang Lien, Xianguo Li, Francis Poulin and Andrea Scott for their support and guidance.

No graduate student makes it through their program without the support of the other students in their research group, since at times it feels like only they can truly understand the stresses and joys of graduate life. A tremendous thank you to Rafat Jami, Farid Samara, Faegheh Ghorbanishohrat, Michael McKinnon, Nicholas Tam and Kobra Gharali.

I also appreciate the support from the University of Waterloo community, especially the faculty and staff in the MME department, with whom I have become quite familiar over the past decade. I feel that my journey at UW came full circle when I was given the opportunity to teach the ME 351 course exactly 9 years after I took the course myself and was teaching alongside professors who taught me during my undergraduate degree. That is an experience that I will hold with me forever.

I would also like to thank the funding support provided by NSERC, the University of Waterloo and my supervisor. This has allowed me to travel independently to present my research at international conferences and gave me the opportunity to spend 4 months abroad at École Centrale de Nantes in France under the supervision of Carolyn Braud.

Finally, I must acknowledge that I could not be where I am today without the unconditional love and support of my family. And of course, that includes the happiness brought to my life by my cats: the button-pressing genius Sheldon and my dearest Penny.

Dedication

To the researchers that came before me and those that continue after.

We are on a collective journey of learning that spans time and location. Together we struggle and rejoice in the successes and failures that come along with piecing together the puzzle of the world around us.

Table of Contents

Examining Committee Membership ii

Author's Declaration iii

Abstract iv

Acknowledgements v

Dedication vi

List of Tables xii

List of Figures xiii

List of Abbreviations xvi

List of Symbols xviii

1 Introduction 1

1.1 Small Wind Turbines 1

1.1.1 Aeroacoustic Noise 2

1.1.2 Dynamic Stall 2

1.2 Motivation 3

1.3 Objectives 4
1.4 Thesis Organization 5

2 Literature Review **7**
2.1 Low Re Airfoil Boundary Layer 7
2.1.1 Airfoil Terminology 8
2.1.2 Natural BL Transition 9
2.1.3 Airfoil Curvature 10
2.1.4 Laminar Separation Bubble 12
2.1.5 Boundary Layer Integral Analysis 14
2.2 Computational Fluid Dynamics 16
2.2.1 Turbulent Energy Cascade 16
2.2.2 CFD Methods 18
2.2.3 LSB Simulation 19
2.2.4 LES Parameters 21
2.3 Aeroacoustics 25
2.3.1 Semi-Empirical Airfoil Self-Noise Prediction 25
2.3.2 Defining Sound 26
2.3.3 Airfoil Self-Noise 28
2.3.4 Acoustic Feedback 30
2.4 Computational Aeroacoustics 33
2.4.1 Acoustic Analogy 34
2.4.2 FW-H Acoustic Analogy 36
2.4.3 CAA of Low Re Airfoils 38
2.5 Dynamic Stall 41
2.5.1 Unsteady Blade Aerodynamics 41
2.5.2 Aerodynamics of Dynamic Stall 42
2.5.3 LSB and Dynamic Stall 45
2.5.4 Simulation of Dynamic Stall 45
2.6 Summary 48

3 Approach and Methodology **49**
3.1 Theoretical Approach - Aeroacoustic Noise . . . 50
3.1.1 CFD and CAA Validation . . . 51
3.1.2 Simulation Phases . . . 53
3.2 Numerical Method - Aeroacoustic Noise . . . 54
3.2.1 LES Method Setup . . . 55
3.2.2 LES Simulation Execution . . . 57
3.2.3 FW-H Acoustic Analogy Setup . . . 58
3.2.4 Domain Geometry . . . 59
3.2.5 Boundary Conditions . . . 61
3.2.6 Mesh and LES Filter Length . . . 63
3.3 Theoretical Approach - Dynamic Stall . . . 70
3.3.1 URANS Validation . . . 71
3.3.2 Simulation Phases . . . 72
3.4 Numerical Method - Dynamic Stall . . . 72
3.4.1 URANS Setup . . . 72
3.4.2 Mesh and Boundary Conditions . . . 74
3.4.3 Grid Coarsening Study . . . 75

4 Time-Averaged LSB Results **78**
4.1 Flow Structure Visualization . . . 79
4.2 Pressure Distribution . . . 81
4.3 Boundary Layer Integral Analysis . . . 83
4.4 Laminar Separation Bubble Visualization . . . 86
4.5 BL Separation and Reattachment . . . 88
4.6 Summary . . . 90

5 Transient LSB Results **92**
5.1 Boundary Layer Mesh Refinements . . . 93
5.2 Time-Averaged LSB . . . 94
5.3 Transient LSB Visualization . . . 97
5.3.1 K-H roll Formation . . . 99
5.4 Propagation of BL Instabilities . . . 102
5.4.1 Fully-Formed LSB . . . 106
5.4.2 LSB Pressure Feedback . . . 108
5.4.3 LSB Feedback Source . . . 116
5.5 BL Velocity Spectra . . . 120
5.5.1 K-H Roll Breakdown . . . 123
5.6 Summary . . . 124

6 Aeroacoustic Noise Results **127**
6.1 Far-Field Acoustic Prediction . . . 128
6.1.1 Acoustic Spectra at 1° AOA . . . 129
6.1.2 Tonal Noise Source . . . 130
6.1.3 Secondary Tone Intermittency . . . 131
6.1.4 Acoustic Spectra at 3° and 5° AOA . . . 134
6.2 Tone Frequency Trends . . . 138
6.3 Acoustic Feedback Loop . . . 141
6.3.1 TE Feedback and LSB Feedback . . . 143
6.3.2 Simulated Feedback Interference . . . 145
6.3.3 Interference at Experimental Frequencies . . . 147
6.4 Summary . . . 149

7 Dynamic Stall Results **151**

7.1 Static Validation 152

7.2 Deep Dynamic Stall 155

7.3 Dynamic LSB 159

7.3.1 SD 7037 LSB 159

7.3.2 S833 LSB 161

7.3.3 Dynamic Bursting of the LSB 163

7.4 LEV Formation 164

7.5 Summary 167

8 Conclusion **170**

8.1 Objectives Achieved and Contributions 170

8.1.1 Aeroacoustic Noise 170

8.1.2 Dynamic Stall 172

8.2 Future Work 174

References **175**

APPENDICES **187**

A Publications and Conferences **188**

List of Tables

3.1 Geometric and aerodynamic details 61
3.2 Mesh parameters for mesh versions 1-3 64
3.3 Dynamic stall geometries and numerical details 73
3.4 Grid coarsening study details 75

4.1 Boundary layer separation, transition and reattachment locations 80

5.1 Boundary layer separation, transition and reattachment locations for 1°, 3° and 5° AOA 95
5.2 Labels for the upstream and downstream propagation of BL pressure and velocity behaviours 104

6.1 K-H roll frequency, tone frequency and SPL for the simulated and experimental results 139
6.2 Summary of the parameters used for the pressure feedback calculation . . . 145

List of Figures

2.1 Airfoil geometry and associated terminology 8
2.2 Boundary layer transition diagram 9
2.3 Relationship between curvature and pressure gradient 11
2.4 Time-averaged LSB on a low Re cambered airfoil 12
2.5 LSB identification using pressure coefficient and skin friction coefficient . . 14
2.6 Diagram of the energy cascade 17
2.7 Airfoil self-noise mechanisms and noise directivity 29
2.8 Acoustic feedback loop diagram and tonal noise ladder structure 31
2.9 Definition of function used for calculating sound sources generated by a surface 37
2.10 Idealized velocity triangle diagram for a wind turbine blade 42
2.11 Wind shear and change in effective AOA for a wind turbine blade 43
2.12 Diagram of dynamic stall C_L cycle and stall severity 44

3.1 Change in microphone location relative to airfoil with AOA 59
3.2 Schematic of airfoil and computational domain 60
3.3 Diagram of simulation boundary conditions 62
3.4 Full domain mesh and close-up of airfoil for mesh versions 1-3 65
3.5 Improvements for mesh wall-normal expansion and filter length 66
3.6 Airfoil LE pressure gradient and filter length for $x/c < 0.025$ 68
3.7 LE curvature and chordwise node distribution for $x/c < 0.03$ 70
3.8 Dynamic stall simulation C-Mesh 74

3.9 Grid coarsening study dynamic C_L cycle results for SD 7037 and S833 airfoils 76

4.1 Q-Criterion iso-surface coloured by non-dimensional velocity magnitude . . 79
4.2 Suction side C_p for all AOAs compared with experimental measurements . 82
4.3 Displacement thickness and momentum thickness for $\alpha = 1°$, $5°$, $7°$ 84
4.4 Suction side H compared with experimental measurements 85
4.5 Contours of $|V|/U_\infty$ vs. x/c with pathlines to visualize LSB 86
4.6 LSB height, h, compared with PIV resolution and suction side C_f 89

5.1 Time-averaged suction-side C_p for $1°$, $3°$ and $5°$ AOA 95
5.2 Time-averaged suction-side C_f for $1°$, $3°$ and $5°$ AOA 96
5.3 Time-averaged suction-side H for $1°$, $3°$ and $5°$ AOA 97
5.4 Q-Criterion iso-surface for $1°$, $3°$, and $5°$ AOA 98
5.5 Diagram of the low Re airfoil BL development 99
5.6 Pressure and velocity of K-H rolls with velocity vectors for $1°$ AOA 101
5.7 Numbering system for key events in the BL transition 103
5.8 Method for tracking coherent structures using the U_s' and P' signals 105
5.9 U_s' and P' signal contours for $5°$ AOA 107
5.10 U_s' and P' signal contours for $5°$ AOA with pressure feedback 109
5.11 C_p and $\bar{U}_s$ chordwise gradient at wall-normal height of $4 \times 10^{-3}c$ for $5°$ AOA 111
5.12 U_s' and P' signal contours for $5°$ AOA with pressure feedback 113
5.13 U_s' and P' signal contours for $1°$ AOA 117
5.14 U_s' and P' signal contours for $3°$ AOA 118
5.15 Single-sided U_s spectra at $1°$, $3°$, and $5°$ AOA 121
5.16 Spanwise coherence of suction side pressure for $1°$, $3°$ and $5°$ AOA 124

6.1 Acoustic SPL spectra for $1°$ AOA and TE pressure and velocity contours . 130
6.2 Q-criterion iso-surface and acoustic spectra for secondary tone identification 132
6.3 Acoustic SPL spectra for $3°$ AOA and TE pressure and velocity contours . 135

6.4 Acoustic pressure signals for a sample $0.01s$ at 1°, 3°, and 5° AOA 136
6.5 Acoustic SPL spectra for 5° AOA and TE pressure and velocity contours . 137
6.6 Acoustic SPL spectra comparison for simulated and experimental AOAs . . 139
6.7 Diagram for interference calculation of LSB feedback and TE feedback . . 143
6.8 LSB feedback pressure signal with estimated TE acoustic pressure feedback 146
6.9 Idealized calculation of the acoustic feedback from the TE 148

7.1 Static SD 7037 C_L and suction side C_p plotted against experimental data . 152
7.2 Static S833 C_L and suction side C_p plotted against experimental data . . . 154
7.3 Dynamic C_L cycle for the SD 7037 airfoil at $Re = 4.1 \times 10^4$ and $k = 0.08$. 156
7.4 Dynamic C_L cycle for the S833 airfoil at $Re = 1.7 \times 10^5$ and $k = 0.06$ . . . 157
7.5 Dynamic ΔC_p for the S833 airfoil at $Re = 1.7 \times 10^5$ and $k = 0.06$ 158
7.6 Static and dynamic BL development for the SD 7037 airfoil 160
7.7 Static and dynamic BL development for the S833 airfoil 162
7.8 Dynamic C_f and z-vorticity contours of the LEV for the SD 7037 airfoil . . 165
7.9 Dynamic C_f and z-vorticity contours of the LEV for the S833 airfoil 166

List of Abbreviations

AOA	Angle of Attack.
BL	Boundary Layer.
BPM	Brooks, Pope and Marcolini.
CAA	Computational Aeroacoustics.
CDS	Central Differencing Scheme.
CFD	Computational Fluid Dynamics.
DDES	Delayed Detached Eddy Simulation.
DNC	Direct Noise Computation.
DNS	Direct Numerical Simulation.
DSV	Dynamic Stall Vortex.
FFT	Fast Fourier Transform.
FW-H	Ffowcs-Williams and Hawkings.
K-H	Kelvin-Helmholtz.
LBL-VS	Laminar Boundary Layer - Vortex Shedding.
LE	Leading Edge.
LES	Large Eddy Simulation.

LEV	Leading Edge Vortex.
LSB	Laminar Separation Bubble.
LUDS	Linear Upwind Differencing Scheme.
MFRT	Mean Flow Residence Time.
PISO	Pressure-Implicit with Splitting of Operators.
PIV	Particle Image Velocimetry.
QUICK	Quadratic Upstream Interpolation for Convective Kinematics.
RANS	Reynolds-Averaged Navier-Stokes.
RMS	Root-Mean-Square.
SGS	Sub-Grid Scale.
SIMPLEC	Semi-Implicit Method for Pressure-Linked Equations - Consistent.
SPL	Sound Pressure Level.
SST	Shear Stress Transport.
SWT	Small Wind Turbine.
T-S	Tollmien-Schlichting.
TBL-TE	Turbulent Boundary Layer - Trailing Edge.
TE	Trailing Edge.
UDS	Upwind Differencing Scheme.
URANS	Unsteady Reynolds-Averaged Navier-Stokes.
WMLES	Wall-Modeled Large Eddy Simulation.

List of Symbols

Roman Symbols

a	Axial induction factor.
a'	Angular induction factor.
b	Airfoil span [m].
c	Airfoil chord length [m] or Speed of sound [m/s].
C_D	Drag coefficient.
C_f	Skin friction coefficient.
C_L	Lift coefficient.
C_p	Pressure coefficient.
f	Frequency [Hz].
H	Boundary layer shape factor.
k	Reduced frequency.
L	Computational domain length.
$\mathcal{L}$	Length scale of geometry [m].
l_0	Length scale of largest turbulent eddies [m].
l_{DI}	Length scale dividing inertial subrange and dissipation range [m].
l_{EI}	Length scale dividing energy containing range and inertial subrange [m].

l_{K-H}	Distance between K-H roll cores [m].
L_p	Sound pressure level [dB].
Ma	Mach number.
p	Pressure [Pa].
$\hat{p}$	Root mean square sound pressure [Pa].
p'	Unsteady pressure [Pa].
R	Computational domain radius.
r	Wind turbine blade segment radial distance from rotor centre [m].
Re	Reynolds number.
Re_{crit}	Critical Reynolds number.
Re_{ind}	Indifference Reynolds number.
St	Strouhal number.
T	Period of oscillation [s].
t	Time [s].
T_{ij}	Lighthill's tensor.
Tu	Turbulent intensity.
U_∞	Free-stream velocity [m/s].
U'_s	Velocity tangent to the airfoil surface [m/s].
W	Wind turbine blade segment relative wind velocity [m/s].
x_r	Boundary layer reattachment location [m].
x_s	Laminar boundary layer separation location [m].
$x_{s,TE}$	Trailing edge boundary layer separation location [m].
x_{tr}	Boundary layer transition location [m].

y^+	Wall-normal height.

Greek Letters

α	Airfoil angle of attack [°].
β	Wind turbine blade pitch [°].
δ	Boundary layer thickness [m].
δ_{ij}	Kronecker delta.
δ^*	Boundary layer displacement thickness [m].
δ_v	Viscous length scale [m].
η	Kolmogorov length scale [m].
γ^2	Magnitude-squared coherence.
λ	Acoustic wavelength [m].
μ	Dynamic viscosity [kg/ms].
ν	Kinematic viscosity [m^2/s].
Ω	Wind turbine rotor rotational speed [rad/s].
ω	Pitching rate [rad/s].
ρ	Density [kg/m^3].
τ_w	Wall shear stress [Pa].
θ	Boundary layer momentum thickness [m].

Chapter 1

Introduction

1.1 Small Wind Turbines

Small wind turbines (SWT) play an important role in the transition to renewable energy by providing power in remote areas not connected to the power grid, which are often dependent on diesel generators, and offsetting fossil fuel dominated grid usage of a household. In comparison to the wind turbines deployed in large wind farms, SWTs are at a smaller scale with blade lengths of 1.5 m to 8 m and shorter tower heights that place the SWT blades closer to the ground. They are often located in residential or industrial areas where proximity to buildings introduces complex inflow conditions such as gusts, wind shear and yaw misalignment that must be accounted for in the aerodynamic design of the SWT blades.

SWTs operate in a low Reynolds number (Re) regime, defined here as a chord-based Re of less than 5×10^5, with typical values ranging from 8×10^3 to 4×10^5. This low Re operation results in a laminar or transitional boundary layer (BL) forming on the surface of the blades, which is more complex than the turbulent BL that forms on the majority of large wind turbine blades. The complexity of the low Re BL is increased when the airfoil curvature results in the formation of a laminar separation bubble (LSB) where the laminar BL separates, transitions to a turbulence and then reattaches to the airfoil surface. The presence of this LSB on the blades of SWTs presents a unique set of design challenges since the LSB alters the aerodynamic and aeroacoustic behaviour of the blades when compared to the behaviour of the turbulent BL of large wind turbines. Two design challenges facing SWTs operating with a LSB are addressed in this thesis: the generation of tonal aeroacoustic noise by the blades and the dynamic stall of the blades under unsteady

wind conditions. The following sections introduce the topics of aeroacoustic noise and unsteady loading during dynamic stall.

1.1.1 Aeroacoustic Noise

The noise generated by SWTs is a combination of the mechanical noise from the physical interaction and vibration of mechanical components in the nacelle, the electromagnetic noise from generator, and the aeroacoustic noise from flow around the blades. The reduction of mechanical and electromagnetic noise can typically be accomplished by enclosing the components in the wind turbine nacelle and using acoustic insulation technologies designed to absorb or dampen the noise at a targeted frequency range. The aeroacoustic noise sources on the blades cannot easily be enclosed or insulated in the same manner therefore there is significant research interest in reducing aeroacoustic noise for SWT blades.

The aeroacoustic noise generated by the blades is due to airfoil self-noise originating from the interaction of the BL at the trailing edge (TE) of the blade. The type of airfoil self-noise generated by the different airfoil profiles is dependent on whether the BL is laminar, transitional or turbulent at the TE. Large wind turbines operating at high Re have a turbulent BL that generates broadband noise across a wide range of frequencies and SWTs operating at lower Re have a laminar or transitional BL that is capable of producing strong tonal noise. This tonal noise occurs when the flow structures that form within a transitional BL, including those formed by a LSB, are located near the blade TE. The analysis of the transitional BL and LSB structures responsible for the tonal airfoil self-noise can be used to inform the aeroacoustic design of future SWT blades and new technologies that can be added to existing blades to reduce tonal noise.

1.1.2 Dynamic Stall

SWT blades are designed to withstand a variation of aerodynamic forces and moments under a wide range of operating conditions to prevent early fatigue failure and increase the lifespan of the SWT. Unsteady wind conditions can result in extreme variation of the blade loading due to the dynamic stall process which poses a challenge for the effective design of SWT blades. Under ideal wind conditions, the static stall of the blade follows a predictable change in aerodynamic forces that closely follows the data used to design the blades. Dynamic stall of the blade can occur if the wind conditions change in a rapid transient manner which causes the forces on the blade to deviate well beyond the predictable static behaviour. This can lead to larger fluctuations in the blade loading which

can increase the fatigue of the blades and also negatively impact the power production of the SWT through reduction in aerodynamic performance.

The unsteady loading caused by dynamic stall is an issue for both SWTs and large wind turbines operating at high Re, however the SWTs have the additional complexity of a transitional BL with the potential for the formation of a LSB. There is a need to understand the dynamic stall process under these low Re operating conditions to be able to design load mitigation strategies that are optimized for SWTs.

1.2 Motivation

The overarching motivation of this research is to remove existing barriers to the installation of wind turbines to increase the usage of renewable energy sources. The aeroacoustic noise generated by wind turbines is a well known issue with the general public and can potentially prevent the installation of new wind farms. Additionally, the early failure of wind turbine blades can lead to costly repairs or decommissioning, which impacts return on investment for the individuals or governments considering the installation of new wind turbines. This work aims to address these issues with SWTs through a numerical modelling approach to make advances towards the integration of the aeroacoustic design and design for dynamic stall into the current aerodynamic and structural design process of SWT blades. A combination of computational fluid dynamic (CFD) methods and computational aeroacoustic (CAA) methods are used to analyze the aeroacoustic and dynamic stall behaviours.

There is a significant gap in the validation of CFD simulations of the complex low Re BL and LSB due to the extremely limited availability of detailed quantitative experimental data. This is especially true for airfoils at a modest Re of less than 1×10^5 which is the operating Re range for the majority of SWTs. Due to the absence of validating data, prior efforts in CFD simulation of this type of flow have been focused on flat plate geometries as well as airfoils not commonly used in low Re applications. Improvements in the application of CFD methods to the low Re BL for airfoils designed for SWT blades and the thorough validation of the simulation of the LSB is crucial before advancing to the more complex CAA simulations and simulations of dynamic stall.

The CAA methods used to predict airfoil self-noise at low Re require input data from a transient CFD simulation of the flow around the airfoil and are highly sensitive to the quality of the transient BL data. The challenge of validating the input CFD data for a low Re airfoil with a LSB has been highlighted above, and therefore the existing CAA research is limited to operating conditions where the LSB is not in close proximity to the airfoil

TE. In addition to the challenges with the input CFD data, this method of aeroacoustic design is prohibitively expensive for use in industry and current best practice is to use the semi-empirical models for aeroacoustic noise prediction which have been included in wind turbine design software. However, these semi-empirical models are based on experimental data sets that do not include the low Re airfoil profiles used for SWT blades and has the potential to provide incorrect aeroacoustic noise predictions for low Re blades. Therefore there is a need for the validation of the CAA methods for low Re airfoil self-noise, which requires a detailed validation of the CFD methods for prediction of small scale transient behaviour in the laminar or transitional BL.

The numerical simulation of dynamic stall using CFD can be useful for analyzing the changes in the blade loading for SWTs and understanding the key source behaviours behind those changes. The findings from the simulation of dynamic stall can also be applied to the low Re operation of helicopter or drone rotors where the advancing and retreating sides of the rotor experience similar changes in wind speeds. Prior CFD simulations of dynamic stall of low Re airfoils fail to predict the correct moment of dynamic stall which leads to incorrect timing of the drastic loading changes responsible for the fatigue of SWT blades. The analysis of the dynamic stall behaviour under low Re conditions with a LSB can be used to improve the design of SWT blades for a range of complex transient wind conditions and extend the design beyond the traditional method that assesses performance across a range of steady wind speeds.

Together these numerical simulations of airfoil self-noise and dynamic stall for low Re airfoils with a LSB can be used to improve the understanding of the aerodynamic behaviours driving these complex design challenges which can then inform new methods to improve the design of future SWT blades. Progress towards the incorporation of these numerical simulations into earlier phases of the design process will result in the improvement of the aeroacoustic and aerodynamic performance of SWT blades and could lead to the increased implementation of the technology.

1.3 Objectives

The research scope covers the numerical simulation, validation and analysis of low Re airfoils that are optimal for use on a SWT and are operating under flow conditions that generate tonal aeroacoustic noise and dynamic stall. The objectives are as follows:

1. Apply CFD methods to low Re airfoils under static conditions to accurately predict the transient behaviours in the transitional BL and LSB

2. Predict the tonal airfoil self-noise generated by a low Re airfoil using CAA and the input data from the CFD simulation

3. Determine the structures in the transitional BL and LSB that are responsible for the tonal airfoil self-noise at low Re

4. Predict the dynamic stall of low Re airfoils with a LSB using unsteady CFD methods

5. Validate the simulated results against available experimental data to quantify the accuracy of each simulation method

6. Reduce computational cost through the selection of appropriate CFD methods and the optimization of the simulation parameters

1.4 Thesis Organization

This thesis is structured as follows:

Chapter 2 provides a literature review of the information required for the full understanding of the BL development for a low Re airfoil and how it relates to the generation of aeroacoustic noise and the dynamic stall process. It also summarizes the theory behind the chosen CFD and CAA methods and the simulation efforts of previous researchers.

Chapter 3 describes the theoretical approach of the simulations and the numerical methods used in each simulation case. It includes discussion of preliminary simulations that determined the optimal parameters applied in the simulations used to generate the results presented in Chapters 4 through 7.

Chapter 4 validates the CFD simulation of the transitional BL and LSB on the low Re airfoil through a comparison with time-averaged experimental data. The results particularly focus on the simulation of the LSB which is present in the BL transition region. These results are published in the *ASME Journal of Fluids Engineering*[1].

Chapter 5 presents the analysis of the transient development of the flow structures in the transitional BL and LSB. A pressure feedback process is identified upstream of the LSB and its effect on the transient BL development is described in detail. A spectral analysis of the BL is completed to establish the frequencies of the dominant flow structures in each

[1]Zilstra, A. and Johnson, D.A. (2022) Large Eddy Simulation of Transitional Separated Flow Over a Low Reynolds Number Cambered Airfoil. ASME. J. Fluids Eng. doi: 10.1115/1.4056280

region of the transitional BL. A portion of these results are published in the proceedings of the *30th AIAA/CEAS Aeroacoustics Conference*[2].

Chapter 6 provides a detailed analysis of the acoustic prediction from the CAA method and validates the results against experimental data. The BL structures responsible for the primary and secondary aeroacoustic tones are identified. An estimation of the acoustic feedback and its interference with the simulated LSB feedback is presented. A portion of these results are published in the *Journal of Physics: Conference Series*[3].

Chapter 7 presents the validation and analysis of the CFD simulation of the deep dynamic stall of two low Re airfoils. A discussion of the role of the LSB in the stall process is included along with CFD simulation requirements to accurately capture the LSB. These results are published in the *AIAA Journal*[4].

Chapter 8 concludes the thesis with a summary of the findings from the research completed and recommendations for future work. It covers the objectives achieved and summarizes the contributions resulting from this research.

[2]Zilstra, A. and Johnson, D.A. (2024) Computational Aeroacoustic Prediction of Tonal Noise for Low Reynolds Number Airfoils. 30th AIAA/CEAS Aeroacoustics Conference. doi:10.2514/6.2024-3362

[3]Zilstra, A. and Johnson, D.A. (2024) Numerical Prediction of Tonal Aeroacoustic Noise Produced by Small Wind Turbines. J. Phys.: Conf. Ser., doi:10.1088/1742-6596/2767/7/072022

[4]Zilstra, A. and Johnson, D.A. (2024) Validated Dynamic Stall Simulation of Pitching Low Reynolds Number Airfoils. AIAA Journal, Vol. 62, No. 10, pp. 3700-3712, https://doi.org/10.2514/1.J063884

Chapter 2

Literature Review

This chapter summarizes the relevant literature for the aerodynamic and aeroacoustic simulation of static and dynamic airfoils at low Reynolds numbers (Re). The primary focus of the review is the behaviour of the laminar separation bubble (LSB) that forms within the transitional boundary layer (BL) and the challenges associated with its accurate simulation. The chapter begins with a review of the BL transition process and the formation of a LSB over a low Re airfoil. This is followed by a summary of the computational fluid dynamics (CFD) methods commonly used to simulate a LSB. Then the focus of the review shifts to the literature on aeroacoustics with a summary of airfoil self-noise and the computational aeroacoustic (CAA) methods applied for low Re airfoil self-noise prediction. Finally, there is a description of the low Re dynamic stall process that occurs on small wind turbine (SWT) blades in the presence of a LSB and the unsteady CFD methods that can be applied to predict the unsteady blade loading. The review of the literature demonstrates the necessity of this research and highlights the absence of thoroughly validated simulations of low Re airfoils with a LSB for the applications of airfoil self-noise and deep dynamic stall.

2.1 Low Re Airfoil Boundary Layer

The development of the BL on the surface of the SWT blades is fundamental to the generation of the aerodynamic forces that rotate the SWT rotor to produce power. The BL development under low Re flow conditions includes the formation of a LSB, which will be shown later in this chapter to play an important role in both the tonal aeroacoustic noise produced by a SWT blade and the unsteady loading of the dynamic stall process.

The following description of the BL transition process is generalized to any application of low Re airfoils which develops a LSB.

2.1.1 Airfoil Terminology

An airfoil profile is the cross-section of any wing or blade designed to generate a lift force and minimize the drag force. The terminology associated with an airfoil is shown in Figure 2.1, where the incoming flow velocity, U_∞, is at an angle of attack, α, with the airfoil. The angle of attack (AOA) is defined in relation to the airfoil chord line, which extends from the leading edge (LE) to the trailing edge (TE) of the airfoil. The chord length, c, is the length of the chord line and properties within the airfoil BL are usually plotted against the dimensionless x-coordinate, x/c. The top of the airfoil is the suction side and the bottom of the airfoil is the pressure side due to the pressure changes that occur along those surfaces. The mean camber line follows the midpoint between the suction side and pressure side at each x/c location [1]. A symmetric airfoil profile will have the camber line coincident with the chord line, and a cambered airfoil has asymmetry about the chord line to further manipulate the pressure differences between the pressure and suction sides of the airfoil.

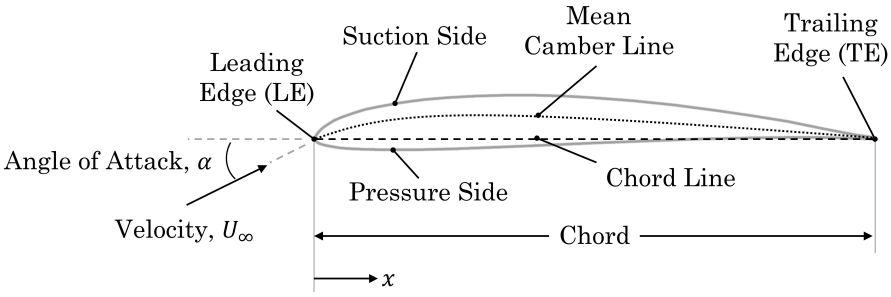


Figure 2.1: Airfoil geometry and associated terminology

The aerodynamic behaviour of an airfoil is classified based on Re, which is defined as

$$Re = \frac{\rho U_\infty c}{\mu} \tag{2.1}$$

where ρ and μ are the density and dynamic viscosity of the fluid. Airfoils operating with $Re < 5 \times 10^5$ are classified as low Re and airfoils with $Re < 1 \times 10^5$ are further classified as operating at modest Re. The Re ranges separate the airfoil performance based on the

type of BL that forms on the surface of the airfoil where low Re operation has a largely laminar or transitional BL. The distinction between low Re and modest Re operation is the chordwise length of the transition region where in general, increasingly modest Re operation results in an elongated transition region and a LSB with a longer chordwise length. The differences between the BL development for airfoils across a range of low Re and AOAs is discussed in Section 2.2.3. The following sections describe the BL transition process for low Re airfoils.

2.1.2 Natural BL Transition

The interaction of the incoming flow with the airfoil surface creates a BL which begins as a laminar BL at the airfoil LE and develops into a turbulent BL through the natural BL transition process. A natural, unforced BL transition occurs without the aid of surface roughness elements or tripping methods. The process is well documented, particularly for flow over a flat plate, and the most common depiction of the BL transition process is shown in Figure 2.2. The transition region is bounded by the indifference Re (Re_{ind}) and the critical Re (Re_{crit}). The Re_{ind} is defined using stability theory [2], and indicates the location where the BL becomes susceptible to the small scale perturbations that develop as the BL grows. The Re_{crit} is a more commonly known Re, and specifies the location where the BL has completely transitioned to turbulence.

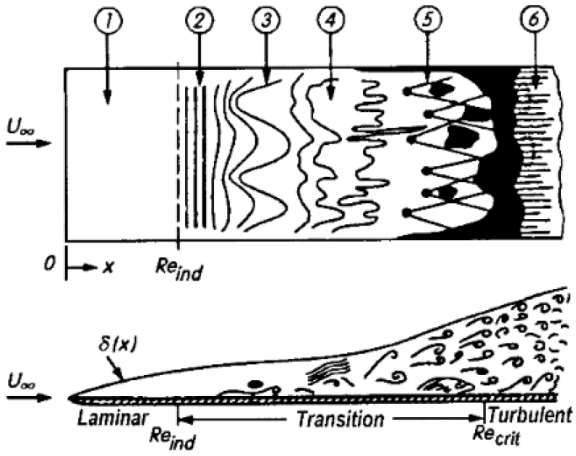


Figure 2.2: BL transition diagram for flow over a flat plate. Reprinted with permission from Schlichting and Gersten [2]

The numbers along the top of Figure 2.2 highlight the key flow behaviours that form in the transitional BL, with (1) as stable laminar flow and (6) as fully turbulent flow. Within the transition region, the behaviours are as follows: (2) Tollmien-Schlichting (T-S) waves, (3) Λ structures, (4) vortex decay and (5) turbulent spots. The T-S waves are unstable 2D fluctuations within the BL that are a result of the amplification of small perturbations after reaching Re_{ind} [2]. The Λ structures occur when secondary BL instabilities introduce 3D behaviour into the T-S waves, causing inconsistent spanwise behaviour to develop [2]. The vortex decay and formation of turbulent spots represent the final stages of transition, where the large structures developed in the early transition break down into small turbulent eddies as the BL thickness grows.

2.1.3 Airfoil Curvature

Airfoil curvature is designed to redirect the airflow and alter the BL formation to generate a lift force through the creation of a pressure difference between the suction side and pressure side of the airfoil. These pressure changes are most commonly represented using plots of pressure coefficient, C_p, versus the non-dimensional length x/c, which highlight the pressure deficit created on the suction side of the airfoil. C_p is defined as

$$C_p = \frac{P - P_\infty}{\frac{1}{2}\rho_\infty U_\infty^2} \tag{2.2}$$

where P is the local static pressure which is compared with the free-stream static pressure, P_∞, and is made dimensionless by the free-stream density, ρ_∞, and velocity, U_∞. The cause of the pressure change along the airfoil surface can be explained with the concept of mass and momentum conservation, where the chordwise acceleration or deceleration of the flow around the airfoil results in a decrease or increase in the pressure, respectively. An example C_p plot for the suction side of an airfoil is shown in Figure 2.3, where there is a negative pressure gradient, termed a favourable pressure gradient, as the flow accelerates over the initial curvature of the airfoil LE. After reaching the location of minimum pressure, which is called the suction peak, the flow decelerates along the remainder of the airfoil causing a positive pressure gradient, called an adverse pressure gradient. The pressure gradient that develops in the chordwise direction alters the development of the BL when compared with a similar transition over a flat plate, which has no pressure gradient.

One effect of airfoil curvature on the BL development is the delay in transition caused by the initial favourable pressure gradient between the LE and the suction peak [2]. The delay is dependent on the AOA of the airfoil, where a higher AOA will move the suction

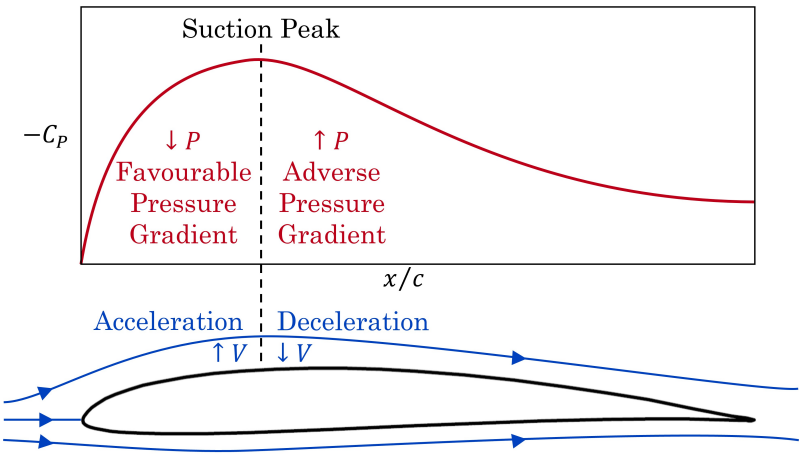


Figure 2.3: Flow acceleration and pressure gradient induced by the curvature of the suction side of an airfoil

peak closer to the airfoil LE. For the example shown in Figure 2.3, the suction peak is at approximately $x/c = 0.25$, and at a higher AOA, this peak C_p would occur further upstream at $x/c < 0.05$. In terms of the natural BL transition defined in Section 2.1.2, the favourable pressure gradient increases the stability of the boundary layer, making it less susceptible to small perturbations [2,3]. The result is a later x/c location of the Re_{ind} and a delayed location of the BL transition region, when compared with BL transition on a flat plate.

Another effect of the airfoil curvature is the laminar BL separation that can be triggered by the adverse pressure gradient that forms after the suction peak [2]. This adverse pressure gradient is associated with the deceleration of the flow caused by the airfoil geometry, as shown in Figure 2.3. The flow deceleration in the laminar BL is further exacerbated by kinetic energy loss due to friction, which results in a further pressure deficit when compared to the free-stream flow adjacent to the BL [4]. The combination of the curvature-induced adverse pressure gradient and pressure deficit due to friction reduces the stability of the BL [2] and at the point of separation the adverse pressure gradient has become sufficiently strong to overcome the low momentum of the laminar or transitioning BL [5].

This separation is generally not possible when a favourable pressure gradient is present because the associated acceleration of the flow increases the BL momentum to keep the laminar BL attached to the surface of the airfoil. The separation of the laminar or transitional BL is a common occurrence for the low Re operation of airfoils since the BL generally does not transition to turbulence until downstream of the suction peak. For higher Re op-

eration, the BL transition occurs over a significantly shorter chordwise length and therefore the BL is turbulent in the region of adverse pressure gradient after the suction peak. Laminar BL separation is a BL behaviour unique to low Re operation of airfoils and can result in the formation of a LSB, the details of which are described in the following section.

2.1.4 Laminar Separation Bubble

A laminar separation bubble is formed when the laminar or transitional BL separates from the airfoil surface and reattaches downstream as a turbulent BL. This is illustrated in Fig. 2.4 where the time-averaged shape of the LSB is shown as a region of stagnant air below the separated transitional BL. Within the attached BL upstream of the LSB, the natural BL transition behaviours develop in a similar manner to the classic flat plate BL transition described by Schlichting [2], until interrupted by laminar separation. A LSB can also form before the attached BL begins the transition process, at which point the transition to turbulence will be initiated after the point of laminar BL separation.

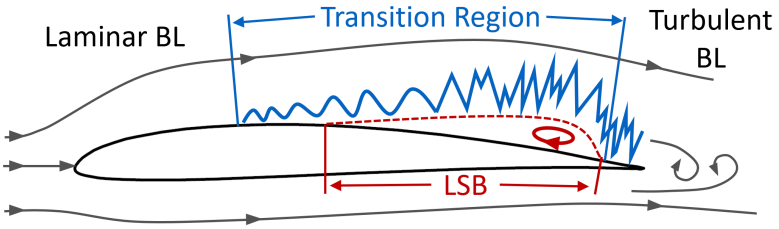


Figure 2.4: Idealized time-averaged LSB on a low Re cambered airfoil, dashed lines for LSB and solid lines for transition region

Conceptually, a laminar BL is organized into parallel flowing shear layers with little to no mixing in comparison with a turbulent BL which has mixing and therefore no defined shear layers. Therefore once the laminar or transitional BL lifts from the airfoil surface due to the adverse pressure gradient, there is a strong distinction between the separated BL and the stagnant or reverse flow between the separated BL and the airfoil surface [6]. The interaction between the separated shear layer and the reverse flow adjacent to the surface results in the development of a Kelvin-Helmholtz (K-H) instability [7]. The amplification of the K-H instability results in the formation of spanwise vortices (also called K-H rolls [8]), which enhances near-wall momentum exchange and increases mixing between the layers, leading to reattachment of the BL to form the LSB [6, 9]. The BL reattachment process occurs due to the transient growth and decomposition of the K-H rolls and therefore

the chordwise location of BL reattachment can only be defined using the time-averaged behaviour as is depicted in Figure 2.4.

The transition from laminar to turbulent BL that occurs in a LSB is due to the eventual decomposition of the K-H rolls upon reattachment of the BL and this is the dominant mechanism of BL transition, rather than the natural BL transition that occurs in an attached BL as described in Section 2.1.2. The decomposition, or breakdown, of the K-H rolls can be quantified through a calculation of the magnitude squared coherence, γ^2, of the pressure or velocity between two spanwise locations of the BL where the γ^2 progressively reduces to zero with increasing spanwise breakdown of the K-H rolls.

The frequency of the K-H instability has been found to be similar to the frequency of the T-S waves that develop during the start of the BL transition in the attached BL [6, 10]. As is shown in Figure 2.4, the LSB often forms after the attached laminar BL has begun to transition and structures that develop within the attached BL have influence on the growth of the K-H rolls and the frequency at which they form. A correlation developed using stability theory on a flat plate can be used to approximate the T-S wave frequency using the displacement thickness and edge velocity of the BL [11], though this has limited applicability for airfoils where the BL develops under the presence of large pressure gradients. The frequency of the K-H rolls can be made dimensionless using a Strouhal number based on the BL properties at the location of separation, which results in a range of 0.005 to 0.016 [6]. The Strouhal number is defined as

$$St_{\theta s} = \frac{f\theta_s}{U_{es}} \tag{2.3}$$

where f is the K-H roll frequency, θ_s is the momentum thickness of the BL at the location of separation and U_{es} is the edge velocity of the BL at separation. The momentum thickness of a BL is determined using Equation 2.6 in Section 2.1.5.

In some cases, such as when laminar separation occurs closer to the airfoil TE [4] the BL is unable to reattach and therefore has a laminar separated BL rather than a fully formed LSB. This results in a complex BL interaction at the airfoil TE where the growing K-H rolls in the separated, suction side BL interact with the pressure side BL in the wake. In literature, LSBs are frequently referred to as transitional separated flow due to the transition to turbulence that occurs during BL separation. This can be seen as a broader term than LSB because it does not require the BL reattachment needed to form a complete LSB, and can still be used to describe the case where the laminar separation occurs near the airfoil TE and does not result in a fully-formed LSB.

A fully-formed LSB can be identified using flow visualization techniques, as well as measurements of C_p and skin friction coefficient C_f at the surface of the airfoil. A C_p plot

with a LSB will feature a transition ramp shown in Figure 2.5 [12], which begins with the levelling off of the C_p curve at the location of laminar separation, x_s, followed by a sharp pressure recovery at reattachment, x_r. The start of the pressure recovery occurs at the location where the separated BL transitions to turbulence, x_{tr}, and the associated increase in BL momentum initiates the pressure recovery that leads to eventual BL reattachment. The skin friction coefficient is defined as,

$$C_f = \frac{\tau_w}{\frac{1}{2}\rho_\infty U_\infty^2} \tag{2.4}$$

where τ_w is the local wall shear stress and is made dimensionless by the free-stream density, ρ_∞, and velocity, U_∞. When calculating C_f using τ_{wall} in the streamwise direction, rather than using the total magnitude, the C_f is positive in regions of attached BL and the regions of BL separation will have a $C_f \leq 0$ due to the stagnant or reversed flow. The time-averaged streamwise C_f can therefore be used to identify the location of the LSB, as is shown in Figure 2.5, where the location that C_f first drops below zero is the location of laminar BL separation and the time-averaged reattachment is the location where the C_f returns to a positive value. The transient location of reattachment varies due to the downstream progression of the K-H rolls in the latter part of the LSB, which is why it is necessary to use the time-averaged C_p and C_f to locate the LSB.

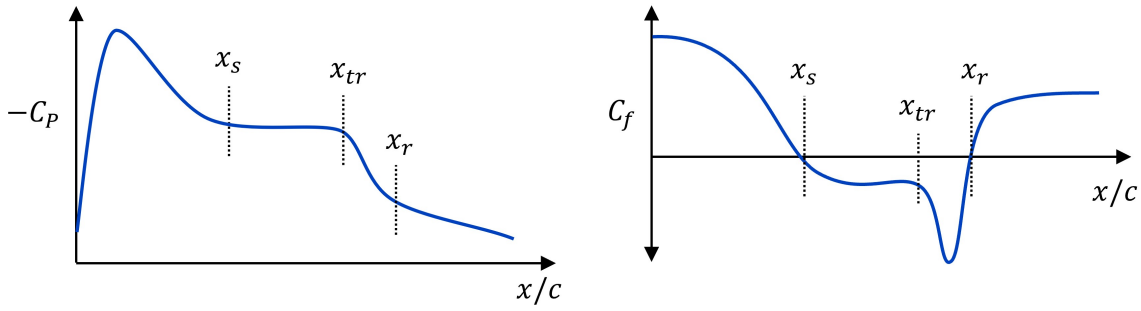


Figure 2.5: Idealized C_p and C_f chordwise trends used for identifying the time-averaged LSB separation, x_s, transition, x_{tr} and reattachment, x_r, locations. Modified from [4, 12]

2.1.5 Boundary Layer Integral Analysis

A fundamental aspect of BL analysis is the accurate determination of integral BL variables which describe the velocity distribution within the BL and can confirm the locations of key

behaviours in the transitional separated BL. These variables are intended to be applied to a flat plate BL where the velocity U is a function of the wall-normal coordinate y, and therefore they must be calculated using the velocity that is tangent to the airfoil surface. Airfoil velocity data is usually collected in a global X-Y-Z coordinate system which must then be converted to an S-N-Z coordinate system where the S-direction is aligned tangent to the curvature of the airfoil surface and the N-direction is normal to the surface. The Z-direction is aligned with the span of the airfoil and does not require alteration to be used in the S-N system. Therefore the calculation of the BL integral properties for an airfoil is completed using the s-velocity, U_s, as a function of the n-coordinate.

The displacement thickness, δ^*, is defined as,

$$\delta^* = \int_0^\delta \left(1 - \frac{U_s}{U_e}\right) dn \tag{2.5}$$

where U_s is the BL velocity profile, U_e is the edge velocity of the BL and δ is the BL thickness [2]. The variation in δ^* along the chord is useful for identifying the location of laminar separation since the added distance between the separated shear layer and the airfoil surface causes a noticeable increase in the measured δ^* [13].

The momentum thickness, θ, is defined as,

$$\theta = \int_0^\delta \frac{U_s}{U_e}\left(1 - \frac{U_s}{U_e}\right) dn \tag{2.6}$$

where the variables are defined the same as for the δ^* calculation. The θ is unaffected by the laminar separation due to the negligible momentum of the fluid trapped within the bubble, however it has a significant increase in magnitude when the separated BL transitions to a high momentum turbulent BL [13, 14].

While δ^* and θ are individually useful for BL analysis, when combined together in the shape factor,

$$H = \frac{\delta^*}{\theta} \tag{2.7}$$

they can be used to characterize the velocity profile of the BL [2]. When using H to analyze a transitional separated BL, a clearly defined peak develops due to the delay in the increase of θ in relation to δ^*. The chordwise location of the peak H value can be used to determine the time-averaged location of BL transition in a LSB [14].

2.2 Computational Fluid Dynamics

The numerical simulation of a low Re airfoil requires an accurate resolution of the natural BL transition as well as the complex behaviours of laminar BL separation and the formation of a LSB. This involves an accurate prediction of the transient production and dissipation of turbulent structures across the wide range of length scales that occur in the natural BL transition process. This section describes the commonly used CFD methods for low Re airfoil simulation, their application to a BL with a LSB and the simulation parameters which impact the accuracy of the BL simulation.

The CFD methods aim to find a numerical solution for a given flow through the application of the differential equations for mass conservation and momentum conservation as well as energy conservation if solving a compressible flow. These equations are more commonly referred to as the continuity equation, Navier-Stokes equations and the energy equation, respectively. This system of equations does not have a general analytical solution for the complexities of length scales and time scales that occur within turbulent flows and therefore CFD methods apply the equations to a discretized grid and complete an iterative calculation procedure in order to find a converged solution of the flow [15]. The main CFD methods in use today are direct numerical simulation (DNS), large eddy simulation (LES) and Reynolds-averaged Navier-Stokes (RANS), which apply different approaches to numerically predict or model the turbulence in the flow. The primary distinction between CFD methods is the degree to which the turbulent structures in the flow are directly resolved versus numerically modelled. Before introducing the details of each CFD method, a review of the turbulent energy cascade is necessary to define the scales of turbulent motion and the length scales associated with the production and dissipation of turbulence.

2.2.1 Turbulent Energy Cascade

Turbulent flow contains eddies of a wide range of length scales which creates a level of complexity that is difficult to accurately predict using numerical methods. Analysis of homogeneous turbulence at very high Re reveals patterns within the behaviour at different length scales, with the larger scales associated with production of turbulent kinetic energy, and the smaller scales associated with the dissipation of this energy through viscous forces [16]. This is the fundamental theory behind the turbulent energy cascade shown in Figure 2.6 [17] and the cascade is divided into three distinct ranges of length scales. The cascade depicted in Figure 2.6 transfers energy from right to left with the right side representing the largest length scales of the energy-containing range and the left side representing the

smallest length scales of the dissipation range. The inertial subrange facilitates the transfer of the turbulent kinetic energy and is bounded by the length scale l_{EI} between the energy-containing range and the inertial subrange and l_{DI} between the dissipation range and inertial subrange.

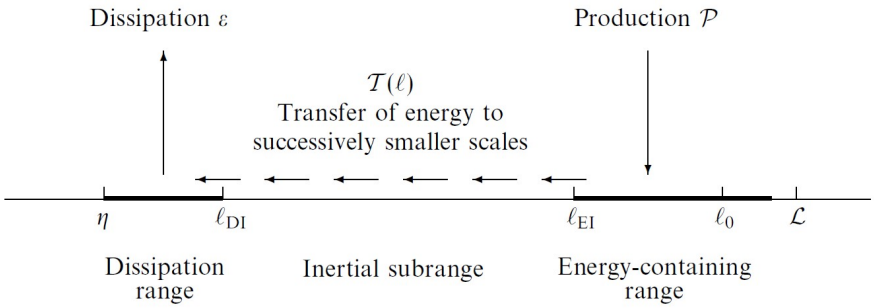


Figure 2.6: Diagram of the energy cascade for homogenous turbulence at very high Re. Reprinted with permission from Pope [17]

The energy-containing range extends from the flow scale of the problem geometry, $\mathcal{L}$, to the length scale l_{EI} and also contains the length scale of the largest turbulent eddies, l_0. The l_{EI} is approximately equal to $\frac{1}{6}l_0$ and is defined as the dividing length scale between the anisotropic large eddies of the energy-containing range and the small isotropic eddies of the inertial subrange. This division is particularly relevant to the numerical approach of the CFD methods since the isotropic eddies that occur for $l < l_{EI}$ have behaviour that is more predictable and simpler to model than the anisotropic large eddies that occur for $l > L_{EI}$ [18].

The bulk of the energy production occurs within the energy-containing range, labelled as production in Figure 2.6, where energy spectra analysis shows that approximately 80% of the turbulent kinetic energy is contained within the range $l_{EI} < l < 6l_0$ [17]. This energy is transferred through the inertial subrange to the dissipation range, where the dissipation range is for length scales ranging from an upper bound of l_{DI} to the smallest length scale, η, known as the Kolmogorov length scale. The bulk of the dissipation occurs between $8\eta < l < 60\eta$ [17].

One caveat of the application of the turbulent energy cascade to low Re airfoil CFD simulation is that the cascade applies to fully-developed homogeneous turbulence and therefore it is not directly applicable wall-bounded flows and flows with developing turbulence. Additionally, analysis of the energy spectra for the length scales present at lower Re has shown differences in the behaviour in the inertial subrange including the disappearance of

the inertial subrange entirely when an overlap between the energy-containing range and the dissipation range occurs [17]. Due to the changes in the turbulent energy cascade in low Re flows and transitional flows, the definitions of the turbulent energy cascade are only applied to the numerical simulations as guidelines from which further tests and optimization are completed.

2.2.2 CFD Methods

Now that the brief theory of the turbulent cascade has been established, the numerical approach of the common CFD methods can be described. The DNS method directly applies the conservation equations in order to resolve the turbulence across all length scales of turbulence in the flow. This requires a computational mesh that is sized to resolve the smallest length scales η in the turbulent cascade to prevent solution instability or numerical error. This is difficult to achieve without extreme computational cost due to the meshing requirements to spatially discretize the domain and is still considered infeasible to achieve high accuracy for applications with complex realistic flows, particularly at higher Re.

The wall-resolved LES method uses a combination of directly resolving and modeling the turbulence to improve the computational efficiency and stability of the flow simulation. A filter is applied to the conservation equations to remove the turbulence with length scales smaller than a set filter length, leaving only the large scale turbulence to be directly resolved [19]. The large scale structures of the energy containing range are typically anisotropic and dependent on the problem geometry, and therefore there is improved accuracy when directly solving these scales of motion. The small scale turbulence is modeled using a sub-grid scale (SGS) stress model since turbulence within the inertial subrange and dissipation range is isotropic and less dependent on the geometry. The Smagorinsky-Lilly SGS stress model [19] and its variations [20, 21] apply the Boussinesq hypothesis to relate the turbulent stresses to the velocity gradient through the eddy viscosity, μ_t. SGS models for μ_t use constants to predict the sub-grid scales of motion and "dynamic" versions [20, 21] of these models include dynamic coefficients which are calculated based on local flow parameters to improve accuracy.

The RANS method has a different approach from the transient DNS and LES methods, and instead applies Reynolds-averaging to the conservation equations to result in a time-averaged flow solution. The effect of the unsteady turbulence on the flow is represented using Reynolds stress terms in the Reynolds-averaged equations and there are many turbulence models that have been derived to model these extra turbulent shear stress terms [15]. This method requires a significantly lower computational cost but is not capable of resolving the small scale fluctuations occurring within the turbulent flow.

The prediction of tonal aeroacoustic noise and dynamic stall of a low Re SWT blade requires different CFD methods due to the level of transient detail required to predict the tonal noise versus the load fluctuations during stall. The CAA prediction method that is described in Section 2.4 requires input data from a CFD simulation that resolves the small scale transient structures within the flow and therefore a simulation to predict aeroacoustic noise requires either a DNS or LES method. The application of DNS and LES to the simulation of a LSB for low Re airfoils is discussed further in the following section.

The simulation of the dynamic stall process for a SWT blade does not require the same level of detail of the transient flow to predict the unsteady loading and therefore a DNS or LES method is not required. Additionally, the computational complexity of the unsteady flow conditions is better suited to the modelling approach of RANS methods. The simulation of dynamic stall for a low Re airfoil is discussed later in Section 2.5.4 after establishing the specifics of the unsteady flow conditions for a SWT in Section 2.5.

2.2.3 LSB Simulation

Numerous computational studies have been conducted on low Re transitional separated flow, also known as a LSB, over the past 20 years. A common method to simplify the geometry for numerical simulations uses an experimental method of a flat plate in a wind tunnel with a curved upper wall to impose the necessary pressure gradient on the surface. Using a flat plate removes the complexities of airfoil curvature by artificially adding the associated pressure behaviour, which allows control over the formation of the LSB and provides a large downstream region for a fully-developed, reattached turbulent BL. The LSB development on a flat plate has been successfully investigated with both DNS [6, 9] and LES [8, 22, 23]. The DNS study by Brinkerhoff and Yaras [6] is a good example of the detailed analysis possible when using the extended streamwise length of a flat plate in comparison to an airfoil of finite chord length. At $\mathrm{Re} = 3.26 \times 10^5$, the authors show the visualization of the roll up of the separated shear layer and subsequent formation of large scale turbulent wave-packets after reattachment. Roberts and Yaras [23] conducted LES simulations on a coarse DNS mesh which reproduced LSB velocity profiles within 15% of experimental data, which they considered good agreement. More recent LES work by Li and Yang [8] examined a flat plate with an elliptical leading edge (LE), which adds complexity when compared to the other mentioned simulations with a slip wall preceding the flat plate and no LE. At $\mathrm{Re} = 8.4 \times 10^4$ they showed the ability of LES to replicate experimental results while requiring a lesser computational expense than a DNS simulation.

However, experimental particle image velocimetry (PIV) results by Burgmann *et al.* [24] call into question the accuracy of this flat plate method through examination of a cambered

SD 7003 airfoil at the modest Re of 2×10^4. The authors found that the change in pressure gradient resulting from different experimental AOAs had a different effect on the LSB characteristics when compared to other studies which altered the pressure gradient over a flat plate.

Simulations that incorporate more complex geometry into the simulation of transitional separated flow are those using airfoil profiles, typically symmetric NACA profiles. These profiles are commonly chosen due to the well established behaviour of these airfoils through past experimental work, and new simulations fill the gaps in knowledge for the transitional separated flow that can occur at low Re. These symmetric NACA profiles have been studied using DNS [25–29] and LES [5,25,30]. The recent work by Smith and Ventikos [25] compares DNS and LES over a NACA 0012 airfoil at $\mathrm{Re} = 1 \times 10^5$ and 4° AOA to assess the impact of LES modeling techniques on the accuracy of the prediction. Ziade *et al.* [5] use LES and PIV to investigate laminar separation and transition on a NACA 0025 airfoil at $\mathrm{Re} = 1 \times 10^5$ and $5°, 12°$ AOA. The Re range for the mentioned NACA studies is generally between 1×10^5 and 5×10^5 or at a high AOA, which places the LSB close to the LE of the airfoil and results in a turbulent BL for the majority of the airfoil surface. For example, Thomareis and Papadakis [26] performed DNS studies on the NACA 0012 airfoil at a more modest Re of 5×10^4 and 5° AOA, where a LSB formed from $x/c = 0.2$ to 0.6. When compared to Smith and Ventikos, with a LSB from $x/c = 0.4$ to 0.6, it is clear that the lower Re causes an elongated LSB. However, in both cases the reattachment is well before the TE and Smith and Ventikos note their findings would not necessarily apply to cases where the BL is transitional at the TE of the airfoil [25]. These studies therefore do not attempt simulation of the interaction of the transitional BL with the TE, which is especially complex when the separated shear layer does not reattach and interacts with the flow from the pressure side. When analyzing the tonal noise generated by low Re applications such as SWTs these BL behaviours must be accurately captured by the transient flow simulation.

An application of interest that falls on the lower end of the Re range is low Re turbomachinery cascades, such as the DNS of a T106a cascade [9] and LES of a V103 compressor cascade [22]. Lardeau *et al.* [22] highlights the complexities that arise in the relatively modest Re experienced by low pressure cascades, in their case $\mathrm{Re} = 1.4 \times 10^5$, and the sensitivity of the separation bubble dynamics to the geometric, inflow, and boundary conditions of the simulation. While compressor cascades often have elongated LSBs that can be located near the TE, the geometry of airfoils specifically designed for low Re applications such as SWTs are generally cambered airfoils with a larger thickness than is found in compressor cascades.

Another significant difference between turbomachinery cascades and the cambered air-

foil applications is the boundary conditions required for the simulations. In the turbomachinery cascades there is a periodicity that occurs in the wall-normal direction due to the adjacent blades on the cascade, which constrains the flow surrounding the airfoil in a way not seen in the external flow conditions of a low Re cambered airfoil application. The channeling of the flow between two blades on the cascade will have an impact on the BL transition and is likely to result in different aerodynamic behaviour. A computational benefit is also present in the cascade, since the periodic constraint of the adjacent blade can greatly reduce the size of the required computational domain, decreasing the computational cost and time required when compared to an external flow cambered airfoil.

LES simulations of cambered airfoils at appropriately modest Re for SWTs have been previously completed using the SD 7003 airfoil [7, 31, 32] and an airfoil profile from a wind turbine blade [33]. These works have been completed for the Re range of 10^4 to 10^5 and at 4° AOA, with the exception of Galbraith and Visbal [31] which covers an AOA range from 2° to 14°. Breuer [32] and Lobo *et al.* [33] investigated the impact of inflow turbulence on the formation of the LSB, confirming that an increase in turbulence intensity causes the LSB length to decrease and eventually vanish. However, as with the other low Re airfoil simulations, the availability of experimental validation data on these less commonly investigated airfoils is limited and therefore prevents the complete validation of the LES simulation of the transitional separated BL behaviour.

The previous efforts to simulate the LSB on a low Re airfoil show that both LES and DNS can be used to predict the formation of a LSB. The use of LES is better suited to the objectives of this thesis since the lower computational expense in comparison to DNS is a more realistic option for using LES coupled with CAA as a future aeroacoustic design tool. Since LES models the sub-grid turbulent structures, this places a greater emphasis on the validation of the simulation to reduce any numerical errors introduced by the SGS model as opposed to the direct solution of the small-scale turbulence used in the DNS method. The details of the LES simulation validation are covered in Section 3.1.

2.2.4 LES Parameters

With LES selected as the ideal CFD method for the transient simulation of the LSB formation on a low Re SWT blade, there are certain simulation parameters that require review to establish best practices for the LES simulation of the LSB. The following LES parameters were found to be of particular importance for the accurate simulation of the low Re BL transition and the LSB. The implementation of these parameters in the LES simulations are described in Sections 3.2.1 and 3.2.5.

Inlet Turbulence

A known issue with LES is the accurate replication of inflow turbulence conditions since the model can be quite dissipative [15], especially when the filter lengths are improperly sized for the turbulent length scales. Dhamankar *et al.* [34] provided a comprehensive overview of turbulent inflow boundary conditions, including the challenges presented by each method. The main categories of inlet turbulence models used in prior simulations of transitional separated flow are turbulence library-based methods and synthetic turbulence generators. The DNS simulations by Wissink and Rodi [9] implemented a turbulence library-based method, determining free-stream disturbances from a LES simulation of isotropic turbulence. Similarly, Lardeau *et al.* [22] applied the inflow perturbations and spectral content from a prior DNS study conducted by other researchers.

The turbulence library method relies on precursor simulations, which is a computationally expensive method to generate reliable turbulence data and requires large amounts of data storage [34]. For this reason, synthetic turbulence generation methods are favoured for practical applications, and are included in commercial CFD software packages. Roberts and Yaras [23] used a synthetic method built-in to ANSYS CFX to generate turbulence at a specified turbulent intensity of 0.5% and length scale of 24 mm.

Accurate turbulence generation is necessary for transitional separated flow due to the sensitivity of the small scale perturbations in the transitional BL to the free-stream turbulence. Increasing turbulence results in a decrease in the bubble length [9, 22] through the upstream shift of the BL reattachment location, and turbulent intensities greater than 1% can potentially initiate a bypass transition where transition occurs due to streamwise turbulent streaks [2] rather than the natural BL transition process outlined in Section 2.1.2. The impact of changing inlet turbulence on compressor cascades has been evaluated in prior LES simulations [22], but has not been examined in the case of a cambered low Re airfoil.

The modelling of the inflow turbulence for the LES simulations in this thesis is described in Section 3.2.5.

Spanwise Boundary Condition

An important LES parameter to consider is the spanwise boundary condition, which impacts the formation of flow structures across the airfoil span. The accurate simulation of spanwise behaviour is important for the BL transition process and affects the transient behaviour of structures in the transitional BL. Spanwise differences begin to appear in

the transition region when the 2D K-H rolls begin to break down into 3D structures as the BL transitions to turbulence, as described in Section 2.1.4, and the spanwise patterns that form during this process can be amplified or dampened based on the type of spanwise boundary condition.

The symmetry boundary acts as a slip wall by applying a velocity of zero and gradients of zero normal to the symmetry plane. It can have a damping effect on the BL patterns that have a wavelength longer than the total simulated span. The periodic boundary condition uses the opposite end of the airfoil span as a neighbouring cell for calculation of velocities and gradients, essentially creating an infinitely looping mesh in the spanwise direction which can encourage spanwise patterns to develop [35]. The periodic boundary condition is the standard selection for simulating transitional separated flow [5–7, 9, 23, 26, 30–33], whereas for certain aeroacoustic simulation methods there is greater concern over the accuracy of using either spanwise boundary condition due to the long wavelengths of acoustic waves in comparison to the wavelengths of the aerodynamic structures [35, 36].

Christophe *et al.* [35] conducted a series of incompressible LES simulations to assess the influence of the spanwise boundary condition, along with spanwise mesh refinement, on the transitional behaviour of a CD airfoil at $Re = 1.6 \times 10^5$. The study had an aeroacoustic focus and concluded that a combination of spanwise mesh refinement and the periodic boundary condition resulted in improved pressure spectra at the TE (to improve the acoustic prediction) while having a negative impact on the energy spectra in the wake. In the wake region, the simulation using a symmetry boundary condition combined with spanwise mesh refinement produced the best agreement with experimental results. The authors suggest that the symmetry and periodic boundary conditions have similar performance and in both cases were improved with spanwise mesh refinement. The CD airfoil geometry is similar to a compressor blade which, as mentioned previously, is a low Re application similar to the low Re cambered airfoil, indicating potential benefits to either spanwise boundary condition for the current study.

The spanwise boundary conditions tested and final implemented boundary condition for the LES simulations in this thesis are described in Section 3.2.5.

Pressure-Velocity Coupling

The pressure-velocity coupling scheme is the general solution algorithm applied within each calculation iteration. The pressure-velocity coupling scheme can impact the accuracy of the BL simulation and alter the required computation time. The segregated schemes commonly used for LES are: "Semi-Implicit Method for Pressure-Linked Equations - Consistent"

(SIMPLEC) [37] and "Pressure Implicit with Splitting Operators" (PISO) [38]. The PISO and SIMPLEC methods are both improvements on the original SIMPLE algorithm where SIMPLEC alters the velocity correction equations and PISO includes two extra corrections to improve the momentum balance resulting in a more stable solution when a larger time step is used [15]. The use of SIMPLEC, or the original version SIMPLE, is common in transitional separated flow, as seen in [7, 8, 29] and PISO is implemented in [25, 26].

PISO can be slower than other forms of the SIMPLE algorithm but the benefit comes from the improved convergence behaviour when using a highly skewed mesh, since this can exacerbate the momentum balance issue that comes with using SIMPLE schemes [15]. In simulations of airfoils, mesh generation in regions of high curvature, particularly the LE, can result in highly skewed cells which could introduce numerical error into the simulation of the BL. Small changes in the BL simulation at the LE could change the location where the BL transition begins and any error would be propagated downstream to alter the LSB formation.

The coupling schemes tested and the final implemented scheme for the LES simulations in this thesis are described in Section 3.2.1.

Spatial Discretization

The spatial discretization scheme is used to calculate the convection and diffusion of flow properties, mainly velocity and pressure, between neighbouring cells. The spatial discretization scheme chosen for the convection terms can have a large impact on the calculated velocity values, as well as the stability of the simulation. The most commonly chosen scheme is the second order central differencing scheme (CDS), which is used in DNS simulations [6, 26, 28, 29] and LES simulations [8, 23, 25]. CDS is often chosen for transitional separated flows due to the low numerical diffusion, meaning the scheme is the most capable of accurately capturing the small scale fluctuations that are important in the BL transition and the acoustic prediction.

The caveat of CDS is the low stability which can lead to dispersion errors as was found by Smith and Ventikos [25] when applied on a mesh of insufficient density. This leads to relatively high computational costs for LES simulations, as seen by Roberts and Yaras [23], where the LES simulations were performed on a mesh density resembling one used for a coarse DNS simulation. To address stability issues with CDS, Lardeau *et al.* [22] implemented CDS with a dynamic limiter designed to prevent numerical oscillations. Smith and Ventikos [25] found success using a blended scheme, which introduces varying amounts of upwinding to provide stabilization to the convection calculations. They found that the

benefit of added stability outweighed the impact of additional dispersion errors when using a mesh density that was coarser than seen for high resolution LES analysis.

Kim *et al.* [30] implemented the "quadratic upstream interpolation for convective kinematics" (QUICK) scheme [39] for separated laminar flow over a NACA 0018 airfoil at $Re = 1.6 \times 10^5$. QUICK is a strong upwinding scheme, and produces the highest dispersion errors when compared to CDS and a blended scheme. Previous research has shown that the use of a blended or QUICK scheme can produce stable and accurate results, and allows LES simulations to move away from quasi-DNS computational costs.

The spatial discretization schemes tested and the final implemented scheme for the LES simulations in this thesis are described in Section 3.2.1.

2.3 Aeroacoustics

With the aerodynamic behaviour for a low Re airfoil BL and the relevant CFD methods thoroughly reviewed, the theory behind the sound generated SWTs can now be covered in depth. The dominant noise source for wind turbines is the airfoil self-noise that is emitted from the TE of the blades, and is a stronger acoustic source compared to the other noise sources such as mechanical noise and noise emitted from the blade tips [40, 41]. The majority of the airfoil self-noise is generated from the outer portions of the blade where the relative velocity of the blade is higher and this is also the region of the blade with the largest contribution to the power production of the wind turbine. An explanation of the relative velocity of wind turbine blades is provided in Section 2.5.1. This poses a challenge for the aeroacoustic design of wind turbine blades, as the focus of the design is to maximize the power contribution from the outer portions of the blade and noise reduction strategies may result in a drop in the efficiency of power extraction from the wind.

This section describes the mechanisms by which airfoil self-noise is generated and section 2.4 describes the CAA methods that can be used to improve the aeroacoustic performance of SWT blades.

2.3.1 Semi-Empirical Airfoil Self-Noise Prediction

Current aeroacoustic design for wind turbine airfoil self-noise is addressed using semi-empirical models [40], where large experimental data sets are used to determine trends in noise generation to establish generalized models. The wind turbine design and simulation

software OpenFAST released by the National Renewable Energy Laboratory (NREL) includes these semi-empirical airfoil self-noise models [42, 43] and applies it to segments of the blade based on local flow parameters to determine the total noise generated by the blade. This prediction consists of two semi-empirical models: Amiet's model for turbulent inflow noise [44] and the Brooks, Pope and Marcolini (BPM) semi-empirical model for airfoil self-noise prediction [45].

Amiet's model addresses the interaction of turbulence in the incoming wind with the LE of the blade which produces broadband noise across a wide range of frequencies [46]. The BPM model includes equations for airfoil self-noise mechanisms that generate noise from the airfoil TE based on extensive experimentation of the NACA 0012 airfoil at varying Re and AOAs [45]. The NACA 0012 airfoil is a symmetric airfoil profile that is commonly used for research however it does not feature the camber used in airfoil profiles designed for operating at low Re. This can require additional experimentation to attempt to tune the Amiet and BPM models to match the noise generation of the specific blade design [40]. These semi-empirical models provide a useful baseline for the expected noise generated by the SWT blades and the accurate aeroacoustic design of SWTs requires a more detailed analysis of the specific airfoil profile.

2.3.2 Defining Sound

The theory of airfoil self-noise generated by SWT blades falls within the larger category of aeroacoustics, which is the study of sound generated by turbulence as well as the unsteady forces arising from fluid-structure interaction. Sound is a source of energy loss in aerodynamic problems and is generally considered to be a negligible loss in the analysis of low speed flows, similar to how the generation of heat through the dissipation of turbulence is often neglected in aerodynamic analysis. Predicting airfoil self-noise therefore requires the calculation of the rate of conversion from the kinetic energy of fluctuations in the flow to the acoustic energy propagated through the fluid as sound waves.

Sound travels as a longitudinal wave, which is defined as the compression and rarefaction of the fluid in the direction of wave propagation. This longitudinal wave results in low amplitude fluctuations of pressure and density that are perceived as sound when interacting with the human ear or an acoustic receiver. The wave propagates at the speed of sound, c, which is a measured fluid property based on how rapidly the molecules in the fluid are able to propagate the compression and rarefaction. Sound is the term used to describe the transmission of these waves without judgement on the quality of the sound, while noise refers to undesired sound. When discussing the theory behind various acoustic prediction

methods, the general term of *sound* will be used and any discussion of the undesired sound from airfoils will use the term *noise*.

Sound is measured using pitch and volume, where the pitch corresponds to the frequency of the sound wave and the volume corresponds to the amplitude of the wave. The human ear is capable of hearing pitches in the range of 20 Hz to 2×10^4 Hz [47] and volumes ranging from a root mean square (RMS) of pressure amplitude, $\hat{p}$, of 2×10^{-5} Pa to 200 Pa [46]. The volumes are typically reported using sound pressure level (SPL), L_p, which is a logarithmic parameter that is measured in units of decibels (dB). The SPL is calculated using

$$L_p = 10 \log \left(\frac{\hat{p}^2}{\hat{p}_{ref}^2} \right) \tag{2.8}$$

where $\hat{p}_{ref}$ is the RMS of the reference acoustic pressure which has a value of 2×10^{-5} Pa [46]. The range of human hearing is from a SPL of $L_p = 0$ dB to $L_p = 140$ dB, where 140 dB is the threshold for pain.

The sound measured in real world applications is made up of a combination of sound waves at different frequencies and amplitudes which are measured at a far-field location, which is a location distanced from the source by at least one acoustic wavelength. To analyze the makeup of the sound waves, measurements are often presented as the SPL spectrum of the signal. Fast Fourier transform (FFT) is used to determine the pressure amplitude for a frequency band width of Δf, which is then converted to the SPL for the different frequency bands. These spectra can be presented as a broadband spectrum or a narrowband spectrum where broadband refers to a wide range of frequencies and narrowband focuses on a specific frequency range. These spectra can be used to identify the levels of broadband or tonal sound, with broadband sound occurring at a similar SPL over a wide range of frequencies and tonal sound occurring at a high SPL for a narrow frequency range. Acoustic analysis is also commonly summarized using octave bands associated with musical octaves, where the upper bound of an octave is double the frequency of the lower bound. The octave band analysis is useful for assessing the overall patterns in broadband sound, and the broadband and narrowband spectra are useful for identifying tonal components in the sound. Due to the focus on tonal noise generated by low Re airfoils, the acoustic results presented will use narrowband spectra to analyze the frequencies of the tones and relate them to the transitional BL behaviour and the LSB.

2.3.3 Airfoil Self-Noise

Airfoil self-noise is a result of the interaction between the transient pressure fluctuations in the airfoil BL and the airfoil surface, and is dominated by noise generated at the airfoil TE. Aeroacoustic analysis has shown that sharp edges, including the airfoil TE, within flows efficiently scatter kinetic energy from turbulent fluctuations as acoustic energy leading to a higher sound intensity than is generated at the airfoil surface or from any turbulence in the wake [48]. The diffraction of waves around the edge and the resulting interference of the sound waves in the vicinity of a sharp edge for a flat plate creates a directivity of $\sin^2(\theta/2)$ [48] and an airfoil with a sharp TE will generate a similar directivity [47]. The directivity represents the changes in the intensity of the sound depending on the radiation direction, and the approximate directivity for airfoil TE noise is shown in Figure 2.7(c) [41]. An observer on the ground will only hear noise from a wind turbine blade when in the downwards portion of the rotation due to this noise directivity pattern. Though the blade is constantly generating this TE noise, the rotation of the blade leads to an amplitude modulation in the noise [41] that can increase the annoyance [40] if above background noise levels of the given environment.

The range of frequencies and sound intensities of the generated noise is dependent on the transient behaviour present in the airfoil BL at the sharp TE. The flow parameters and airfoil geometry will result in either a laminar, turbulent or separated BL at the TE, and each flow condition has an associated airfoil self-noise mechanism. These mechanisms were defined during the creation of the BPM model [45], which was introduced in Section 2.3.1. The dominant airfoil self-noise mechanisms for low Re airfoils are turbulent BL-TE (TBL-TE) and laminar BL-vortex shedding (LBL-VS), with visualizations shown in Figure 2.7(a) and 2.7(b).

The TBL-TE mechanism [45] creates broadband noise which is described as a swishing sound and contains acoustic pressure fluctuations across a wide range of frequencies. The noise is generated by eddies contained within the turbulent boundary layer, which scatter their energy in the form of acoustic pressure when passing the sharp trailing edge [46]. For large wind turbines operating at high Re, the TE noise from the blades is generated through the TBL-TE airfoil self-noise mechanism. Broadband noise is difficult to mitigate, since it is caused by the turbulence that is inherent to the turbulent BL. Strategies for reducing TBL-TE noise typically involve modifying the boundary layer interaction and directivity at the trailing edge with brushes or saw-tooth serrations [40, 49].

The LBL-VS mechanism creates broadband noise with tonal components which can be described as a whistling noise. The sound is produced as the laminar BL passes over the TE creating vortex shedding at a regular frequency and with a high spanwise coherence.

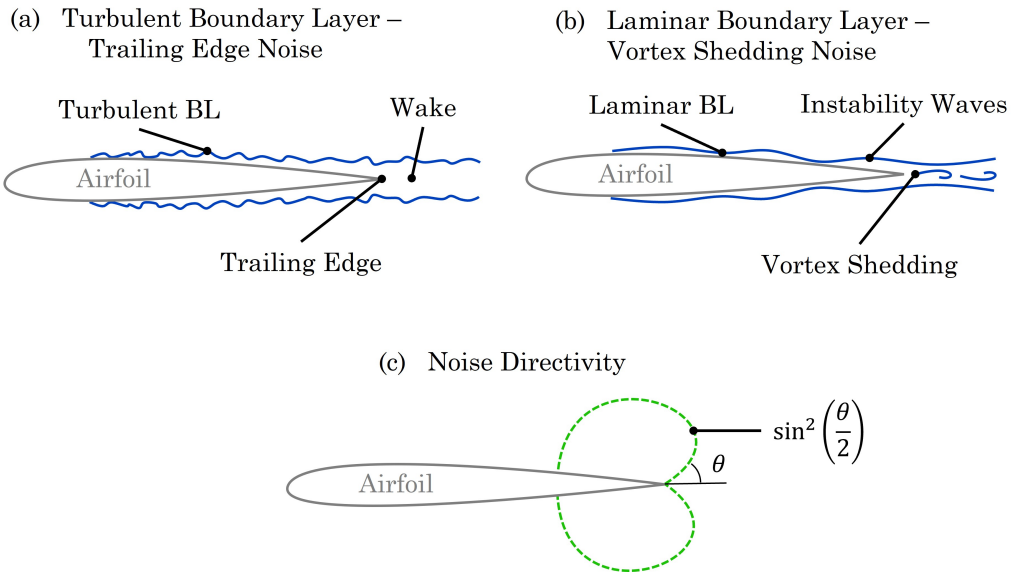


Figure 2.7: Airfoil self-noise mechanisms (a) Turbulent BL-TE and (b) Laminar BL-Vortex Shedding. Modified from [45]. (c) Airfoil self-noise directivity. Modified from [41]

Due to the organized nature of a laminar BL in comparison to the random fluctuations of a turbulent BL, there is little variation in the vortex shedding across the span leading to high spanwise coherence. The consistent TE pressure and velocity fluctuations across the span creates a loud tone at the vortex shedding frequency [50] and the smaller fluctuations within the vortex shedding create broadband noise across a wider range of frequencies. SWTs operating in a low Re regime generate noise through either the LBL-VS or TBL-TE noise depending on the blade design and operating conditions [46,51]. It is well established that laminar BL tonal noise can be mitigated by tripping the suction side BL [46] to change the noise mechanism to TBL-TE however, this method is not ideal for airfoils designed for use in low Re applications since the airfoil profile is optimized to take advantage of the laminar BL.

While the LBL-VS mechanism was defined with TE vortex shedding in mind [45], the regular frequency structures at the TE can originate from within a transitional BL or in a LSB [46]. Several experimental works have proven that K-H rolls at the TE, as described in Section 2.1.4, are often responsible for the tonal TE noise for low Re airfoils [52–56] and it has been experimentally shown that K-H rolls at the airfoil TE occur at a different frequency than the expected TE vortex shedding frequency [57]. The different frequencies of the flow structures present in the transitional BL and LSB will introduce differing tonal

frequencies that are not accounted for in the original BPM model. Therefore for the aeroacoustic design of SWT blades, a more detailed acoustic prediction method is required to predict and mitigate the tonal noise generated by a laminar or transitional BL.

The airfoil self-noise mechanisms were also defined using data collected for the NACA 0012 airfoil, which has more recently been shown to have simultaneous suction side and pressure side LSBs contributing to the tonal noise generation [53, 54, 56]. These works identify a complex interaction of the K-H rolls from the pressure and suction side BLs at the TE, where the suction side is the dominant tonal noise source at lower Re and the pressure side dominates at higher Re. However, for cambered low Re airfoils such as the controlled-diffusion (CD) airfoil [58] and SD 7003 airfoil [56] the tonal noise source has been found to originate from K-H rolls from a suction side LSB only. This highlights the importance of accurately capturing the BL transition and LSB location for low Re airfoil simulations, since the structures present at the TE could interact to generate complicated tonal TE noise.

2.3.4 Acoustic Feedback

The LBL-VS mechanism includes a proposed acoustic feedback process [45] or acoustic coupling [46, 59] where acoustic waves travel upstream to the unstable laminar BL and initiate the formation of BL structures at the tonal noise frequency. The use of NACA 0012 by Brooks *et al.* has led to many researchers selecting NACA 0012 for analysis of this acoustic feedback process, but the complexity of the pressure side and suction side LSB has resulted in many intricate theories on acoustic feedback that may only apply to the unique LSB placement of the NACA 0012 airfoil. The overarching theme of the proposed feedback loops is that the acoustic pressure waves originating at the TE travel upstream and amplify the disturbances (i.e. T-S waves) in the laminar BL [45, 60–65]. The feedback loop is illustrated in Figure 2.8(a) based on the description by Longhouse [63] for the feedback loop on low Re axial fan blades. The now amplified T-S waves propagate downstream in the BL and result in BL transition structures with an amplified pressure fluctuation at the TE thus generating louder tonal noise and creating a positive feedback loop. The feedback is said to "lock" the frequency of the BL transition structures onto the acoustic frequency.

The acoustic feedback process creates a ladder structure in the dominant tone frequency where an increasing Re for a given AOA will result in a discontinuity in the dominant tone frequency trend as it jumps to a higher frequency. This ladder structure is illustrated in Figure 2.8(b) where the overall trend of the dominant tone frequency for the ladder

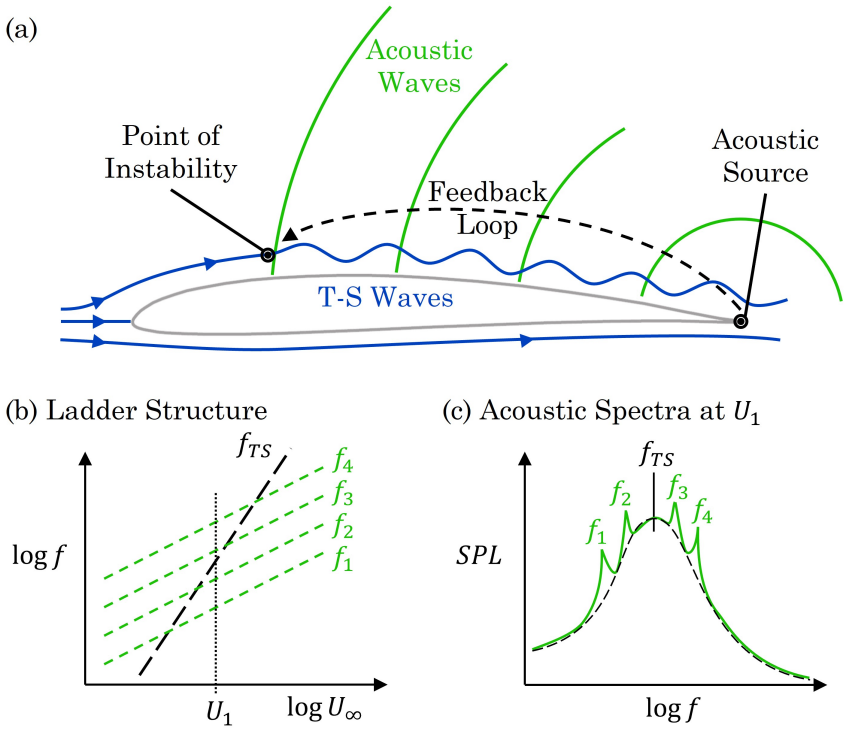


Figure 2.8: (a) Acoustic feedback loop diagram for tonal TE noise modified from [63], (b) dominant tone frequency ladder structure and (c) sample acoustic spectrum for a sample free-stream velocity $U_\infty = U_1$ modified from [66]

structure scales with $f \propto U_\infty^{1.5}$ [60] which is shown by the black dashed line labelled f_{TS}. The exact dominant tone frequency jumps between ladder "rungs" which scale with $f \propto U^{0.8}$ [60, 61], which are shown in 2.8(b) with green dashed lines. This structure is generated because a laminar BL is susceptible to excitation of T-S waves at a range of frequencies [2] and therefore the acoustic waves may amplify numerous T-S wave frequencies depending on the phase change between the two locations [67]. Figure 2.8(c) shows a sample acoustic spectrum for the free-stream velocity U_1 in the Figure 2.8(b) ladder structure [66]. The resulting acoustic spectrum features a broadband hump centred on the dominant T-S wave frequency, f_{TS}, where the width of the broadband hump corresponds to the T-S wave frequency range. Superimposed on the broadband hump is a series of regularly spaced tones that correspond to the acoustically amplified T-S frequencies of the ladder structure. For the sample spectrum, the tone at f_3 is the dominant tone however the f_2 tone is still present in the spectrum at a similar magnitude.

It should be emphasized that the acoustic feedback does not generate tones at frequencies not inherently present in the natural BL transition process for the airfoil. The feedback can amplify the SPL at frequencies within the broadband hump corresponding to the T-S wave frequency range above the SPL of other tones in the T-S wave frequency range. This causes the ladder structure of the dominant tone frequencies, where a change in Re can switch which of the existing tones is most amplified and causes a perceived jump in the tone frequency. However, when examining the corresponding acoustic spectra used to construct the ladder structure plots this jump to the next ladder rung merely means the amplification of one tone has overtaken the other while both tones remain at a similar SPL, as is shown in Figure 2.8(c). In terms of aeroacoustic design, all of these tone frequencies in the ladder structure should be considered rather than solely the dominant tone for the given Re as this can present a misleading picture of the tonal noise behaviour of the given airfoil.

This ladder structure has been theoretically estimated [66] using a stability theory analysis of the pressure side of the NACA 0012 airfoil to determine that the central T-S wave frequency scales proportional to $U_\infty^{1.55}$ and that the discrete tones align with the expected ladder runs proportional to $U_\infty^{0.8}$. The method for the calculation of the ladder tone frequencies was proposed by Kingan and Pearse [67], where the total phase change between the initial T-S instability and the returning acoustic wave are determined by combining: the phase change of the T-S wave propagation between its initiation location and the TE, a positive 180° phase change due to the dipole acoustic source at the TE, and the phase change of the acoustic wave propagation to the T-S wave initiation location.

The focus on the ladder structure originates from the rigorous study of the NACA 0012 symmetric airfoil where both a suction side and pressure side LSB occur near the TE and contribute to the tonal noise to create a complex acoustic feedback structure that has led to many proposed feedback loops [45, 60–62, 64, 65]. For tone frequency trends measured at low AOAs for NACA 0012 [53, 54, 56], this ladder structure is more evident at $Re > 1 \times 10^5$ where the pressure side LSB has been identified as the dominant tonal noise source while the suction side LSB, located further upstream from the TE, also contributes to the tonal noise.

However, cambered airfoils that are designed specifically for low Re operation have often been found to only have a suction side LSB contributing to tonal TE noise [56, 58, 63] which reduces the complexity of the BL interaction at the TE. The absence of the pressure side LSB appears to weaken the ladder structure as is shown in the results of Yakhina *et al.* [56] for the SD 7003 airfoil, where at $Re > 1 \times 10^5$ the dominant tone meanders without adhering to specific rungs of the ladder structure. Therefore it seems possible that the ladder structure is less pronounced on certain cambered airfoils designed for operation in

a low Re regime due to the absence of the pressure side LSB. Additionally, the study of modest Re of less than 1×10^5 for the cambered airfoils as well as NACA 0012 shows a consistent trend of one to two dominant tones at low AOAs rather than the multiple tones that are necessary to produce the abrupt jumps in the dominant tone frequency found in a ladder structure. The scope of this thesis does not include the analysis at multiple Re therefore the ladder structure will not be examined. The feedback process that generates the ladder structure will still need to be considered for its role in the amplification of tonal noise SPL.

2.4 Computational Aeroacoustics

Fully-analytical CAA methods are capable of predicting the sound emitted from a fluid flow without the use of experimental data. The methods predict the amount of kinetic energy of the flow converted to acoustic energy and the propagation of the generated acoustic waves away from the source. CAA methods require a detailed, transient flow field provided by a CFD simulation to determine the source of the sound and how it will propagate. The CAA methods can be divided into two main subcategories: direct computation and acoustic analogy [68].

In direct CAA, also called direct noise computation (DNC), the aerodynamic and aeroacoustic fields are calculated simultaneously using a compressible CFD method which computes the propagation of sound waves through the flow field. DNC is capable of predicting the reflection and diffraction of sound waves as well as the development of acoustic feedback, as described in Section 2.3.4, where the acoustic waves trigger instabilities in the aerodynamic BL behaviour. This method is challenging and computationally expensive to complete since it requires high-fidelity compressible flow simulations to prevent excess numerical dissipation of the low energy acoustic field [69] as well as fine mesh sizing requirements between the source and the receiver [70].

An acoustic analogy simplifies the CAA solution by assuming that a bounded region in the flow can be solved as an acoustic source and the sound can then be linearly propagated in the surrounding area using the general wave equation [71, 72]. The quality of the aeroacoustic prediction from an acoustic analogy is dependent on the quality of the transient CFD simulation of the pressure and velocity fluctuations within the acoustic source region. In comparison to DNC, the CFD simulation is of lower computational expense since it is not required to account for the compressibility associated with acoustic wave propagation and the mesh requirements for adequate flow resolution are restricted to the acoustic source region only rather than the entire domain. The acoustic analogy method is limited

to flows at a low Mach number with an unobstructed path from the source to the far-field receiver, which is the case for complex rotating flows such as propellers and helicopter rotors [68, 73] and therefore is an ideal method for aeroacoustic prediction of SWTs. The following sections include a detailed description of the theory behind and development of the acoustic analogy for prediction of noise generated by flows around solid surfaces which includes, but is not limited to, the flow around airfoils.

2.4.1 Acoustic Analogy

The propagation of small amplitude sound waves is governed by the homogeneous wave equation which has many applications outside of acoustics and has well-established solutions. The general form of an acoustic analogy is an inhomogeneous wave equation, meaning a wave equation with source terms, and is derived from the application of conservation of mass and momentum to a fluid region containing turbulent flow. In order to determine the strength of the sound source, the relationship between the turbulent fluctuations in the fluid and the acoustic source strength must be derived.

A proportional relationship between the density, ρ, and the hydrostatic pressure, p,

$$p = c^2 \rho \tag{2.9}$$

where c is the speed of sound is used to represent the compression and rarefaction of a fluid when a longitudinal acoustic wave propagates through a fluid at rest [71]. This hydrostatic pressure can be interpreted as the acoustic energy required to generate the acoustic wave propagation in a fluid at rest. When a fluid is in motion, this acoustic energy is still present but it is masked by the significantly larger magnitude pressure and density fluctuations associated with the turbulent kinetic energy of the flow. Acoustic energy is a type of energy loss that is typically neglected in aerodynamic analysis due to its low magnitude, however to determine the strength of the sound source the acoustic energy must be accounted for and subtracted from the kinetic energy of the flow. Since Equation 2.9 is in the form of a normal stress, this energy lost to acoustic energy must be subtracted from the total representative stresses acting on the fluid. This is accomplished through Lighthill's tensor [71],

$$T_{ij} = \rho u_i u_j + p_{ij} - c^2 \rho \delta_{ij} \tag{2.10}$$

where u is the velocity component in the i or j direction, p_{ij} is the stress tensor including normal and shear stresses and δ_{ij} is the Kronecker delta. This tensor includes the momentum flux term, $\rho u_i u_j$, (also called fluctuating Reynolds stresses) which are representative

stresses to account for the momentum of the turbulent flow [71]. The final term is the subtraction of the energy lost to the acoustic wave propagation which is applied in the normal stress direction only to be consistent with Equation 2.9.

The substitution of Lighthill's tensor into the conservation of momentum equation and combination with the conservation of mass equation was used to derive Lighthill's acoustic analogy [71]

$$\frac{\partial^2 \rho'}{\partial t^2} - c^2 \frac{\partial^2 \rho'}{\partial x_i^2} = \frac{\partial^2 T_{ij}}{\partial x_i^2 x_j^2} \tag{2.11}$$

here written for the propagation of density fluctuations, $\rho' = \rho - \rho_0$, where ρ_0 is the density of the fluid at rest. This is accompanied by the following form of the Lighthill's tensor

$$T_{ij} = \rho u_i u_j + p_{ij} - c^2 \rho' \delta_{ij} \tag{2.12}$$

for density fluctuations. When assuming negligible viscous stresses and energy lost to heat conduction, Lighthill's tensor can be simplified to $T_{ij} = \rho u_i u_j$, meaning the acoustic source is dependent on the fluctuating Reynolds stresses of the flow. Lighthill's analogy requires the transient details of the velocity within the turbulent flow field to be able to calculate the source of sound through Lighthill's tensor on the right hand side of Equation 2.11. This source is then propagated to the far-field as density fluctuations using the wave equation terms on the left hand side of the Equation 2.11. The solution to the analogy results in a quadrupole directivity where the strength is dependent on Lighthill's tensor [71]. Lighthill's analogy was developed for predicting the aeroacoustic noise from free jets [74], and has a restriction that the flow must be unbounded and therefore is not applicable to flows around a body.

The expansion of Lighthill's acoustic analogy to include solid surfaces was first completed by Curle [50], by utilizing a differing solution of the inhomogeneous wave equation which includes surface integrals. The resulting solution includes the quadrupole term from Lighthill's solution as well as an additional term that represents the surface as a series of dipole sources. Dipoles are an elementary solution to the homogenous wave equation and are a result of a fluctuating force field applied to the fluid [46]. For a turbulent flow in contact with a solid surface, the source strength of the dipoles is dependent on the fluctuating force acting on the fluid by the surface. The solution also proves that the quadrupole sources from free-stream turbulence will have a frequency that is double the frequency of the velocity fluctuations, whereas dipole sources have a frequency the same as the velocity fluctuations [50].

An improved solution to Lighthill's analogy was completed by Ffowcs-Williams and Hall [48] which focused on the inclusion of sound emitted from the sharp edges of a half-plane. The new solution applied a Fourier transform and used Green's functions to be

able to account for the diffraction of the sound waves at the sharp edge without requiring any limiting conditions that dampened the effect in previous solutions. When turbulence reaches the edge of a surface, the forces acting on the fluid from the surface that generate the dipole sound source abruptly disappear and are replaced by forces from the adjacent fluid. This change results in additional kinetic energy being transferred to acoustic energy, and for this reason sharp edges are referred to as efficient scattering centres for acoustic energy [48]. The diffraction and interference of the propagated sound waves around the sharp edge results in a directivity pattern of $\sin^2(\theta/2)$, which was shown for an airfoil with a sharp TE in Figure 2.7(c), where no sound is propagated downstream from the edge of the half-plane surface into the wake. The generated sound is of higher intensity than both the quadrupole source from the flow turbulence and the dipole source from the solid surface [48], therefore it is important to ensure the solution to the acoustic analogy includes the sound emission from any sharp edge present.

The extensions of Lighthill's analogy by Curle and Ffowcs-Williams and Hall were incorporated into a generalized analogy for turbulent flow around solid surfaces in motion, called the Ffowcs-Williams and Hawkings (FW-H) acoustic analogy [75]. This analogy and its implementation in CFD software are described in the following section.

2.4.2 FW-H Acoustic Analogy

The FW-H acoustic analogy [75] is an inhomogeneous wave equation that includes three source terms to determine the generation of sound from turbulent flow over a surface in arbitrary motion. The analogy has a general form so as to be applicable in a wide range of fluid-structure interactions and includes Lighthill's quadrupole source term [71], a dipole source term at the surface [50] and a monopole source term to represent the surface acceleration. The surface-related source terms include the surface function, f, that describes the shape of the surface and its motion throughout the domain with time [75]. The function defines regions of $f < 0$ as solid, $f > 0$ as fluid and is equal to zero at the surface. The function is included in the form $\delta(f)(\partial f/\partial x_i)$ where the delta function is zero everywhere except the surface, and the partial differential applies the source outwards from the surface into the fluid. An example of the implementation of this function is shown in Figure 2.9 for an airfoil surface defined by a body contour, S.

Using this new surface function, the analogy is as follows

$$\frac{\partial^2 \rho'}{\partial t^2} - c^2 \frac{\partial^2 \rho'}{\partial x_i^2} = \frac{\partial^2 T_{ij}}{\partial x_i^2 x_j^2} - \frac{\partial}{\partial x_i}\left(p_{ij}\delta(f)\frac{\partial f}{\partial x_j}\right) + \frac{\partial}{\partial t}\left(\rho_0 v_i \delta(f)\frac{\partial f}{\partial x_i}\right) \tag{2.13}$$

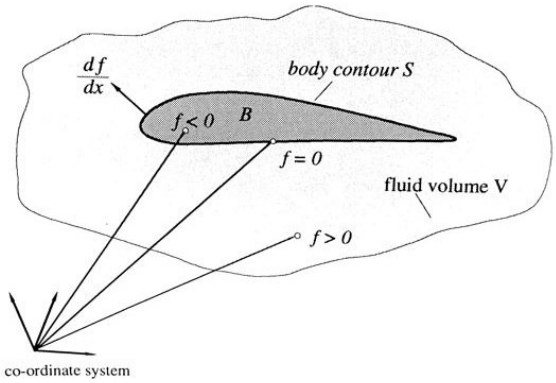


Figure 2.9: Definition of function, f, used for calculating sound sources generated by a surface defined by body contour, S. Reprinted with permission from Wagner *et al.* [46]

where T_{ij} is of the form of Equation 2.12, p_{ij} is the compressive stress tensor and v_i is the normal velocity of the surface in the x_i direction. The source term which includes p_{ij} is the dipole source, as derived by Curle [50], which is dependent on the fluctuating forces (or loading) on the surface and is therefore commonly referred to as the loading noise term [73]. The term including the time derivative of surface velocity v_i is in the form of a monopole source, which is another elementary solution to the homogenous wave equation which represents the surface motion as the addition or removal of mass [46]. This monopole term is also called the thickness noise term [73]. From this equation, it is clear that the sound generated by the interaction of the flow with a solid surface can be represented by a distribution of acoustic source monopoles and dipoles along the surface.

The solution to the FW-H inhomogenous wave equation is presented as a summation of the solutions to the three individual source terms [75]. The solution uses the Fourier transform and Green's function method laid out by Ffowcs-Williams and Hall [48] to capture sharp edge noise. The solution to acoustic analogies are concerned with measuring the acoustic pressure at a far-field location, as a microphone would measure, therefore the solutions for each term are presented as acoustic pressure fluctuations p' where $p' = c^2\rho'$ as was introduced in Equation 2.9. The solution then appears as

$$p'(\vec{x},t) = p'_Q(\vec{x},t) + p'_L(\vec{x},t) + p'_T(\vec{x},t) \tag{2.14}$$

where p'_Q is the acoustic pressure fluctuations for the quadrupole source, p'_L is for loading noise and p'_T is for thickness noise. The solutions also account for the propagation time for the sound wave to travel from the source to the far-field receiver location, and includes the retarded time, τ, which is the time that an acoustic wave was generated at the source

in order to reach the receiver at time, t [46]. A limitation of the solution to Lighthill's analogy and the FW-H analogy is that it applies to source regions that are acoustically compact. Acoustical compactness is a condition where a source region of size l must have acoustic wavelengths, λ, that are much larger in length [75]. Airfoil self-noise is considered to be acoustically compact [71] particularly for applications with little to no interference from reflecting sound such as wind turbines or helicoper/drone rotors [68]. This condition simplifies the calculation of the sound propagation to the far-field since it assumes a point source and does not consider the negligible change in retarded time from different sources within the source region [46].

The implementation of the FW-H analogy in CFD codes has resulted in a modified solution by Brentner and Farassat [73] which rearranges the solution terms to isolate the commonly used form of the conservation variables ρ and ρu_i. This solution is implemented in the commercial code ANSYS Fluent and uses the Formulation 1A [73] solutions for p'_L and p'_T and the solution for p'_Q are presented in detail by Brentner [76]. An additional modification is removing the requirement that the surface defined by the function f must be coincident with the solid surface and instead introduces a permeable surface that can be offset from the solid surface to include quadrupole sources in the turbulent flow. In the case of airfoil self-noise, the quadrupole source term is often neglected for low speed flows since the noise generation is dominated by the thickness and loading noise terms [73]. Therefore implementation of FW-H in CFD codes omits the calculation of quadrupole sources unless a permeable surface is used to enclose a portion of the turbulent flow. This emphasizes the importance of the small-scale transient data in the CFD simulation of a low Re airfoil BL, since the calculation of the thickness and loading noise sources are dependent on the flow parameters at the surface of the airfoil.

2.4.3 CAA of Low Re Airfoils

The application of CAA methods to low Re airfoils requires accurate transient simulation of the flow around the airfoil from a DNS or LES simulation. The prediction of airfoil self-noise at low Re requires a highly accurate prediction of the transient behaviour of the structures in the BL transition, including the K-H rolls formed in the LSB. These transient BL behaviours are discussed in Section 2.1.4 and their relation to the airfoil self-noise mechanisms is described in Section 2.3.3. The numerical approach for the DNS and LES simulation of a low Re transitional BL and LSB is discussed in detail in Section 2.2.3 as well as the challenge of validating the aerodynamic behaviour due to the absence of detailed experimental data. Recent CAA research takes advantage of increasing computational

power and uses direct CAA methods to predict the tonal TE noise and the amplification of the tonal noise through the acoustic feedback process outlined in Section 2.3.4.

Direct CAA is used to generate a detailed prediction of the near-field acoustic behaviour using compressible DNS or LES [58, 69, 77] and predicts the interaction of the acoustic waves from multiple sources within the BL as well as the acoustic feedback process. The far-field acoustic behaviour is then predicted using an acoustic analogy to propagate the acoustic behaviour to a receiver location that is typically outside of the computational domain. The acoustic analogies are used for far-field acoustic prediction for compressible DNS and LES simulations (i.e. direct CAA methods) [58, 77] and are used for acoustic prediction from incompressible LES simulations which omit the more complex effects of acoustic feedback [59]. These CAA simulations primarily focus on the validation of the results through comparisons of the simulated acoustic spectra with experimental spectra and often do not fully validate the transient BL development of the BL transition or the formation of the LSB. The simulated works summarized in this section apply CAA methods to low Re cambered airfoils with an elongated LSB and feature results that are fully validated using a combination of aerodynamic and aeroacoustic experimental data.

Direct CAA has been performed on low Re compressor blades that have elongated LSBs to study the tonal noise sources, particularly for the complex case where the LSB is near the TE [78]. The DNS work by Sanjose *et al.* [58] of a CD airfoil at $Re = 1.5 \times 10^5$ and 5° AOA identified the K-H rolls in the LSB located near the TE as the source of the tonal TE noise. The far-field acoustic prediction was generated through the application of the FW-H acoustic analogy using the DNS simulation data at the airfoil surface. The predicted acoustic tones occurred in a similar frequency range to the experimental tones, with a difference of 0.2 kHz in the dominant tone frequency and a minor under-prediction of the tone SPL. They also identified intermittency in BL transition which resulted in "intense" periods with tonal noise and energetic K-H rolls at the TE and "quiet" periods without tonal noise and thin K-H rolls. Later experiments by Jaiswal *et al.* [55] of the CD airfoil at $Re = 1.4 \times 10^5$ and 5° AOA found intermittency in the dominant tone and confirmed the K-H rolls at the airfoil TE as the source of the tone. Modal analysis of the tomographic particle image velocimetry (PIV) results showed that the 2D K-H rolls undergo 3D breakdown upstream of the TE, which is assumed to be related to the detected tone intermittency.

The Ffowcs-Williams and Hall acoustic analogy, which is a similar formulation to FW-H described in Section 2.4.1, was applied to the NACA 6512-63 airfoil at a Re of 1.9×10^5 by Winkler *et al.* [59] to predict the broadband noise spectrum. They used an incompressible LES simulation to simulate the LSB in close proximity to the TE where the BL transition in the LSB featured spanwise vortical structures which broke down into smaller structures

at the TE. The resulting acoustic prediction featured a broadband hump rather than a distinct tone which was in agreement with experimental acoustic spectra. The broadband hump was associated with the pressure fluctuations within the LSB due to the broken down spanwise vortical structures.

The LSB has also been identified as a source of tonal noise when located near the airfoil LE, which typically occurs at higher AOAs or at Re at the higher end of the low Re range. The DNS simulations of the CD airfoil at $Re = 1.5 \times 10^5$ and 8° AOA by Wu *et al.* [77] identified a LSB near the airfoil LE ($x/c < 0.1$) as a source of noise separate to the turbulent BL TE noise and noise generated in the near wake. They found that the far-field acoustic spectra predicted using FW-H was dominated by the turbulent BL and wake noise and therefore no tonal noise from the LSB propagated to the far-field receiver location. The compressible LES simulations by Deuse and Sandberg [69] of the CD airfoil at $Re = 1 \times 10^5$ and 8° AOA also found the LSB near the LE ($x/c < 0.2$) to be a separate source of sound from the TE noise, however their results showed that the tonal LSB noise was a dominant source. They found that the pressure fluctuations from the LSB convect downstream to the TE to contribute to the TE noise and an acoustic feedback loop between the TE and the LSB. It should also be noted that their LES simulations were validated against a DNS simulation rather than experimental data.

It is unclear from these DNS and LES simulations [69, 77] if a low Re airfoil with a LSB located upstream of the TE should have the LSB-related frequencies present at the TE. Deuse and Sandberg [69] speculate that the inclusion of the effects of the shear layer from an open jet wind tunnel, as is done in the simulations by Wu *et al.*, interferes with the acoustic behaviour of the LSB. The open jet anechoic wind tunnels typically used for aeroacoustic analysis have a shear layer form at the edges of the open jet which has been shown to alter the aeroacoustic noise measured for the same airfoil across different wind tunnel facilities [78]. This poses a challenge for validating simulations using a free-stream flow condition against the experimental data from open jet wind tunnels. Therefore it is common to include the installation effects of the wind tunnel shear layer in compressible DNS and LES simulations to simulate the alteration of the acoustic wave propagation and the acoustic feedback process [58, 77]. However, the far-field microphones used to measure the acoustic spectra of the low Re airfoil are located outside of the open jet shear layer and therefore experiments and simulations with the open jet shear layer could limit the validation of the LSB as a source of tonal noise. This highlights the importance of understanding the limitations of the validating acoustic data and why it is critical to have simultaneous validation of the CFD and CAA results for simulations of low Re airfoil tonal noise.

The numerical methods applied in this work for the CFD and CAA simulations of tonal

noise generated by low Re SWT blades are described in Section 3.2 and the validating experimental data for the simulated cases is summarized in Section 3.1.

2.5 Dynamic Stall

The dynamic stall that occurs under unsteady wind conditions is another challenge facing the design of SWTs. The prior sections discussing the low Re BL development and associated airfoil self-noise have assumed that the low Re airfoil is operating at a static AOA, however for a SWT in unsteady wind conditions there can be a significant change in the blade AOA throughout one complete rotation. This has an impact on the formation of the BL transition and LSB of the SWT blade and can induce the process of dynamic stall on the blade. This will in all likelihood lead to unique aeroacoustic behaviour for the SWT blade, however the analysis of dynamic stall in this work focuses on the effect on the transitional BL and LSB as well as the change in the aerodynamic forces on the blade. In this section, the theory behind the dynamic stall process on SWT blades is reviewed followed by a summary of the CFD methods that can be used to simulate the effects of dynamic stall on the aerodynamic loading of the SWT blade.

2.5.1 Unsteady Blade Aerodynamics

Wind turbines of any size experience unsteady blade loading due to gusts as well as variation in wind speeds across the rotor plane such as wind shear and yaw misalignment. The relative air velocity, W, for a rotating SWT blade is a combination of wind speed, U_∞, and the velocity caused by blade rotation, Ωr, as shown in the velocity triangle diagram in Figure 2.10 [79]. The axial induction factor, a, is applied to U_∞ to account for the kinetic energy extracted by the SWT to generate power, and the tangential induction factor, a', is applied to the relative velocity in the rotor plane to account for the effects of wake rotation [79]. These two components form an idealized velocity triangle that dictates the effective AOA, α, of the blade, where an increase in wind speed and/or a decrease in rotational speed corresponds to an increase in AOA [80]. This concept is used to approximate changes in incoming wind speed through the change in effective AOA alone, greatly simplifying the analysis of complex wind patterns on a SWT blade.

This idealized method of analyzing the unsteady loading of a SWT blade uses a 2D blade with a pitching motion applied to correspond to the change in effective AOA that occurs during unsteady wind conditions. When representing linear wind shear (horizontal

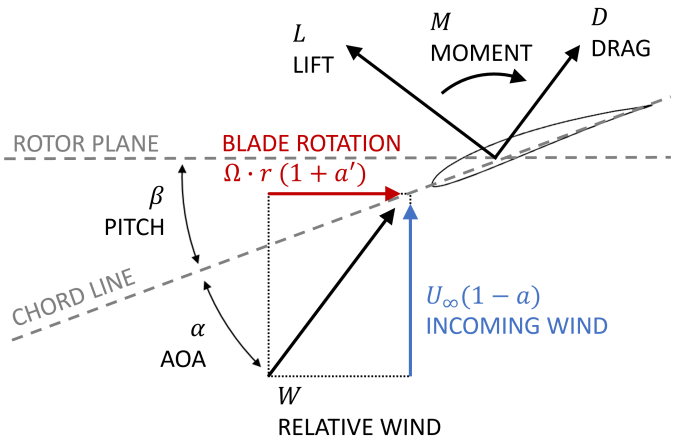


Figure 2.10: Idealized velocity triangle diagram for a wind turbine blade, including blade loading. Modified from [79]

or vertical) or yaw misalignment, the effective AOA oscillates in a sinusoidal pattern for each rotation of the blade [80]. For example, the change in effective AOA for a horizontal wind shear is shown in Figure 2.11, where the new idealized velocity triangles and effective AOAs are shown for the maximum wind speed (location II) and minimum wind speed (location IV) in the rotor plane. In this approach to representing AOA variation [80, 81], the pitching motion is governed by the following equation for effective AOA, α:

$$\alpha = \alpha_{mean} + \alpha_{amp} \sin(2\pi f t) \tag{2.15}$$

where α_{mean} is the average AOA, α_{amp} is the amplitude of the pitch oscillation and f is the frequency of oscillation. This oscillation in effective AOA for SWTs is often significant enough to initiate the dynamic stall process, which can cause extreme loading changes in comparison to static stall of SWT blades.

2.5.2 Aerodynamics of Dynamic Stall

Dynamic stall occurs during rapid changes in AOA, and creates hysteresis in the blade loading [82]. The changes in blade loading compared to the static behaviour and the degree of hysteresis that occurs are difficult to predict and thus hard to account for in the design of the SWT blade. An important parameter that impacts the degree of dynamic stall is the reduced frequency, k, of the pitching motion. Reduced frequency is defined as:

$$k = \frac{\pi f c}{U_\infty} \tag{2.16}$$

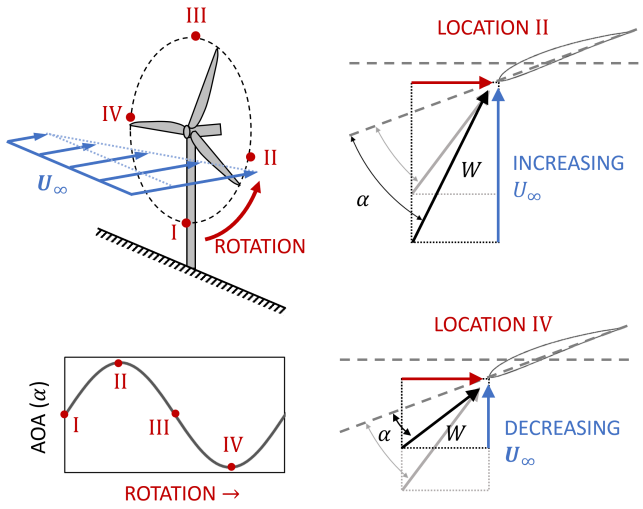


Figure 2.11: Relationship between incoming wind shear and idealized change in effective AOA for a wind turbine blade

where f is the pitching frequency from Equation 2.15. A steady airfoil has a k of 0, and unsteady motion is defined by the range of $0.05 < k \leq 0.2$ [83]. Below 0.05 is considered quasi-steady behaviour, where behaviour can often be approximated using static analysis, and above 0.2 is highly unsteady, where acceleration effects dominate the flow. Dynamic stall is known to occur within the unsteady range, and the scope of the dynamic stall analysis of this thesis will concern pitching frequencies within that range. The dynamic stall process is reported to be relatively insensitive to the airfoil Re, and is instead dependent on k and the range of AOAs of the pitching motion, as well as the airfoil geometry [82].

The deep dynamic stall process is illustrated in Figure 2.12(a) and can be divided into two regions: the pitch up motion where AOA is increasing, and the pitch down motion where AOA is decreasing. In the pitch up motion, the C_L increases linearly as it would for static changes in AOA, however the C_L magnitude is often higher than the static lift curve for a given AOA. After the static stall AOA, α_{ss}, the dynamic C_L continues to increase due to the formation of a leading edge vortex (LEV), which is also referred to as a dynamic stall vortex (DSV) [84]. This LEV causes the C_L to increase well above the maximum static C_L and delays the stall to a higher AOA, as is shown in the C_L versus α plot in Figure 2.12(a).

The dynamic stall of the airfoil can be initiated by either the shedding of the LEV or the dynamic effects of the start of the pitch down motion and is categorized as light stall or

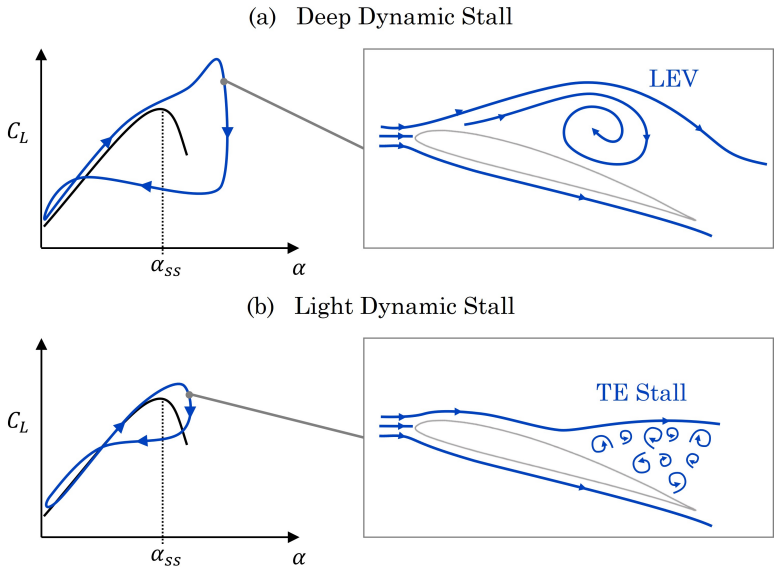


Figure 2.12: Idealized static C_L vs. α curve in black with dynamic stall C_L in blue and diagrams of the severity of stall behaviour for (a) deep dynamic stall and (b) light dynamic stall. Modified from [82]

deep stall depending on the severity of the stall behaviour [85]. Light dynamic stall occurs when the AOA is close to the static stall AOA and generally has stall initiated by the pitch down motion. This is shown in Figure 2.12(b) and results in minimal C_L hysteresis in comparison to the static C_L behaviour and the airfoil wake at stall is on the order of the airfoil thickness [82]. Deep dynamic stall can occur when the AOA far exceeds the static stall AOA, as is shown in Figure 2.12(a) and the severity of the stall results in the width of the airfoil wake being on the order of the airfoil chord length [82]. Once deep stall occurs, there is a prolonged recovery period with low C_L, and the airfoil does not regain its lift properties until the pitch down motion has reached a low AOA in the pitching cycle, ending the hysteresis.

Dynamic stall from sinusoidal pitching can create a repeating pattern of extreme loading in comparison to the expected static behaviour for a SWT blade. Understanding how to mitigate or interrupt the loading changes in the dynamic stall process can lead to improvements in blade design or control strategies to improve aerodynamic performance and reduce the fatigue on SWT blades.

2.5.3 LSB and Dynamic Stall

When dynamic stall occurs at low Re there is an additional complexity due to the reaction of the transitional BL and LSB to the unsteady motion. As an airfoil AOA increases and the aerodynamic behaviour approaches stall, the adverse pressure gradient moves upstream towards the LE which also causes the LSB to move towards the LE. A full description of LSB formation and its relationship with the chordwise pressure gradient can be found in Sections 2.1.3 and 2.1.4. At a certain critical AOA, the separated laminar BL will not have sufficient development of the K-H instability to result in BL reattachment, leaving a fully separated BL. This phenomenon is known as the bursting or breakdown of the LSB [86], since the disappearance of the reattachment point means there is no longer a defined end point of the separation bubble. When the bursting of the LSB occurs independently from turbulent BL separation at the trailing edge (TE), it results in an abrupt loss of lift and is classified as LE stall [87]. Depending on the airfoil geometry and Re, TE stall can occur on airfoils with a LSB, where the turbulent BL separation progresses upstream resulting in a loss of lift without bursting the LSB [86].

These definitions of LSB related stall behaviour were determined from analysis of several data sets at a high Re of 5.8×10^6 [86, 87] where the chordwise length of the LSB is on the order of $0.01c$ and is located at the LE [86]. Since the chordwise length of the LSB is known to increase with decreasing Re, it can be expected that the reattachment location of a long, low Re, LSB may interact with the turbulent BL TE separation location and result in a combination of LE stall and TE stall behaviours. For the purposes of this work, the definition of LSB bursting includes the abrupt BL separation that occurs when the TE separation approaches the reattachment location of the LSB.

2.5.4 Simulation of Dynamic Stall

When simulating dynamic stall for low Re airfoils, the dynamic nature of the simulations and the long time periods of the pitching cycle (relative to typical simulation time step sizes) requires a lower computational cost method than for the simulation of the static airfoil simulations summarized in Section 2.2.3. Of the common CFD methods used to simulate low Re airfoils with a LSB summarized in Section 2.2.2 the simulations of dynamic stall are limited to LES and unsteady RANS (URANS) methods. The complex method of natural BL transition and LSB bursting is considered to be difficult to model with traditional URANS models, leading some researchers to opt for the more computationally expensive LES to capture the dynamic stall behaviour for low Re airfoils [88–91].

In CFD simulations, dynamic stall is induced through the motion of the entire domain using Equation 2.15 to replicate the expected change in effective AOA for the given application. This technique has been previously used in LES simulations of dynamic stall [88–92] which captures high levels of detail in the formation and shedding of the LEV. The LES simulations by Kim and Xie, Boye and Xie, Geng *et al.*, and Huang *et al.* [88, 90–92] examined the sinusoidal pitching of a NACA 0012 airfoil at a Re of 1.35×10^5 and $k = 0.1$ to gain insight into the unsteady loading of wind turbine blades. The predicted C_L through the pitching cycles were in general agreement with the experimental data in Lee and Gerontakos [93], however all the LES simulations predict early stall, likely due to an early shedding of the LEV. Kim and Xie [88], who also simulated $k = 0.025$ and 0.05, attributed the differences in stall AOA to experimental error due to the effect of high frequency pitching on the surface pressure measurement accuracy. When looking at the latter part of the pitching cycle, Boye and Xie [91] identified additional LEVs shedding after the initial LEV that occurs at stall, which contributes to the unsteady loading of the wind turbine blade.

It is common for these high fidelity simulations to examine only the pitch up (or ramp-up) motion to isolate the shedding of the LEV from the pitch down motion. This is the case for the LES studies by Visbal and Garmann [89] and Benton and Visbal [94] and the delayed detached eddy simulation (DDES) by Batther and Lee [95]. These works simulate a NACA 0012 airfoil at a Re of 2×10^5 undergoing rapid pitch up motion, with Visbal and Garmann concluding that the LSB formation and subsequent bursting are critical for the formation of the LEV in their case. Contrary to this, the Lee and Gerontakos [93] experimental analysis of the NACA 0012 airfoil at a Re of 1.35×10^5 and $k = 0.1$ concluded that the LSB bursting was not involved in the initiation of the LEV, while noting that LSB bursting is commonly believed to play a role. Instead, they found the upstream progression of the flow reversal under the separated turbulent BL resulted in the breakdown of the BL (i.e. TE stall) that then led to the formation of the LEV. Visbal and Garmann had no TE BL separation occur, indicating LE stall behaviour which may be due to the constant rate of pitch-up motion versus the decelerating pitch rate occurring during LEV formation in the Lee and Gerontakos experiments.

Due to the potential importance of the LSB in the formation of the LEV, Visbal and Garmann call into question the ability of URANS turbulence models to accurately predict the onset of dynamic stall. Batther and Lee showed that DDES, which uses URANS at the airfoil surface to reduce computational cost, is able to capture the complex separated shear layer BL transition that is required to accurately simulate the LSB behaviour. However, they cautioned that they did not assess the sensitivity of the results to different URANS transition models and were validating the results against LES rather than experimental data.

Similar to the LES studies mentioned above, there have been many URANS simulations completed using the parameters of the NACA 0012 case reported in Lee and Gerontakos [93] for $k = 0.1$ [92, 96–99] and $k = 0.05$ [100]. Overall, these URANS studies suffered from the same early prediction of stall that was present in the LES simulations, with the exception of Xu et al. [100] which predicted the correct stall AOA but also predicted a second LEV that was not present in the validating experimental data. All URANS simulations cited above used a variation of the shear stress transport (SST) $k-\omega$ turbulence model. Honarmand *et al.* [97] used the base SST model, while Gharali and Johnson [96] applied the low Re correction to better account for the BL transition and Wu *et al.* [98] used the γ SST model which adds an additional intermittency, γ, equation to aid the onset of transition. The remaining simulations [92, 99, 100] used the $\gamma - Re_{\theta t}$ SST model [101], which adds two additional equations to improve the triggering of BL transition, including cases with transitional separated flow. A comparative study of RANS models by Liu *et al.* [102] found that the $\gamma - Re_{\theta t}$ SST $k-\omega$ model was most accurate compared to the γ SST and low Re correction options for predicting a LSB on static low Re airfoils. As Xu *et al.* [100] predicted the correct stall AOA with the $\gamma - Re_{\theta t}$ model and others using the same model did not, it is possible that other factors such as higher mesh density at the LE are required to resolve the LSB at the LE to accurately capture the LEV formation and dynamic stall AOA.

Additional URANS studies have been completed for different dynamic pitching cases, including the Gharali and Johnson [103] simulation of the SD 7037 airfoil at $Re = 4 \times 10^4$ and $k = 0.08$ using $\gamma - Re_{\theta t}$ SST. The simulations accurately predicted the stall AOA as well as the timing of the formation of a second LEV. Tseng and Cheng [104] simulated the NACA 0012 airfoil at $Re = 2.5 \times 10^6$ and $k = 0.15$ using the SST model with the low Re correction. The prediction of the stall location is in agreement with the experimental results, however there is larger disagreement in the downstroke with an over-prediction of the C_L during the formation of a second LEV. A NACA 0015 study at $Re = 2 \times 10^5$ and $k = 0.1$ was completed by Tseng *et al.* [105] using the $\gamma - Re_{\theta t}$ SST model. The study had a focus on the BL transition and LSB that is present at the LE ahead of the LEV formation, and found that the base formation of the SST $k-\omega$ model prematurely predicted suction collapse and stall in comparison with the $\gamma - Re_{\theta t}$ SST model. Analysis of the dynamic stall found that the LSB reattachment location progressed downstream simultaneously with the upstream progression of the turbulent BL TE separation until eventual bursting of the LSB and suction collapse. Tseng *et al.* also had a similar conclusion to Visbal and Garmann [89] that the formation and bursting of the LSB is critical to predicting the correct stall AOA.

The consistent prediction of early dynamic stall and the role of the LSB in the dynamic stall process requires further investigation. The correct stall timing within the pitching

cycle is critical to understanding the flow phenomena that are responsible for the large load fluctuation in deep dynamic stall of SWT blades and is necessary to design techniques for reducing the unsteady loading of SWT blades.

2.6 Summary

This chapter has clearly established the need for the in depth analysis of several flow phenomena related to SWT operation. The operation of SWT in the low Re regime results in the development of a complex BL on the SWT blades which involves an elongated chordwise region of BL transition and the formation of a LSB due to the adverse pressure gradient caused by the airfoil curvature. The design challenges that arise due to the presence of the LSB are the tonal aeroacoustic noise that can be generated by the K-H rolls within the LSB and the deep dynamic stall under unsteady flow conditions which may be exacerbated by the bursting of the LSB. The analysis of these phenomena using CFD and CAA methods requires a comprehensive experimental data set to be able to fully validate the transient details of the BL transition and LSB. The lack of validating data for cambered airfoils designed for operation at appropriately modest Re has prevented the necessary analysis of the role of the LSB in airfoil self-noise and deep dynamic stall which limits the ability to improve the design of future SWT blades. The simulations and analysis completed in this work aim to address these gaps in the literature for the low Re operation of SWT blades.

Chapter 3

Approach and Methodology

This chapter covers the theoretical approach and numerical methods of the computational fluid dynamic (CFD) and computational aeroacoustic (CAA) simulations used to study the tonal aeroacoustic noise and dynamic stall that occurs on small wind turbine (SWT) blades. The low Reynolds number (Re) operation of SWTs often leads to the presence of a laminar separation bubble (LSB) in the transitional boundary layer (BL) on the blades. The LSB was shown to influence both the aeroacoustic noise and dynamic stall behaviours in Chapter 2 which also established the need for the fully-validated numerical analysis of the role of the LSB in these behaviours. The simulations outlined in this chapter use the low Re airfoil profiles SD 7037 and S833 operating at a modest Re which results in a LSB of elongated chordwise length that is in close proximity to the airfoil trailing edge (TE) at low angles of attack (AOA). The validation and analysis of the aerodynamic and aeroacoustic results with a focus on the LSB behaviour are explained in detail in Chapters 4 to 7.

The simulation of aeroacoustic noise and dynamic stall require different numerical methods and therefore the contents of this chapter is divided into two parts. The approach and methodology for the aeroacoustic simulations using CFD and CAA are described in Sections 3.1 and 3.2 followed by the information for the dynamic stall CFD simulations in Sections 3.3 and 3.4.

The theoretical approach and numerical methods presented in this chapter are an expansion on the information published in peer-reviewed journals. The CFD method used to generate the aeroacoustic predictions is published in the *ASME Journal of Fluids En-*

gineering[1] and the dynamic stall CFD method is published in the *AIAA Journal*[2]. The details of the implementation of the CAA method have been published in peer-reviewed conference proceedings, most recently in the proceedings of the *30th AIAA/CEAS Aeroacoustics Conference*[3], and the full list of articles published in conference proceedings is included in Appendix A.

3.1 Theoretical Approach - Aeroacoustic Noise

The blades of a SWT generate aeroacoustic noise due to the airfoil self-noise mechanisms described in Section 2.3.3 and the type of noise generated depends on the BL behaviour interacting with the sharp TE of the blade. The low Re operation of SWTs, defined as a chord-based $Re < 5 \times 10^5$, can result in tonal airfoil self-noise due to the regular frequency structures that form in the laminar or transitional BL. This includes the Kelvin-Helmholtz (K-H) rolls which are spanwise vortical structures that form within the LSB as described in Section 2.1.4. At modest Re, defined as $Re < 1 \times 10^5$, the LSB has been shown to have an elongated chordwise length, as was discussed in Section 2.2.3, which increases the likelihood that the K-H rolls in the LSB interact with the TE to generate tonal noise. Another behaviour that is more likely to occur at modest Re is a transitional separated BL at the airfoil TE which occurs when the laminar BL separation occurs closer to the TE and the BL is unable to reattach to form the LSB. This results in K-H rolls with high spanwise coherence passing the TE rather than the spanwise breakdown of the K-H rolls that occurs after the BL reattachment location when there is a fully-formed LSB.

The reduction of tonal noise for SWT blades operating at modest Re requires analysis of the tonal airfoil self-noise generation in cases where a fully-formed LSB is in close proximity to the TE and when there is a transitional separated BL at the TE. The numerical simulation and analysis of this behaviour requires a comprehensive set of experimental data to simultaneously validate the complex process of the transient BL development and the generated airfoil self-noise. The challenge of validating the aerodynamic behaviour of the LSB was discussed in Section 2.2.3 where the majority of published numerical studies of a LSB are validated against a direct numerical simulation (DNS) due to the limited

[1] Zilstra, A. and Johnson, D.A. (2022) Large Eddy Simulation of Transitional Separated Flow Over a Low Reynolds Number Cambered Airfoil. ASME. J. Fluids Eng. doi: 10.1115/1.4056280

[2] Zilstra, A. and Johnson, D.A. (2024) Validated Dynamic Stall Simulation of Pitching Low Reynolds Number Airfoils. AIAA Journal, Vol. 62, No. 10, pp. 3700-3712, https://doi.org/10.2514/1.J063884

[3] Zilstra, A. and Johnson, D.A. (2024) Computational Aeroacoustic Prediction of Tonal Noise for Low Reynolds Number Airfoils. 30th AIAA/CEAS Aeroacoustics Conference. doi:10.2514/6.2024-3362

availability of experimental data [7,25–27,31–33]. The validated CAA analysis summarized in Section 2.4.3 has only been completed for airfoils with a LSB near the TE at $Re > 1\times10^5$ with a fully-formed LSB of short chordwise lengths of approximately 20% of the airfoil chord, c [58,59]. The simulations in this work are completed for a low Re cambered airfoil operating at modest Re to investigate the tonal TE noise generated by a fully-formed LSB as well as when there is transitional separated flow at the TE. The experimentally measured aerodynamic and aeroacoustic behaviour of the SD 7037 airfoil is described in Section 3.1.1 and this data is used for the validation of the CFD and CAA simulations in this work.

The numerical prediction of tonal airfoil self-noise is completed using a CFD simulation of the flow around the airfoil followed by the application of a CAA method to predict the noise generated by the flow. The CFD method must be able to capture the details of the low Re BL transition and the formation of a LSB to result in the accurate transient BL behaviour at the TE. The theory behind the common CFD methods are summarized in Section 2.2 and the theory of the CAA methods are described in Section 2.4. The primary decision when selecting the numerical methods is whether the effects of acoustic feedback and compressibility are required to predict the tonal airfoil self-noise. It was established in Section 2.3.4 that the acoustic feedback and associated ladder structure that can occur during tonal airfoil self-noise is less relevant to the tonal noise generation for airfoils operating at modest Re [53,54,56] and for cambered low Re airfoil profiles [56,58,63]. This eliminates the need for a the simulation of the acoustic waves used in a direct CAA approach and therefore the Ffowcs-Williams and Hawkings (FW-H) acoustic analogy, as described in Section 2.4.2, can be used to predict the tonal noise. The CFD method used to simulate the flow can therefore be an incompressible solver, and when that considering research objective #6 is to reduce the overall computational cost of the simulations, a wall-resolved large eddy simulation (LES) method is more appropriate than a direct numerical simulation (DNS) method. The details of the implementation of the wall-resolved LES and FW-H methods to the simulation of low Re airfoil self-noise are provided in Section 3.2.

3.1.1 CFD and CAA Validation

The accuracy of the simulated BL development and associated airfoil self-noise prediction are determined through validation against a unique set of experimental data for the aerodynamic performance [4] and aeroacoustic performance [49] collected by previous researchers at the University of Waterloo. The prior experimental studies were performed at modest Re on the SD 7037 airfoil which is a cambered airfoil designed for low Re applications and

is well suited for use on a SWT [106]. The studies were completed using a 2D blade segment with a constant chord, zero twist, and span of 152.4 mm in a closed loop wind tunnel with a 152.4 mm square cross-section. The wind tunnel has a hard-walled test section and acoustic treatments of sound-absorbing foam between the fan and test section were applied by Orlando [107] to reduce the background noise level of the tunnel for frequencies greater than 0.5 kHz.

The aerodynamic behaviour of the airfoil is validated through comparison with the experimental results from the particle image velocimetry (PIV) study of the development of the LSB on the suction side of the SD 7037 airfoil by Ghorbanishohrat [4]. The experiments were conducted at $Re = 4.1 \times 10^4$ with an airfoil chord of $c = 0.0258$ m and for 1°, 3°, 5°, 7°, and 9° AOAs. The time-averaged data for the suction side BL includes the pressure coefficient, C_p and skin friction coefficient, C_f, as defined in Sections 2.1.3 and 2.1.4 as well as the integral BL parameters defined in Section 2.1.5. These experimental results were used to identify the trends in the locations of BL separation, transition and reattachment associated with the LSB and shows that the modest Re flow results in an elongated LSB with an average chordwise length of $0.39c$. A discussion of the difference in near-wall resolution of the PIV method and the CFD mesh and associated impact on the time-averaged results is included in Sections 4.2, 4.3, 4.5 and 5.2. The AOAs of interest are at 1° and 3° AOA where there is transitional separated flow at the airfoil TE and at 5° AOA where there is a fully-formed LSB with time-averaged reattachment of the BL $0.17c$ upstream of the TE.

The collection of data using PIV resulted in a chordwise resolution of $0.004c$ (0.105 mm) [4] for all suction side BL parameters which is necessary for validating the BL transition process within the LSB. This high chordwise resolution gives extra confidence to the CFD validation process in comparison with the discrete chordwise C_p data generated through surface pressure measurements using pressure taps. The rarity of this detailed experimental data set will be further explained during the validation of the time-averaged LSB simulation in Chapter 4.

An aeroacoustic study of the SD 7037 airfoil was conducted by Tam [49] with $c = 0.025$ m at $Re = 4.0 \times 10^4$ and for AOAs of 0°, 1°, 2°, 3°, 5°, 10°, 15° and 20°. The aeroacoustic noise for each AOA was measured for 100 s using a microphone placed directly below the quarter-chord of the airfoil in the wind tunnel wall and the resulting acoustic spectra are an ensemble average of the fast Fourier transform (FFT) of signals 1 s in length. Analysis of the spectra identified that tonal noise occurs at two dominant frequencies of 3.4 kHz and 4.1 kHz across all experimental AOAs. The loudest tone was measured at 122 dB at 1° AOA which was shown by Ghorbanishohrat [4] to have a transitional separated BL at the TE. The details of the tonal noise trends at the low AOAs are discussed further during

the validation of the CAA simulation results in Chapter 6.

The experimental data shows that interesting and complex aerodynamic and aeroacoustic behaviour occurs for the SD 7037 airfoil at modest Re due to the presence of an elongated LSB and a transitional separated BL at the TE. The combination of these experimental data sets provides a unique opportunity to thoroughly validate the CFD and CAA simulation. This gives confidence to the subsequent analysis to determine the sources of the aeroacoustic tones and the role of the LSB in the tonal noise generation. Therefore the CFD and CAA simulation of the SD 7037 at $Re = 4.1 \times 10^4$ is an ideal case for determining the accuracy of the chosen numerical methods and the potential for their use in the design and analysis of the aeroacoustic performance of SWT blades.

3.1.2 Simulation Phases

The CFD and CAA simulations were completed in three phases to incrementally validate the increasingly complex aerodynamic and aeroacoustic behaviours. The first phase is a continuation of the previous Master's research [108] which applied the same numerical methods to the SD 7037 airfoil to predict the tonal airfoil self-noise. However, the validation and analysis for the previous work was focused on the aeroacoustic prediction and the relationship between the tonal noise and the transient fluctuations in the lift and drag coefficients. This approach to the simulations resulted in accurate predictions of the broadband aeroacoustic behaviour and limited success in the prediction of tonal noise related to the transitional separated BL. Therefore the first phase of this work re-examines the prior implementation of the LES method and thoroughly validates the time-averaged LSB against the experimental PIV data [4].

The LES parameters relevant to the accurate simulation of the LSB in the low Re BL are described in Section 2.2.4 and the findings of these preliminary studies are incorporated into the description of the numerical method in Section 3.2. Additionally, improvements were made to the simulation mesh to create Mesh 1 which is described in Section 3.2.6 and addresses the required sub-grid filter length in the airfoil BL. The validation of the time-averaged behaviour in the BL and LSB are reported in Chapter 4 for AOAs of 1°, 5° and 7°. The selected AOAs cover the full range of LSB behaviour with 1° AOA having a transitional separated BL at the TE and 7° AOA having a LSB located near the LE with a turbulent BL at the TE.

The second phase of the simulations focuses on the validation of the transient behaviour in the BL and LSB through a series of targeted mesh refinements in the BL. The analysis of the simulations throughout the first phase of this work showed that with increasing

mesh refinements the time-averaged BL results, such as C_p and C_f, remained relatively constant while the transient behaviour varied significantly. The accuracy of the aeroacoustic prediction from the FW-H acoustic analogy is dependent on the quality of the transient data generated by the LES method and therefore it is necessary to validate the transient behaviour in the BL and LSB. Since the PIV data [4] is time-averaged, the transient results are validated through a convergence of the transient behaviour with increasing mesh refinements. Additionally, the frequencies of the pressure fluctuations associated with the dominant transition structures in the laminar BL and LSB can be validated against the dominant tonal noise frequencies at each AOA. The final mesh versions Mesh 2 and Mesh 3 are described in Section 3.2.6 and the transient results from simulations at 1°, 3° and 5° AOAs are reported in Chapter 5.

The final phase of the simulations applies the FW-H acoustic analogy to the LES simulations at 1°, 3° and 5° AOAs reported in Chapter 5 and validates the predicted acoustic spectra against the experimental acoustic spectra [49]. The application of the FW-H acoustic analogy is detailed in Section 3.2.3 and the aeroacoustic results are reported in Chapter 6. The detailed validation of the time-averaged and transient behaviour of the BL and LSB in Chapters 4 and 5 is used to determine the source behaviour of the tonal noise for the SD 7037 airfoil. There is also an estimation of the effect of the acoustic feedback process on tonal noise generation which includes the interference between the TE acoustic feedback and the LSB pressure feedback identified in Chapter 5.

This three phase process for the setup and validation of the CFD and CAA simulations was found to be the most effective approach for accurately predicting the airfoil self-noise generated by a low Re airfoil with a LSB.

3.2 Numerical Method - Aeroacoustic Noise

The prediction of the aeroacoustic noise for the SD 7037 airfoil is completed using wall-resolved LES as the CFD method and the FW-H acoustic analogy as the CAA method. The selection of these methods is described in Section 3.1 and this section summarizes the findings of numerous test simulations used to determine the ideal simulation setup for each method. The simulations were performed using the commercial software ANSYS Fluent releases 19.2, 20.2 and 22.2 where all numerical methods used are built-in to the software and did not require modification through user-defined functions.

The LES method and FW-H acoustic analogy are solved independently and the dominant computational effort is due to the LES simulation of the flow field. The FW-H

calculation is performed as a post-processing operation on acoustic source data files generated during the LES simulation. This section discusses the setup and execution of the LES simulations and the FW-H acoustic analogy setup. This is followed by a detailed discussion of the simulation domain, boundary conditions and the mesh versions used for the results presented in Chapters 4, 5 and 6.

3.2.1 LES Method Setup

The wall-resolved LES method applies low-pass filtering to the flow field to resolve the large scale turbulent structures and employs a model for the small scale turbulent structures. The details of the wall-resolved LES method are provided in Section 2.2.2 and the description of the length scales within a turbulent flow is included in Section 2.2.1. The dynamic Smagorinsky-Lilly model [19–21] is used as the sub-grid scale (SGS) stress model to calculate the structures smaller than the filter length. The use of LES methods to simulate a LSB is summarized in Section 2.2.3 and the analysis by Smith and Ventikos [25] showed that the LES simulation of a LSB is better captured using a dynamic SGS stress model. The dynamic Smagorinsky-Lilly model, as implemented in ANSYS Fluent [109], applies a second filtering operation to locally calculate the Smagorinsky constant, C_s, and limiting the value between 0 and 0.23 rather than using a constant value of 0.1.

The mass and momentum conservation equations are solved in the incompressible form as it has been shown in literature that compressibility is not necessary to resolve the BL transition behaviour and LSB location [6]. An incompressible simulation does not calculate the density changes required to directly simulate the acoustic wave propagation that is necessary for the prediction of the proposed acoustic feedback loops [45,60–62,64,65] and the resulting ladder structure of the tonal noise frequencies described in Section 2.3.4. As was discussed in Section 3.1, the incompressible simulation method is sufficient for the tonal noise prediction for the SD 7037 airfoil at $Re = 4.1 \times 10^4$ due to the absence of a defined ladder structure for low Re cambered airfoils. Simulations in the prior Master's research [108] and preliminary simulations in this work included compressibility to capture potential acoustic feedback and test the feasibility of direct CAA, however it was found that compressibility is not necessary to predict the tonal noise at the correct frequency for this low Re case.

The application of different pressure-velocity coupling schemes and spatial discretization schemes can be used to improve the numerical stability of a LES simulation and reduce the numerical error introduced by insufficient simulation mesh resolution of quality. The schemes commonly used for the simulation of low Re flow with a LSB are discussed in

Section 2.2.4 and the schemes tested for the present work are described here. The "semi-implicit method for pressure-linked equations - consistent" (SIMPLEC) and "pressure implicit with splitting operators" (PISO) pressure-velocity coupling schemes were compared using a preliminary version of the simulation mesh to determine any impact of the mesh quality on the BL simulation. The PISO scheme is preferred for minimizing numerical error introduces by any highly skewed cells located at the LE [15], however there was no variation in the development of the BL between the simulation using PISO and SIMPLEC. Therefore the SIMPLEC scheme was found to be the appropriate pressure-velocity coupling scheme for the simulation mesh and is the scheme used for all the presented LES results.

Similarly, preliminary simulations were completed to compare the effect of the spatial discretization scheme on the BL transition and LSB for the SD 7037 airfoil. The bounded central differencing scheme (CDS) and "quadratic upstream interpolation for convective kinematics" (QUICK) spatial discretization schemes were applied to determine the impact of the different levels of stability in the scheme on the BL simulation. The bounded CDS scheme in ANSYS Fluent uses the Normalized Variable Diagram (NVD) approach to create a composite scheme that maximizes the order of accuracy while ensuring stability through comparison with convection boundedness criteria [109]. This composite scheme primarily utilizes a CDS scheme which is the preferred scheme for simulations of a LSB [6, 8, 23, 25, 26, 28, 29] due to the low numerical diffusion, as described in Section 2.2.4. When stability issues are identified through the NVD approach, the spatial discretization scheme is modified to either a blended scheme of CDS and linear upwind differencing (LUDS) scheme or the highest stability upwind differencing (UDS) scheme. This is a similar blended scheme to that used by Lardeau *et al.* [22] and Smith and Ventikos [25] for the simulation of low Re airfoils with a LSB. The QUICK scheme is implemented using a combination of CDS and LUDS and therefore has a consistently high stability to prevent numerical oscillations in the solution. In the test simulations for the SD 7037 airfoil, it was found that the stronger upwinding of the QUICK scheme resulted in dampening of the turbulence in the BL transition and therefore the bounded CDS spatial discretization scheme was used for the presented LES results.

The time integration method for the transient LES simulation was selected as bounded second order implicit, which applies boundedness criteria to the second-order implicit scheme to ensure numerical stability [109]. Numerous test cases were used to determine the ideal time step sizes of 2×10^{-6} s and 4×10^{-6} s that provided a balance between calculation effort and simulation run-time. The time step applied for each mesh version is dependent on the mesh distribution and is summarized in Table 3.2. The time step size, Δt, is selected in order to meet convergence criteria for each time step, which are 5×10^{-5}

for continuity and the x-, y-, z-momentum equations, within 15 to 30 calculation iterations. The following section includes the details of the execution of the LES simulations and when the fluctuations of the transient results are considered statistically steady with time.

3.2.2 LES Simulation Execution

The LES simulations were run using the Graham[4] high-performance compute cluster in the Digital Research Alliance of Canada network [110] to reduce the wall-clock time of the simulations. Analysis of the performance of the LES simulation on the compute cluster resulted in the optimal wall-clock time when using 96 to 128 cores. Preliminary simulations prior to the optimization of the domain size and mesh distribution required wall-clock times of 350 hours, with between 10000 and 20000 core-hours. The optimized simulations outlined in this chapter have a wall-clock time ranging between 55 to 160 hours, which translates to 5300 to 20200 core-hours.

The computational resources required for a LES simulation are reduced when providing detailed initialization data and therefore the simulations were initialized using a Reynolds-averaged Navier-Stokes (RANS) method. The chosen initialization RANS model was $\gamma - Re_{\theta t}$ shear stress transport (SST) $k - \omega$, which is the model used for the dynamic stall simulations in this work as described in Section 3.4.1 and the theory behind the model is included in Sections 2.2.2 and 2.5.4. In some cases, the simulations were continued from a previous LES simulation at a similar AOA which further reduced the total wall-clock time for the simulations.

For transient CFD simulations, the simulated flow field is considered ready for analysis once certain key parameters have become statistically steady. For the LES simulations, the stabilization of the mean value of the lift coefficient and the inflow turbulent intensity were used to determine if the solution is statistically steady. The solution for all simulated cases became statistically steady within the first domain-based mean flow residence time (MFRT), which is defined as:

$$MFRT = \frac{U_\infty t}{l} \tag{3.1}$$

where the characteristic length, l, is the length of the domain in the flow direction (here as $R + L$ as shown in Figure 3.2(b)), t is the total time simulated, and U_∞ is the free-stream velocity. Erring on the side of caution, the entire first domain-based MFRT of data is considered to be initialization of the transient solution and is omitted from all

[4]Graham specifications: docs.alliancecan.ca/wiki/Graham

analysis. All the unsteady statistics for the flow field are reset at this time to ensure the time-averaged parameters do not include any initialization effects.

After the initialization domain-based MFRT, the simulation was continued for a minimum of 0.056 s up to a maximum of 0.128 s to collect data for the aerodynamic analysis of the BL development and generate the acoustic source data files needed for the FW-H acoustic analogy described in Section 3.2.3. It is useful to report these simulation times as a chord-based MFRT for comparison between the SD 7037 simulations cases using different domain dimensions (see Table 3.2) and analysis completed by other researchers for different airfoil dimensions. In this metric, the initialization was 18 to 24 chord-based MFRT and the analysis was completed for 44 to 92 MFRT. The identification of intermittent changes in the dominant tonal aeroacoustic noise has been shown to require longer simulation times than would be expected for aerodynamic analysis with Sanjose *et al.* [58] requiring 50 chord-based MFRT, as was described in Section 2.4.3. This behaviour was also identified in preliminary LES simulations of the SD 7037 airfoil at low AOAs and for this reason several simulations were extended to identify any intermittency in the predicted tonal aeroacoustic noise. This tonal noise intermittency analysis is reported in Section 6.1.3.

The transient analysis of the BL transition in the LSB region is completed for 18 to 37 chord-based MFRT, where signals of the velocity components and static pressure are collected at chordwise spacings of $0.05c$ and at a wall-normal distance from the airfoil surface of $3 \times 10^{-2}c$ and $4 \times 10^{-3}c$. The global X-Y-Z coordinates are converted to S-N-Z coordinates, as described in Section 2.1.5, where the s-velocity, U_s, is tangent to the local airfoil curvature. The transient analysis of these collected velocity and pressure signals is reported in Sections 5.4 and 5.5 and is then used to determine the relationship between flow frequencies and the tonal TE noise frequencies in Section 6.1.

3.2.3 FW-H Acoustic Analogy Setup

The implementation of the FW-H acoustic analogy requires the selection of an impermeable or permeable surface to be the source of the noise and for all simulations the surface of the airfoil is selected as the impermeable source. The theory and derivation of the FW-H acoustic analogy are described in detail in Section 2.4.2. The solution of the FW-H acoustic analogy employed by ANSYS Fluent simplifies to Formulation 1A [111] when the source surface is coincident to the airfoil surface. Therefore these simulations only consider monopole and dipole noise sources and quadrupole sources within the airfoil BL are assumed to be negligible, as was described in Section 2.4.2.

The model also requires the defining of a far-field receiver location to which the noise is propagated, and this is set at the microphone location used to collect the validating experimental data [49]. The microphone was located in the lower wall of the wind tunnel, at a distance of $3.0c$ below the quarter-chord location of the airfoil. The geometry of the simulation domain results in the global coordinate system defined for an airfoil AOA of 0° AOA, therefore location of the microphone relative to the airfoil changes with AOA, α as shown in Figure 3.1. For the simulations, the receiver location is defined as $x = 3.0c \sin \alpha$ and $y = -3.0c \cos \alpha$ relative to the quarter chord at 0° AOA.

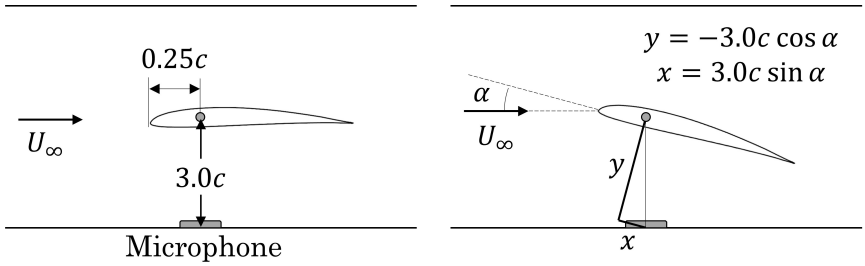


Figure 3.1: Change in microphone location relative to airfoil with AOA

The FW-H calculation was performed after the completion of the LES simulation and uses acoustic source files containing the information at the surface of the airfoil that are generated for each time step of the LES simulation. ANSYS Fluent also has the option to simultaneously calculate the LES and FW-H solution, however the use of source files allows for the modification or addition of receiver locations after the simulation has been completed which gives more freedom to analyze the acoustic propagation, if needed. The FW-H acoustic analogy generates an acoustic signal consisting of the acoustic pressure fluctuations at the receiver location for each time step of the simulation. This signal can then be processed using fast Fourier transform (FFT) and converted to SPL, as is described in Section 2.3.2, to determine the frequency content and SPL magnitude of the aeroacoustic noise. The analysis of the acoustic results predicted by the FW-H acoustic analogy are reported in Section 6.1.

3.2.4 Domain Geometry

The airfoil used for the CFD and CAA simulations is the SD 7037c version of the SD 7037 profile [112], and a rounded TE of $r = 0.045$ mm was applied to match the manufactured airfoil used in the experiments [4]. The airfoil was designed to have a 26 mm chord length

and resulted in a manufactured chord length of 24.8 mm after surface treatments were applied to reduce reflection for the PIV experiments. In the simulation geometry, the rounded TE was included as shown in Figure 3.2(a) to account for the difference between the designed and manufactured airfoil profiles.

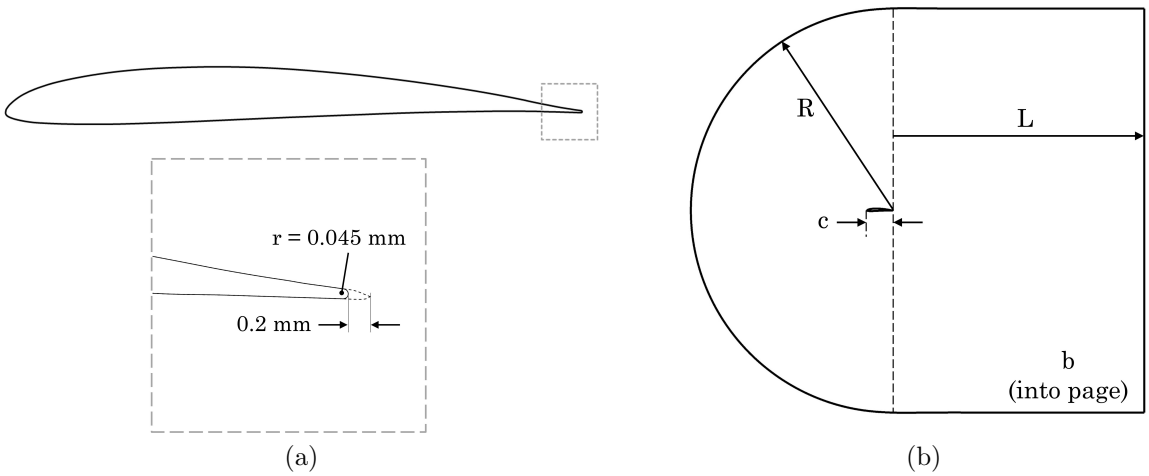


Figure 3.2: Schematic of (a) airfoil geometry and (b) computational domain geometry

The fluid domain surrounding the airfoil is a C-mesh as shown in Figure 3.2(b) which is an ideal geometry for the structured mesh that will be described in Section 3.2.6 since the curved surface aligns well with the curved surface of the airfoil. The dimensions of the domain are scaled with the chord length, c, and several different domain sizes have been used through the course of the simulations. The general recommendation is to have the boundary offsets of the radius, R, and downstream length, L, be between $12c$ and $20c$ to prevent interference of the boundary conditions with the flow around the airfoil. The summary of the geometry details for the computational domain can be found in Table 3.1 along with the aerodynamic parameters for the simulations.

Preliminary simulations as well as the previous Master's research [108] were completed using $20c$ offsets which were changed to $12c$ in order to reduce computational resources needed as mesh refinements were completed. The smallest domain used has offsets of $R = 8c$ and $L = 10c$ and the reduction in the boundary offsets was found to cause no change to the flow around the blade. A similarly small C-mesh of $R = 4c$ and $L = 10c$ has previously been used by Smith and Ventikos [25] for DNS and LES simulations of a LSB on a NACA 0012 airfoil at a Re of 1×10^5.

Airfoil Profile		SD 7037
Angle of Attack	α	1°, 3°, 5°, 7°
Chord	c	0.0258 m
Span	b	$0.2c$
Radius	R	$8c$ to $12c$
Downwind Length	L	$10c$ to $12c$
Inflow Velocity	U_∞	23.8 m/s
Reynolds Number	Re	4.1×10^4
Mach Number	Ma	0.07
Turbulent Intensity	Tu	1%

Table 3.1: Geometric and aerodynamic details

The spanwise length of the domain, b, was initially set at a length of $0.4c$ and was later reduced to $0.2c$ after tests showed no impact on simulation of the BL transition. The spanwise extent is consistent with the $0.2c$ commonly seen in simulations of transitional flow over symmetric NACA airfoils [25, 26] and cambered airfoils [31–33].

3.2.5 Boundary Conditions

The boundary conditions used for the simulation domain are shown in Figure 3.3. The airfoil surface is defined as a no-slip wall and the vertical outlet is defined as a pressure outlet. The curved and horizontal edges of the domain are set as velocity inlets, where the free-stream velocity of $U_\infty = 23.8$ m/s is angled with the horizontal by the airfoil AOA, α. The application of inflow turbulence and the spanwise boundary condition are explained in the following sections.

Inflow Turbulence

A known issue with LES is the difficulty of generating an accurate replication of inflow turbulence conditions, since the model can be quite dissipative [15, 22] as was discussed in Section 2.2.4. Accurate turbulence generation is necessary for transitional separated flow since increasing turbulence has been shown to be one of the causes of a decrease in the bubble length [9, 22, 32, 33]. Synthetic turbulence generation methods are generally favoured for practical applications [34], and are included in commercial computational fluid

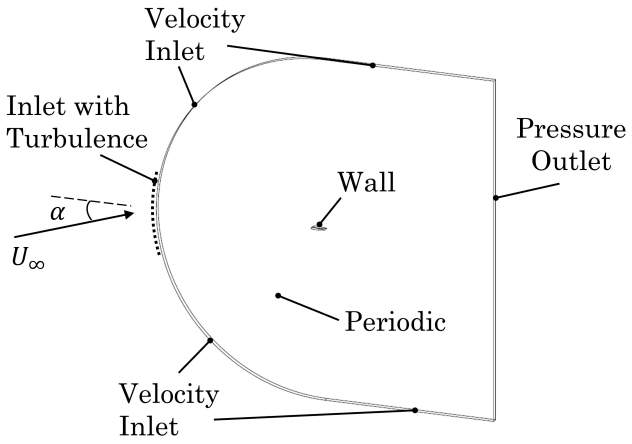


Figure 3.3: Diagram of simulation boundary conditions

dynamics software packages. Roberts and Yaras [23] used a synthetic method built-in to ANSYS CFX to generate turbulence for the simulation of transitional separated flow on a flat plate. For this work, the ANSYS Fluent built-in Spectral Synthesizer method was chosen and the inflow turbulence was introduced in a $4.75c$ segment for $R = 12c$ and $3.16c$ segment for $R = 8c$ of the curved inlet located directly upstream of the airfoil, as shown in Figure 3.3. This generates the desired level of inflow turbulence at the airfoil while keeping the computational cost low by reducing the complexity of the calculations in the far-field of the domain.

The mesh distribution between the inlet and the airfoil was controlled to ensure the SGS filter length was smaller than the inflow turbulence length scale of 11 mm to prevent excessive dissipation. An in-depth discussion of the SGS filter length for the simulations is found in Section 3.2.6. The turbulent intensity at the inlet was artificially increased to account for the dissipation that occurs between the inlet and the airfoil [22], which resulted in a turbulent intensity of 1% at a location 24 mm upstream of the LE as measured experimentally [4,107], as summarized in Table 3.1. Tests of the inlet turbulence dissipation determined the ideal specified inlet turbulent intensity to be 4.4% for domains with $R = 12c$ and 3.3% for domains with $R = 8c$.

Periodic Boundary Condition

The spanwise boundary condition has the potential to influence the formation of the spanwise structures in the transitioning BL as is discussed in Section 2.2.4. The symmetry and

periodic boundary conditions were tested using a prior domain with a spanwise extent of $b = 0.4c$ and it was found that there was a difference in the length of the LSB and the number of aeroacoustic tones predicted. However, later inspection of simulations using a improved spanwise and wall-normal mesh resolution in the BL found a similar prediction of the BL transition when using a periodic or spanwise boundary condition. This is in agreement with the findings of Christophe *et al.* [35] for incompressible LES of low Re airfoil self-noise, where both the symmetry and periodic condition can provide adequate results as long as the mesh is sufficiently refined.

The domain was reduced to a spanwise extent of $b = 0.2c$ to reduce computational expense, after which only the periodic boundary condition was used. As previously mentioned in Section 3.2.4, the $0.2c$ span is commonly used for low Re transitional separated flow and the spanwise boundary condition used with this domain span is the periodic boundary condition [25, 26, 31–33]. The spanwise extent and spanwise boundary condition are of greater concern for compressible direct CAA simulations, which require the development and propagation of spanwise acoustic waves. The current simulations generate the aeroacoustic prediction through incompressible LES with the FW-H acoustic analogy and therefore the current selection of the periodic boundary condition will not introduce any problematic spanwise aeroacoustic patterns.

3.2.6 Mesh and LES Filter Length

The structured hexahedral mesh is generated using ANSYS ICEM CFD releases 19.2, 20.2 and 22.2, which is an ideal software for strict control of the mesh sizing and expansion. The mesh sizing is important for LES not only to have sufficient resolution of the velocity and pressure gradients, but also because the SGS filter length used is dependent on the mesh sizing where the filter length, Δ, is equal to the cubed root of the cell volume [109]. As was described in Sections 2.2.2 and 2.2.4, if the mesh sizing and associated filter length is coarse for the local length scales of the turbulence (see Section 2.2.1) then the simulation will excessively dissipate the turbulence. This is most crucial in the airfoil BL but is also necessary upstream of the airfoil to correctly propagate the inflow turbulence specified at the domain inlet which was addressed in Section 3.2.5.

Near to the airfoil surface, blocking of the domain into smaller regions is used to control the mesh distribution in the BL. The far-field of the mesh also features several expansion regions to ensure smooth transition of the cell sizes and prevent convergence issues. The mesh versions presented here involve successive alterations to the mesh distribution in the near-wall region as well as changes in the domain boundary offsets R and L. The

mesh generation and refinements described in this section aim to meet mesh filter length criteria for both the attached BL and the separated flow in the LSB to create an accurate simulation of the BL on the SD 7037 airfoil.

BL Filter Length

The first mesh version, Mesh 1, consists of 2.6 million elements with 300 chordwise and 50 spanwise divisions and the mesh distribution is shown in Figure 3.4 and with geometric and simulation details summarized in Table 3.2. The first layer height at the airfoil surface is 0.005 mm with a wall-normal expansion ratio of 1.1. The best-practice for a LES simulation mesh is to have a first layer height of $y^+ \leq 1$, where y^+ is a dimensionless wall-normal height defined as $y^+ = y/\delta_v$. The viscous length scale, δ_v is defined as

$$\delta_v \equiv \nu \sqrt{\frac{\rho}{\tau_w}} \tag{3.2}$$

and is dependent on the local shear stress, τ_w, in the BL along with the fluid properties of density, ρ, and kinematic viscosity, ν. Mesh 1 has a wall y^+ of less than 0.5 at the airfoil surface for all simulated AOAs, with the average y^+ ranging from 0.21 for 1° AOA to 0.27 for 7° AOA.

Mesh #	1	2	3
Radius, R	$12c$	$12c$	$8c$
Downwind Length, L	$12c$	$12c$	$10c$
Number of Elements	2.6×10^6	4.5×10^6	8.8×10^6
Chordwise Divisions	300	300	570
Chordwise Divisions $x/c < 0.3$	30	30	60
Spanwise Divisions	50	50	75
Inlet Turbulence, Tu	4.4%	4.4%	3.3%
Angle of Attack, α	1°, 5°, 7°	1°, 3°, 5°	3°, 5°
Time Step, Δt [s]	4×10^{-6}	2×10^{-6}	4×10^{-6}

Table 3.2: Mesh parameters for mesh versions 1-3

A BL mesh criterion is suggested by Pope [17] where accurate wall-resolved LES requires 80% of the turbulent kinetic energy to be resolved (i.e. not calculated through SGS modelling). This is based on the production range, or energy containing range, of the turbulent cascade (see Section 2.2.1) where 80% of the energy is contained in eddies of that

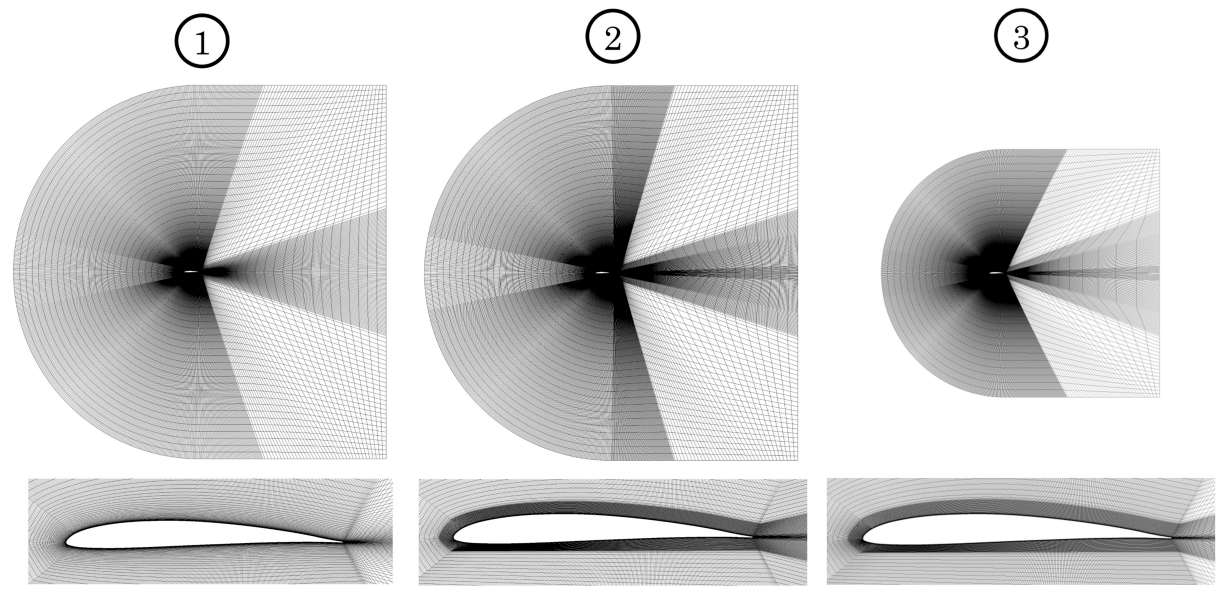


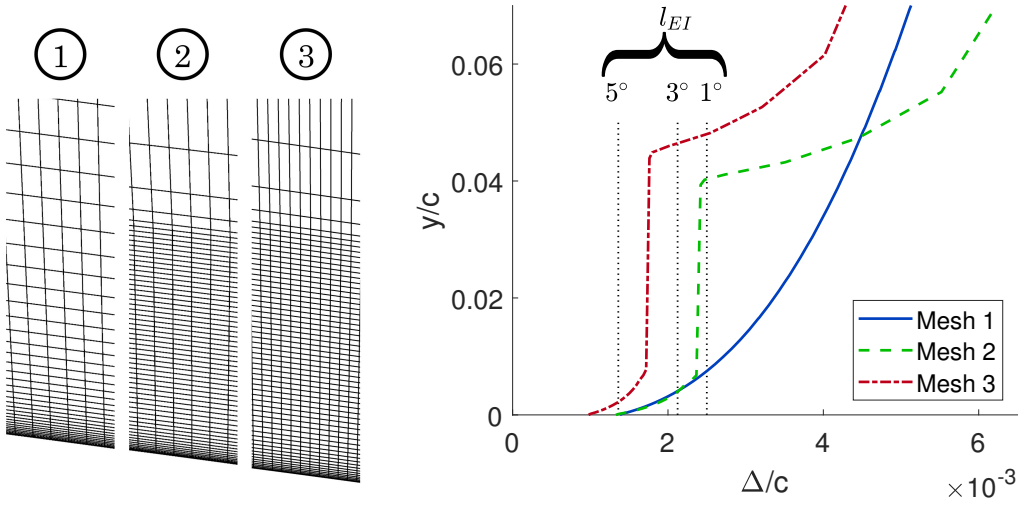
Figure 3.4: Full domain mesh and close-up of airfoil for mesh versions 1-3

length scale. To achieve this in the BL, Pope recommends that the sub-grid filter length Δ is on the order of the viscous length scale, δ_v, for $y^+ < 20$. Since $y^+ = y/\delta_v$, this is the basis of the criteria that the wall y^+ should be less than or equal to 1, however the true criteria is based on the volume which also depends on Δx^+ and Δz^+. Meeting this BL mesh criterion requires an iterative mesh refinement process since the τ_w changes as the mesh is improved, though the region of highest importance for this criteria is near the LE where the velocity in the BL is high, and therefore so is τ_w. After examining the 1° and 7° AOA cases for Mesh 1, the BL was found to meet this condition with $\Delta \leq 10\delta_v$ for the suction side BL and with an average of $2.4\delta_v$ at the surface and $4.5\delta_v$ at $y^+ = 20$.

K-H roll Filter Length

Mesh 2 consists of 4.5 million elements as shown in Figure 3.4 and uses the same chordwise, spanwise and wall mesh distribution as Mesh 1. This mesh focuses on improving the resolution of the separated BL that occurs during the LSB where the BL is offset from the wall and therefore the formation of the K-H rolls occurs in a coarser region of the mesh. To resolve this, the mesh distribution for Mesh 2 includes an additional band of uniform sized cells offset from the airfoil surface, achieved by halting the wall-normal mesh expansion in the regions of K-H roll formation. This region was measured from the results of Mesh 1

simulations at 1°, 5° and 7° AOAs to be at wall-normal distance from $0.007c$ to $0.04c$ and can be seen as the darker band of cells surrounding the Mesh 2 airfoil in Figure 3.4. A close up view of the BL mesh distribution is shown in Figure 3.5(a) where the improved resolution has 40 nodes within the K-H roll region in comparison to the 15 in the same region for Mesh 1. Additionally, the near-wake region of the mesh was refined to allow for proper development of the vortex shedding at the airfoil TE as it relates to the tonal noise generation.



(a) (b)

Figure 3.5: Improvements for mesh versions 1-3 of (a) wall-normal expansion at same location, and (b) filter length near the wall with approximate l_{EI} for the separated BL

In order to further improve the filter length in the separated region of the BL, a different mesh criterion for free shear flows is applied to the regions where BL separation occurs. In these types of flows, Pope [17] recommends that the sub-grid filter length, Δ, is "somewhat smaller" than l_{EI} and therefore is within the inertial subrange of the turbulent cascade. As described in Section 2.2.1, the turbulent cascade definitions were generated for idealized isotropic turbulence, therefore they do not strictly apply to the developing turbulence that occurs during the K-H roll formation over the LSB. However, there are no other criteria to apply to the filter length for free shear flows, so it is assumed that this criteria will serve as a guideline for the LSB mesh. The energy containing range is defined as being between the integral length scale, l_0, and l_{EI}. The largest length scales in the flow, $\mathcal{L}$, can be approximated as $6l_0$ and also $l_{EI} \approx l_0/6$. Approximating that the K-H roll length scale,

l_{KH} (the spacing of the rolls) is close to $\mathcal{L}$, then $l_{EI} \approx l_{KH}/36$. Therefore the new filter length criteria for the LSB region of the mesh is $\Delta < l_{KH}/36$ or $\Delta < l_{EI}$.

Using Mesh 2 results for 1°, 3° and 5° AOAs, the distance between the centres of the K-H rolls were measured for several different time steps. The K-H roll formation for Mesh 2 at 1° AOA is shown in detail in Section 6.1.1, Figure 5.6 where the spacing of the K-H rolls can be clearly defined to measure l_{KH}. The spacing of the K-H rolls is smaller earlier in the LSB then increases as the roll grows in strength and at 5° AOA the minimum measured l_{KH} was 1.26 mm with an average of 1.64 mm. Measurements estimated from mode 1 of the proper orthogonal decomposition (POD) by Ghorbanishohrat [4] resulted in values of l_{KH} ranging from 1.07 to 1.46 mm. Since the values from Ghorbanishohrat were lower than the values measured from the simulation of same AOA, the new mesh criteria uses the minimum l_{KH} for each simulated AOA. At 1° AOA the minimum l_{KH} was measured at 2.32 mm and was 1.97 mm for 3° AOA. The corresponding l_{EI} for each minimum l_{KH} is shown in Figure 3.5(b) as vertical dotted lines to compare the filter length in the K-H roll region of the mesh with the new criterion. The previously refined K-H roll region from Mesh 2 meets this criterion for 1° AOA since the filter length does not exceed the l_{EI} until after the top of the K-H roll region. However the 3° and 5° AOA simulations require further mesh refinements to meet this free shear flow criterion.

Mesh 3 is shown in Figure 3.4 and was designed to meet this free shear flow criteria at AOAs higher than 1° to improve the LSB simulation and aeroacoustic prediction. This posed a challenge since Mesh 2 exceeded the desired filter length for 3° AOA before reaching the K-H roll region of the mesh, and the 5° AOA criterion was only met at the airfoil surface. Since the cells in this near wall region have the largest dimensions in the chordwise and spanwise direction, new nodes were added in those directions rather than further altering the resolution in the wall-normal direction. The chordwise nodes were increased from 300 to 570 (as shown in Figure 3.5(a)) and the spanwise nodes were increased from 50 to 75. This results in Mesh 3 meeting the filter length requirement in the separated BL for 3° AOA, and also meets the requirement at 5° AOA when calculating l_{EI} using the average l_{KH} rather than the minimum value. The total number of elements increased significantly, which required reduction of the boundary offsets of the C-mesh to $R = 8c$ and $L = 10c$ to not exceed memory requirements of the computer used to locally set up and post-process the simulations. The final number of elements in Mesh 3 is 8.8 million, with the other parameters summarized in Table 3.2. Mesh 3 also features a chordwise re-distribution of the LE mesh without adding additional elements and this modification is described in the following section.

Leading Edge Filter Length

An additional improvement to Mesh 3 was added in response to the challenge of simulating the LE BL in the presence of the favourable pressure gradient caused by the flow acceleration around the airfoil curvature. As AOA increases, the magnitude of the C_p suction peak increases while the x/c location of the suction peak decreases (shifts towards the LE) which causes an increase the pressure gradient at the LE. It should be noted that the filter length criterion for an attached BL is intended for resolving a turbulent BL without a pressure gradient [17], and therefore it may be an insufficient criterion for the LE laminar BL with a large pressure gradient. However, this criterion is at the very least useful for identification of regions of concern in the BL for the higher AOA simulations and indicates where additional refinements are required. When comparing the Mesh 2 pressure gradient, dC_p/dx, simulations for $x/c < 0.025$ in Figure 3.6(a) it is clear that the majority of the difference in pressure gradient for AOAs ranging from 1° to 5° AOA occurs for $x/c < 0.002$. This corresponds to a length of 0.05 mm where Mesh 1 and Mesh 2 have only six chordwise nodes to resolve this aggressive pressure gradient.

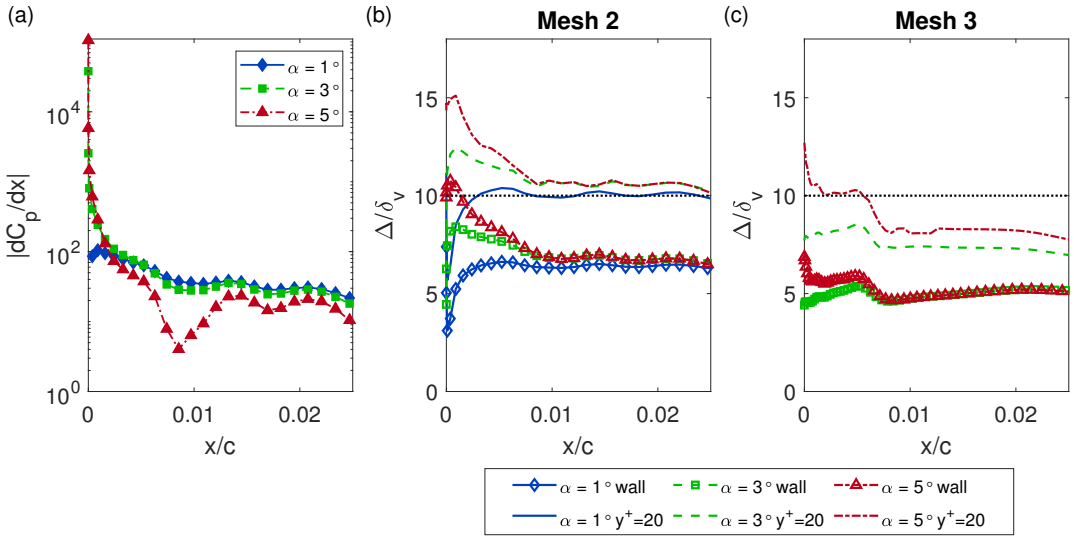


Figure 3.6: Airfoil LE information for $x/c < 0.025$ of (a) Mesh 2 dC_p/dx, (b) Mesh 2 Δ/δ_v for $y^+ < 20$ and (c) Mesh 3 Δ/δ_v for $y^+ < 20$

In terms of the filter length criterion in the attached BL at the LE, the favourable pressure gradient and flow acceleration around the LE curvature results in an increase in the wall shear stress with increasing AOA and therefore a decrease in δ_v (see Equation 3.2).

This requires smaller filter lengths at the LE for the higher AOAs to ensure the criterion of $\Delta/\delta_v \leq 10$ is met for the first few chordwise nodes of the laminar BL. The analysis of the filter length criterion for $y^+ < 20$ in Mesh 1 and Mesh 2 was completed at a chordwise spacing of $0.025c$ with the first x/c location at $x/c = 0.025$. At this chordwise location there was little variation of δ_v across the simulated AOA range, however when considering the lower δ_v induced by the pressure gradient at the LE for 3° and 5° AOA the filter length is insufficient for $x/c < 0.025$. This is shown in Figure 3.6(b) where the filter length data from Mesh 2 at $x/c = 0.025$ is compared with δ_v for $x/c < 0.025$ to assess if it meets the criterion of $\Delta/\delta_v \leq 10$. For the x/c ranging from 0.01 to 0.025 there are minimal differences between the adequacy of the filter length and for $x/c < 0.01$ the higher AOAs fail to meet the criterion. At 5° AOA the nodes closest to the LE do not meet the criterion at the wall meaning that the entire BL in this critical high pressure gradient region has an insufficient filter length. The filter length in that region for 3° AOA meets the criterion at the wall but not at $y^+ = 20$ and therefore also requires correction to improve the LE filter length.

The improved LE filter length in the BL was achieved through a doubling of the chordwise nodes for $x/c < 0.03$ from the 30 nodes used in Mesh 1 and Mesh 2 to 60 nodes in Mesh 3. The initial tests of refining the LE mesh identified that the curvature in the imported airfoil geometry was of a coarser resolution than the required chordwise mesh spacing for $x/c < 0.025$ which resulted in surface roughness that produced small oscillation of the C_f in the region of $x/c < 0.025$. It was decided to replace the original airfoil LE coordinates for $x/c < 0.006$, or $x < 0.15$ mm, with a perfectly rounded LE under the assumption that the manufacturing process for the experimental geometry would not be capable of replicating the small scale of the anomalies found in the numerical geometry. The LE curvature and chordwise node distribution for $x/c < 0.03$ are shown in Figure 3.7 for Mesh 2 and Mesh 3. Since the LE filter length is a concern for $x/c < 0.01$ an exponential chordwise distribution was used for the 60 nodes near the LE, which increased the density and therefore decreased the filter length at the LE. The significant improvement in the filter length for Mesh 3 is shown for 3° and 5° AOA in Figure 3.6(c), where 3° AOA now meets the mesh criterion for $y^+ < 20$ and 5° AOA meets the criterion except for $x/c < 0.005$ at $y^+ = 20$.

This concludes the details of the implementation of the wall-resolved LES method and the FW-H acoustic analogy for the purposes of predicting the tonal airfoil self-noise from the SD 7037 airfoil at a modest Re. The results of the LES simulation using Mesh 1 are reported in Chapter 4 and the LES and FW-H simulations using Mesh 2 and Mesh 3 are reported in Chapters 5 and 6.

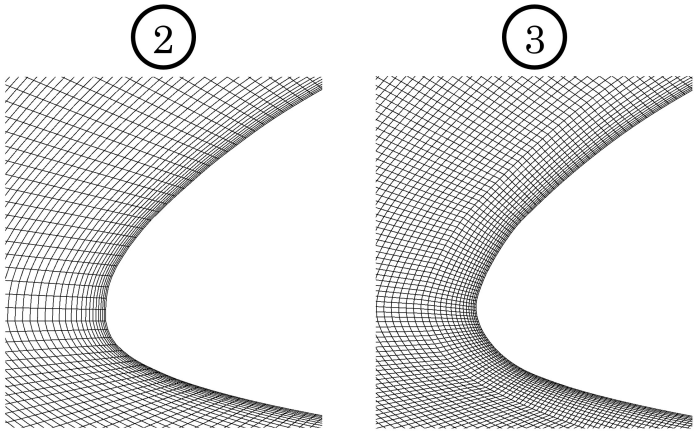


Figure 3.7: LE curvature and chordwise node distribution for $x/c < 0.03$ for Mesh 2 and Mesh 3

3.3 Theoretical Approach - Dynamic Stall

Dynamic stall of SWT blades is a complex transient process that can occur due to the changes in effective AOA of the blade during its rotation and was explained in detail in Section 2.5. The unsteady aerodynamic loading that occurs during dynamic stall is a concern for the design of SWT blades and the need for the accurate simulation of the dynamic stall process at low Re was established in Section 2.5.4. The discussion in Sections 2.5.3 and 2.5.4 summarized the potential role of the LE LSB burst in the stall process for low Re blades which poses a challenge to the accurate simulation of dynamic stall.

Ideally, the simulations of dynamic stall would be completed using the LES method outlined in Section 3.2 however, the LSB at the time of dynamic LSB burst is located in the thin BL at the LE of the airfoil. The near-wall mesh criterion and the free-shear mesh criterion for the development of the BL over the LSB are increasingly difficulty to meet at the LE. In Section 3.2.6 the mesh criterion applied to Mesh 3 at 5° AOA was unable to fully meet the criterion at the LE and this would be further challenged at the approximate 15°-20° AOA needed for simulation of the bursting of the LE LSB during dynamic stall. For this reason, the dynamic stall analysis is completed using the unsteady RANS (URANS) method, which was initially found to accurately predict the time-averaged formation of the LSB during the flow field initialization of the LES simulations described in Section 3.2.2. The numerical method used for the URANS simulations of dynamic stall is described in Section 3.4.

3.3.1 URANS Validation

The majority of the published dynamic stall simulations summarized in Section 2.5 are completed using the NACA 0012 airfoil [88–92, 95–100, 104] and are validated using the same experimental data set [93]. The validated simulations in this work were completed using two different airfoil profiles designed for operation at low Re and are useful for studying the expected behaviour during dynamic stall for current low Re applications such as SWT. The dynamic stall simulations are validated against experimental data sets for the low Re airfoil profiles SD 7037 [4, 103] and S833 [113], both of which are operating at low Re and have similar deep dynamic stall cycles.

The distinction between deep dynamic stall and light dynamic stall is described in Section 2.5.2 where a typical lift coefficient, C_L, cycle for deep dynamic stall is shown in Figure 2.12(a). The experiments were both completed under controlled conditions in closed-loop wind tunnels with a 2D blade segment with a constant chord length and no blade twist. The dynamic stall was initiated through the sinusoidal pitching of the blade relative to the incoming free-stream velocity to alter the blade AOA. Section 2.5.1 explained the theory behind how the sinusoidal pitching of an airfoil can be used to replicate the change in effective AOA of a SWT blade under unsteady wind conditions.

The experimental study of the SD 7037 airfoil was completed using PIV by Gharali and Johsnon [103] and Ghorbanishohrat [4] which applied the same flow condition as the validating data for the LES simulations (see Section 3.1.1) with $c = 0.0258$ m and $Re = 4.1 \times 10^4$. The applied pitching cycle has a mean AOA of 11° and amplitude of 11° and the frequency of the pitching cycle resulted in a reduced frequency of $k = 0.08$. The reduced frequency is defined in equation 2.16 and the experimental value is within the unsteady range as defined in Section 2.5.2.

The S833 airfoil profile is part of the NREL family of airfoils designed for a SWT with a rotor diameter of 1 to 3 m [114]. The experiments completed by Samara and Johnson [113] measured the aerodynamic loads on the blade using surface pressure measurements on the S833 airfoil with $c = 0.178$ m and at $Re = 1.7 \times 10^5$. This operation is within the low Re range of $Re < 5 \times 10^5$ however it is approximately four times larger than the SD 7037 simulations which are in the modest Re range of $Re < 1 \times 10^5$. The S833 experiments applied a pitching cycle with a mean AOA of 10° and an amplitude of 10° and the reduced frequency for this case is $k = 0.06$ which also falls within the unsteady range.

3.3.2 Simulation Phases

The first phase of the dynamic stall simulations addressed the simulation of the SD 7037 airfoil since the initial tests of the URANS model accuracy at static AOAs could be validated against both the experimental data and the LES simulations completed as a part of Section 3.2. After validation of the dynamic URANS simulation of the SD 7037 airfoil, the geometry and mesh were scaled up to the operating conditions of the S833 case. This process required several test simulations for the mesh, inlet turbulence parameters and the simulation time step before arriving at the final simulation setup. The details of the numerical method are included in Section 3.4 and the results of the dynamic stall simulations are reported in Chapter 7.

3.4 Numerical Method - Dynamic Stall

3.4.1 URANS Setup

The URANS simulations of dynamic stall at low Re were performed using the $\gamma - Re_{\theta t}$ SST $k - \omega$ turbulence model, known as the transition SST model in ANSYS Fluent. The commonly used URANS turbulence models for low Re simulations of dynamic stall are summarized in Section 2.5. The transition SST model [109, 115] is a four-equation model that expands on the standard SST model [116] and is designed to account for the transitional BLs that develop at low Re and can predict localized regions of separation, including a LSB. The accuracy of the prediction of the LSB was assessed through test simulations of the SD 7037 airfoil at $Re = 4.1 \times 10^4$ and at static AOAs using the following RANS models available in Fluent: Spalart Allmaras (S-A), strain-based S-A, SST, SST with a low Re correction and transition SST. The S-A and base SST models were unable to predict laminar BL separation and the low Re correction was able to predict laminar separation, but not reattachment. The transition SST model was the only model tested that was capable of predicting the LSB for this case, which reflects the findings of Liu *et al.* [102] and Tseng *et al.* [105].

The simulations were run in the incompressible form, and all residuals were set at 1×10^{-5}. The SIMPLEC pressure-velocity coupling scheme was used, with bounded CDS as the discretization scheme and bounded second order implicit as the time integration method. These are the same schemes applied to the LES simulations, as described in Section 3.2.1, and the details of the schemes can be found in Section 2.2.4. To decrease

computing time, simulations were run using a high performance computer cluster in the Digital Research Alliance of Canada network [110] as described in Section 3.2.2.

The dynamic change in AOA is represented through the sinusoidal rotation of the computational domain with respect to the global coordinate system using Equation 2.15. This motion is applied using the Mesh Motion feature incorporated into the ANSYS Fluent software, which can rotate the entire mesh to generate the dynamic airfoil motion and does not require any alteration of the inlet boundary conditions. The dynamic mesh motion method was successfully applied by Gharali [81] for an unsteady RANS study of similarly oscillating low Re airfoils. To implement this motion in Fluent, the rotational speed in rad/s is provided for each time step through a data file. The axis of rotation is located at the quarter-chord location of the airfoil, which is the rotation axis location for the experimental data sets [4, 103, 113]. The simulations were run for at least 5 complete pitching cycles, where the first 1-2 cycles are an initialization and the final 3 cycles, which had no variation, are used for the analysis.

The simulation time step size for each airfoil was determined through numerous test cases, and was selected based on a balance of number of time steps required per pitching cycle and the number of solution iterations required for each time step. The SD 7037 simulations use a time step of 5×10^{-5} s which resulted in an average of 60 iterations per time step and the S833 simulation uses a larger time step of 1×10^{-4} s due to the longer duration of the cycle resulting in an average of 32 iterations per time step. The complete details of each airfoil and its corresponding pitching motion are summarized in Table 3.3.

Airfoil Profile		SD 7037	S833
Reynolds Number	Re	4.1×10^4	1.7×10^5
Chord	c	0.0258 m	0.178 m
Inflow Velocity	U_∞	23.8 m/s	15 m/s
Turbulent Intensity	Tu	1%	0.1%
Reduced Frequency	k	0.08	0.06
Cycle Period	T	0.043 s	0.62 s
Mean Angle of Attack	α_{mean}	11°	10°
Pitching Amplitude	α_{amp}	11°	10°
Time Step	Δt	5×10^{-5} s	1×10^{-4} s

Table 3.3: Dynamic stall geometries and numerical details

3.4.2 Mesh and Boundary Conditions

The simulation domain for each airfoil is a 2D C-mesh with $20c$ offsets as shown for the SD 7037 airfoil in Figure 3.8(a), and the S833 airfoil in Figure 3.8(b). The vertical outflow surface was defined as a pressure outlet and the surface of the airfoil was set as a no-slip wall. The remaining outer boundaries of the C-mesh were set as velocity inlets, with the velocity magnitude and direction remaining a constant horizontal velocity in the global reference frame. The pitching motion was applied purely through the rotation of the domain, meaning no change in inlet velocity direction was required. This is identical to the method of sinusoidal pitching used in the validating experimental data, where the airfoil is pitched relative to the constant horizontal velocity of the wind tunnel [4,103,113].

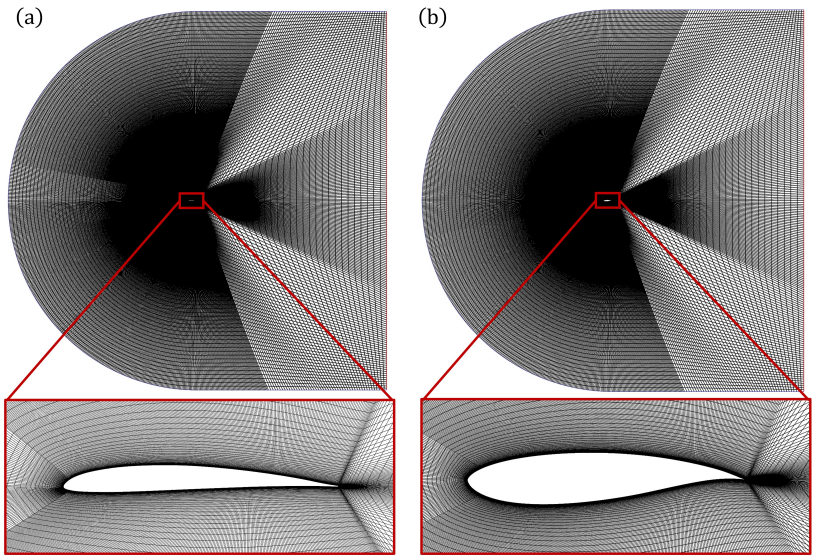


Figure 3.8: Dynamic stall simulation C-Mesh distribution for both airfoils and mesh quality around the airfoil for (a) SD 7037 and (b) S833

The inflow turbulence conditions were set to account for the dissipation of inflow turbulence between the inlet and the airfoil, which requires specifying an elevated turbulent intensity at the domain inlets. For the SD 7037 case, this required the use of a turbulent intensity of $Tu = 12\%$ at the inlet to achieve a value of 1% at a location 0.9c upstream of the LE to agree with the experimental data [107]. For the S833 case, a value of $Tu = 0.12\%$ was used at the inlet which dissipated to 0.1% at a location of 1.7c upstream of the LE [113].

The mesh consists of 6.8×10^4 cells and the airfoil has 300 nodes along the chord length

with a wall y^+ of less than 0.5 for the AOAs with an attached BL. Assessment of the URANS simulation of the LSB determined that the LSB prediction benefits from a finer mesh than is typically recommended for URANS analysis. For this reason, the near-wall mesh sizing is identical to that used in Mesh 1 in Figure 3.4 with the far-field distribution from a prior LES mesh when the boundary offsets were still set at $20c$. Due to the mesh-dependent sub-grid filtering used during LES simulations, the near-wall mesh spacing had been optimized for up to $y^+ = 20$ rather than only ensuring that the first node height was at $y^+ < 1$. The creation of Mesh 1 is described in detail in Section 3.2.6.

3.4.3 Grid Coarsening Study

A grid coarsening study was completed to determine the sensitivity of the dynamic stall process to the mesh density by increasing the wall y^+ and decreasing the wall-normal and chordwise nodes in the airfoil BL. The key parameter monitored through the study was the magnitude and AOA of the peak C_L in the dynamic stall cycle, which is used as an indicator of the correct timing of the simulation of the LEV formation and the subsequent drop in lift that occurs at stall. The first mesh version altered the first layer height (FLH) at the airfoil surface, where the wall-normal height of the first node was doubled to increase the wall y^+ from $y^+ < 0.5$ to $y^+ < 1.2$. The second mesh version reduced the number of wall-normal nodes (WNN) within a wall-normal distance of $0.4c$ from the airfoil surface from 50 to 25 and has the same $y^+ < 1.2$ as the FLH mesh. The third and final mesh used the wall-normal spacing of the WNN mesh and coarsened the number of chordwise nodes (CWN) from the original value of 300 nodes along the chord to 150 nodes. The mesh details are summarized in Table 3.4 and all mesh versions had a wall-normal expansion ratio set at 1.1.

Mesh Version	y^+	BL Nodes	Chordwise Nodes
Original	< 0.5	50	300
FLH	< 1.2	50	300
WNN	< 1.2	25	300
CWN	< 1.2	25	150

Table 3.4: Grid coarsening study details

The C_L values through the pitching cycle for each coarsened mesh version are shown in Figure 3.9 and are compared against the C_L cycles from the original mesh results reported in Section 7.2 and the experimental data [103, 113]. The FLH case resulted in no change in

the magnitude or timing of the C_L cycle for both airfoils which indicates that the low y^+ of the original LES-quality mesh is not necessary for the correct peak C_L AOA prediction. The alteration that resulted in the prediction of early peak C_L and stall for both airfoils was the reduction of the number of wall-normal nodes in the WNN case. This resulted in peak C_L AOAs that occurred earlier in the pitching cycle by 0.9° for the SD 7037 airfoil (Fig. 3.9(b)) and 0.8° for the S833 airfoil (Fig. 3.9(d)). The alteration of the chordwise nodes in the CWN mesh did not alter the peak C_L AOA in any significant manner beyond the change already seen from the WNN results.

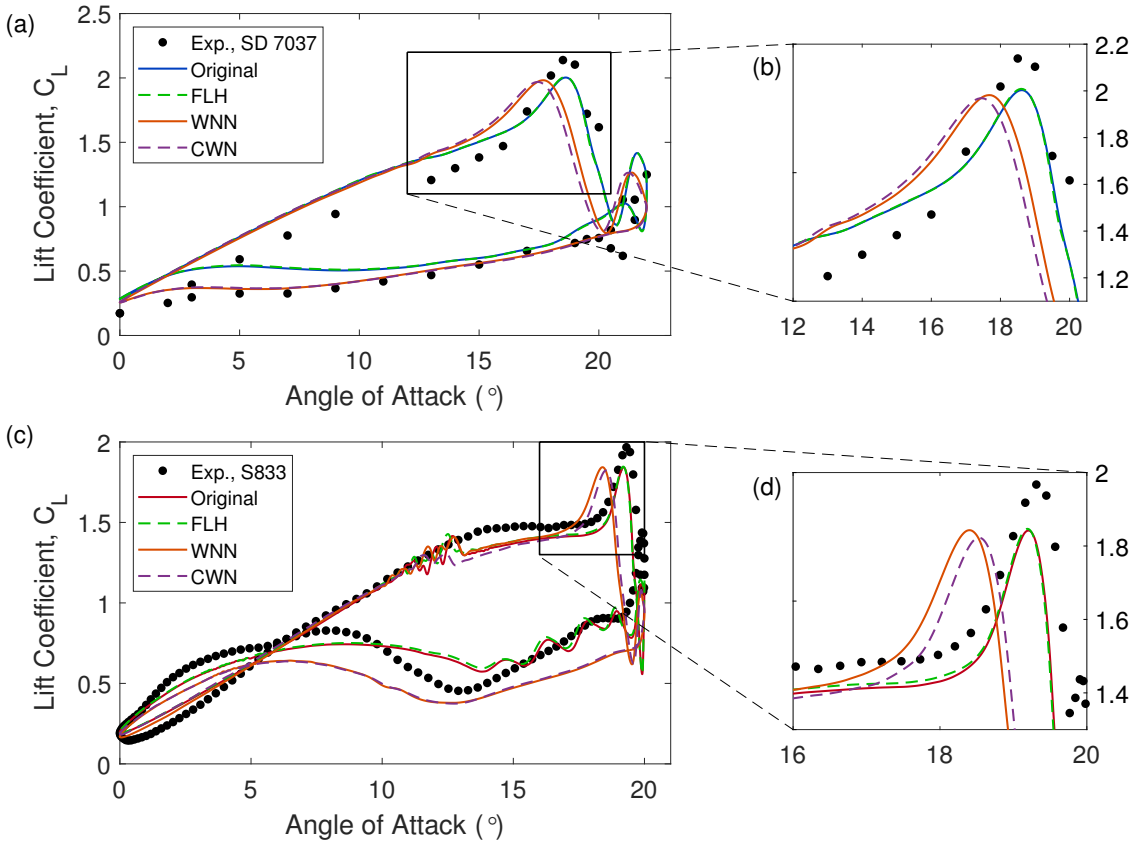


Figure 3.9: Grid coarsening study results for the dynamic C_L cycle compared against experimental data for (a) SD 7037 [103] and (c) S833 [113]. Detailed views of the C_L peak are shown for (b) SD 7037 and (d) S833.

The number of nodes in the BL were compared in the attached laminar BL upstream of LSB formation for a range of dynamic AOAs before the peak C_L. For the SD 7037

airfoil this was assessed at $x/c = 0.02$ from 0° to 9° AOA and the S833 comparison is completed for 0° to 13° AOA at the LE ($x/c = 0.002$) due to the LSB location at high AOAs. The number of wall-normal nodes in the attached BL was 10 to 11 for the original mesh, 7 to 9 for the FLH mesh and 6 to 7 for the WNN and CWN meshes. Therefore in both cases a minimum of 8 nodes within the laminar BL at the airfoil LE is required to prevent the early stall behaviour seen in the WNN and CWN mesh versions. The impact of the wall-normal resolution of the BL is evident in the dimensionless BL thickness, δ/c, where the original mesh has a value of 0.004 for the SD 7037 airfoil at $x/c = 0.02$ and 0.0012 for the S833 airfoil at $x/c = 0.002$. The BL thickness at those locations remained constant for the FLH SD 7037 mesh but increased by a factor of 1.25 for the FLH S833 mesh. The larger change in wall-normal spacing in the WNN and CWN mesh versions increased the BL thickness by a factor of 1.5 for the SD 7037 simulation and 1.7 for the S833 simulation. These changes in the simulated BL thickness at the airfoil LE will alter the downstream development of the BL transition and the LSB. The importance of the correct LSB simulation at high AOAs and its relevance to the accurate prediction of the LEV will be discussed at length in the results section.

The WNN and CWN results in Figure 3.9 show a similar early C_L peak behaviour to previous URANS studies [92, 96–99] where the prediction of the peak C_L AOA occurs approximately 2° early in comparison with experimental data. These prior studies were completed at Re values that fall between the 4.1×10^4 of the SD 7037 simulation and the 1.7×10^5 of the S833 simulation, and therefore it is probable that the requirement of 8 nodes within the laminar BL at the airfoil LE would be applicable to those prior studies. Through this study, it can likely be concluded that the improvement in the stall AOA prediction gained through the usage of the LES-quality mesh is due to the increased wall-normal mesh density in the BL. The original mesh and the FLH mesh both provide accurate predictions of peak C_L AOA and feature the same total number of elements and associated computational expense. However, since the original mesh has 10 to 11 nodes in the laminar BL compared to the 7 to 9 in the FLH mesh, the remainder of the simulations in this paper are completed using the original LES-quality mesh to better meet the new recommendation of 8 nodes in the laminar BL.

This concludes the details of the implementation of the URANS method for the simulation of dynamic stall for the SD 7037 and S833 airfoils at low Re. The results of the simulations using the LES-quality mesh are reported in Chapter 7.

Chapter 4

Time-Averaged LSB Results[1]

This chapter presents the first phase of the validation of the large eddy simulation (LES) of the laminar separation bubble (LSB) on the suction side of the SD 7037 airfoil at a Reynolds number of $Re = 4.1 \times 10^4$ and at 1°, 5° and 7° angles of attack (AOA). This validation and analysis was required before proceeding with the computational aeroacoustic (CAA) simulations to predict the tonal aeroacoustic noise generated by the airfoil trailing edge (TE) since this requires the accurate simulation of the BL development and the formation of the LSB, as is described in Sections 2.3.3 and 2.4.3. The formation of a LSB on a low Re airfoil is explained in Section 2.1.4 and the simulation of a LSB is summarized in Section 2.2.3. The approach and numerical method for the LES simulations is covered in detail in Sections 3.1 and 3.2 and all results in this chapter are generated using Mesh 1 shown in Figure 3.4 with other simulation details summarized in Tables 3.1 and 3.2.

This phase of the simulation validation and analysis is focused on the time-averaged parameters in the boundary layer (BL) which are used to assess the accuracy of the BL transition and LSB formation and are compared against experimental data summarized in Section 3.1.1. The results and analysis reported in this chapter address the research objectives #1, #5 and #6 in Section 1.3 for the numerical prediction of tonal aeroacoustic noise for small wind turbine (SWT) blades operating at low Re with a LSB. The contents of this chapter have also been published in the peer-reviewed *ASME Journal of Fluids Engineering*[1].

[1]Published by Zilstra, A. and Johnson, D.A. (2022) Large Eddy Simulation of Transitional Separated Flow Over a Low Reynolds Number Cambered Airfoil. ASME. J. Fluids Eng. doi: 10.1115/1.4056280

4.1 Flow Structure Visualization

Before presenting the quantitative results for the simulation of the LSB, the visualization of the suction side LSB is presented to provide context to the analysis in this chapter. A useful method of visualizing the coherent flow structures within the BL transition is through iso-surfaces of Q-Criterion, defined as the second invariant of the velocity gradient [117]. Figure 4.1 shows the Q-criterion iso-surface at a value of 5×10^7 s^{-2} for the final time step of each simulated AOA. Flow is from the lower left to the top right, showing the suction side of the airfoil and can be compared with the transition process outlined Section 2.1.4 and the diagram in Figure 2.4. The Q-criterion is coloured with the velocity magnitude, $|V|$, made dimensionless with the inflow velocity, U_∞, to better visualize the height and shape of the structures formed over the LSB and after BL reattachment. The locations of BL separation and reattachment are indicated by the white dashed lines, where applicable, and exact x/c values for these locations, found in Table 4.1, were determined using the skin friction coefficient results presented in Section 4.5. The time-averaged locations of BL transition in Table 4.1 were determined using the shape factor, H, results in Section 4.3.

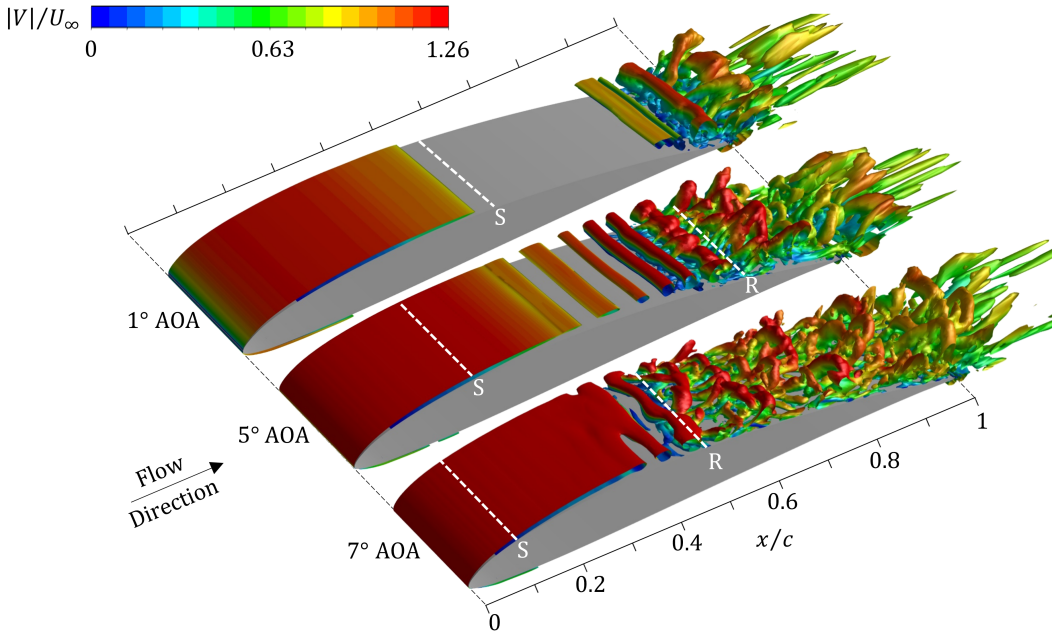


Figure 4.1: Q-Criterion iso-surface of 5×10^7 s^{-2} for 1°, 5° and 7° AOAs, coloured by non-dimensional velocity magnitude. White dashed lines indicate location of BL separation (S) and reattachment (R), where applicable

Angle of Attack	Mesh #	x/c Location		
		Separation	Transition	Reattachment
1°	1	0.54	0.88	- -
5°	1	0.30	0.65	0.84
7°	1	0.13	0.40	0.54

Table 4.1: Boundary layer separation, transition and reattachment locations, $Re = 4.1 \times 10^4$

For 1° AOA, laminar separation is approximately seen at the abrupt stop of the Q-Criterion iso-surface which forms from the leading edge (LE) of the airfoil. At the TE, the transitional BL remains largely two-dimensional (2D) and due to insufficient growth of K-H instabilities it does not progress into the portion of the transition process where significant spanwise decomposition, or spanwise breakdown, occurs, as is described in Section 2.1.4.

The development of increasingly complex spanwise structures occurs after BL reattachment, as seen the 5° and 7° AOA results. The elongated LSB and accompanying slower transition to turbulence in the 5° AOA case shows the growth of the 2D K-H rolls defined in Section 2.1.4 that are initiated by the K-H instability in the separated BL [8], and the formation of horseshoe vortices after BL reattachment [2]. The horseshoe vortices have elongated legs extending down to the airfoil surface with the heads of the horseshoes aligning with the K-H rolls that developed in the separated shear layer.

These waves of horseshoe vortices developing in the reattached BL are a similar scale to other studies completed at modest Re, defined as $Re < 1 \times 10^5$ in Section 2.1.1. This includes the numerical study of a cambered airfoil at $Re = 6 \times 10^4$ by Galbraith and Visbal [31] and Breuer [32], the symmetric NACA airfoil simulation at $Re = 5 \times 10^4$ by Thomareis and Papadakis [26], and the flat plate results of Brinkerhoff and Yaras [6]. In airfoil simulations at a higher Re [5, 22, 25, 33], the scale of the horseshoe structures in the reattached BL is smaller in comparison to the airfoil chord, K-H roll size and LSB chordwise length. This trend can be clearly seen in a comparison of the symmetric NACA airfoil simulation by Thomareis and Papadakis [26] at a modest Re and the works of Smith and Ventikos [25] and Ziade *et al.* [5] at a similar AOA and double the Re.

The 7° AOA BL transition contains similar structures as the 5° AOA result, however it is visibly much more disorganized with increasing x/c. This indicates an accelerated transition to turbulence, which is expected due to the shortened LSB as well as the higher pressure gradient and velocity gradient. The 7° AOA results are similar to those seen

in previous simulations of transitional separated flow [5, 25], which use symmetric NACA airfoils at a higher Re on the order of 10^5 and 4° or 5° AOAs. In these higher Re cases, the BL transition occurs earlier and the LSB formation process is condensed into a shorter chordwise distance. Due to the accelerated transition in those studies, any remnant of the K-H spanwise rolls disappears at reattachment, meaning that the horseshoe vortices and other complex structures are no longer in spanwise alignment. The mentioned differences in LSB chordwise length and the scale of the horseshoe vortices in the attached BL clearly show the importance of numerically investigating the transitional separated BL at increasingly modest Re, since the sensitive transition process includes larger structures that will have a greater impact on airfoil performance.

4.2 Pressure Distribution

The time averaged pressure coefficient, C_p, results are shown for the suction side of the airfoil in Figure 4.2, compared against the experimental results [4]. The simulated C_p as defined in Equation 2.2 has a consistently higher magnitude than the experimental results, and this is most notable at the suction peak (minimum C_p). A unique aspect of the experiments by Ghorbanishohrat [4] is that surface pressure measurements were determined through integration of the particle image velocimetry (PIV) velocity measurements in the BL. This method of pressure determination was necessary since the small scale of the airfoil prevented the usage of static pressure taps. While the reported statistical uncertainty for averaged velocity components was 0.42%, the accuracy of this method of calculating C_p is limited by the PIV resolution close to the wall, and introduces more error closer to the LE of the airfoil where the BL is thin [4]. It is therefore expected that the experimental suction peak measurements will be of lower magnitude than the simulated values, which is the case for the presented results. This is also expected to be the reason for the greater magnitude of the C_p values generated by the LES simulation, placing more emphasis on the agreement of the changes in C_p gradient with respect to x/c for validating the pressure behaviour at the airfoil surface. Additional analysis comparing the PIV resolution to the near-wall resolution of the LES simulation can be found in Section 4.5.

A C_p plot with a fully formed LSB will feature the indicative transition ramp [12], as described in Sections 2.1.3 and 2.1.4, which begins with the levelling off of the C_p curve at the location of laminar separation (labelled S in Figure 4.2) followed by a sharp pressure recovery at reattachment (labelled R in Figure 4.2). Exact x/c locations of BL separation and reattachment can be found in Table 4.1. In the 1° AOA result in Figure 4.2(a), the decreasing gradient indicating laminar separation can be seen at approximately $x/c = 0.55$,

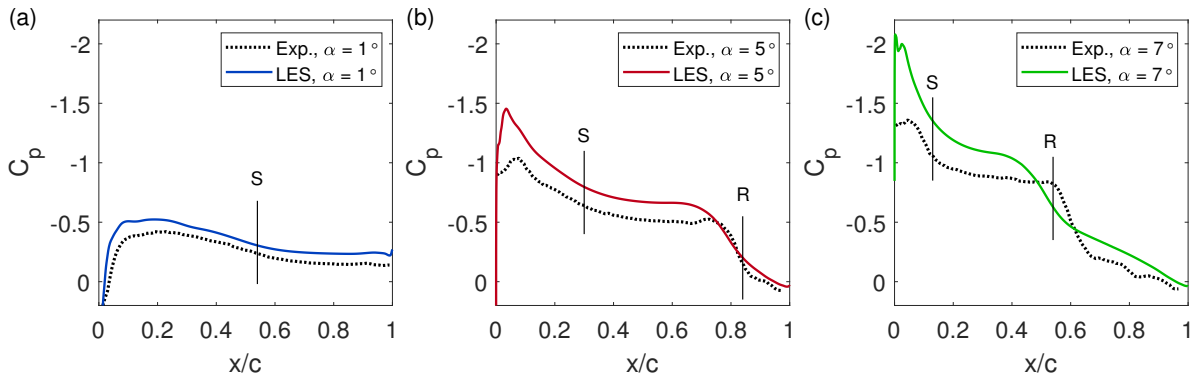


Figure 4.2: Suction side C_p for (a) 1° AOA (b) 5° AOA and (c) 7° AOA compared with experimental measurements [4]. Locations of BL separation and reattachment are marked with S and R, respectively

and there is no pressure recovery since the BL does not reattach resulting in a transitional separated BL at the TE.

The transition ramp in the C_p curve for the 5° and 7° AOA simulations can be identified in Figure 4.2(b) and 4.2(c), since both AOAs have a fully formed LSB. The location of separation can be seen to be in agreement with the experimental findings due to the parallel C_p curves at the initiation of the transition ramp. This occurs at approximately $x/c = 0.3$ for 5° AOA and $x/c = 0.13$ for 7° AOA. However, the pressure recovery occurs earlier in the LES results, showing that the BL reattaches earlier than it was found to in experiments. This can be seen when the LES and experimental results intersect at around $x/c = 0.8$ for 5° AOA and $x/c = 0.6$ for 7° AOA. Deviation of the reattachment location is more likely to occur since the separated BL is more sensitive to simulation parameters such as the free-stream turbulence where Section 2.2.4 showed that higher turbulence will lead to earlier BL reattachment [9, 22, 32, 33]. This indicates the possibility that the inlet turbulence model used in the LES simulations likely generated free-stream turbulence that was slightly elevated in comparison to the experimental conditions.

Similar transition ramps have been simulated previously for cambered airfoils [7, 31–33] and NACA airfoils [25–27], though the C_p results in those cases are either unvalidated or validated against DNS results rather than experimental data. This removes the complexity of replicating the experimental free-stream turbulence conditions. Ziade *et al.* [5] validated the LES generated C_p against experimental surface pressure measurements, generating an accurate C_p curve with the exception of a delay in the location of BL reattachment. This

was attributed to the laminar free-stream conditions (i.e. no prescribed inlet turbulence) used in the LES simulation in comparison with experimental results which were collected with an inflow turbulence intensity of 0.08%. In the presented work, the LES turbulence intensity is in agreement with the measured experimental turbulence intensity of 1% at a location 24 mm upstream of the LE [107] and therefore resulted in a more accurate prediction of the location of pressure recovery in the C_p curve. It is clear from the presented results and those of Ziade *et al.* [5] that minor differences in inflow turbulence, while not affecting the laminar separation location, can have a significant impact on the reattachment location. This further highlights the importance of high resolution experimental validation data and accurate inflow turbulence replication in LES simulations of transitional separated flow.

4.3 Boundary Layer Integral Analysis

The theory and expected trends of the BL integral parameters when a LSB forms in the transitional BL is summarized in Section 2.1.5. The simulated displacement thickness, δ^*/c, for each AOA is shown in Figure 4.3(a) with comparisons against the experimental measurements of Ghorbanishohrat [4]. The LES mean velocity profiles used to calculate δ^* (see Equation 2.5) were collected at a spacing of $x/c = 0.025$ (0.645 mm) in planes perpendicular to the airfoil surface. As was seen in the C_p data, the simulated magnitude of δ^*/c is larger than what was measured experimentally but the gradient of δ^*/c with x/c is in agreement. The early transition of the 7° AOA separated BL can also be seen in this data, where the simulated peak at approximately $x/c = 0.4$ occurs before the experimental peak at approximately $x/c = 0.5$.

The simulated momentum thickness, θ/c, results calculated using Equation 2.6 and presented in Figure 4.3(b) very clearly show the abrupt increase in boundary layer momentum expected at the location of BL transition. This location coincides with the x/c location of the initiation of the pressure recovery of the transition ramp in the C_p results, which is another indication of the location of BL transition. All results are in agreement with the experimental data, with minor differences in the θ/c gradients for the 5° and 7° AOA after BL transition. An interesting feature of the 7° AOA θ/c is the increase and then brief plateau that occurs twice between $x/c = 0.5$ and 0.8. This could be due to complex flow structures (such as the horseshoe vortices visualized in Figure 4.1) developing at a consistent location with time and these jumps in BL momentum are likely the reason for the predicted early BL reattachment at this AOA.

A notable difference in the δ^*/c and θ/c trend occurs when $x/c \leq 0.2$, where the

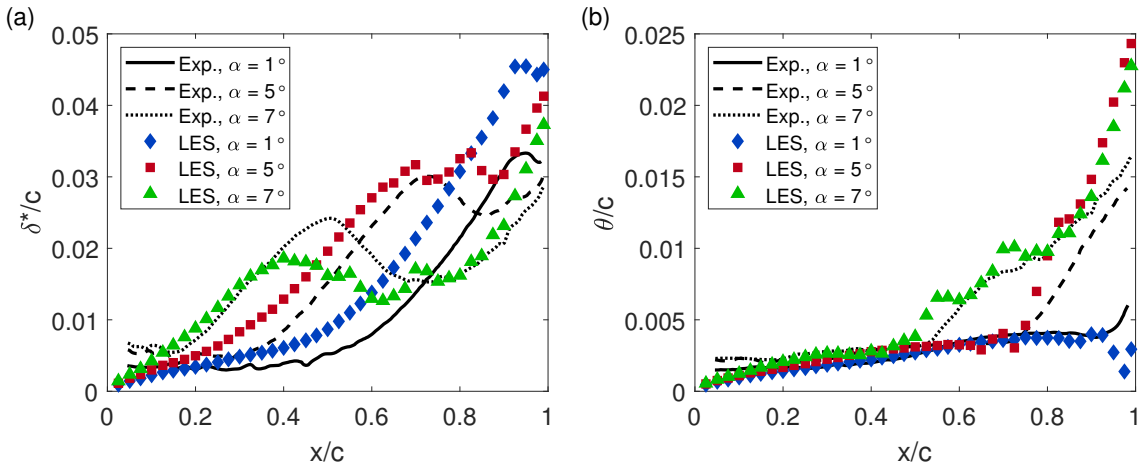


Figure 4.3: (a) Non-dimensional displacement thickness, δ^*/c vs. x/c and (b) non-dimensional momentum thickness, θ/c vs. x/c compared against experimental data [4] for $\alpha = 1°, 5°, 7°$

gradient of the experimental data is approximately zero and the simulated data has a gradient consistent with the data when $x/c > 0.2$. This shows the impact of near-wall PIV resolution on the experimental results, since the thin laminar BL near the LE is more accurately captured by the finer resolution used in the LES simulation.

The simulated shape factor, H, results calculated using Equation 2.7 and presented in Figure 4.4 show H increases at the same location as δ^* and reaches a maximum at the location where θ begins to increase. The chordwise location of this well-defined H peak aligns with the experimental results [4], with the exception of the upstream shift in LSB reattachment location that was also identified in the 7° AOA C_p results (Figure 4.2). In the 1° AOA result, the values from $x/c = 0.9$ to the TE are elevated, which is attributed to the unsteady nature of the separated suction side BL interacting with the pressure side BL. This difference is only seen in the 1° AOA result, since the 5°and 7° AOAs have a more stable turbulent BL at the TE. A further discussion of the H peak validation and the impact of the differing near-wall resolution of the PIV method and LES simulations is included in Section 5.2.

Shape factor, H, results provide a very clear location of BL transition as described in Section 2.1.5 and summarized in Table 4.1 which is difficult to resolve using either the C_p plots or through visualization methods. This H behaviour is not commonly included in the analysis of low Re airfoil simulations, however the LES results of Lobo *et al.* [33],

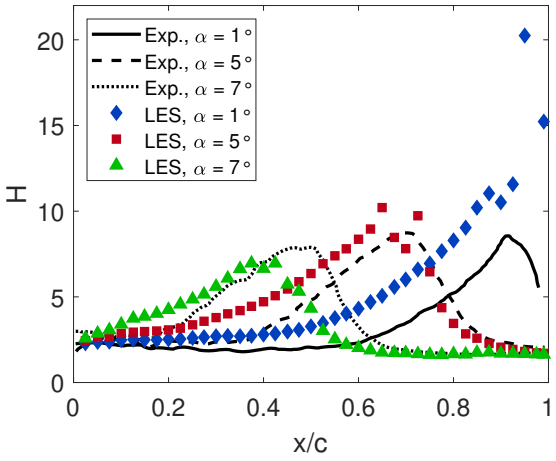


Figure 4.4: Suction side H for $\alpha = 1°, 5°, 7°$, compared with experimental measurements [4]

the experimental measurements by McAuliffe and Yaras [14] and the simulated flat plate results by Lardeau *et al.* [22] and Wissink and Rodi [9] captured a similar H pattern, with peak H values in the range of 6 to 12. Additionally, while Ziade *et al.* does not present H as a function of x/c for their simulated airfoil H was found to range from 5.9 in the attached BL up to a peak value of 22 [5]. The simulated H values for each AOA fall within the range found for other transitional separated BLs with peak values of 11, 10.2, and 7.0, and more importantly these values are in agreement with the experimental data available for the SD 7037 airfoil [4]. This indicates that the LES simulation captured the correct velocity distribution and BL profile shape compared to the experimental results, validating the accuracy of the mean velocity behaviour through the complex flow behaviour in the transitional separated BL.

As the BL completes the transition to turbulence, θ increases in relation to δ^* and causes H to decrease to a magnitude lower than the value in the laminar BL. For a flat plate BL with no pressure gradient, the typical H values are approximately 2.4 for a laminar BL and 1.7 for a turbulent BL [9]. In agreement with these values, the laminar BL at the LE of the airfoil for all simulated AOAs has H ranging between 2.3 to 2.6, and 5° and 7° AOA have H values of 1.7 and 1.6 in the turbulent BL at the TE of the airfoil. Additionally, the location where H values begin to plateau at the turbulent BL value of 1.7 aligns with the simulated reattachment location predicted from the end of the transition ramp in the C_p plots. The analysis of the transitional separated BL using H has excellent agreement with the experimental data, and strongly validates the LES prediction of the complex BL

transition behaviour occurring in the separated BL.

4.4 Laminar Separation Bubble Visualization

With the location of the LSB more clearly defined using H, Figure 4.5 shows a close-up view of the transient behaviour in the LSB for each AOA. These images are from the same time step as the Q-criterion images in Figure 4.1, and feature one set of pathlines that begins at the LE and a second set beginning within the LSB. For context, a contour of the non-dimensional velocity at the midplane of the airfoil span shows the low velocity within the LSB and the increase in velocity in the separated BL. All of the pathline scenes are on the same scale, which highlights the decrease in LSB thickness as the AOA increases.

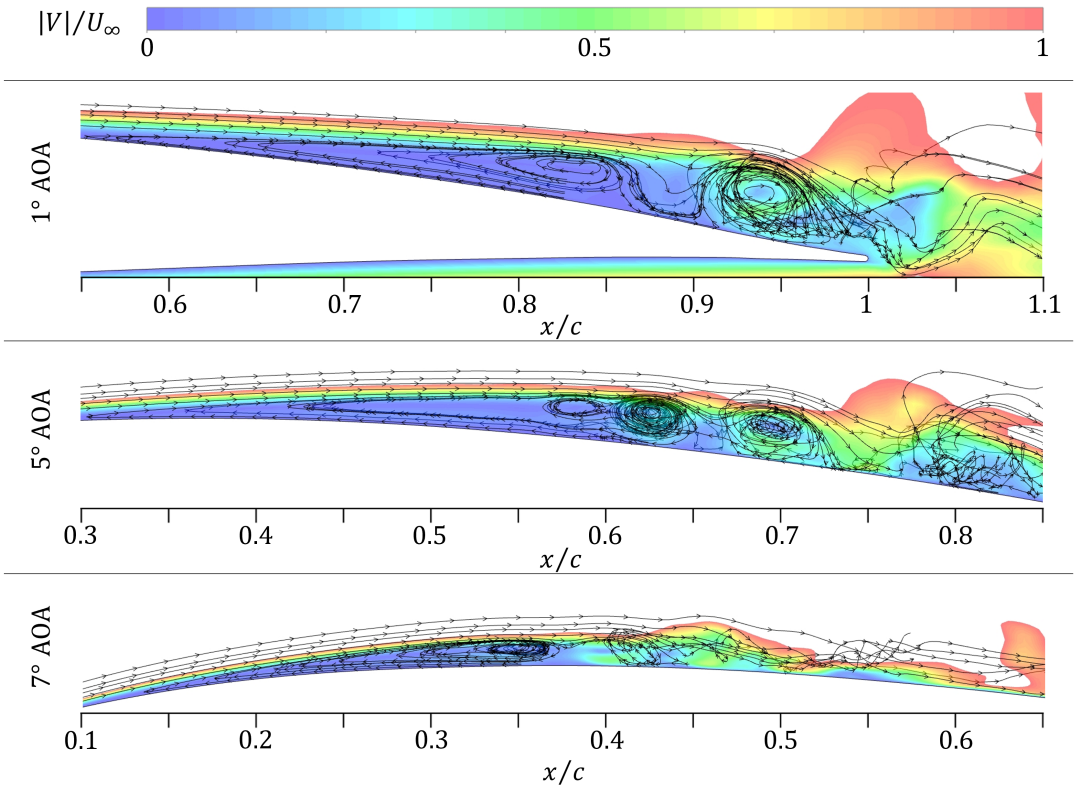


Figure 4.5: Contours of $|V|/U_\infty$ vs. x/c for $\alpha = 1°$, $5°$, $7°$ with pathlines to visualize LSB. Image scale is consistent, with different x/c ranges

For 1° AOA, the pathlines show laminar separation occurring at approximately $x/c = 0.55$, and multiple recirculation vortices within the LSB. These clockwise recirculation vortices are formed within the LSB due to the shear caused by the separated boundary layer [12], as shown in Figure 2.4. Analysis by Roberts and Yaras [23] similarly identified multiple clockwise vortices, with local BL reattachment between them. This local reattachment can be seen clearly in the 1° AOA results when pathlines are pulled from the separated BL down to the surface by one vortex (at $x/c = 0.875$), only to be pulled back up to the separated BL by the following vortex (at $x/c = 0.9$). Even though there is local transient reattachment, the separated boundary layer does not fully reattach to the suction side of the airfoil. From experiments [4], it is known that the suction side has a fully reattached BL at 3° AOA, and that trends in the location of the LSB indicate the separated shear layer is very near reattachment at the TE of the 1° AOA case. The pathlines do give the impression of a fully formed LSB due to the deviation of the suction side streamlines in the airfoil wake, caused by the interaction between the suction and pressure side BLs.

The 5° AOA pathline scene extends from $x/c = 0.3$ to 0.85, which is the length of the LSB as predicted by the time-averaged C_p and H. At the time step selected for the image, the BL does not fully reattach until $x/c = 0.9$ due to a pocket of low velocity which contains some reverse flow centred around $x/c = 0.8$. This low velocity region corresponds to the final spanwise roll and horseshoe structures, which can be seen in the Q-criterion results in Figure 4.1 as the final dark red spanwise region before the TE. Additionally, the location of each vortex within the LSB (from $x/c = 0.55$ to 0.75) aligns with the x/c location of the K-H rolls in the separated BL visualized using Q-criterion (Figure 4.1). The downstream progression of the K-H rolls and associated vortices leads to instantaneous pockets of low velocity and BL separation after the time-averaged BL reattachment location. This poses a challenge when defining the location of BL reattachment, since the time-averaged LSB does not provide a good representation of the transient behaviour occurring in the back half of the LSB.

A similar trend is seen in the 7° AOA pathlines, where the BL appears on the verge of reattachment from $x/c = 0.45$ to 0.6. This appears to be in disagreement with the quick development of complex flow structures visualized in Figure 4.1, since it would be expected that this would result in a shorter LSB that reattaches earlier than the other simulated AOAs. However, it has instead resulted in a very thin and elongated LSB that is more disorderly when nearing reattachment. It is clear that while the BL transition appears to occur faster at 7° AOA than for the other simulated AOAs, it is not sufficient to cause earlier BL reattachment.

A detailed transient analysis of the formation of the K-H rolls in the LSB is presented in Section 5.3.1 for the 1° AOA simulation completed using Mesh 2.

4.5 BL Separation and Reattachment

The location of BL separation and reattachment is difficult to identify using the previous results, since C_p and H indicate the start and end of the LSB through gradual slope changes and visualization using Q-criterion or pathlines are dependent on the time step selected. The skin friction coefficient, C_f, in the streamwise direction as described in Section 2.1.4 and calculated using Equation 2.4 provides a time-averaged location of BL separation and reattachment because an attached BL has positive C_f and regions of BL separation will have $C_f \leq 0$. The simulated C_f is calculated using the time-averaged x-direction wall shear stress, and due to the airfoil curvature this is an approximation of the streamwise wall shear stress. The LSB for the simulated AOAs are located in regions of lower curvature where the error using the x-direction wall shear stress is minimal.

The 5° and 7° AOA cases clearly demonstrate the expected C_f behaviour, shown in Figures 4.6(b) and (d), due to their fully formed LSBs. The LSB wall-normal height, h, is plotted in Figures 4.6(a) and (c) to visualize the LSB shape associated with the presented C_f behaviour, where h is defined as the location of zero time-averaged s-velocity, U_s (velocity tangent to the airfoil surface). After separation, C_f plateaus at a negative value and begins to decrease at a x/c location just before the BL transition location identified by the H peak (x/c of 0.65 for 5° AOA and 0.4 for 7° AOA). After the BL transition, there is a negative peak with a steep recovery to a positive C_f to indicate BL reattachment. This stronger region of reverse flow (negative C_f) at the airfoil surface can be attributed to growth of the clockwise vortices in the latter portion of the LSB, as seen in Figure 4.5. The locations of BL separation and reattachment determined using C_f for all simulated AOAs are summarized in Table 4.1.

These C_f trends are similar to previous LES and DNS works for transitional separated flow over cambered airfoils [7, 31–33], symmetric NACA airfoils [26, 27], a compressor cascade [22] and flat plate geometries [8, 22]. As with the C_p results for this type of flow, the results in the referenced works are either unvalidated or validated against DNS results due to the lack of reliable experimental C_f data. Therefore the PIV post-processing technique used by Ghorbanishohrat [4] to experimentally determine C_f provides a unique opportunity to validate the BL wall shear behaviour predicted using LES.

The LES results predicted early BL separation in comparison to the experimental results for all simulated AOAs, though only the results for 5° and 7° are presented here. This is in contrast to the agreement in BL separation location found using C_p (Figure 4.2), where experimental results were calculated using the same PIV data. This difference can be attributed to the PIV resolution at the airfoil surface, since the C_f accuracy is dependent

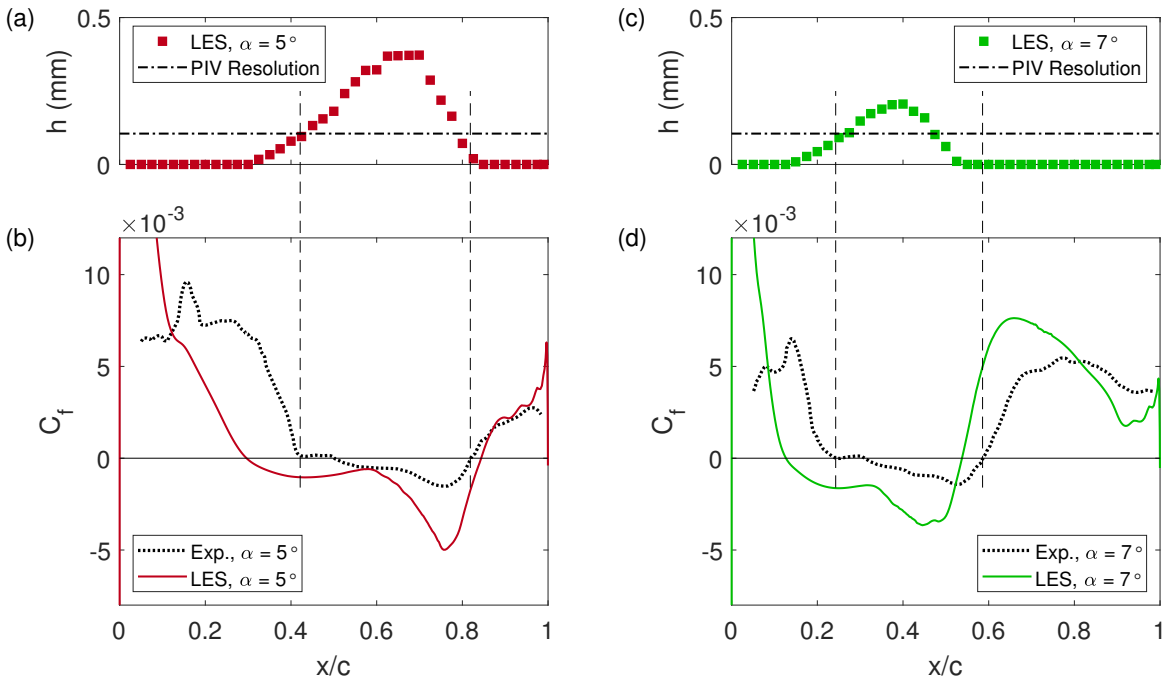


Figure 4.6: LSB height, h, compared with PIV resolution at (a) $\alpha = 5°$ and (c) $\alpha = 7°$. Suction side C_f compared with experimental measurements [4] at (b) $\alpha = 5°$ and (d) $\alpha = 7°$. Vertical lines indicate experimental BL separation and reattachment

on the measured velocity gradient close to the wall, whereas the C_p was calculated through integration of the entire velocity profile [4]. The PIV resolution of 0.105 mm is plotted against the LSB h in Figures 4.6(a) and (c), showing that the near-wall mesh resolution in the LES simulation determines the velocity gradient closer to the wall than the PIV data. Due to this difference in near-wall resolution, any simulated h below the PIV resolution line would be experimentally measured as an attached BL, and therefore generate a positive C_f.

The vertical dashed lines on Figure 4.6 are aligned with the experimentally predicted BL separation and reattachment locations, which are then compared against the LSB h. The experimental separation location is the same x/c location as the intersection between the simulated LSB h and the PIV resolution. This means that if the LES simulation had the same near-wall resolution as the PIV experiments, or vice versa, then the BL separation prediction would be in complete agreement. In terms of BL reattachment, the 5° AOA

location is in agreement when factoring in the PIV resolution and the 7° AOA location has a similar upstream shift in reattachment to what was found in the C_p and H results. This shows that the difference in BL separation and reattachment locations in the C_f data is due to the differences in near-wall resolution only, validating the LES results for the highly transient and sensitive transitional separated BL on a cambered low Re airfoil.

4.6 Summary

This chapter presented the time-averaged results of the wall-resolved LES simulation of the SD 7037 airfoil using Mesh 1 at 1°, 5° and 7° AOA and thoroughly validated the simulation of the LSB against experimental data. Previous DNS and LES simulations of a transitional separated BL focused on flat plates, symmetric airfoils or compressor cascades, which differ in many ways including geometry from a modern cambered airfoil typically used in low Re applications. High quality experimental data on cambered airfoils at modest Re is very limited, and the results were validated against a particulary unique set of experimental data which included C_f. The range of AOAs selected for LES simulation covered a range of LSB locations, and the simulated behaviours of the transitional separated BL were validated at these different AOAs using multiple methods of comparison.

The qualitative analysis of the Q-criterion showed the expected behaviour of a transitional separated BL, including the formation of K-H rolls over the LSB which then broke down into large horseshoe vortices at BL reattachment. These horseshoe vortices were found to be on a larger scale with respect to the LSB length and size of the K-H rolls, when compared to higher Re simulations of symmetric NACA profiles. Additional visualization of the LSB using pathlines showed the transient nature of the BL reattachment, with large clockwise vortices within the LSB at the same instantaneous location as the K-H rolls. Within the LSB, these vortices created regions of local BL reattachment between them, and were found to continue into the reattached BL and created pockets of transient BL separation past the time-averaged location of reattachment. The formation and downstream propagation of these vortical structures are examined further in Chapter 5 and the relationship between these structures and the tonal aeroacoustic noise is discussed in Chapter 6.

The LES predicted suction side C_p results were of higher magnitude than the experimental data, however this was attributed to the near-wall PIV resolution and potential error introduced by the integration method used to calculate the experimental C_p. Of greater importance was the agreement of the C_p gradient with x/c, and the location of the transition ramp that is used to identify the LSB location on the airfoil surface. The

location of the pressure recovery in the transition ramp for the 5°, and 7° AOA predicted a shorter LSB than was found experimentally, pointing to the possibility of a slight over-production of inflow turbulence using the built-in inlet turbulence model. The simulation of the time-averaged BL reattachment location is analyzed further in Section 5.2 for the simulations using Mesh 2 and Mesh 3.

Analysis of the integral boundary layer properties was conducted to determine the locations of boundary layer separation, transition and reattachment. The δ^* and θ were compared to experimental data individually and then combined to analyze trends in the shape factor, H. There was strong agreement with experimental data for the trends of all three parameters, with the exception of the early BL reattachment for 7° AOA. The values of H for the laminar and turbulent portions of the BL were aligned with expected flat plate values, and the peak H value used to indicate BL transition was a similar magnitude to previous works simulating a transitional separated BL.

Lastly, a comparison of simulated C_f with the unique low Re airfoil experimental data showed discrepancies in the locations of BL separation and reattachment, with PIV data predicting a shorter LSB. Through analysis of the simulated LSB height, this was determined to be caused solely by the difference in near-wall resolution between the LES and PIV data. The agreement of the C_f predicted separation and reattachment locations was a useful finding since the C_f predictions of the simulation provide a quick and accurate method of determining the precise LSB location on the suction side of the airfoil.

The presented analysis validated the wall-resolved LES simulation of the time averaged LSB behaviour for the cambered SD 7037 airfoil through the pressure behaviour, velocity profiles, and the locations of BL separation, transition and reattachment. The modest Re case chosen for these simulations posed a computational challenge when compared to previous computational works at higher Re, mainly due to the elongated chordwise region of natural BL transition and LSB formation. These results have clearly shown the ability of LES to accurately capture the complex behaviour involved in the formation of a LSB on a cambered airfoil at a modest Re that is typical of SWT operation. Chapter 5 continues the analysis of the LES simulation by examining the transitional BL and LSB to improve the understanding of the transient behaviours that result in the generation of tonal airfoil self-noise during the low Re operation of SWTs.

This chapter makes significant progress in the fulfillment of research objectives #1, #5, and #6 through providing a thorough validation of the LSB simulation which will serve as the foundation for the transient analysis of the aerodynamic and aeroacoustic behaviours in Chapters 5 and 6.

Chapter 5

Transient LSB Results

This chapter presents the second phase of the analysis of the large eddy simulation (LES) of the laminar separation bubble (LSB) on the suction side of the SD 7037 airfoil at a Reynolds number of $Re = 4.1 \times 10^4$ and at 1°, 3° and 5° angles of attack (AOA). The analysis of the LES simulations builds on the validation and analysis of the time-averaged LSB results presented in Chapter 4 and uses refined simulation meshes to further improve the LSB simulation in comparison to the experimental data summarized in Section 3.1.1. The formation of a LSB on a low Re airfoil is explained in Section 2.1.4 and the simulation of a LSB is summarized in Section 2.2.3. The approach and numerical method for the LES simulations are covered in detail in Sections 3.1 and 3.2 and the results in this chapter are generated using Mesh 2 and Mesh 3 shown in Figure 3.4 with other simulation details summarized in Tables 3.1 and 3.2.

In this chapter, the transient behaviour in the LES simulation of the LSB is examined with a focus on the coherent flow structures that are relevant to the generation of tonal aeroacoustic noise as is summarized in Sections 2.3.3 and 2.4.3. The results and analysis reported in this chapter address the research objectives #1, #3, #5 and #6 in Section 1.3 for the numerical prediction of tonal aeroacoustic noise for small wind turbine (SWT) blades operating at low Re with a LSB. A portion of the contents of this chapter has also been published in the peer-reviewed proceedings of the *30th AIAA/CEAS Aeroacoustics Conference*[1].

[1]Zilstra, A. and Johnson, D.A. (2024) Computational Aeroacoustic Prediction of Tonal Noise for Low Reynolds Number Airfoils. 30th AIAA/CEAS Aeroacoustics Conference. doi:10.2514/6.2024-3362

5.1 Boundary Layer Mesh Refinements

The sound pressure level (SPL) and frequency content of the tonal aeroacoustic noise generated by the airfoil TE is directly related to the magnitude of the pressure fluctuations in the boundary layer (BL), their spanwise coherence and the rate at which these fluctuations propagate past the TE, as is described in Section 2.3.3. It is therefore important to examine the LES simulation of the development of coherent flow structures in the transitional BL, with a focus on the Kelvin-Helmholtz (K-H) rolls that form in the LSB, to gain a thorough understanding of the source behaviour of the tonal airfoil self-noise. Before completing this analysis, several improvements were applied to Mesh 1 to create Mesh 2 and Mesh 3, which are shown in Figure 3.4 and are designed to meet the filter length criterion discussed in Section 3.2.6.

These mesh refinements were determined to be necessary after application of the Ffowcs-Williams and Hawkings (FW-H) acoustic analogy, as described in Section 3.2.3, to the Mesh 1 simulations presented in Chapter 4. The time-averaged LES results in Chapter 4 were in agreement with the validating time-averaged experimental data [4] however only the 1° AOA simulation predicted tonal noise in agreement with experimental data [49] and for the 5° AOA simulation, no tonal noise was predicted. The experimental acoustic data for the SD 7037 airfoil is summarized in Section 3.1.1 and the details of the self-noise mechanisms and prediction of tonal noise using FW-H are summarized in Sections 2.3.3 and 2.4. The tonal airfoil self-noise for a low Re airfoil with a LSB has been previously shown to be generated from the high spanwise coherence of the K-H rolls and the associated pressure fluctuations in the BL at the airfoil TE [52–56]. The lack of tonal noise prediction for the 5° AOA Mesh 1 simulation is a clear indication that LES simulated K-H rolls visualized in Figures 4.1 and 4.5 have a transient development and spanwise coherence differing from the coherent structures at the TE in the acoustic experiments [49].

To improve the transient prediction of the K-H rolls in the LES simulation, the mesh was re-examined and the LES sub-grid scale (SGS) filter length criteria were applied more rigorously to create Mesh 2 and Mesh 3. The full details of the mesh refinement method and the final mesh distribution are included in Section 3.2.6. The mesh refinements in Mesh 2 were strategically targeted to improve the LES sub-grid filter length for the region of the separated BL where the K-H rolls develop over the LSB. The mesh filter length in the separated BL for Mesh 1 was found to be insufficient for all AOAs when using the recommended filter length criterion for free-shear flows [17]. The 1° AOA simulation analyzed in this chapter was completed using Mesh 2 since the time-averaged and transient results were found to be consistent with the results from Mesh 1 and thus independent of the filter length in the BL.

The 3° and 5° AOA simulations in this chapter are completed using Mesh 3, which was necessary to meet the filter length requirements in the separated BL as well as in the thin laminar BL at the airfoil leading edge (LE) for $x/c < 0.025$. The 3° and 5° AOA simulation results for Mesh 3 were assessed for filter length independence in the BL through comparison with the results from the test simulations completed using Mesh 2. At 3° AOA, the Mesh 3 results were found to be independent of the filter length and for 5° AOA the time-averaged results were independent of the filter length. The transient data at 5° AOA is largely independent of the filter length with some minor improvements in the consistency of the dominant K-H roll frequencies found between Mesh 2 and Mesh 3. As was discussed in Section 3.2.6, the memory limitation of the local computer used for post-processing prevented the Mesh 3 refinements from fully meeting the filter length criteria at 5° AOA. Comments on the effect of further filter length improvements at 5° AOA are included, where applicable, when discussing the Mesh 3 results.

5.2 Time-Averaged LSB

The time-averaged parameters used to validate the LSB prediction in Chapter 4 are revisited to assess any change in the simulated LSB and BL transition due to the mesh refinements in Mesh 2 and Mesh 3. These parameters are: the suction side pressure coefficient, C_p, chordwise skin friction coefficient, C_f, and shape factor, H. The definition of these parameters and their expected trends in a BL with a LSB are summarized in Sections 2.1.3, 2.1.4 and 2.1.5.

The time-averaged C_p for each simulated AOA is shown in Figure 5.1 in comparison to the experimental data [4] where the simulated x/c locations of BL separation, S, and reattachment, R, are labelled according to the values summarized in Table 5.1. The changes in the C_p gradient with x/c are in excellent agreement with the experimental data for all AOAs and the expected reason for the higher C_p magnitude in the simulations was addressed in Section 4.2. As was established in the validation of the Mesh 1 simulations in Chapter 4, the 1° AOA case is a complex low Re BL where there is laminar BL separation with a transitional BL at the airfoil TE, rather than a fully-formed LSB with a reattached BL. The 3° AOA case also has a transitional separated BL at the TE, although it does have the beginning of the pressure recovery of the C_p transition ramp, as described in Section 2.1.4, at $x/c > 0.9$ in Figure 5.1(b). The separated BL at 3° AOA is therefore closer to reattachment at the airfoil TE than the 1° AOA case.

The simulation of the 5° AOA BL using Mesh 1 was also previously validated in Chapter 4 and features a fully-formed LSB with a time-averaged reattachment point. The location

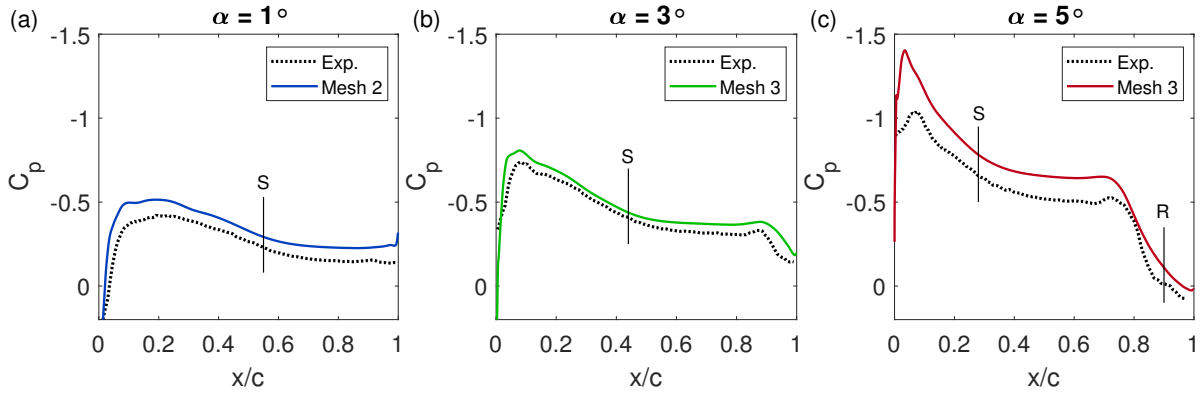


Figure 5.1: Time-averaged suction-side pressure coefficient, C_p, for (a) 1° AOA (b) 3° AOA and (c) 5° AOA compared against experimental data [4]. Locations of BL separation and reattachment are marked with S and R, respectively

Angle of Attack	Mesh #	x/c Location		
		Separation	Transition	Reattachment
1°	2	0.55	0.925	- -
3°	3	0.44	0.75	- -
5°	3	0.28	0.65	0.90

Table 5.1: Boundary layer separation, transition and reattachment locations for 1°, 3° and 5° AOA

of pressure recovery in the C_p transition ramp for 5° AOA at $x/c = 0.8$ in Figure 5.1(c) is in better agreement with the experimental data in comparison to the Mesh 1 result in Figure 4.2(b) where the C_p recovery intersects with the experimental data. The improvement in the simulation of the pressure recovery between Mesh 1 and Mesh 3 proves that the SGS filter length in the BL is a factor in the simulated pressure recovery location. In Chapter 4, the early pressure recovery was hypothesized to be due to an increased inflow turbulent intensity in comparison with the experimental conditions and was described in Section 2.2.4 that the turbulent intensity is known to influence chordwise location of BL reattachment [9, 22, 32, 33]. The differences that are still present between the simulated and experimental C_p recovery in Figure 5.1(c) are expected to be due to the differences in turbulent intensity between the simulation and experiment.

The time-averaged chordwise C_f results presented in Figure 5.2 are used to determine

the chordwise location of laminar BL separation and reattachment, where applicable, which are summarized for each simulated case in Table 5.1. The reason for the difference between the simulated and experimental BL separation and reattachment locations seen in Figure 5.2 has already been addressed in Section 4.5. When comparing the chordwise difference between the simulated and experimental [4] BL separation location, all presented AOAs have consistent behaviour with the simulated separation occurring upstream from the experimental location at an approximate distance of $0.2c$. The separation location for 1° and 5° AOA in Chapter 4, Table 4.1 are largely the same as those reported in Table 5.1. The downstream shift in the time-averaged reattachment location for 5° AOA between Mesh 1 and Mesh 3 is consistent with the changes in the C_p pressure recovery in Figure 5.1(c). The other notable change in the 5° AOA C_f compared with the result in Section 4.5 is the increased magnitude of the $-C_f$ peak which indicates increased reverse flow at the wall associated with the touchdown of the K-H rolls (see Section 5.3.1).

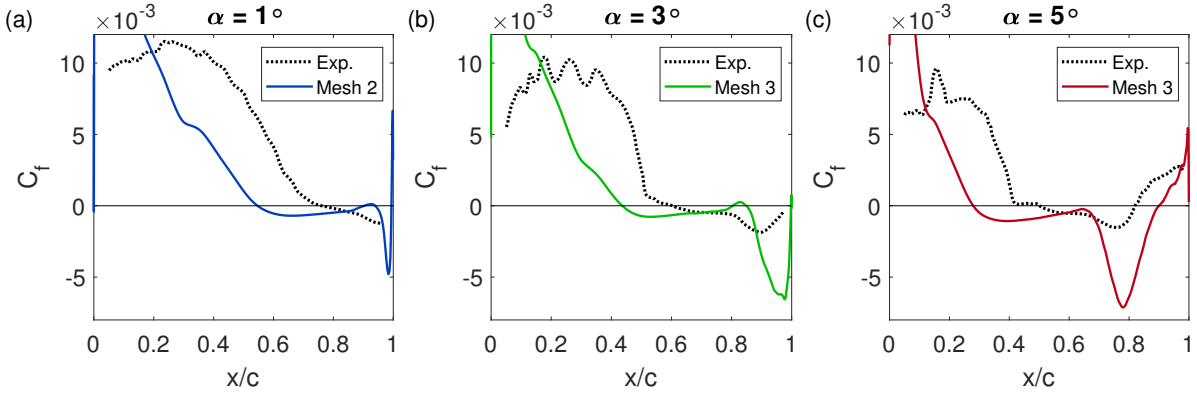


Figure 5.2: Time-averaged suction-side skin friction coefficient, C_f, for (a) 1° AOA (b) 3° AOA and (c) 5° AOA compared against experimental data [4]

Table 5.1 also includes the BL transition location which is determined from H shown in Figure 5.3. The time-averaged H is calculated using the BL integral parameters in Section 2.1.5 at a chordwise spacing of $0.025c$ and thus has a lower chordwise resolution than the separation and reattachment locations. The results at 1° and 5° AOA can be compared to the Mesh 1 results for the same AOAs in Table 4.1 with a larger shift in the 1° AOA transition location due to the $0.025c$ chordwise spacing of the H calculation.

The 1° AOA time-averaged H in Figure 5.3(a) has a peak location that is more consistent with the trends in the experimental data [4] than the H trend seen at the TE for Mesh 1 in Figure 4.4(a). The 3° and 5° AOA H has an interesting double-peak pattern

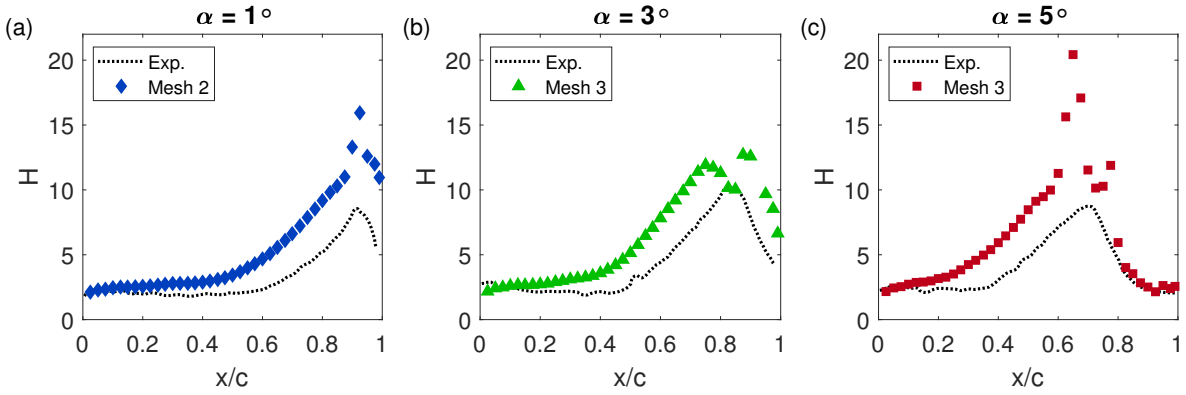


Figure 5.3: Time-averaged suction-side shape factor, H, for (a) 1° AOA (b) 3° AOA and (c) 5° AOA compared against experimental data [4]

that is not present in the experimental results, with the trough between the peaks aligning with the experimental H peak. For the simulations, the first H peak is selected as the time-averaged transition location reported in Table 5.1. As will be shown in Section 5.3.1, the BL is highly transient in the region surrounding the transition location due to the formation of the K-H rolls and small counter-rotating vortices near the wall. These small counter-rotating vortices occur within 0.1 mm of the wall, which is not captured in the experimental data due to the PIV resolution [4] and could alter the H calculation causing two H peaks in the simulations and a single peak in the experimental results.

5.3 Transient LSB Visualization

The K-H rolls that form in the LSB are visualized in Figure 5.4 using Q-criterion iso-surfaces generated for the final time step of each simulated AOA. The Q-criterion iso-surface, as defined in Section 4.1, is at a value of 5×10^7 s^{-2} and the surface is coloured with the non-dimensional velocity magnitude $|V|/U_\infty$ to highlight the wall-normal height and shape of the structures. The flow direction is from lower left to upper right and the chordwise locations of separation and reattachment summarized in Table 5.1 are labelled with S and R, respectively. The comparison of the Q-criterion iso-surfaces for the simulated AOAs gives an insight into how the AOA and proximity of the LSB to the TE alters the scale and spanwise coherence of the K-H rolls at the TE.

The K-H rolls forming in the suction side BL at 1° and 3° AOA have a high spanwise

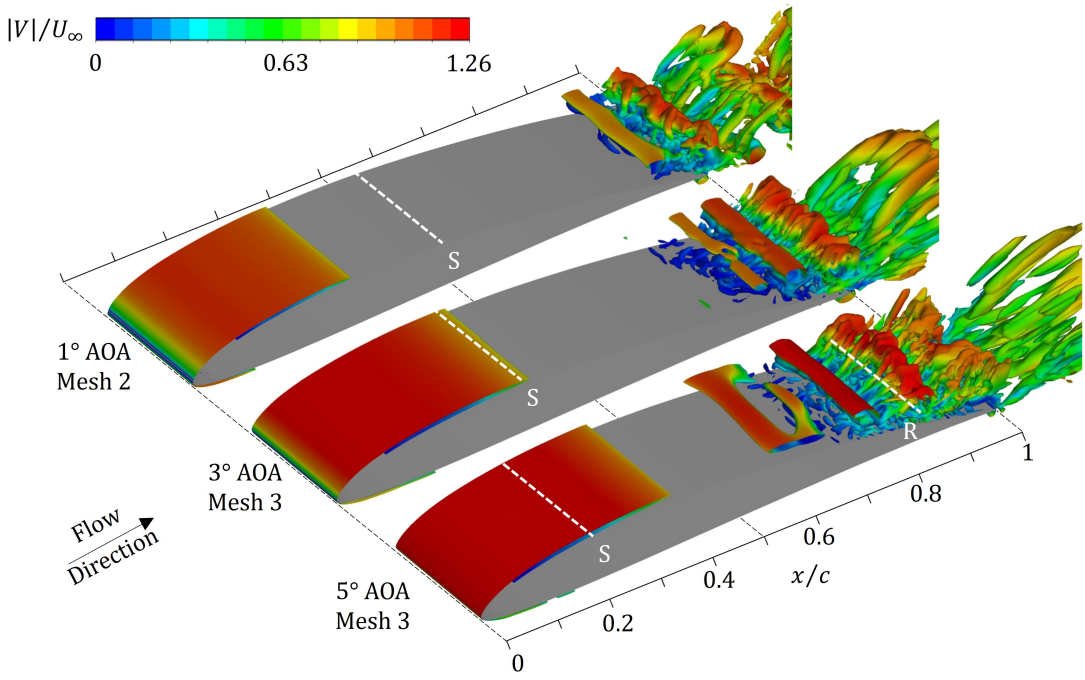


Figure 5.4: Q-Criterion iso-surface of 5×10^7 s^{-2} at 1°, 3°, and 5° AOA coloured by non-dimensional velocity magnitude. White dashed lines indicate location of BL separation (S) and reattachment (R), where applicable

coherence at the TE and are visualized from $x/c = 0.9$ to the TE for 1° AOA and from $x/c = 0.8$ to the TE for 3° AOA. In comparison to 1° AOA, the K-H rolls at 3° AOA have visible spanwise variation with small horseshoe structures, as described in Section 4.1, indicating that the 3° AOA separated BL is further along in the transition process and the K-H roll breakdown has begun. At 5° AOA, the breakdown of the K-H roll at the BL reattachment location has similar horseshoe structures to the 3° AOA K-H roll at the TE.

In comparison to the K-H rolls visualized for Mesh 1 at 5° AOA in Figure 4.1, the 5° AOA K-H rolls in Figure 5.4 have a higher spanwise coherence at the reattachment location and the structures in the broken down K-H roll visualized at the TE maintain the spanwise coherence. The maintained spanwise coherence is an indication that there is a delay in the BL transition for the Mesh 3 simulation when compared to Mesh 1. This is in agreement with the improvements in the time-averaged results in Section 5.2, where the Mesh 3 simulation had a delay in pressure recovery and reattachment which was in better agreement with the experimental data for $x/c > 0.6$.

5.3.1 K-H roll Formation

The examination of the formation process for the K-H rolls in the LSB is necessary to establish the relationship between the transient velocity and pressure fluctuations in the transitional BL and how the K-H rolls interact with the pressure side BL at the TE of the airfoil. This is completed through analysis of the 1° AOA Mesh 2 simulation which has K-H rolls with high spanwise coherence form in the suction side BL near the TE, as was shown in Figure 5.4. The findings from this analysis will then be used in Chapter 6 to relate the detailed transient aerodynamic behaviour of the BL with the predicted tonal aeroacoustic noise generated by the airfoil TE.

The transient behaviour of the LSB is summarized in Figure 5.5 to provide a simplified version of the results examined in this section. The diagram visualizes the formation of the K-H rolls, also called K-H roll pinch-off, from the reverse flow region of the LSB and includes details not present in the time-averaged LSB diagram shown in Figure 2.4. The K-H roll pinch-off process creates counter-rotating spanwise vortices between each K-H roll and these structures propagate downstream in the BL at the same chordwise speed. The diagram shows a LSB with a time-averaged BL reattachment location where the K-H rolls would begin spanwise breakdown before reaching the TE, as is shown for 5° AOA in Figure 5.4. The interaction of a K-H roll with the TE is shown on the right of Figure 5.5 which includes the generation of a counter-rotating vortex from the pressure side BL. The path of the downstream propagation for the cores of the K-H rolls and counter-rotating vortices are included in black dashed lines.

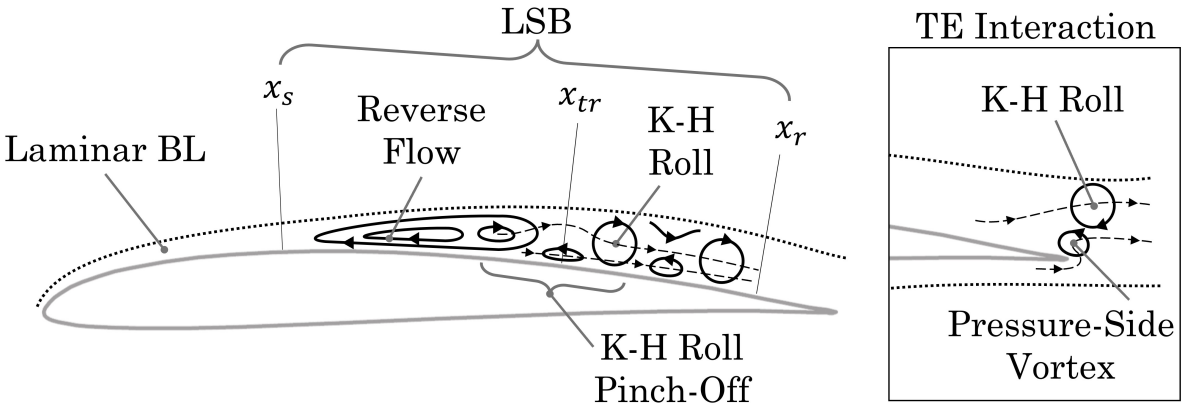


Figure 5.5: Diagram of the transient development of the LSB and details of K-H roll interaction with the TE. Dashed lines show path of vortex core

The pinch-off and growth of the K-H rolls for the 1° AOA simulation are shown using contours of gauge pressure and velocity at time intervals of 5×10^{-5} s (or 25 simulation time steps) in Figure 5.6. The left column shows the pressure contours and the right column shows the corresponding velocity magnitude contours which are normalized by the free-stream velocity, U_∞. The contours are overlaid with constant length velocity vectors to show flow direction, and the black dashed lines are added to track the chordwise location of the core of the K-H rolls with time. The red dashed lines track the location of the counter-rotating vortices that form between the K-H rolls at the surface of the airfoil, which remain at a low velocity magnitude in comparison to the K-H rolls.

The pinch-off of a new K-H roll from the low velocity, reverse flow region of the LSB is shown in Figure 5.6 at time (iii) along with its corresponding counter-rotating vortex at the airfoil surface. The new K-H roll can be seen at approximately $x/c = 0.9$ where it has detached from the reverse flow under the separated BL and the new center of rotation in the reverse flow region develops at approximately $x/c = 0.8$. A thin, counter-rotating vortex forms at the wall at $x/c = 0.825c$ between the new K-H roll and the reverse flow region as a response to the pinch-off behaviour and the red dashed line shows that it propagates downstream at a similar velocity to the K-H roll. After the formation of the K-H roll at time (iii), the velocity magnitude at the outer circumference of the K-H roll increases and the low pressure at the centre of the K-H roll grows continuously as it approaches the TE. As this growth occurs, the wall-normal height of the K-H roll core increases from time (iii) to (v), likely in reaction to the impeding presence of a downstream counter-rotating vortex located from $x/c = 0.925$ to $x/c = 0.975$. At time (vi) the core of the K-H roll has passed the time-averaged BL transition location of $x/c = 0.925$, indicated by the white line, and the K-H roll core then begins to reduce wall-normal height as it approaches the TE.

The change in wall-normal height of the core at the transition location of $x/c = 0.925$ corresponds to the small region of positive skin friction coefficient, C_f, in the middle of the LSB (see Figure 5.2(a)). By examining the velocity direction near the wall at $x/c = 0.925$ in Figure 5.6, this location experiences reverse flow associated with the K-H roll from times (v) to (vi) and at all other times has a positive s-velocity, U_s, tangent to the wall due to the counter-rotating vortices. Therefore the small counter-rotating vortex at the wall is responsible for the positive time-averaged C_f at the transition location within the LSB. The path of the K-H roll and counter-rotating vortex cores at the time-averaged BL transition location are included in Figure 5.5.

Downstream from the time-averaged BL transition location, the decrease in the wall-normal height causes an interaction between the newly formed roll and the airfoil surface, which will be referred to as K-H roll touchdown. The K-H roll touchdown results in a high magnitude reverse flow that covers a chordwise length of $0.05c$ and is best visualized in

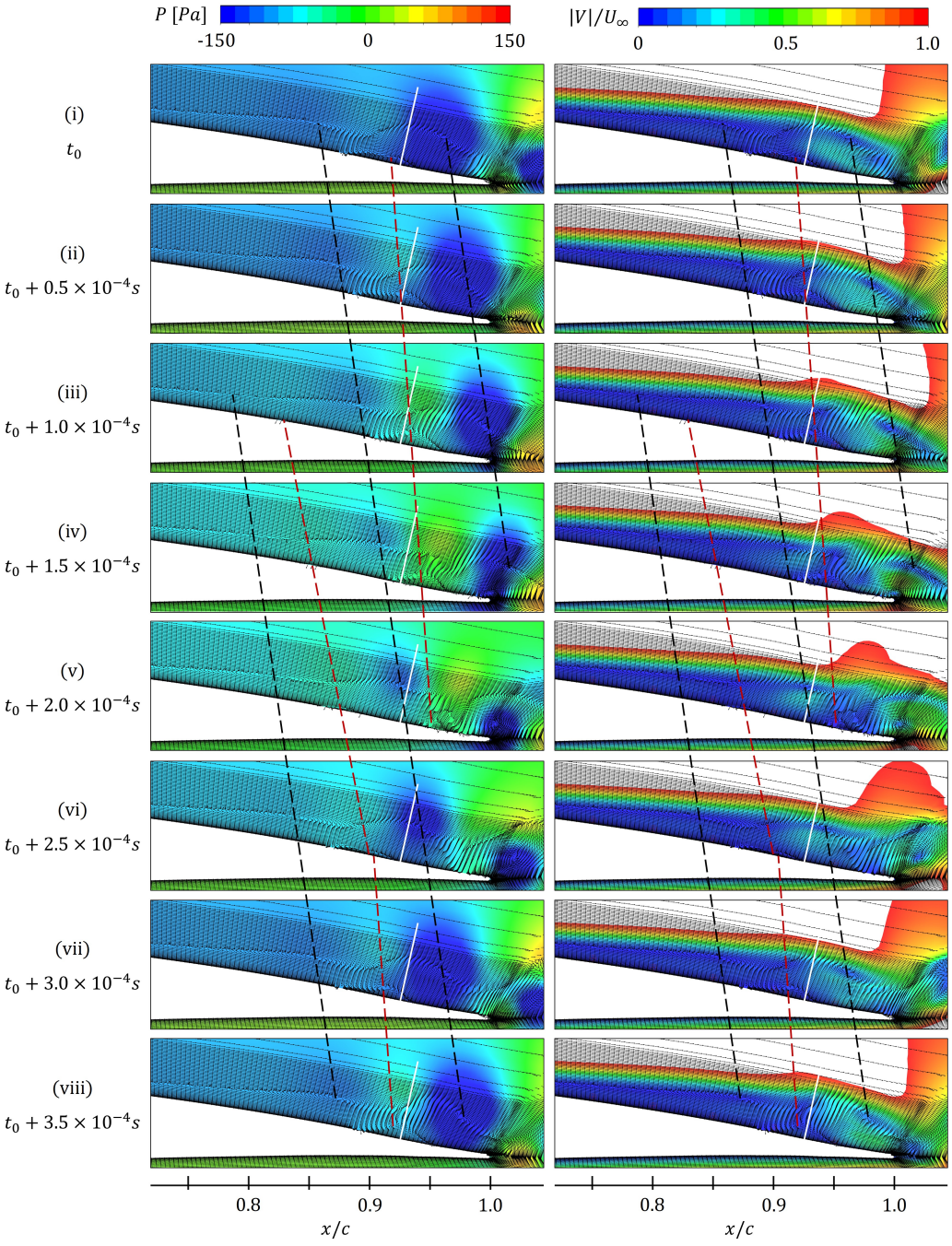


Figure 5.6: K-H roll gauge pressure contours (left) and velocity contours (right) with constant length velocity vectors for 1° AOA. Black and red dashed lines indicate K-H roll cores and counter-rotating vortex cores, respectively. White lines indicate time-averaged BL transition location.

times (ii) and (viii) in Figure 5.6. This corresponds to the high magnitude negative C_f in Figure 5.2(a) and therefore the presence of fully-formed K-H rolls with a low pressure core can be determined from the time-averaged C_f.

The interaction of the low pressure K-H roll with the TE is shown using the fully-formed K-H roll nearest to the TE at time (i) in Figure 5.6. In a case where the LSB reattaches before the TE, the motion of the K-H roll towards the wall after the time-averaged BL transition location would result in the breakdown of the K-H roll and the time-averaged reattachment of the BL, as is shown in Figure 5.5. However, as the K-H roll approaches the TE at time (iii), the core begins to increase in wall-normal height due to the formation of a counter-rotating vortex developing from the pressure side of the TE. This counter-rotating vortex continues to grow on the suction side of the airfoil at times (iii) and (iv) and the low pressure associated with the rotation of this vortex is present on both the suction side and pressure side of the TE. At times (vi) and (vii) the counter-rotating vortex is convected downstream into the near-wake and is replaced with a pocket of high pressure at the TE. The approximate size and propagation path of the pressure side counter-rotating vortex is shown in Figure 5.5 in the TE interaction detail on the right side of the diagram. Therefore the pressure oscillation at the TE occurs due to the interaction of the suction side K-H roll and attached pressure side BL through the formation and shedding of a low pressure counter-rotating vortex from the pressure side BL. The relevance of this TE pressure fluctuation to the tonal airfoil self-noise is discussed in Section 6.1.2.

5.4 Propagation of BL Instabilities

In this section, the pressure and velocity fluctuations on the suction side BL are analyzed to determine how the initial instabilities in the laminar BL develop into the K-H roll pinch-off identified in Section 5.3.1. The s-velocity, U_s, which is the velocity tangent to the airfoil surface, and the gauge pressure, P, was measured in the BL for a total of 1×10^4 time steps for each AOA at chordwise spacings of $0.05c$. The LE and TE measurements were taken at $x/c = 0.025$ and $x/c = 0.99$, respectively, which is in alignment with the chordwise locations nearest to the LE and TE for calculating the integral BL parameters such as H presented in Figure 5.3. The measurement locations were placed at a wall-normal distance of $4 \times 10^{-3}c$ (0.1 mm) to measure the behaviour near the wall and at $3 \times 10^{-2}c$ (0.75 mm) to capture behaviours offset further from the wall in the LSB. The P and U_s signals were measured at the mid-span of the simulated airfoil segment as well as at $0.05c$ spanwise offsets from the mid-span to generate three spanwise signals at each x/c location and wall-normal distance for a total of 126 measurement locations.

A bandpass filter was applied to each signal from 1 kHz to 10 kHz to remove low frequency oscillation and higher frequencies, this places a focus on the flow structures which develop at frequencies nearest to the tonal noise frequencies of 3.4 kHz and 4.1 kHz identified experimentally [49] as is summarized in Section 3.1.1. The lowpass filter on frequencies below 1 kHz performs a similar function to subtracting the mean from the signal to get the fluctuating component and therefore the filtered signals are referred to as U_s' and P' in this analysis. These U_s' and P' signals are used to examine the transient connection between the instabilities in the attached laminar BL and the LSB as well as their speed of chordwise propagation in the BL. The identification of the relationship between the pressure and velocity fluctuations in the different regions of the BL will also be used to determine the role of acoustic feedback in the formation of the K-H rolls.

A numbering system for the BL and LSB behaviours shown in Figure 5.5 is introduced in Figure 5.7 and these numbered labels will be used to ease the discussion for the remaining sections in this chapter. The blue labels represent the natural BL transition behaviours, as are described in Sections 2.1.2 and 2.1.4, that propagate downstream in the suction side BL. The transient behaviours associated with each numbered region are named in Table 5.2. Also included in the numbering system are red labels that correspond to behaviours that will be shown to be propagating upstream through the laminar and separated BL in Sections 5.4.2 and 5.4.3.

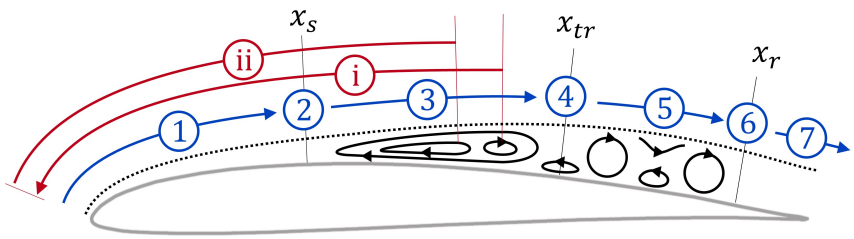


Figure 5.7: Numbering system for downstream propagating behaviour in blue and upstream propagating behaviour in red. Black labels note the time-averaged location of BL separation, x_s, transition, x_{tr}, and reattachment, x_r

The method of presenting the U_s' and P' signals is shown in Figure 5.8 for sample locations of $x/c = 0.7$ and $x/c = 0.75$ within region (5) where the behaviour of interest is the downstream propagation of the K-H rolls and the counter-rotating vortices. The idealized visualization of these structures passing the measurement locations at a wall-normal distance of $4 \times 10^{-3}c$ are shown in Figure 5.8(a) at three key times corresponding to the labelled locations in the U_s' and P' signals in Figure 5.8(b).

Downstream Propagating Behaviour	
1	T-S wave
2	BL Separation
3	K-H instability
4	BL Transition / K-H roll pinch-off
5	K-H roll
6	BL Reattachment
7	K-H roll breakdown
Upstream Propagating Behaviour	
i	Pressure wave
ii	Pressure-induced U_s instability

Table 5.2: Labels for the upstream and downstream propagation of BL pressure and velocity behaviours

At t_1, the negative P' of the K-H roll is at $x/c = 0.7$ and the reverse flow between the K-H roll core and the wall results in a negative U_s' measurement. The positive U_s' and P' measurement occurs when the counter-rotating vortex moves to $x/c = 0.7$ at t_3 and the U_s' and P' is zero when $x/c = 0.7$ is in the space between the two vortical structures at t_2. Therefore the negative U_s' and P' fluctuations close to the airfoil surface can be used to track the K-H rolls and the positive U_s' and P' fluctuations track the positioning of the counter-rotating vortices.

The downstream propagation of these structures are tracked across multiple x/c locations by presenting the U_s' and P' signals as a contour plot with the format shown in Figure 5.8(c). Each x/c location has a horizontal strip of contour where the x-axis is time and the amplitude of the signal is represented using the colourmap with negative values in blue and positive values in red. This is demonstrated for chordwise locations of $x/c = 0.7$ and $x/c = 0.75$, where the K-H roll positioned at $x/c = 0.7$ at t_1 in Figure 5.8(a) propagates downstream to $x/c = 0.75$ by t_3. In the contour format, the motion of the K-H roll from t_1 to t_3 is shown with the black arrow where the slope of the arrow can then be used to determine the K-H roll chordwise propagation speed, U_{KH}. The calculation of U_{KH} and the speeds of other instabilities in the BL will be used in Section 6.3.

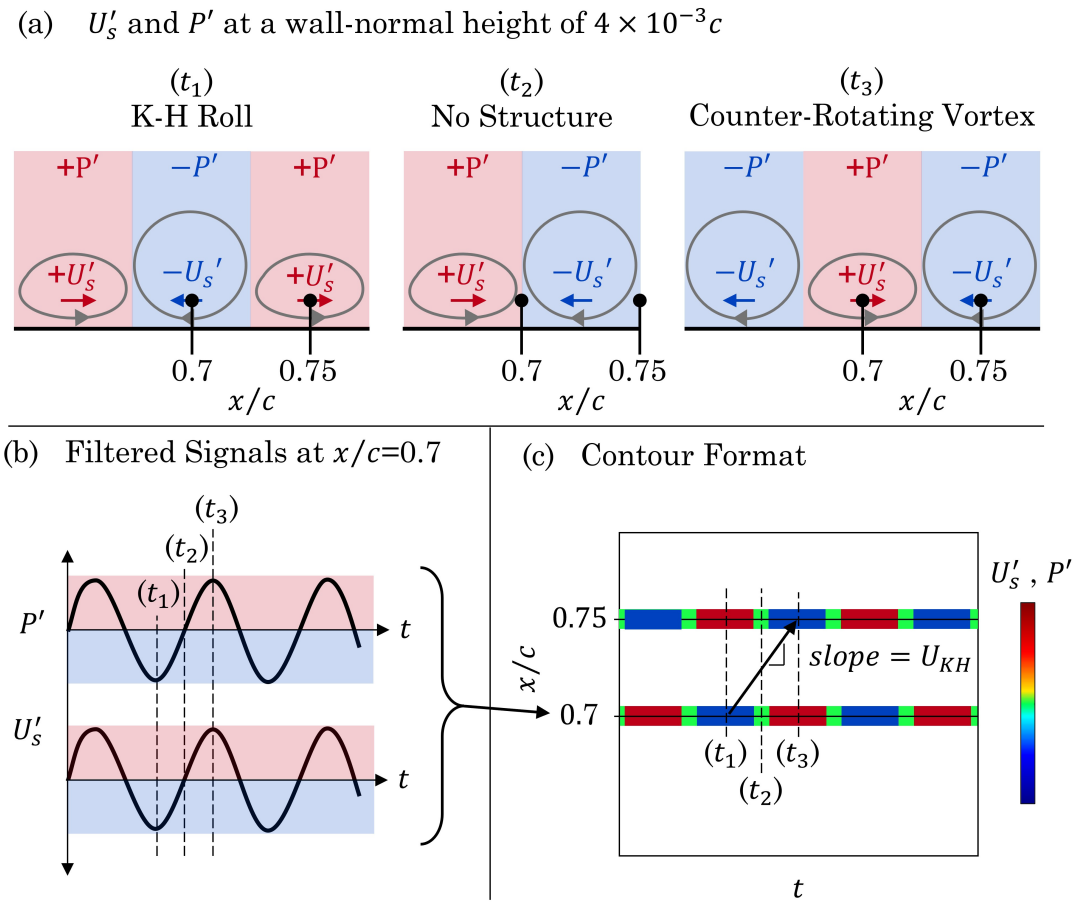


Figure 5.8: Illustration of method for tracking coherent structures using the U_s' and P' signals at a wall-normal distance of $4 \times 10^{-3}c$. (a) Visualization of idealized structures passing $x/c = 0.7$ and $x/c = 0.75$, (b) U_s' and P' signals for $x/c = 0.7$ and (c) contour plot of U_s' or P' signals

5.4.1 Fully-Formed LSB

The chordwise propagation of the BL instabilities for a fully-formed LSB are examined first using the 5° AOA Mesh 3 simulation results. The reason for analyzing the 5° AOA BL first is that it is the only of the simulated AOAs to have a time-averaged reattachment location (see Table 5.1) and therefore is the only suction side BL that captures the downstream propagation of the behaviours labelled (1) through (7) in Figure 5.7.

The U_s and P signals from the mid-span of the simulated airfoil segment at a wall-normal height of $4 \times 10^{-3}c$ are presented using the contour method shown in Figure 5.8. A sample time period of 2.5×10^{-3} s was selected from the full signal length of 0.04 s and the resulting U_s' contour is shown in Figure 5.9(a) and the corresponding P' contour is shown in Figure 5.9(b). The U_s' contour is divided into three horizontal segments with dividing lines at $x/c = 0.475$ and $x/c = 0.575$ with each segment having a different contour range to visualize the increasing amplitudes of the fluctuations with increasing x/c location. Similarly, the P' contour has two horizontal segments with a dividing line at $x/c = 0.625$. The time-averaged locations of BL separation, (2), transition, (4), and reattachment, (6), are included as horizontal dashed lines labelled in accordance with Figure 5.7 and are at the x/c locations reported in Table 5.1.

The downstream propagation of the U_s' and P' behaviour is explained by following the development and growth of an initial U_s' fluctuation from the LE through the entire suction side BL to the airfoil TE. The downstream propagation of a sample negative U_s' peak (blue contour colour) is tracked using black arrows labelled with (1), (3), (5) and (7) in Figure 5.9(a). The labelled U_s' fluctuations in Figure 5.9 demonstrate the expected downstream propagation of the natural BL transition and LSB behaviours shown in Figure 5.7. The locations of these arrows are duplicated on the P' plot in Figure 5.9(b) to be able to determine when the P' fluctuations are in phase with the U_s' fluctuations.

In region (1) before the location of BL separation, the laminar BL has low amplitude U_s' fluctuations that do not have any associated P' fluctuation indicating that the U_s' fluctuations are not related to large coherent structures in the laminar BL. The U_s' fluctuations are at a very low amplitude of $U_s' = 0.05$ m/s at the location of BL separation, (2), which is 0.21% of U_∞. The U_s' amplitude of T-S waves for a flat plate BL transition as shown in Figure 2.2 has been experimentally reported [3] at 0.3% to 1% of the free-stream velocity at the location of breakdown into 3D BL transition structures. At location (2) in the simulations, the BL behaviour has not yet developed to the stage of BL transition where the 3D structures form, as is shown in Figure 5.4, and therefore the percentage of U_∞ at location (2) should be lower than the experimentally reported values. Therefore the U_s'

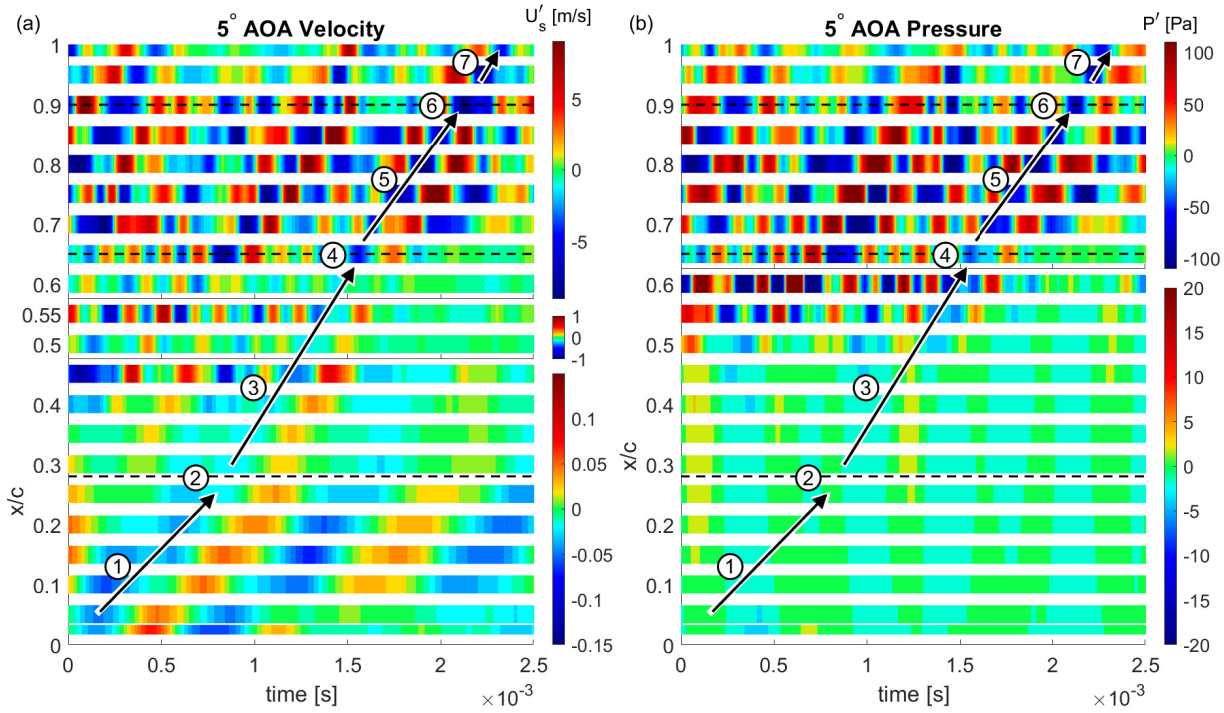


Figure 5.9: Chordwise propagation of BL instabilities with time at 5° AOA and wall-normal height $4 \times 10^{-3}c$ for (a) U_s' and (b) P'. U_s' contour range changes at $x/c = 0.475$ and $x/c = 0.575$ and P' contour range changes at $x/c = 0.625$ according to colourbars on the righthand side

fluctuations in region (1) are assumed to be the low amplitude fluctuations of the early development of T-S waves in the attached BL.

After time-averaged BL separation at $x/c = 0.28$, labelled (2), the T-S waves of the laminar BL propagate downstream in region (3) of the separated BL and grow in amplitude as a result of the K-H instability in the separated shear layer. The T-S waves have been shown to initiate the K-H instability in the separated BL [6] which will be discussed further in Section 5.5 when examining the frequency of the U_s' fluctuations throughout the BL transition process. The K-H instability in the separated BL propagates downstream at a constant speed that is of higher magnitude than the T-S waves, which is indicated by the increase in slope of the arrows between region (2) and (3).

In region (3) at larger x/c values, the U_s' fluctuations have grown in amplitude and develop associated P' fluctuations. This synchronized U_s' and P' behaviour is evidence of

the rotation of a newly developing K-H roll in the aft portion of the reverse flow region of the LSB. This can be seen in Figure 5.6 (i) and (ii) for 1° AOA where the rotation of the flow at the downstream end of the reverse flow region develops an associated low pressure before the K-H pinch-off occurs at time (iii). In Figure 5.9, the K-H roll pinch off is labelled as location (4) and aligns with the time-averaged BL transition location.

In region (5), the fully-formed K-H rolls propagate downstream with marginally slower velocity than the K-H instability in region (3) shown by the change in the slope of the arrows tracking their downstream propagation. As was shown in Figure 5.8, when the measurement location is at the wall-normal height of $4 \times 10^{-3}c$, the U_s' and P' fluctuations are correlated with a negative fluctuation occurring due to a K-H roll and a positive fluctuation is due to a counter-rotating vortex. In Figure 5.9(a) the negative U_s' fluctuation is tracked in region (5) and in Figure 5.9(b) there is a synchronized negative P' fluctuation.

After time-averaged BL reattachment, (6), the majority of the high amplitude U_s' and P' fluctuations are no longer present which indicates the breakdown, or decomposition, of the K-H rolls and counter-rotating vortices in the reattached BL of region (7). However, some K-H rolls and counter-rotating vortices continue to propagate to the airfoil TE, including the counter-rotating vortex tracked by the black arrow labelled (7). The U_s' and P' amplitudes of the K-H rolls and counter-rotating vortices at each x/c location in region (7) varies across the sample time period shown in Figure 5.9. Most K-H rolls and counter-rotating vortices propagate downstream at a similar speed to the labelled K-H roll, however some of the lower amplitude structures in region (5) do not have a clear downstream path. This indicates that the lower amplitude vortices are prematurely breaking down into smaller structures, as described in Section 5.3, and are merging with the nearby vortical structures from the adjacent broken down K-H rolls and counter-rotating vortices. The inconsistency in the K-H roll formation for 5° AOA will be explored further in the following section.

5.4.2 LSB Pressure Feedback

The examination of the BL instability propagation for all simulated AOAs led to the identification of an upstream pressure feedback process originating in the LSB which is included in Figure 5.7. This pressure feedback occurs intermittently in the 5° AOA BL and therefore the 5° AOA results are used to describe the alteration of the BL transition process in the presence of feedback in Figure 5.10 in comparison with the natural BL transition in Figure 5.9. The U_s' and P' contours in Figure 5.10 show an example of the pressure feedback occurring 1×10^{-3} s before the time period displayed in Figure 5.9. The

time axis in Figure 5.10 is relative to the start time of the contours (time of 0 s) in Figure 5.9 and the region (1) label from Figure 5.9 is duplicated in Figure 5.10.

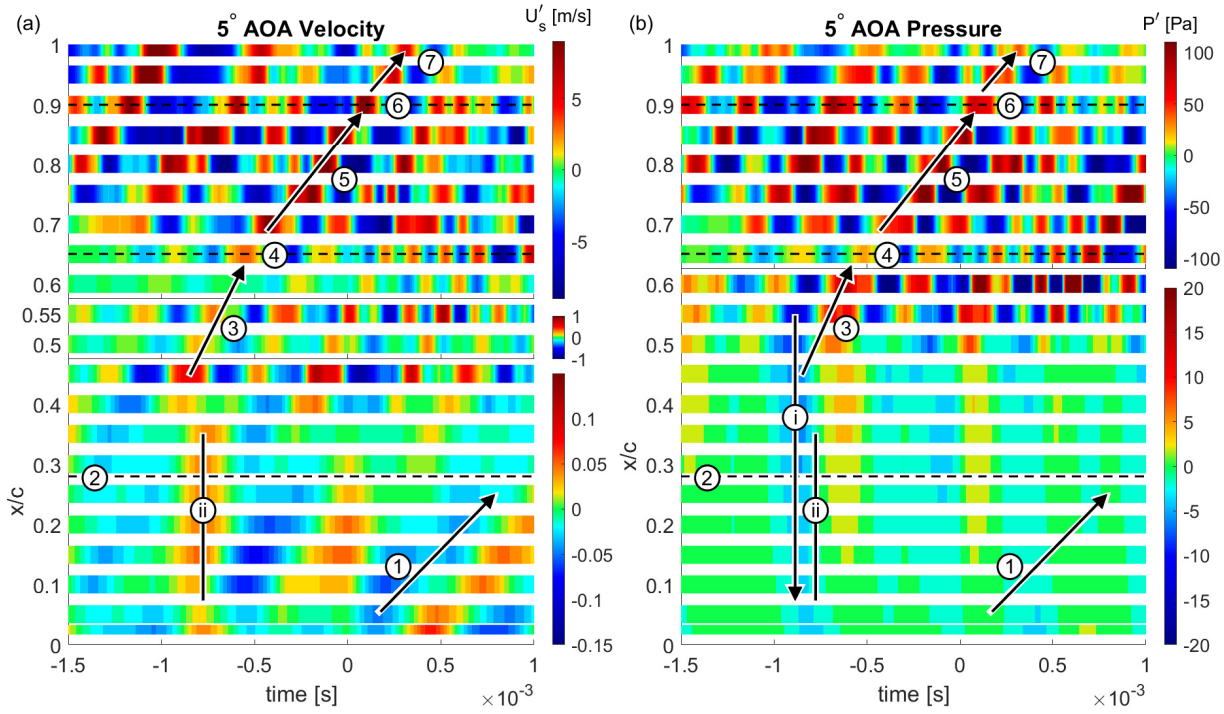


Figure 5.10: Pressure feedback influence on chordwise propagation of BL instabilities with time at 5° AOA and wall-normal height $4 \times 10^{-3}c$ for (a) U_s' and (b) P'. U_s' contour range changes at $x/c = 0.475$ and $x/c = 0.575$ and P' contour range changes at $x/c = 0.625$ according to colourbars on the righthand side. Time 0 refers to time 0 in Figure 5.9

The downstream propagation of a positive U_s' fluctuation, which was shown to correspond to a counter-rotating vortex in Figure 5.8, is labelled (3) to (7) in Figure 5.10(a). The downstream propagation of this fluctuation for $x/c > 0.45$ occurs at the same downstream propagation speeds as the labelled negative U_s' fluctuation in Figure 5.9(a), and thus corresponds to development, growth and breakdown of the counter-rotating vortex in regions (3), (5), and (7), respectively. However for $x/c < 0.4$ the U_s' fluctuation occurs simultaneously at a time of -0.78×10^{-3} s in Figure 5.10(a) and is labelled with (ii). This U_s' fluctuation does not have the expected downstream propagation speed of the negative U_s' fluctuation labelled (1), which was identified as naturally forming T-S waves in Section 5.4.1.

The downstream propagation of the T-S wave at (1) is 8 m/s at the wall-normal height of $4 \times 10^{-3}c$ based on the slope of the arrow in Figure 5.10(a), and has the same speed as the positive U_s' fluctuation of a T-S wave which starts at the LE at 0.45×10^{-3} s. When comparing the time evolution at each x/c location of the positive U_s' fluctuation of the T-S wave with the positive U_s' fluctuation (ii), it is clear that the magnitude and duration of the U_s' fluctuation is the same for the two behaviours. At each x/c location, the fluctuations of U_s' with time occur in a sinusoidal manner, as was shown in the idealized U_s' signal in Figure 5.8(b), and for the (ii) and (1) U_s' fluctuations in Figure 5.10(a) the peak magnitude of the fluctuation is approximately 0.05 m/s (as was reported in Section 5.4.1) and the total time duration of the positive U_s' fluctuation is approximately 2.6×10^{-4} s (or 65 time steps of the simulation). The similarities between the time evolution of the U_s' fluctuation at the x/c locations within the regions labelled (ii) and (1) would indicate that the behaviour at (ii) is similar to a T-S wave (1) and yet the U_s' fluctuation at (ii) occurs simultaneously, rather than propagating downstream at 8 m/s. The presence of the simultaneous positive U_s' fluctuation (ii) across the entire chordwise length of both the reverse flow portion of the LSB ($0.25 < x/c < 0.35$) and of the laminar BL ($0.025 < x/c < 0.25$) cannot be fully explained using the natural BL transition theory summarized in Section 2.1.2 and therefore the remainder of this section will provide evidence that the U_s' fluctuation (ii) is a result of pressure feedback from the LSB.

The U_s' fluctuation (ii) label is duplicated on the pressure contour in Figure 5.10(b), where the U_s' fluctuation is shown to occur at a short time delay after a negative P' fluctuation labelled with (i). The peak of the P' fluctuation occurs simultaneously for $x/c < 0.55$ at a time of -0.89×10^{-3} s, which is 0.11×10^{-3} s (or 27 time steps) before the peak of the positive U_s' fluctuation. The P' fluctuation has a magnitude of 12 Pa at $x/c = 0.55$, which is 5.3% of the $\bar{P}$ for the gauge pressure signal collected at $x/c = 0.55$, and decreases to 2.5 Pa at $x/c = 0.025$, which is 0.6% of the $\bar{P}$ at $x/c = 0.025$. The time evolution of the P' fluctuation at each x/c location is sinusoidal, as is shown for the idealized P' signal in Figure 5.8(b), and the negative P' fluctuation (i) also has the same total time duration of 2.6×10^{-4} s as the U_s' fluctuation (ii). In comparison, the P' fluctuations occurring for $x/c < 0.5$ from times 0 s to 1×10^{-3} s, which is during the natural formation of the T-S waves at (1), have a maximum magnitude of 2.5 Pa, which ranges from 0.6% to 1.1% of the $\bar{P}$ for $x/c < 0.5$. Therefore the natural formation of the T-S waves occurs when the P' fluctuation is a lower magnitude, and a higher magnitude P' fluctuation at (i) corresponds to the simultaneous U_s' fluctuation (ii) for $x/c < 0.35$.

Section 2.1.3 discusses the relationship between the time-averaged pressure and velocity in the airfoil BL due to conservation of mass and momentum, where an adverse pressure

gradient in the chordwise direction causes an associated chordwise deceleration in U_s. For 5° AOA, there is a time-averaged adverse pressure gradient for $x/c > 0.034$ as is shown in Figure 5.1(c) and the C_p for $x/c < 0.6$ calculated at the wall-normal height of $4 \times 10^{-3}c$ using the time-averaged pressure, $\bar{P}$, of the pressure signal is shown in Figure 5.11(a). The corresponding chordwise gradient of the time-averaged s-velocity, $\bar{U}_s$, at the wall-normal height of $4 \times 10^{-3}c$ is shown in Figure 5.11(b) for $x/c < 0.6$. The transient fluctuation of the adverse pressure gradient due to the negative P' fluctuation at (i) in Figure 5.10(b) is shown in Figure 5.11(a) where C_p is calculated using $\bar{P} - P'$. This transient reduction of the chordwise adverse pressure gradient would be expected to cause a similar transient reduction to the chordwise velocity gradient in Figure 5.11(b). The U_s' fluctuation at (ii) is multiplied by a factor of 100 and added to $\bar{U}_s$ in Figure 5.11(b) to visualize the change in chordwise velocity gradient that occurs during the U_s' fluctuation at (ii) in 5.10(a). The positive U_s' fluctuation has an average peak magnitude of 0.04 ± 0.01 m/s for $x/c < 0.35$ which does not alter the chordwise velocity gradient in response to the change in chordwise pressure gradient. It is possible that the development of an altered chordwise U_s gradient would require a prolonged change in the chordwise C_p gradient and the 2.6×10^{-4} s duration of the P' fluctuation at (i) is too transient to alter the chordwise U_s gradient. Therefore the negative P' fluctuation at (i) is assumed to alter the U_s through a different transient process, rather than through the alteration of the chordwise pressure gradient.

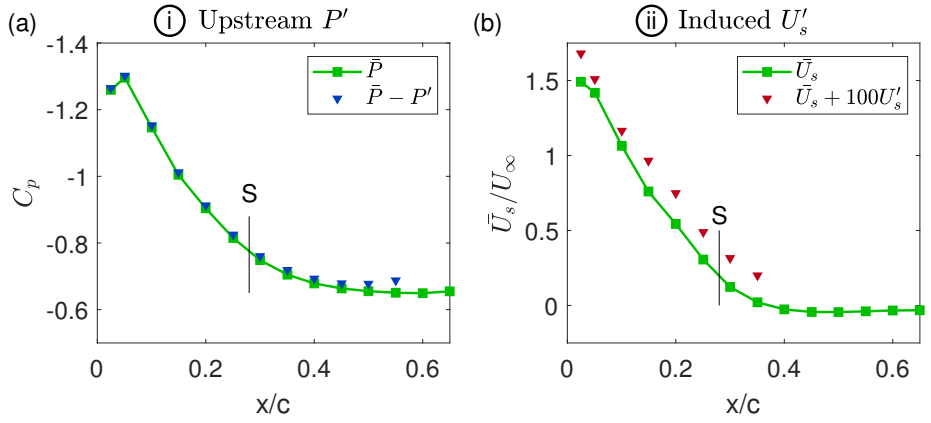


Figure 5.11: Time-averaged and transient chordwise behaviour of the P and U_s signals at the wall-normal height of $4 \times 10^{-3}c$ at 5° AOA showing (a) C_p (b) $\bar{U}_s/U_\infty$. Connecting lines are for visualization only

As discussed above, the magnitude of the U_s' fluctuation at (ii) has a similar time evolution to the T-S waves forming naturally in the BL at (1). This indicates that the transient

process inducing the U_s' fluctuation at (ii) could occur through the same mechanism that generates the initial velocity instability of the T-S waves in a laminar BL. When considering stability theory, as discussed in Section 2.1.2, the T-S waves develop in the laminar BL due to the susceptibility of the BL to small-scale, random velocity fluctuations [2]. The presence of a chordwise pressure gradient alters the stability of the BL due to changes in the BL velocity profile adjacent to the airfoil surface [3], where a favourable pressure gradient can suppress the velocity fluctuations and an adverse pressure gradient increases the susceptibility to velocity fluctuations. For the 5° AOA results, an adverse pressure gradient occurs between the suction peak at $x/c = 0.034$ and the reverse flow region of the LSB at $x/c = 0.4$, as seen in Figures 5.1(c) and 5.11(a), therefore the stability of the BL for $0.034 < x/c < 0.4$ is lowered in comparison to a BL without an applied pressure gradient.

This low stability BL corresponds to the location of the positive U_s' fluctuation at (ii) in Figure 5.10(a) which would cause the BL to be susceptible to naturally developing instabilities within the BL as well as instabilities induced by transient fluctuations from other sources in the flow. The time evolution of the negative P' fluctuation at each x/c location in the region (i) can therefore be assumed to induce the positive U_s' fluctuation at each x/c location within the region (ii) through this mechanism based on the principles of BL stability and susceptibility. Further evidence of the P' fluctuation inducing the U_s' fluctuation is the same 2.6×10^{-4} s duration of the fluctuations when examining the time evolution at each x/c location. The anti-correlated nature of the U_s' fluctuation in response to the P' fluctuation follows the principles of mass and momentum conservation, where in Figure 5.10(b) the negative P' fluctuation is shown to induce a positive U_s' fluctuation. Therefore the U_s' fluctuation at (ii) is not propagating through the BL in the chordwise direction, rather the U_s' fluctuation at (ii) has been shown to be locally induced at each x/c location by the transient P' fluctuation (i). The explanation for the presence of the simultaneous P' fluctuation (i) for $x/c < 0.6$ will be provided later in this section.

The P' fluctuation can also be shown to be inducing the U_s' fluctuation through the comparison of the U_s' and P' fluctuations at the two measured wall-normal heights of $4 \times 10^{-3}c$ (0.1 mm) and $3 \times 10^{-2}c$ (0.75 mm). The contours in Figures 5.9 and 5.10 were created using the measurements near the wall at $4 \times 10^{-3}c$, and Figure 5.12 shows the signals at $3 \times 10^{-2}c$ for $x/c < 0.6$ using the same time period and label positioning as Figure 5.10. For the naturally forming T-S waves at (1), the U_s' fluctuations at both wall normal heights have magnitudes of approximately 0.05 m/s but have different downstream propagation speeds. For the positive U_s' fluctuation at the LE at 4×10^{-4} s, the downstream propagation speed is 21 m/s (or 88% of U_∞) for $3 \times 10^{-2}c$ in Figure 5.12(a) in comparison

to the 8 m/s speed (or 35% of U_∞) of the T-S wave closer to the wall in Figure 5.10(a). The measurements at the wall-normal height of $3 \times 10^{-2}c$ are located near the maximum BL thickness for the laminar BL ($x/c < 0.3$) and therefore the mean flow speed at that location is higher and the U_s' fluctuations propagate downstream at a higher speed.

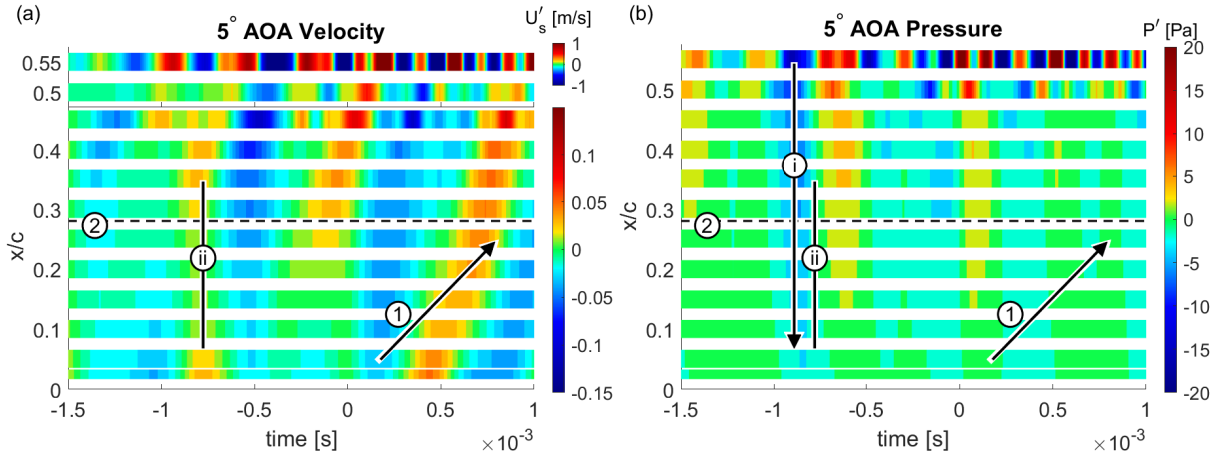


Figure 5.12: Pressure feedback influence on chordwise propagation of BL instabilities with time at 5° AOA and wall-normal height of $3 \times 10^{-2}c$ for (a) U_s' and (b) P'. U_s' contour range changes at $x/c = 0.475$ according to colourbars on the righthand side

These downstream propagation speeds of the T-S wave fluctuations do not directly correspond to the differences in the $\bar{U}_s$ between the two wall normal heights, which can be seen by comparing the propagation speed of 35% of U_∞ at the wall-normal height of $4 \times 10^{-3}c$ at (1) in Figure 5.10(a) with the chordwise trend in $\bar{U}_s/U_\infty$ in Figure 5.11(b) which ranges from 150% of U_∞ at $x/c = 0.025$ to 12% of U_∞ at $x/c = 0.30$. However, the identical time evolution of the positive U_s' fluctuation at each x/c location within region (ii) in Figure 5.10(a) and in Figure 5.12(a) shows a synchronization of the U_s' fluctuation (ii) through the entire BL thickness that is not present during the naturally forming T-S waves. The time evolution of the negative P' fluctuation for each x/c location in region (i) occurs at the same magnitude and duration at both wall-normal heights in Figures 5.10(b) and Figure 5.12(b) and therefore the P' fluctuation induces the U_s' fluctuation (ii) at both wall-normal heights through the BL instability mechanism described above. This is further evidence of this LSB pressure feedback process since it overrides the natural formation of the T-S waves throughout the entire thickness of the laminar BL.

Now that the P' fluctuation labelled (i) has been identified as the source of the simultaneous U_s' fluctuation for $x/c < 0.35$, analysis of the P' fluctuation is completed to

determine why it occurs simultaneously for $x/c < 0.55$. While the propagation of the U_s' fluctuation in the BL is dependent on the mean flow speeds of the BL, a sudden pressure change in the BL can propagate through the flow at speeds up to the speed of sound.This type of pressure fluctuation is different from the positive or negative gauge pressure fluctuations associated with the K-H rolls or counter-rotating vortices in region (5), rather it is an instantaneous pressure fluctuation that rapidly equalizes through an undisturbed flow like a sound wave. In an incompressible simulation, the speed of sound is infinite and therefore a pressure wave travelling at the speed of sound will travel instantaneously through the domain. This would mean that the P' fluctuation for $x/c < 0.55$ is capturing the instantaneous propagation of a pressure wave through the BL at the speed of sound. The speed of sound relative to the size of the SD 7037 airfoil used in the simulations means that there is little difference in the travel time of the pressure wave between an infinite speed of sound and the standard speed of sound of 343 m/s. The travel time from $x/c = 0.55$ to the LE is would be 4.1×10^{-5} s when considering compressibility and in comparison, the downstream propagation of the natural BL transition has a travel time of 1.2×10^{-3} s (average speed of 12 m/s) at a wall-normal height of $4 \times 10^{-3}c$ as is shown in Figure 5.9.

The P' fluctuation occurring for $x/c < 0.55$ would require a source behaviour either upstream of the LE or downstream of $x/c = 0.55$ to initiate this type of pressure equalization wave. In Section 5.3.1, the K-H roll pinch-off and K-H roll touchdown within the LSB was found to occur at the time-averaged BL transition location, which is $x/c = 0.65$ for the 5° AOA simulation. There is no such behaviour occurring at the LE of the airfoil that could reasonably be assumed to cause the P' fluctuation for $x/c < 0.55$. Additionally, the magnitude of the P' fluctuation is the greatest at $x/c = 0.55$ and decreases in magnitude as it approaches the LE. Therefore the formation of the K-H rolls with an associated negative P' fluctuation and the counter-rotating vortices with a positive P' fluctuation is a source for the upstream P' fluctuation (i). The K-H roll touchdown as the source for the upstream P' fluctuation will be explored in detail in Section 5.4.3.

Since the P' fluctuation travels through the BL at the speed of sound, it is necessary to confirm it does not propagate through the free-stream flow to the far-field of the domain to alter the behaviour and/or cause numerical errors at the inlet or outlet boundary conditions. The P' fluctuation associated with the LSB feedback was not detected at a $5c$ distance from the quarter-chord location of the airfoil, which is approximately half the distance from the airfoil to the far-field boundary conditions. This test was performed using the 1° AOA Mesh 2 simulation, which will be shown in Section 5.4.3 to have the highest amplitude pressure feedback of all the simulated AOAs. This test shows that the pressure wave dissipates before reaching the boundary and does not cause numerical error due to interaction with the boundaries of the domain. Additionally, the measurement $5c$

upstream of the airfoil confirmed that the inlet turbulence model, whose implementation is described in Section 3.2.1, is not introducing turbulent fluctuations at a frequency that would induce the P' fluctuation (i).

The BL behaviour of regions (3) to (7) in Figure 5.10 indicates differences in the development of the BL occurring downstream of the P' fluctuation (i) and the induced U_s' fluctuation (ii) in comparison to the natural BL transition process in Figure 5.9. After the time-averaged BL reattachment location (6), the U_s' and P' magnitudes of the K-H rolls and counter-rotating vortices in region (7) remain at a high magnitude. In Section 5.4.1, it was shown that the high magnitude U_s' and P' fluctuations in region (7) indicates that the vortices do not break down immediately after the time-averaged reattachment of the BL.

In comparison to the natural BL development shown in Figure 5.9, the U_s' and P' fluctuations in region (7) in Figure 5.10 shows that less K-H roll and counter-rotating vortex breakdown occurs when the upstream P' fluctuation (i) is inducing the U_s' fluctuation (ii) in the laminar BL and reverse flow region of the LSB. Therefore the presence of the upstream P' fluctuation for $x/c < 0.55$ increases the amplitude of the U_s' and P' fluctuations at the TE. This is a similar amplification effect that has been reported for the TE acoustic feedback described in Section 2.3.4. In the case of the TE acoustic feedback, the acoustic waves generated at the TE propagate upstream and amplify the T-S waves in the laminar BL which then propagate downstream to create amplified aeroacoustic noise at the TE. For this reason, the P' fluctuations (i) and the induced U_s' fluctuation (ii) will be referred to as LSB pressure feedback for the remainder of this work, where instead of TE acoustic waves as the source of the feedback, the source is the pressure fluctuations generated within the LSB. Further discussion of the TE acoustic feedback and the LSB pressure feedback can be found in Section 6.3.

While this LSB pressure feedback has not previously been reported, there is some evidence of the LSB as a source of pressure fluctuations in numerical works that identify the LSB as a source of aeroacoustic noise. Compressible direct numerical simulation (DNS) of the controlled-diffusion (CD) airfoil by Wu *et al.* [77] and compressible LES simulations by Deuse and Sandberg [69] found that a LSB located near to the LE was a source of aeroacoustic noise separate from the TE noise, as is summarized in Section 2.4.3. The simulation domain used by Wu *et al.* [77] included the effects of the shear layer that forms at the edge of the open jet wind tunnel which resulted in a reduced strength of the tonal noise source from the LSB in comparison to the simulations by Deuse and Sandberg at a similar Re and AOA. It is a known phenomenon that the shear layer of an open jet anechoic wind tunnel can restrict or prevent the propagation of lower amplitude sound waves to the

far-field [78] which poses a challenge for the experimental validation of the LSB as a source of pressure waves causing a feedback effect in the BL upstream of the LSB.

The identification of the LSB as an acoustic source in DNS and LES works [69, 77] indicates that an uninvestigated transient behaviour within the LSB is producing high amplitude pressure fluctuations which propagate radially to the far-field from a location within the LSB. This radial propagation includes pressure waves travelling upstream through the laminar BL to the LE of the airfoil which has been shown in this research to cause LSB pressure feedback. The upstream pressure feedback from the LSB and the source behaviour of the pressure waves was not explored in their works and therefore it is undetermined if the LSB pressure feedback is present for the CD airfoil simulations as well. What is clear is that their simulations, which account for compressible effects, predict that high amplitude pressure waves are generated by the LSB. From the identification of the LSB pressure feedback in this research, it can be assumed that a re-examination of the DNS and LES results [69,77] would find a similar LSB pressure feedback due to the upstream propagation of the acoustic pressure waves through the laminar BL.

5.4.3 LSB Feedback Source

The LSB pressure feedback process identified in Section 5.4.2 occurs continuously in the 1° and 3° AOA simulations and there is no evidence of the downstream propagation of naturally forming T-S waves shown in Section 5.4.1. The consistent occurrence of the LSB pressure feedback with time is also associated with increased consistency of the formation of the K-H rolls and counter-rotating vortices in the LSB and therefore the relationship between the coherent structures in the LSB and the pressure feedback can be established.

The contour plots generated using the method in Figure 5.8 and numbering system in Figure 5.7 to illustrate the chordwise propagation of the U_s' and P' fluctuations are shown for 1° AOA in Figure 5.13 and for 3° AOA in Figure 5.14. The upstream P' fluctuation (i) occurs for $x/c < 0.85$ at 1° AOA in Figure 5.13(b) and for $x/c < 0.75$ at 3° AOA in Figure 5.14(b). The anti-correlated U_s' fluctuations (ii) induced by the pressure feedback occur at a time lag of 0.06×10^{-3} s (15 time steps) for 1° AOA and 0.084×10^{-3} s (21 time steps) for 3° AOA which is similar to the lag of 0.11×10^{-3} s (27 time steps) at 5° AOA. The magnitude of the U_s' fluctuations (ii) for 1° and 3° AOA is 0.13% to 0.17% of U_∞ at the location of BL separation (2) which is consistent with the amplitude of the early development of T-S waves in a laminar BL [3] and is further evidence that the U_s' fluctuation (ii) is induced through the BL instability mechanism discussed in the previous section.

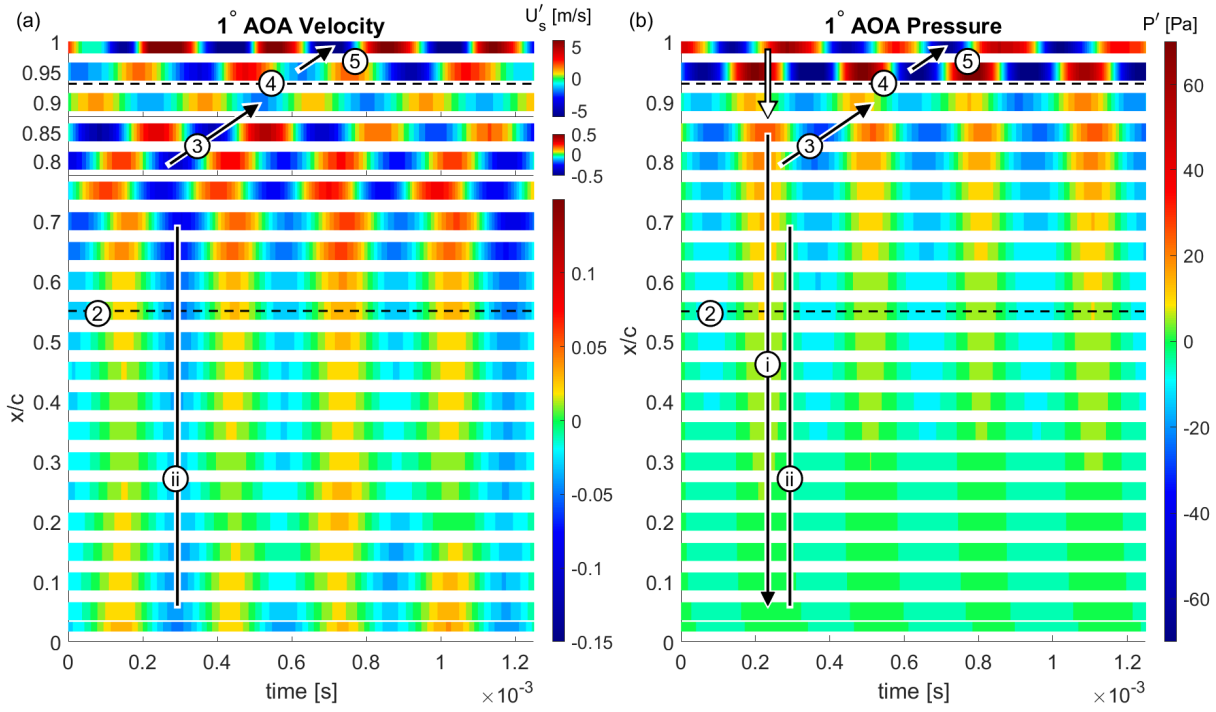


Figure 5.13: Chordwise propagation of BL instabilities with time at 1° AOA and wall-normal height $4 \times 10^{-3}c$ for (a) U_s' and (b) P'. U_s' contour range changes at $x/c = 0.775$ and $x/c = 0.875$ according to colourbars on the righthand side

The source of the pressure feedback within the LSB can be determined through the combined analysis of the 1° AOA U_s' and P' contours in Figure 5.13 and the K-H roll pinch-off visualization in Figure 5.6. The process of K-H roll formation from the reverse flow region of the LSB is summarized in Figure 5.5 where the path of the newly formed K-H roll is shown to increase in wall-normal height at the time-averaged BL transition location (x_{tr} in Figure 5.5 and labelled (4) in Figure 5.13) followed by the K-H roll touchdown. This process was described in detail in Section 5.3.1 with a focus on the growth and downstream propagation of the K-H rolls and counter-rotating vortices. However, when examining the gauge pressure contours shown in Figure 5.6, there is a noticeable fluctuation in the gauge pressure for $x/c < 0.85$ which corresponds to the location of the upstream P' propagation (i) in Figure 5.13(b).

In Figure 5.6, times (i) and (viii) are representative of the transient behaviour when there is a minimum gauge pressure for $x/c < 0.85$ and therefore corresponds to a negative P' fluctuation in Figure 5.13(b). During the negative P' fluctuation at times (i) and

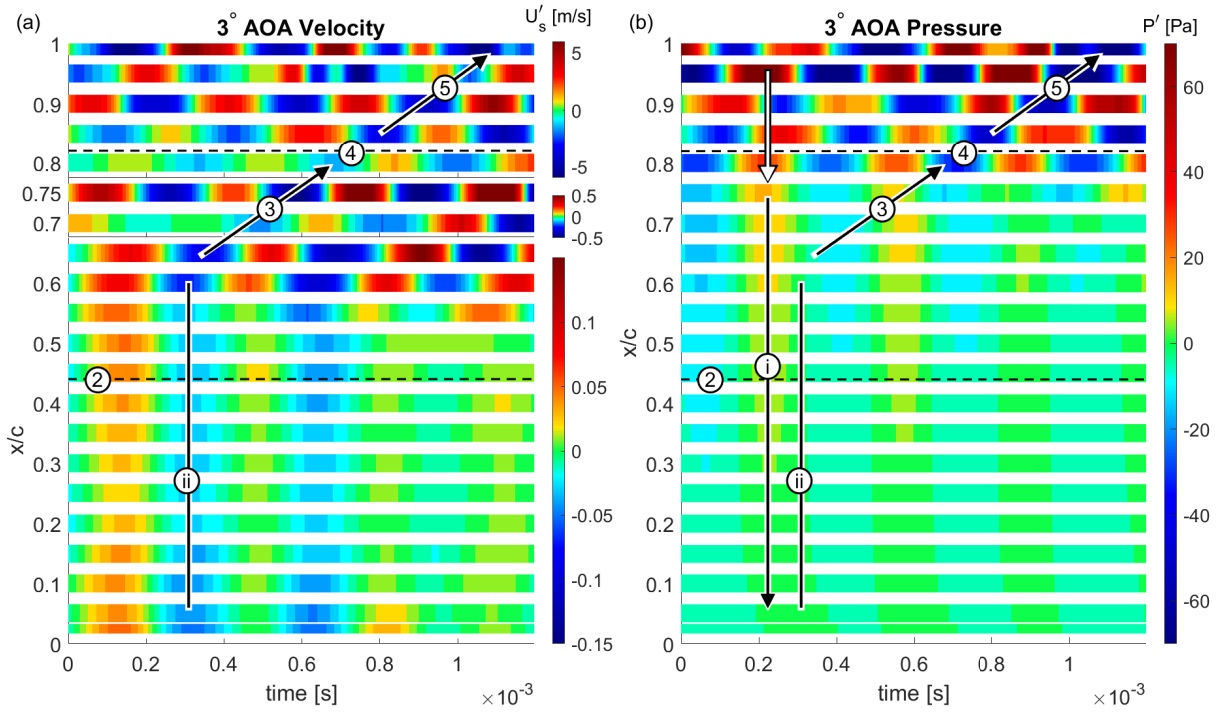


Figure 5.14: Chordwise propagation of BL instabilities with time at 3° AOA and wall-normal height $4 \times 10^{-3}c$ for (a) U_s' and (b) P'. U_s' contour range changes at $x/c = 0.675$ and $x/c = 0.775$ according to colourbars on the righthand side

(viii), the fully-formed K-H roll has grown to its maximum velocity and minimum gauge pressure and the core of K-H roll is located at the touchdown location of $x/c = 0.975$. This touchdown of the fully-formed K-H roll causes a high magnitude reverse flow at the airfoil surface which is shown through the minimum C_f at $x/c = 0.98$ in Figure 5.2(a). The localized transient fluctuation of the gauge pressure and velocity caused by the touchdown of the K-H roll has a strong correlation with the upstream propagation of the P' fluctuation and therefore is assumed to be the source behaviour for the LSB feedback mechanism.

The maximum gauge pressure for $x/c < 0.85$ occurs at time (v) in Figure 5.6 and corresponds to a positive P' fluctuation such as the sample fluctuation labelled (i) in Figure 5.13(b). This positive P' fluctuation at time (v) in Figure 5.6 occurs when the counter-rotating vortex core is positioned at the K-H roll touchdown location. The counter-rotating vortex has a lower gauge pressure magnitude than the K-H rolls, however it does not have a positive gauge pressure and therefore the counter-rotating vortex acts as a pressure recovery from the effect of the low pressure K-H roll. In Figure 5.13(b), the

synchronization of the positive P' fluctuation of the counter-rotating vortex at the K-H roll touchdown location of $x/c = 0.975$ and the upstream positive P' fluctuation (i) is shown with a white arrow. In Figure 5.13(b) the chordwise spacing of the measured P' signals limits the identification of the K-H roll and counter-rotating vortex locations to $x/c = 0.95$ and $x/c = 0.99$ and therefore the time that the K-H rolls and counter-rotating vortices are located at $x/c = 0.975$ are determined by assuming a constant downstream propagation speed given by the slope of the arrow for the K-H rolls, labelled (5). This clearly shows how the contour method described in Figure 5.8 can be applied to determine that the source behaviour of the LSB pressure feedback is the K-H roll touchdown downstream of the time-averaged BL transition location (4).

The analysis of the source behaviour for the LSB pressure feedback for 3° AOA is completed using the information in the U_s' and P' contours in Figure 5.14 along with the time-averaged C_f in Figure 5.2(b). The time-averaged BL transition labelled (4) in Figure 5.14 was altered from the value of $x/c = 0.75$ reported in Table 5.1 to $x/c = 0.82$ to improve the accuracy of the transient analysis. The transition location in Table 5.1 was determined from the H peak location, however the 3° AOA H in Figure 5.3(b) had a double peak leading to the selection of the first chordwise peak as the transition location at $x/c = 0.75$. Analysis of the 1° AOA K-H pinch-off behaviour in Section 5.3.1 showed that the time-averaged BL transition location is aligned with the small region of positive C_f that appears in the LSB before K-H roll touchdown. At 3° AOA, the positive C_f location of $x/c = 0.82$ is similar to the experimental H peak location of $x/c = 0.83$ and also is the location of the trough between the two simulated H peaks. Therefore it is appropriate to modify the transition location for the 3° AOA analysis in Figure 5.14.

If the 3° AOA LSB has the same source of the pressure feedback as the 1° AOA LSB, the source will occur downstream of the time-averaged BL transition location when the fully-formed K-H roll touchdown occurs. The time-averaged touchdown location of the K-H roll at 3° AOA occurs between $x/c = 0.96$ and $x/c = 0.98$ according to the negative C_f peak in Figure 5.2(b). The P' fluctuations in the K-H roll touchdown region are measured at $x/c = 0.95$ and $x/c = 0.99$ and Figure 5.14 shows that the fluctuations at $x/c = 0.95$ align with the upstream P' wave for $x/c < 0.7$. The white arrow in Figure 5.14(b) shows the source counter-rotating vortex at $x/c = 0.95$ for the positive P' fluctuation (i). Therefore at both 1° and 3° AOA, the source of the LSB pressure feedback is the K-H roll touchdown in the LSB.

Now that the LSB feedback source has been identified as the K-H roll touchdown, the 5° AOA results can be briefly revisited to determine the reason for the infrequency of the feedback behaviour at that AOA. The time-averaged C_f at 5° AOA in Figure 5.2(c) does not have the small region of positive C_f before K-H roll touchdown, which likely indicates

an irregular location of K-H pinch-off and K-H roll touchdown. The negative C_f peak associated with K-H roll touchdown at 5° AOA is a higher magnitude than at 1° AOA and therefore the K-H roll touchdown at 5° AOA should be capable of generating the same LSB feedback pattern. However, the inconsistency of the U_s' and P' amplitudes associated with the K-H rolls in region (5) of Figures 5.9 and 5.10 must prevent the LSB pressure feedback from developing with the consistency seen in the 1° and 3°AOA results. For the 5° AOA simulation, it was not confirmed that the transient behaviour in the BL is independent of the mesh filter length in the BL, as described in Section 5.1. It is possible that further improvements of the filter length at the wall and in the region of K-H roll formation, beyond the improvements described in Section 3.2.6, would increase the consistency of the LSB pressure feedback. The method of potential future investigation of the effect of the mesh filter length on the LSB pressure feedback will be provided in Section 8.2.

5.5 BL Velocity Spectra

The development of the frequencies of the BL transition structures are analyzed using spectral analysis of the U_s signals presented in Section 5.4. The U_s was collected for 1×10^4 time steps, which is a total time of 0.02 s for 1° AOA and 0.04 s for 3° and 5° AOA. The U_s spectra was calculated using fast fourier transform (FFT) of the full 0.02 s signal for 1° AOA and an ensemble average of the FFT of the signal divided into two 0.02 s signals for 3° and 5° AOA. In Figure 5.15, the single-sided U_s spectra are presented for five x/c locations to show the frequencies present at different phases of the BL transition process with the dominant frequency at each AOA indicated with a vertical dotted line. The labels included in the top right corner of each plot corresponds to the numbering system described in Figure 5.5 and Table 5.2 and the exact x/c location is in the plot legend. All AOAs have the spectra at the LE, the time-averaged BL transition location (4) and the TE as well as a spectra for an x/c location within the reverse flow region of the LSB (3) and the region of fully-formed K-H rolls region (5).

The spectra for the LE of the airfoil at $x/c = 0.025$ represents the frequency content of the attached laminar BL which includes either the naturally forming T-S waves in Figure 5.9 or the U_s fluctuations caused in response to the LSB pressure feedback shown in Figures 5.10, 5.13 and 5.14. At 1° and 3° AOA there is a dominant frequency of 3.45 kHz and 3.00 kHz, respectively, which is due to the frequency of the pressure feedback in the laminar BL. The dominant frequency for 1° and 3° AOA is present throughout the entire transitional BL with the U_s' fluctuation increasing in magnitude with increasing x/c location. The dominant presence of the LSB pressure feedback at these AOAs is clear from the analysis

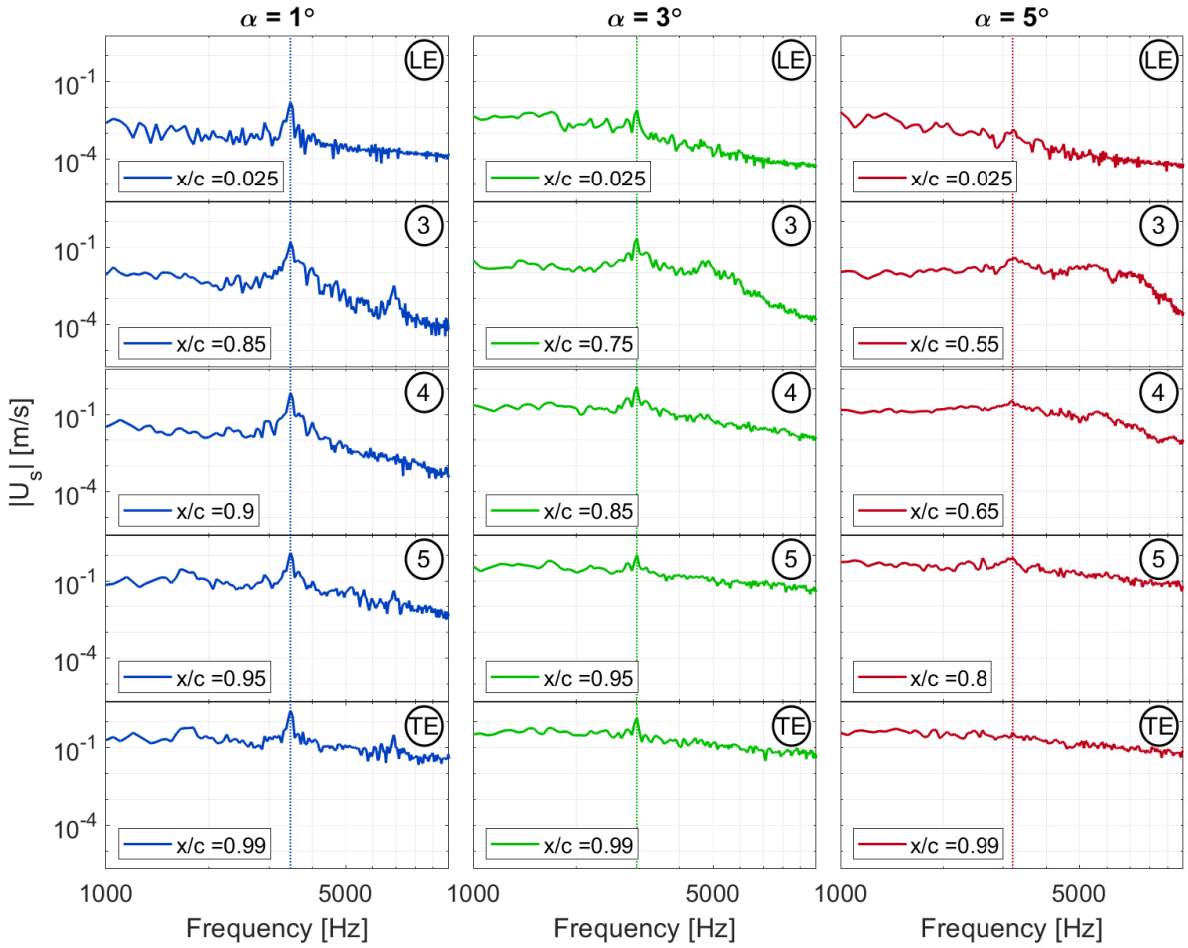


Figure 5.15: Single-sided U_s spectra at a wall-normal distance of $4 \times 10^{-3}c$ at 1°, 3°, and 5° AOA and x/c locations corresponding to the definitions in Table 5.2

in Section 5.4.3, which means that the laminar and reverse flow region of the LSB have induced U_s' fluctuations occurring at the K-H roll touchdown frequency. And since the K-H rolls are present at the TE with little to no breakdown (see Figure 5.4) the K-H roll frequency is measurable at all chordwise locations of the BL. The dominant frequency at 1° AOA is in agreement with the experimental acoustic tone frequency of 3.4 kHz, as described in Section 3.1.1, which is a strong indicator that the transient formation of the K-H rolls and the LSB pressure feedback process is occurring correctly in the LES simulations. The relationship between the frequencies of the U_s fluctuations in the BL transition structures and the tonal aeroacoustic noise frequencies will be explored further in the analysis of the aeroacoustic prediction in Sections 6.1 and 6.2.

In comparison, the 5° AOA U_s spectra at the LE shows that the velocity fluctuations occur over a broadband frequency range with a minor increase in U_s' amplitude at 3.20 kHz. The spectra within the LSB from locations (3) to (5) also weakly show this 3.20 kHz frequency, which corresponds to the frequency of the K-H instability and the K-H rolls in the separated BL. The transient analysis in Section 5.4 found that the 5° AOA BL development has significant variation of the frequency and magnitude of the transitional structures, as well as intermittent pressure feedback from the LSB. Additionally, in Figure 5.9 it was shown that the frequency of the K-H instability and K-H rolls in region (3) and (5) were higher than the frequency of the naturally developing T-S waves. The spectra at the LE has a higher magnitude U_s' fluctuations at lower frequencies compared to the other AOAs, which is explained by the presence of lower frequency naturally developing T-S waves. Also, the intermittent LSB feedback would explain the low amplitude peak in the laminar BL at the K-H roll frequency of 3.20 kHz.

The Strouhal number, $St_{\theta s}$, calculated using Equation 2.3 is a dimensionless frequency that can be used to compare the dominant K-H roll frequency from different LSBs and was defined in Section 2.1.4. The K-H roll frequency measured for region (5) in Figure 5.15 for 1°, 3° and 5° AOA results in $St_{\theta s}$ values of 0.009, 0.007 and 0.005, respectively, which is in agrement with the range of 0.005 to 0.016 observed in other works as summarized by Brinkerhoff and Yaras [6].

The similarity between the T-S wave and K-H roll frequencies and the possible interaction between these behaviours has been identified previously [6, 10]. Brinkerhoff and Yaras [6] applied DNS to a LSB on a flat plate and performed a test case with and without the LSB to determine that the T-S wave frequency in the attached BL developed at the given frequency independently of the K-H instability in the LSB. Their work shows that the K-H instability in the separated BL amplifies the naturally developing T-S wave frequency that is present in the BL at the point of laminar separation and therefore the K-H

instability occurs at the same frequency as the T-S waves in the laminar BL. When considering the LSB pressure feedback described in Section 5.4.2, the K-H rolls should only form at frequencies that are naturally present in the laminar BL and therefore the upstream pressure wave from the K-H roll touchdown occurs at a frequency within the range that would be expected for T-S waves to develop in the absence of the LSB. This is evidence that the LSB feedback process only serves to amplify the magnitude of the pressure and velocity fluctuations of the K-H roll at a specific frequency and does not artificially shift the fluctuations in the laminar BL to a frequency outside the range expected for the naturally forming T-S waves.

The 5° AOA simulation has time-averaged reattachment of the LSB at $x/c = 0.9$ and Section 5.4.2 showed that the magnitude of the pressure and U_s fluctuations associated with the downstream propagating K-H roll dissipated quickly after reattachment, indicating K-H roll breakdown. The single-sided U_s spectra at the airfoil TE in Figure 5.15 shows a broadband spectra without any elevated U_s amplitude at the K-H roll frequency. Section 5.4.2 showed that the presence of LSB pressure feedback caused the U_s fluctuations of the K-H rolls to propagate to the TE without dissipating, however this does not occur frequently enough to be able to detect the K-H roll frequency in the TE U_s spectra.

5.5.1 K-H Roll Breakdown

The level of K-H roll breakdown at each AOA is quantified using the magnitude-squared coherence, γ^2, of the pressure signals, as described in Section 2.1.4, at each x/c location across a spanwise distance of $0.1c$. The pressure signals were collected for the same simulated time period as the U_s signals used to generate the spectra in Figure 5.15, and γ^2 is reported for the dominant K-H roll frequency identified for each AOA with a value of $\gamma^2 = 1$ indicating perfect spanwise coherence. The γ^2 values are presented in Figure 5.16 with the time-averaged location of BL separation, transition and reattachment labelled, where applicable, using the x/c values reported in Table 5.1. The transition location labelled for 3° AOA is the $x/c = 0.82$ location used in Figure 5.14, as explained in Section 5.4.3.

As expected based on the Q-criterion visualization in Figure 5.4, the spanwise coherence of the K-H rolls for 1° AOA and 3° AOA in Figure 5.16(a) and (b) is maintained at the TE with a minimum coherence of $\gamma^2 = 0.88$ at 3° AOA. Across all AOAs, the time-averaged location of BL transition is where the spanwise coherence of the K-H rolls begins to decrease. This corresponds to the region (5) spectra in Figure 5.15, where the dominant K-H roll frequency is present, however there is an increase in the broadband spectra which indicates

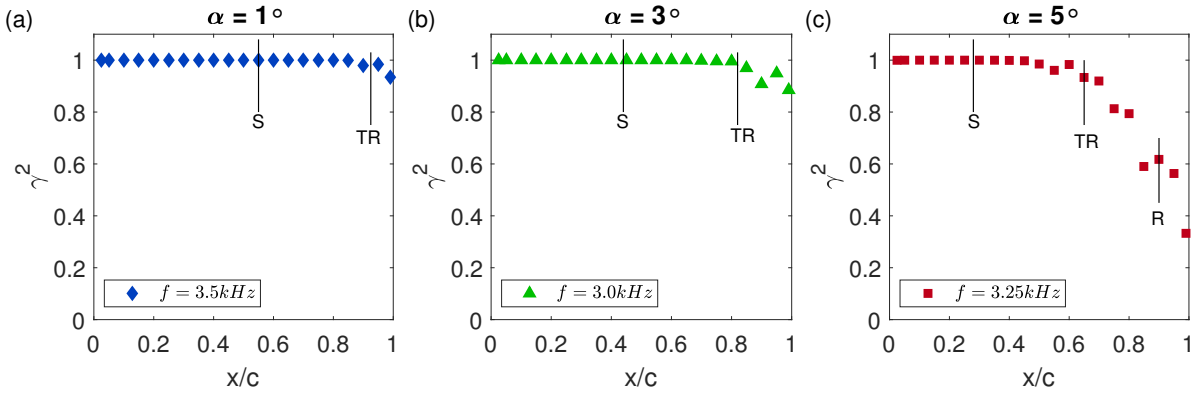


Figure 5.16: Magnitude-squared coherence, γ^2, of gauge pressure at the dominant K-H roll frequency and a spanwise spacing of $0.1c$ for (a) 1° AOA (b) 3° AOA and (c) 5° AOA. Locations of BL separation, transition and reattachment are marked with S, TR and R, respectively

that the initiation of the K-H roll breakdown is introducing random turbulent fluctuations into the flow at a wide range of frequencies. By the time-averaged BL reattachment at 5° AOA, the spanwise coherence in Figure 5.16(c) has dropped significantly to $\gamma^2 = 0.6$ and decreases further to $\gamma^2 = 0.3$ at the TE, providing an explanation for the absence of the K-H roll frequency in the TE spectra in Figure 5.15. The spanwise coherence of the pressure behaviour in the K-H rolls is relevant to the tonal airfoil self-noise prediction presented in Chapter 6 since tonal noise generation at the airfoil TE (see Section 2.3.3) requires pressure fluctuations with a high spanwise coherence.

5.6 Summary

This chapter presented the validation and analysis of the LES simulation of the transient behaviour in the BL transition process over the SD 7037 airfoil at 1°, 3° and 5° AOA. The modest Re of $Re = 4.1\times10^4$ produced an elongated LSB where the transient development of the BL transition structures within the different regions of the LSB were clearly visualized. This provided a significant advantage over previous simulations of low Re airfoils where the transition behaviours and the transient patterns that develop in the LSB are obscured by the rapid BL transition and accelerated breakdown of the K-H rolls. Additionally, the 1° and 3° AOA simulations had transitional separated flow at the TE which has a complex interaction of the K-H rolls from the suction side LSB with the pressure side BL that

has not be rigorously investigated in prior numerical simulations of low Re airfoils. The detailed analysis of the formation of the K-H rolls and the associated pressure and velocity behaviour is critical to determine the source of the aeroacoustic noise generated by the airfoil TE, which will be presented in Chapter 6.

The validation of the results from the new mesh versions Mesh 2 and Mesh 3 and comparison against the Mesh 1 results in Chapter 4 showed that there was minimal change in the results at 1° AOA and an improvement to the LSB reattachment location at 5° AOA. The issue of early LSB reattachment has been identified by previous researchers as being due to incorrect inflow turbulent intensity, however the 5° AOA results showed that insufficient SGS filter lengths in the LE BL and the separated BL were responsible for the early transition and reattachment of the BL. This improvement in the simulated LSB behaviour at 5° AOA was confirmed through the spanwise breakdown of the K-H rolls occurring further downstream due to the improved filter length for the separated BL in Mesh 3. However, the Mesh 3 simulation for 5° AOA did not fully meet the filter length criteria and discussion of potential future investigation of the role of the filter length in the LSB simulation is included in Section 8.2.

The detailed analysis of the 1° AOA simulation was completed to establish the process of formation of the K-H rolls within the LSB and the interaction of the K-H rolls with the pressure side BL at the airfoil TE. The visualization of the instantaneous pressure and velocity behaviour in the LSB identified the process of K-H roll pinch-off from the reverse flow region of the LSB and the creation of counter-rotating vortices between the K-H rolls. The comparison of these behaviours with the time-averaged C_f showed that the touchdown of the K-H roll after the pinch-off process occurred at a consistent chordwise location and corresponded to the negative C_f peak that occurs before time-averaged BL reattachment. It was also shown that the small region of positive C_f in the LSB is related to the chordwise location of the counter-rotating vortex during the K-H roll pinch-off process and that this location corresponds to the time-averaged BL transition location in the LSB. The relationship between the transient K-H roll pinch-off process and the time-averaged C_f can be applied to other airfoils to interpret the transient behaviour of the LSB from time-averaged data from either lower fidelity simulations or experimental methods that are not time resolved.

The 1° AOA simulation also has a transitional separated BL at the TE, which shows the interaction of the low gauge pressure K-H rolls with the airfoil TE. When a K-H roll passes the TE, a low gauge pressure counter-rotating vortex was formed from the pressure side BL. The relevance of the interaction of the K-H roll and pressure side counter-rotating vortex at the airfoil TE to the generation of tonal aeroacoustic noise is discussed further in Section 6.1.

The chordwise propagation of the instabilities associated with the BL transition were analyzed to determine the relationship between the development of the T-S waves in the attached laminar BL and the K-H roll formation in the LSB. At 5° AOA an intermittency in the rates of downstream propagation of the instabilities was identified and showed that at certain times the expected natural BL transition behaviours occurred and at others a LSB pressure feedback altered the behaviour in the attached laminar BL. Analysis of the LSB pressure feedback across all simulated AOAs showed that the touchdown of the K-H roll in the LSB initiated an upstream pressure wave which then induces a s-velocity fluctuation that resembled a naturally forming T-S wave. The LSB pressure feedback process alters the development of the T-S waves and resulted in the amplification of the pressure and velocity fluctuations associated with the K-H rolls. This amplification was found to occur in a similar manner to the proposed acoustic feedback loops caused by tonal aeroacoustic noise at the airfoil TE. The effect of this LSB pressure feedback is discussed further in Chapter 6 with its impact on the tonal noise generation examined in Section 6.1 and an estimation of the interference with TE acoustic feedback explored in Section 6.3.

Finally, the frequencies of the transient BL transition structures were determined through spectral analysis of the velocity fluctuations in the BL and the trends in the spanwise coherence after the time-averaged BL transition location were used to quantify the K-H roll breakdown. The LSB pressure feedback was found to cause a consistency in the frequencies of the T-S waves and the K-H rolls at 1° and 3° AOA. The effect of the intermittent LSB pressure feedback at 5° AOA was also present in the T-S wave and K-H roll frequencies which were not as well-defined in comparison to the other AOAs. Additionally, the time-averaged reattachment of the BL at 5° AOA was shown to reduce the spanwise coherence of the K-H rolls at the TE. The dominant frequencies at each AOA are in agreement with or similar to the experimentally measured tonal noise frequencies and the differences between the simulated and experimental tonal noise frequencies will be discussed in detail in Section 6.2.

This chapter completes the validation of the LES simulation of the BL and LSB on the SD 7037 airfoil operating at modest Re. The analysis fulfils objectives #1 and #5 for the LES simulations by accurately simulating the transient behaviours in the LSB, which was a continuation of the validation of the simulations in Chapter 4. The optimization of the simulation domain and mesh distribution combined with the assessment of the simulation parameters detailed in Section 3.2 fulfils objective #6 by simulating the complex behaviour of the LSB without requiring a computationally expensive DNS simulation. Additionally, significant progress was made towards fulfilling objective #3 by identifying the transient formation of the structures in the transitional BL which will be used to determine the source of the tonal aeroacoustic noise in Chapter 6.

Chapter 6

Aeroacoustic Noise Results

This chapter presents the final phase of the analysis of the simulation of the laminar separation bubble (LSB) on the SD 7037 airfoil at the Reynolds number of $Re = 4.1 \times 10^4$ and at 1°, 3° and 5° angles of attack (AOA). The Ffowcs-Williams and Hawkings (FW-H) acoustic analogy is applied to the large eddy simulations (LES) presented in Chapter 5 to generate a prediction of the tonal aeroacoustic noise generated by the airfoil trailing edge (TE). The mechanisms of airfoil self-noise are described in Section 2.3.3 and the application of the FW-H acoustic analogy to low Re airfoils is summarized in Section 2.4. The tonal noise prediction is validated against the experimental data summarized in Section 3.1.1 and the source of the tonal noise is determined using the analysis of the transient structures in the LSB presented in Chapter 5. The approach and numerical method for the LES and FW-H simulations are covered in detail in Sections 3.1 and 3.2 and the results in this chapter are generated using Mesh 2 and Mesh 3 shown in Figure 3.4 with other simulation details summarized in Tables 3.1 and 3.2.

In this chapter, the sources of the tonal aeroacoustic noise are identified for the SD 7037 airfoil and the combined effect of TE acoustic feedback and the LSB pressure feedback identified in Section 5.4 on the tonal noise sound pressure level (SPL) is estimated. The results and analysis reported in this chapter address the research objectives #2, #3 and #5 in Section 1.3 for the numerical prediction of tonal aeroacoustic noise for small wind turbine (SWT) blades operating at low Re with a LSB. A portion of the contents of this chapter has also been published in the peer-reviewed *Journal of Physics: Conference Series*[1] and preliminary results were published in the conference proceedings listed in Appendix A.

[1]Zilstra, A. and Johnson, D.A. (2024) Numerical Prediction of Tonal Aeroacoustic Noise Produced by Small Wind Turbines. J. Phys.: Conf. Ser., doi:10.1088/1742-6596/2767/7/072022

6.1 Far-Field Acoustic Prediction

The theory behind the prediction of aeroacoustic noise from transient aerodynamic data using computational aeroacoustic (CAA) models is described in Section 2.4 and the details of the FW-H acoustic analogy used in this work are covered in Section 2.4.2. The FW-H analogy was applied to the results from the Mesh 2 and Mesh 3 LES simulations presented in Chapter 5 using the numerical method described in Section 3.2.3 to generate an acoustic pressure signal at a far-field location $3.0c$ below the quarter-chord of the airfoil (see Figure 3.1). The initial portion of the acoustic signals were truncated to remove the transient numerical effects from the initialization of the simulation, as is described in Section 3.2.2, resulting in a signal length of 0.10 s, or 92 chord-based mean flow residence times (MFRT), for 1° AOA and 0.048 s (44 MFRT) for 3° and 5° AOAs. The acoustic spectrum of each acoustic signal was generated through fast fourier transforms (FFT) of the full signal length at 3° and 5° AOA. For 1° AOA, an ensemble average was completed of FFTs from the acoustic pressure signal divided into two equal segments due to the extended length of the signal. The acoustic pressure was then converted to SPL using Equation 2.8 to produce the final acoustic spectra predicting the aeroacoustic noise from the full-span SD 7037 blade.

The simulated blade segment used to predict the acoustic spectra has a span of $0.2c$ which is 3.4% of the experimental blade span of $5.9c$. According to the airfoil self-noise theory in Section 2.3.3, the smaller span of the simulations will predict a lower SPL due to the reduced surface area of the airfoil interacting with the coherent structures in the airfoil BL. The extrapolation of the acoustic results from the simulated span of $0.2c$ to the full span of $5.9c$ requires confirmation that the simulated behaviour of the airfoil BL, particularly at the TE, is an accurate representation of the behaviour across the full span. The magnitude squared coherence of the pressure at a spanwise spacing of $0.1c$ presented in Section 5.5.1 showed that the transitional BL on the suction side of the airfoil has a high spanwise coherence at the airfoil TE. The behaviour of the Kelvin-Helmholtz (K-H) rolls at the airfoil TE is also visualized in Figure 5.4, which shows that the K-H rolls are spanwise structures with horseshoe structures of short spanwise length forming as the rolls begin to break down. The spanwise coherence of the airfoil BL indicates that the BL behaviour of a blade segment with a larger span would be identical to the $0.2c$ span used for the simulations. Therefore the simulated acoustic prediction was extrapolated to a blade span equivalent to the experimental blade by multiplying the simulated acoustic pressure for each frequency band by 5.9/0.2 before conversion to SPL using Equation 2.8.

The predicted acoustic spectra are compared with the experimental results [49] summarized in Section 3.1.1 for the narrowband frequency range of 1 kHz to 10 kHz associated with tonal behaviour for the airfoil. The dominant tones identified in the experiments are

at frequencies of 3.4 kHz and 4.1 kHz and the prediction of these tones using FW-H is the focus of the aeroacoustic analysis. The experimental spectra also contain the first harmonic of the 3.4 kHz tone as well as a series of tones in the 5 to 6 kHz range that are assumed to be due to installation effects of the airfoil in the acoustically-treated closed-loop wind tunnel which had a hard-walled test section. These tones are not present in the tunnel background noise spectrum and a test case performed in an open jet wind tunnel (acoustic spectra shown in Figure 6.6(b)) did not produce any tones in that frequency range [49]. The background noise spectrum was subtracted from the measured experimental spectra to provide a direct comparison with the simulated spectra.

6.1.1 Acoustic Spectra at 1° AOA

The narrowband acoustic spectrum predicted by the FW-H acoustic analogy for the Mesh 2 simulation at 1° AOA is shown in Figure 6.1(a) and is compared with the measured experimental spectra [49]. The aerodynamic behaviour at the airfoil TE is shown in Figure 6.1(b) for the final time step of the simulation to serve as an example of the gauge pressure behaviour and the associated velocity behaviour which both include constant-length velocity vectors to show the local flow direction. These contours were generated in the same manner as the contours in Figure 5.6, and Section 5.3.1 includes a detailed description of the identification of the K-H rolls and counter-rotating vortices using these gauge pressure and velocity magnitude contours. The contours in Figure 6.1(b) are generated from the same time step as that used to generate the Q-criterion iso-surfaces in Figure 5.4, and shows two K-H rolls with the cores located at $x/c = 0.9$ and $x/c = 0.98$. The relationship between the K-H rolls and the predicted tonal TE noise is discussed in Section 6.1.2.

The predicted dominant tone in Figure 6.1(a) is at a frequency of 3.47 kHz and SPL of 86.6 dB and is at the center of a broadband hump of elevated SPL that ranges from approximately 2 kHz to 4.5 kHz. The high SPL of the tonal noise is clearly defined above the broadband SPL for the presented narrowband spectrum, which has an average SPL of 50 dB. The simulated spectrum is in excellent agreement with the experimental spectrum [49], which measured the dominant tone at a frequency of 3.39 kHz and an SPL of 122.2 dB and contains the same broadband hump centred on the tonal frequency. The broadband SPL is also in agreement with the experimental data for $f > 2$ kHz. The accuracy of the tonal noise prediction shown in Figure 6.1(a) fully validates the LES and FW-H method for prediction of tonal TE noise from low Re airfoils.

As described in Section 3.2.1, the incompressible simulation method does not simulate the propagation of acoustic waves generated from TE and therefore is not able to account

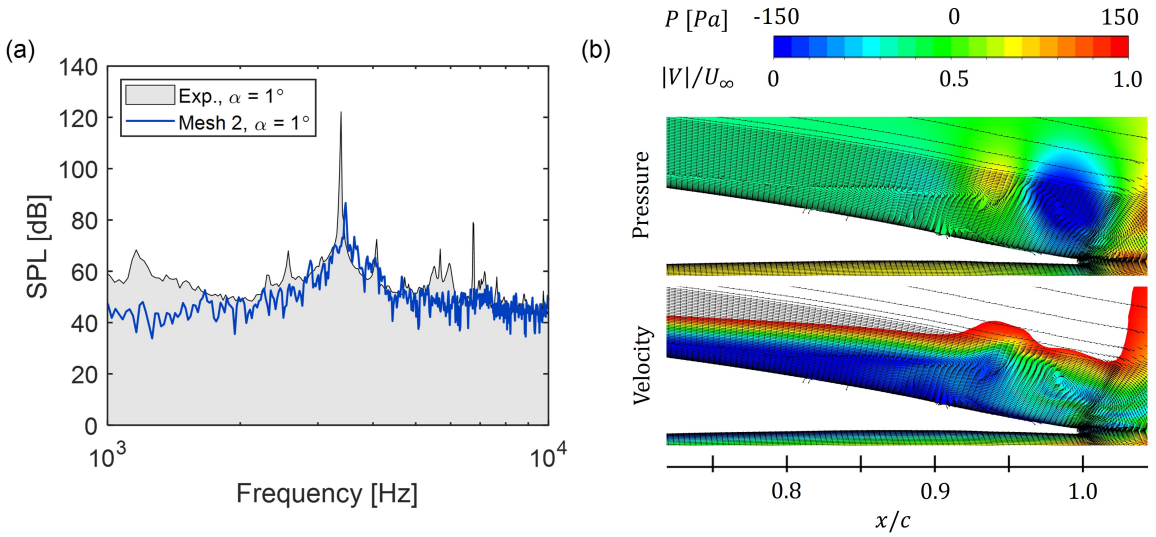


Figure 6.1: (a) Acoustic SPL spectra compared with experimental measurements [49] and (b) TE gauge pressure and velocity magnitude contours overlaid with flow direction vectors for 1° AOA Mesh 2

for the amplification of tonal noise through the TE acoustic feedback discussed in Section 2.3.4. The incompressible simulation domain does not include the walls of the wind tunnel and therefore also does not predict any amplification of tonal noise due to the sound wave reflection within the hard-walled test section of the wind tunnel used to collect the data [49]. This is seen in the spectrum in Figure 6.1(a), where the dominant tone SPL is under-predicted by 36 dB whereas the SPL of the rest of the spectra is in excellent agreement with the experimental SPL. An estimate of the influence of the TE acoustic feedback on the amplification of the dominant tone will be presented in Section 6.3 along with the interference from the LSB feedback identified in Section 5.4.2.

6.1.2 Tonal Noise Source

With the tonal noise frequency identified, the LES results can be examined to determine the source of the tonal noise at the airfoil TE. The airfoil self-noise theory summarized in Section 2.3.3 states that the generation of tonal noise of an airfoil requires a high spanwise coherence of the pressure fluctuations in the BL at the TE [50] and that when a LSB is located near the TE the K-H rolls are often responsible for the tonal noise [52–56]. The analysis of the 1° AOA LES results in Chapter 4 confirmed the presence of a LSB on the

suction side of the airfoil without a time-averaged BL reattachment location and with K-H rolls of high spanwise coherence passing the TE. In Chapter 5, the formation of the K-H rolls in the LSB was thoroughly examined in Section 5.3.1 which included their interaction with the pressure side BL at the TE. The K-H rolls are vortical structures where the rotation of the roll results in low pressure at the centre of the roll and the regions between the K-H rolls feature a higher pressure, or a pressure recovery. It was shown for 1° AOA in Figure 5.6 that when the suction side K-H roll passes the TE, a complementary low pressure counter-rotating vortex forms from the pressure side BL as is summarized in Figure 5.5. The counter-rotating vortex wraps around the TE causing a low pressure fluctuation and when it is subsequently shed into the wake the pressure recovers causing a high pressure fluctuation at the TE. At the time shown in Figure 6.1(b), there is no counter-rotating vortex from the pressure side BL and there is a positive pressure that has propagated downstream from the TE. This K-H roll positioning and pressure behaviour at the TE aligns with time (ii) in Figure 5.6, which is immediately before the new counter-rotating vortex forms at the TE.

The high spanwise coherence of the K-H rolls at the TE, as was shown in Figure 5.16, indicates that the entire span of the airfoil TE has a synchronized fluctuation between low and high pressure as the suction side K-H rolls and pressure side counter-rotating vortices are shed into the wake. The sharp TE of the airfoil is an efficient scattering centre of acoustic energy [48], leading to the tonal noise at the K-H roll frequency propagating to the far-field receiver location. K-H rolls present due to a suction side and/or pressure side LSB have been previously shown to be the source of the TE tonal noise through experimental [52–56] and numerical [58] studies of low Re airfoils with a LSB near the TE. The spectral analysis of the s-velocity, U_s, in the suction side BL in Section 5.5 found that the K-H rolls develop in the LSB at a frequency of 3.45 kHz, and that this frequency is present throughout the entire chordwise length of the BL due to the LSB feedback shown in Section 5.4.3. The K-H roll frequency is the same as the predicted dominant tonal noise frequency of 3.47 kHz and therefore is confirmed to be the source of the tonal noise.

6.1.3 Secondary Tone Intermittency[2]

The 1° AOA simulation was extended to a total duration of 118 chord-based MFRT in order to perform analysis on the secondary 4.1 kHz tone identified experimentally [49]. It was found that after 84 MFRT the secondary tone of 4.0 kHz intermittently appeared for

[2]Zilstra, A. and Johnson, D.A. (2024) Numerical Prediction of Tonal Aeroacoustic Noise Produced by Small Wind Turbines. J. Phys.: Conf. Ser., doi:10.1088/1742-6596/2767/7/072022

durations of approximately 0.005 s (or 4.6 MFRT) within the acoustic signal. While this tone is at a low SPL for 1° AOA, it was identified as the dominant tone at 2° AOA in experiments [49] and it is therefore important to be able to identify this tonal frequency using the FW-H acoustic analogy. The intermittency of the secondary tone was identified through calculation of the SPL for short signals of length 0.008 s which were selected to be a sufficiently short length to identify time periods of the secondary tone intermittency while also resulting in FFT bin widths that are able to resolve the difference between the 3.5 kHz and 4.1 kHz tones. A sample region of the acoustic pressure signal is shown in Figure 6.2(d) where both tones are present in signal #1 which is immediately followed by signal #2 with a dominant 3.5 kHz tone. The acoustic spectra corresponding to these signals are shown in Figure 6.2(c) where both tones for the signal #1 spectra are of equal magnitude. Additionally, the contours examining the formation of the K-H rolls in Figure 5.6 were generated from time steps within signal #2 and therefore examines the K-H roll formation when the 3.5 kHz tone is dominant.

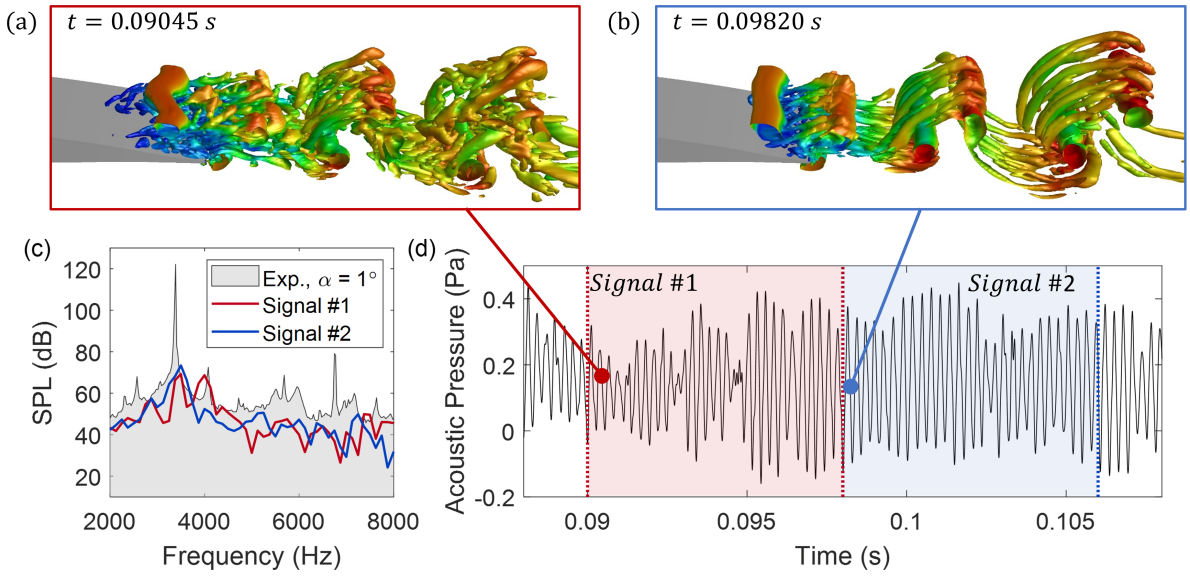


Figure 6.2: Q-criterion iso-surface of 1×10^8 s^{-2} for 1° AOA for (a) signal #1 and (b) signal #2. (c) Acoustic spectra for signal #1 and signal #2 compared with experimental measurements [49]. (d) Acoustic pressure for signal #1 and signal #2

A change in the tonal TE noise frequency and SPL must correspond to a change in the BL behaviour at the airfoil TE, which can be seen in Figure 6.2(a) and 6.2(b). These

Q-criterion iso-surfaces are at a magnitude of 1×10^8 s^{-2} which is a higher magnitude than those in Figure 5.4 to visualize the interaction of the smaller structures at the TE. The representative times were selected to show the K-H roll at a similar proximity to the TE, and therefore a clear difference can be seen in the spanwise coherence of the roll. In signal #1 where both tones are present, there is a spanwise instability forming in the K-H roll that is not seen in the pure tone case of signal #2. This instability appears alongside a large number of smaller 3D structures near the TE and in the wake, indicating that the BL has transitioned further towards turbulence. The structures formed in the BL and wake during signal #2 do not exhibit this level of BL transition, and K-H rolls with high spanwise coherence are seen well into the wake. This behaviour is also associated with higher amplitude acoustic pressure fluctuations shown in Figure 6.2(d) which in turn results in a higher SPL that is in line with the high SPL of the 3.4 kHz tone measured experimentally.

The coherence of the pressure signal in the BL at a spanwise spacing of $0.1c$ in Figure 5.16 found a small decrease in the spanwise coherence after the BL transition location of $x/c = 0.925$. For the 0.02 s time period that the BL pressure signal was recorded, the associated acoustic pressure signal behaviour was similar to signal #2 in Figure 6.2(d) and therefore the coherence values at the TE is for K-H rolls without a spanwise instability. The spanwise instability seen in Figure 6.2(a) occurred very infrequently during the extended run time of the 1° AOA simulations, but this behaviour would be detectable through the intermittent decrease in the spanwise coherence after the time-averaged BL transition location.

This spanwise instability associated with the secondary tone has been previously identified through a series of works using the CD airfoil, where the DNS simulations of Sanjose *et al.* [58] and the LES simulations of Winkler *et al.* [59] identified the spanwise instability followed by the experiments by Jaiswal *et al.* [55] which directly related this spanwise instability to the tonal noise intermittency. The experimental study of the NACA 0012 airfoil by Probsting *et al.* [52] detected amplitude modulation of the acoustic pressure signal resembling the appearance of the spanwise instability in Figure 6.2(d) signal #1 and they speculated that periodic modulation of the acoustic feedback mechanism and the receptivity of the laminar BL to this feedback is responsible for this behaviour. A similar intermittency of feedback in the laminar BL was shown in the analysis of the LSB pressure feedback at 5° AOA in Section 5.4.2, where the presence of LSB pressure feedback reduced the spanwise breakdown of the K-H rolls in comparison to the K-H rolls that formed in the absence of a strong pressure feedback. However, the study by Probsting *et al.* was limited to 2D analysis of the K-H rolls at the TE and therefore were unable to comment on the presence of spanwise instabilities in relation to the amplitude modulation of the

acoustic signal. Similarly, the experimental analysis by Yakhina *et al.* [56] of the tonal noise from the LSB on the SD 7003 airfoil suggested the transition or jump of the frequency of the acoustic feedback mechanism led to the measured intermittent switching of the dominant tone frequency at $Re = 1.26 \times 10^5$ and two simultaneous tones with varying SPL at $Re = 1.5 \times 10^5$. In the case of the SD 7003 and CD airfoils, the intermittency of the tonal noise behaviour is only detectable in signals multiple seconds in length [55, 56] which was also found to be the case for the experimental data collected for the SD 7037 airfoil by Tam [49]. This extended length of acoustic signal is more realistic for experimental examination of the tonal noise, however this 1° AOA simulation shows that an extended run of the simulation was able to detect the intermittency, as was also found in the simulations of Sanjose *et al.* [58].

6.1.4 Acoustic Spectra at 3° and 5° AOA

The 1° AOA LES and FW-H simulation produced an accurate tonal noise prediction and led to the identification of the K-H rolls from the suction side LSB as the source of the TE tonal noise. The analysis of the 3° and 5° AOA LES results in Chapter 5 showed that they also feature a suction side LSB that is in close proximity to the TE, with an approximate 10% to 20% upstream shift in LSB separation and transition locations with increasing AOA, as summarized in Table 5.1. This change in the LSB location with AOA alters the BL behaviour at the TE, as shown in Figure 5.4, and should have a corresponding alteration of the tonal aeroacoustic noise generated at the TE.

The 3° AOA acoustic spectra predicted by the FW-H acoustic analogy is shown in Figure 6.3(a) in comparison to the experimentally measured spectra [49]. The simulation predicts a dominant tone at 3.01 kHz with a SPL of 79.0 dB in comparison to the experimental tone at 3.36 kHz at a SPL of 71.2 dB. The SPL of the tone and the overall broadband noise is in agreement with the experimental SPL, and there is a difference of 0.35 kHz between the predicted and measured tone frequency. The predicted tone frequency is in agreement with the K-H roll frequency detected in the suction side BL in Fig. 5.15, and therefore the same K-H roll mechanism identified in the 1° AOA simulations is responsible for the tonal TE noise production at 3° AOA.

The tonal noise source is visualized in Figure 6.3(b) where a K-H roll with low gauge pressure and high velocity magnitude is located from $x/c = 0.925$ to the TE. The K-H roll positioning relative to the TE resembles the 1° AOA contours in Figure 6.1(b) and time (ii) in Figure 5.6. In Section 6.1.2, this K-H roll positioning was identified as being after the high pressure recovery at the TE and before the formation of the new low pressure

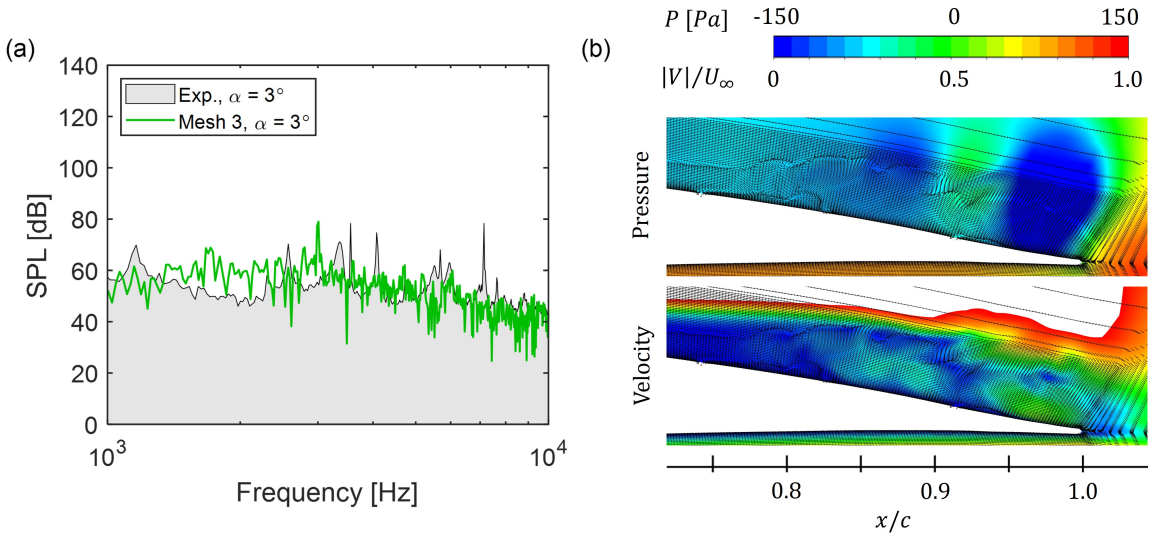


Figure 6.3: (a) Acoustic SPL spectra compared with experimental measurements [49] and (b) TE gauge pressure and velocity magnitude contours overlaid with flow direction vectors for 3° AOA Mesh 3

counter-rotating vortex from the pressure side. The 3° AOA contours are also created at the same instant in time as the Mesh 3 Q-criterion iso-surface from Figure 5.4, which shows that the K-H roll has a high spanwise coherence at the TE. The magnitude squared coherence of the BL pressure at 3° AOA in Figure 5.16(b) confirms the consistency with respect to time of the high spanwise coherence of the K-H rolls at the TE, with only a marginally lower coherence at the TE when compared to 1° AOA.

The gauge pressure magnitude and spanwise coherence of the K-H rolls at the TE for 1° AOA and 3° AOA are very similar, however the SPL magnitude of the predicted tone at 3° AOA is lower than the 1° AOA 86.6 dB tone. This difference can be explained due to the increased spanwise breakdown of the K-H rolls at 3° AOA which creates random pressure and velocity fluctuations and marginally decreases the spanwise coherence at the airfoil TE. A comparison of the U_s spectra in Figure 5.15 at the TE shows that the amplitude of the 3° AOA U_s fluctuations at 3.01 kHz is a similar magnitude to the 1° AOA instability at 3.47 kHz while 3° AOA has higher amplitude U_s fluctuations across the entire broadband frequency range. A comparison of 0.01 s of the acoustic pressure signals is shown in Figure 6.4 with a low pass filter applied to remove frequencies greater than 10 kHz to isolate the desired tonal frequency range. The introduction of additional frequencies can be seen in the predicted acoustic pressure signals shown in Figure 6.4(a) and 6.4(b), where 3° AOA

has periods of time with a higher amplitude pressure fluctuation at a similar frequency to 1° AOA and at other times there are lower amplitude fluctuations that include higher frequency components.

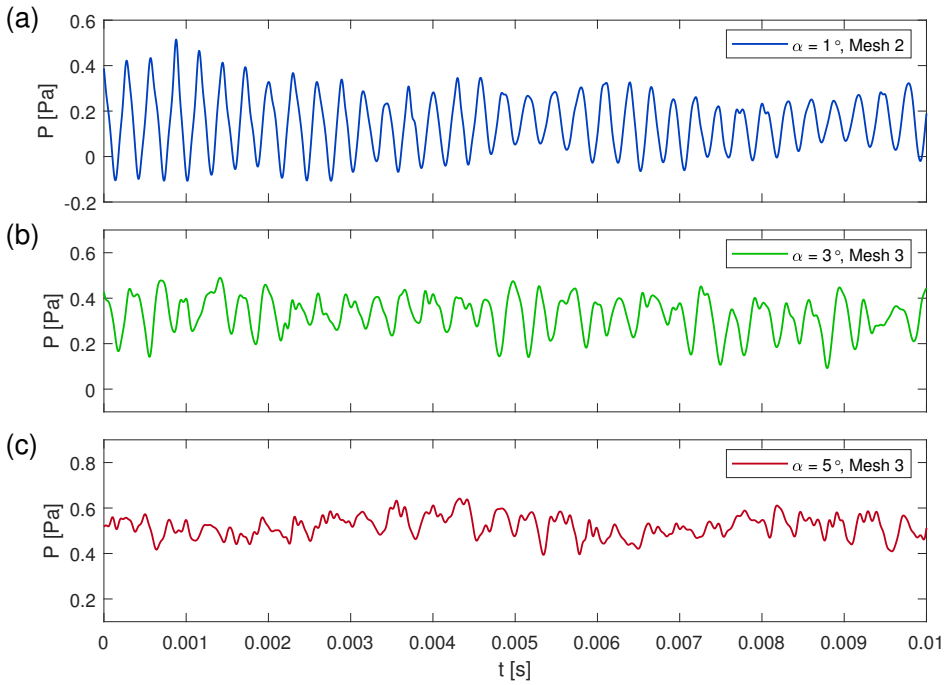


Figure 6.4: Acoustic pressure signals at the receiver location for a sample $0.01s$ at (a) 1° AOA (b) 3° AOA and (c) 5° AOA

The 5° AOA acoustic spectra predicted using FW-H is shown in Figure 6.5(a) in comparison with the experimental spectra [49]. The experimental results identified a dominant tone of 95 dB measured at a frequency of 3.34 kHz and the simulated spectra predicts broadband noise with low SPL tones of 65.4 dB at 2.65 kHz and 62.2 dB at 3.20 kHz. The BL spectra for 5° AOA in Figure 5.15 showed that the K-H rolls form at a frequency of 3.20 kHz and that lower frequency behaviours are present in the T-S waves at the airfoil LE which could be responsible for the elevated SPL at 2.65 kHz.

At 5° AOA there is a time-averaged reattachment of the LSB at $x/c = 0.90$ which indicates that the BL has transitioned to a turbulent BL although there are coherent structures in the reattached BL at the TE which are the remnants of the broken down K-H rolls. The pressure and velocity contours in Figure 6.5(b) show low pressure associated with the K-H rolls while the velocity magnitude and direction shows that there is the

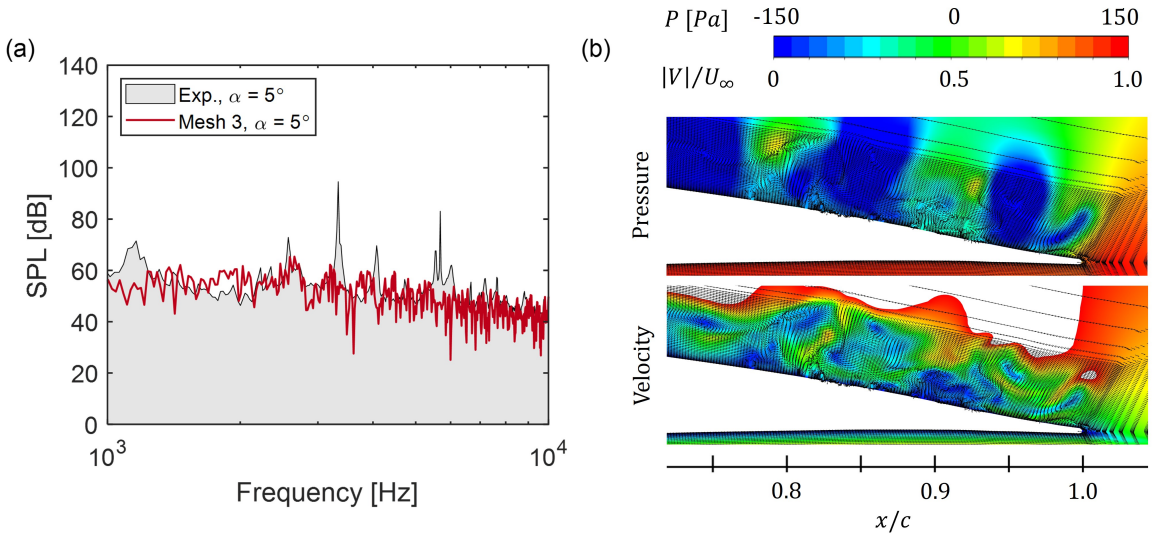


Figure 6.5: (a) Acoustic SPL spectra compared with experimental measurements [49] and (b) TE gauge pressure and velocity magnitude contours overlaid with flow direction vectors for 5° AOA Mesh 3

breakdown and mixing of multiple vortical structures. As with the other AOAs, these contours correspond to the same instant of the Q-criterion iso-surface for Mesh 3 in Figure 5.4, which shows that the broken down K-H roll at the TE maintains a high spanwise coherence. However the magnitude squared coherence of the pressure at the TE in Figure 5.16(c) shows that over the measured signal length of 0.02 s the coherence at the TE drops to $\gamma^2 = 0.3$, indicating that a high level of K-H roll breakdown occurs for the majority of time for the 0.02 s signal. Additionally, the TE spectra in Figure 5.15 is broadband with only a minor increase in U_s amplitude at the K-H roll frequency of 3.20 kHz. Therefore the majority of the time, the K-H roll breakdown has reduced the spanwise coherence at the airfoil TE and the remnants of the K-H rolls pass the TE at an irregular frequency. Only for short periods of time do the broken down K-H rolls continue to have a high spanwise coherence at the TE as is shown in Figure 5.4 and this is why the K-H roll frequency of 3.20 kHz is detected at a low SPL in the acoustic spectra.

The inconsistency of the K-H roll breakdown at the airfoil TE for 5° AOA was explored in Sections 5.4.1 and 5.4.2, where the LSB pressure feedback was found to occur sporadically. When the LSB feedback did occur, the high U_s and gauge pressure fluctuations of the K-H rolls were present after the time-averaged BL reattachment location, as was shown in Figure 5.10. The LSB feedback is a possible explanation for the high spanwise coherence

of the K-H roll at the TE in Figure 5.4 and the low pressure seen at $x/c = 0.95$ in Figure 6.5(b). The spectral analysis of the BL behaviour in Section 5.5 indicates that the LSB feedback does not occur frequently at this AOA and that the majority of the simulated time has K-H roll breakdown in advance of the TE as is seen in Figure 5.9.

The experimental spectrum in Figure 6.5(a) predicts a dominant tone at 5° AOA at a frequency similar to the simulated K-H roll frequency which indicates that the experimental BL has K-H rolls with high spanwise coherence consistently present at the TE. Based on the findings of the simulation, this would require the consistent presence of the LSB pressure feedback to have the K-H rolls survive after the time-averaged BL reattachment location. The possible reasons for the inconsistent LSB pressure feedback in the 5° AOA simulations were discussed at the end of Section 5.4.3. As has been previously mentioned, the incompressible simulation method does not account for the effects of the TE acoustic feedback (see Section 3.2.1) which could further amplify the velocity and pressure fluctuations of the K-H rolls in a similar manner to the LSB pressure feedback. The estimated TE acoustic feedback will be examined in Section 6.3 to determine whether constructive interference with the LSB feedback would further amplify the K-H rolls at 5° AOA thus increasing the tonal noise SPL.

The identification of intermittent K-H roll breakdown and appearance of the secondary tone completed in Section 6.1.3 was not possible at 3° and 5° AOA due to the previously discussed inconsistent frequency behaviour in the BL velocity signals and the acoustic signals. As is shown in Figure 6.4 there is no consistent frequency pattern present in the 3° or 5° signals to identify regions where the secondary tone is introduced to be able to complete the examination of the BL behaviour that was performed on the 1° AOA results.

6.2 Tone Frequency Trends

The K-H rolls that form on the suction side LSB have been established as the source of tonal noise for the SD 7037 airfoil at a $Re = 4.1 \times 10^4$ for AOAs of 1° , 3° and 5°. The analysis in the previous section showed that there are K-H rolls with a high spanwise coherence at the TE for 1° and 3° AOA generating the synchronized pressure fluctuation at the TE necessary for tonal TE noise and there is reduced spanwise coherence at the TE for 5° AOA producing low SPL tones. The K-H roll frequency was shown to change with AOA in Section 5.5 which in turn caused a change in tone frequency with AOA and the increased K-H roll breakdown at higher AOAs resulted in a decreased tonal noise SPL with increasing AOA. This is in contrast to the experimental spectra [49] which maintains a consistent dominant tone frequency and measures a clearly identifiable dominant tone

across all AOAs. The simulated spectra are compared in Figure 6.6(a) alongside the experimental spectra in Figure 6.6(b) which are both shown for a narrow frequency range to emphasize the trends in the tonal noise. The dominant tonal frequencies and SPL are summarized in Table 6.1 along with the K-H roll frequencies identified using Figure 5.15.

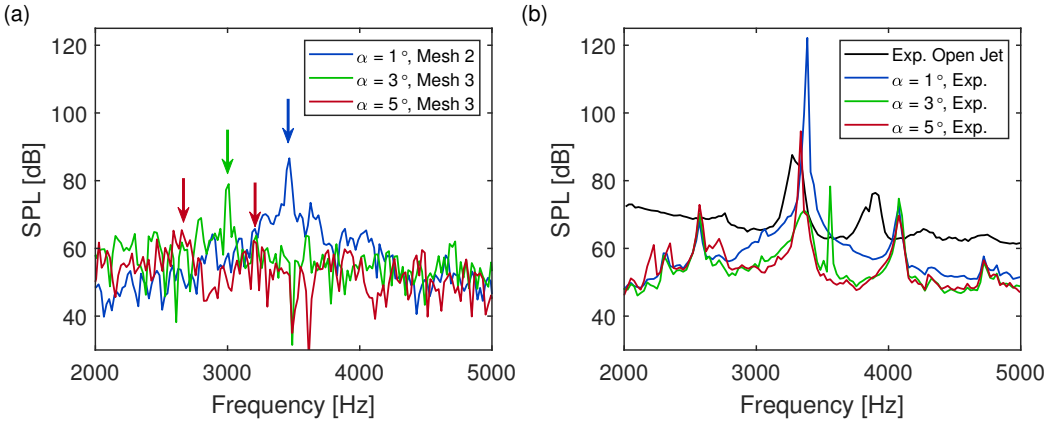


Figure 6.6: Acoustic SPL spectra for all AOAs from (a) simulations and (b) experimental measurements [49]

AOA	Simulated			Experimental	
	K-H roll f [kHz]	Tone f [kHz]	SPL [dB]	Tone f [kHz]	SPL [dB]
1°	3.45	3.47	86.6	3.39	122.2
3°	3.00	3.01	79.0	3.36	71.2
5°	3.20	2.65, 3.20	65.4, 62.2	3.34	94.6
Open Jet	- -	- -	- -	3.27	87.6

Table 6.1: Summary of the simulated K-H roll frequency (from Section 5.5) and the tone frequency and SPL for the simulated and experimental [49] acoustic spectra

The dominant frequency of the K-H rolls for the 1° and 3° AOA BL spectra results presented in Chapter 5 were determined to be independent of the mesh filter length after test simulations with incremental mesh refinements (see Section 3.2.6). Therefore the simulated frequency of the T-S waves in the laminar BL and the K-H rolls in the LSB are inherent to the development of the BL on the SD 7037 airfoil and the frequency shift of the tonal noise at 3° AOA is a result of this change in the transient BL development.

Since the simulation geometry is a free-stream flow while the experiment is completed in a hard-walled test section, it is reasonable to assume that tunnel effects such as resonance or acoustic reflections could alter the frequency behaviour in the airfoil BL. In this case, the free-stream flow of the simulation geometry is more representative of the flow over the blades of a SWT as well as the rotors and wings of other low Re flight applications. Therefore, the tunnel effects should not be included in the simulation and yet an understanding of the alteration of tone frequency due to tunnel effects is necessary to properly validate the aeroacoustic prediction generated by the FW-H acoustic analogy.

The effects of resonance and acoustic reflection in the test section were addressed during the original experiments [49] through the completion of a test case in an open jet wind tunnel, which removes some of the reflection and installation effects but still includes effects from the shear layer that forms at the edges of the open jet [78]. The spectrum from this test, which is from an unreported low AOA, is included in Figure 6.6(b) and the tone frequency and SPL are included in Table 6.1. There is a minimal lowering of the tonal frequency measured using the open jet tunnel which shows that the tunnel effects are capable of shifting the tonal noise frequency. However, it was not established whether the open jet tonal frequency changed with AOA to determine if the hard-walled wind tunnel is artificially fixing the frequency at a constant value through some undetermined effect.

Past experimental studies of tonal noise for an airfoil typically consists of establishing the trends of the dominant tones for a single AOA with changing Re, therefore it is difficult to establish the expected tonal patterns for a low Re airfoil across multiple AOAs. These studies are most commonly completed in anechoic wind tunnels, and therefore the effects of a hard walled test section and spurious acoustic feedback are removed and replaced by the lesser effect of the open jet shear layer. There are a handful of studies that report the tonal noise across multiple AOAs for the NACA 0012 airfoil. To provide a valid comparison to the SD 7037 airfoil, only NACA 0012 data for modest Re are considered as the tonal noise source is dominated by the suction side LSB and does not produce the multiple tones that create the ladder structure seen at higher Re, as is discussed in Section 2.3.4. The spectra and dominant tone trends published by Probsting *et al.* [54] show the NACA 0012 dominant tone frequency trends for 0°, 1°, 2° and 4° AOA for a Re range from 3×10^4 to 2.3×10^5 using an anechoic wind tunnel. When focusing on the dominant tones for 0° to 2° AOA for the modest Re range of $Re < 6 \times 10^4$, the suction side LSB produces a single dominant tone and the frequency of the tone decreases with increasing AOA. This trend is in agreement with the simulated tones for the SD 7037 airfoil and is evidence that the wind tunnel used in the experiments by Tam [49] does have an effect on the tone frequency.

It is possible that without tunnel effects, the 5° AOA spectrum should consist of the multiple tones seen in Figure 6.6(a) rather than the single dominant tone at 5° AOA in

Figure 6.6(b). The 4° AOA spectra reported by Probsting *et al.* [54] for the same low Re range discussed above consisted of several tones over a narrow frequency range with the dominant tone often occurring at a frequency between the single dominant tones for 1° and 2° AOA. This follows the same pattern of the simulated SD 7037 spectrum at 5° AOA, where multiple low SPL tones appear in the same frequency range as the single tones in the 1° and 3° AOA spectra in Figure 6.6(a).

Nash *et al.* [118] completed experiments with the NACA 0012 airfoil in a quasi-anechoic tunnel at 2° and 3° AOA which showed sporadic variation of dominant tone frequency by approximately 0.5 kHz for Re ranging from 5×10^5 to the minimum tested Re of 2×10^5. Tests completed by Nash *et al.* in the same wind tunnel prior to the quasi-anechoic modifications found that the original hard-walled test section generated Parker β mode resonance that resulted in a constant tone frequency for the same Re range. This could provide an explanation for the consistent tone frequency in the hard-walled test section of the SD 7037 experiments completed by Tam [49]. The SD 7037 experimental setup was designed to eliminate this type of hard-walled tunnel resonance [49, 107] however it was speculated that a different unidentified resonance type may be present due to the consistency of the tone frequency with increasing AOA [49].

In the absence of tunnel resonance, it stands to reason that K-H roll frequency that develops in the LSB should differ with AOA due to the change of the BL development at LE of the airfoil. Section 3.2.6 shows that the pressure gradient and flow acceleration at the LE varies significantly with AOA which would alter the development of the laminar BL, as described in Section 2.1.3. The K-H roll frequency has been shown to be dependent on the frequency of the T-S waves that develop before laminar BL separation [6], as was discussed in Section 5.5, and the frequency of the T-S waves is dependent on the stability of the BL profile [3]. The change in the K-H roll frequency and tone frequency with AOA summarized in Table 6.1 can be assumed to be due to the altered development of the laminar BL and therefore the tone frequencies are correct for the free-stream flow condition used in the simulations.

6.3 Acoustic Feedback Loop

The tonal TE noise predictions for the SD 7037 airfoil were generated using aerodynamic data from incompressible LES simulations which omit the effect of acoustic feedback since the acoustic waves emitted from the sharp TE require compressibility to propagate. The acoustic feedback loop between the airfoil TE and the upstream laminar BL is described in Section 2.3.4 where the phase alignment of the pressure fluctuation of the acoustic waves

with the BL instabilities in the laminar BL amplifies the velocity fluctuations of T-S waves at a specific frequency. These T-S waves then propagate downstream and grow into larger coherent structures, such as the K-H rolls that form in the LSB, which then generate tonal TE noise at the feedback frequency. The amplification of the K-H roll pressure and velocity amplitudes due to feedback has already been discussed in the simulated results in Section 5.4 where the LSB pressure feedback was shown to be caused by the touchdown of the K-H rolls in the LSB. The intermittent feedback at 5° AOA showed that the feedback process altered the T-S wave development in both the laminar BL and the reverse flow region of the LSB, which in turn resulted in the amplification of the K-H rolls. An estimation of the effect of the TE acoustic feedback on the laminar BL for the SD 7037 airfoil therefore requires an interference calculation with the LSB feedback already present in the laminar BL. The method of this interference calculation is explained in Section 6.3.1, which uses a modified version of the theoretical method proposed by Kingan and Pearse [67] introduced in Section 2.3.4. The estimation of this feedback interference is presented first using the simulated and then using the experimental tone frequencies in Sections 6.3.2 and 6.3.3, respectively.

In Section 6.1.2 the analysis of the 1° AOA simulated results showed that the 3.4 kHz tone is caused by the low pressure K-H rolls passing the TE, while Section 6.1.3 showed that the 4.1 kHz tone was caused by the intermittent spanwise breakdown of the K-H rolls. The K-H rolls develop at a frequency dependent on the T-S wave frequency in the laminar BL [6] and the T-S waves are the BL instability that is altered by the acoustic feedback. Therefore the tone associated with the dominant K-H roll frequency, as summarized for the simulations and experiments in Table 6.1, will be the focus of the TE feedback analysis for the SD 7037 airfoil simulations.

Typically the analysis of the TE acoustic feedback loop includes discussion of the ladder structure of the dominant tones, which is described in Section 2.3.4. The ladder structure involves more complex feedback from the pressure or suction side LSB and generates multiple tones clustered in a narrow frequency range. The trends in the published data for ladder structures show that airfoils operating at modest Re of less than 1×10^5 [53, 54, 56] or with cambered profiles [56, 58] do not exhibit a strong ladder structure and typically have one to two dominant tones. The acoustic spectra measured experimentally for the SD 7037 airfoil [49] also follows this trend and produces the dominant tones at 3.4 kHz and 4.1 kHz and therefore the discussion of the ladder structure for the SD 7037 airfoil at the current Re is not relevant to the acoustic feedback analysis.

6.3.1 TE Feedback and LSB Feedback

The combined effect of the TE acoustic feedback and the LSB pressure feedback is illustrated in Figure 6.7 which is a modified version of the transient LSB development diagrams shown in Figures 5.5 and 5.7. The upstream propagation of the LSB pressure feedback caused by the K-H roll touchdown is shown in red, with the location x_F labelled as the start of the upstream propagation in the BL. The TE acoustic feedback is shown in green, where the source of the pressure fluctuations is caused by the interaction of the K-H rolls with the TE, as is described in Section 6.1.2. Upstream of x_F, the combined effect of the TE feedback and the LSB feedback alter the development of the reverse flow region of the LSB and the laminar BL through the feedback process described in Section 5.4.2. Both feedback behaviours occur at the K-H roll frequency and propagate upstream at the speed of sound, c, minus the average U_s, $\bar{U}_s$, in the BL. Therefore the phase difference between the two feedback sources upstream of x_F will remain constant. Due to the constant interference upstream of x_F, the interference between the TE and LSB feedback will be estimated at the location of x_F for each AOA.

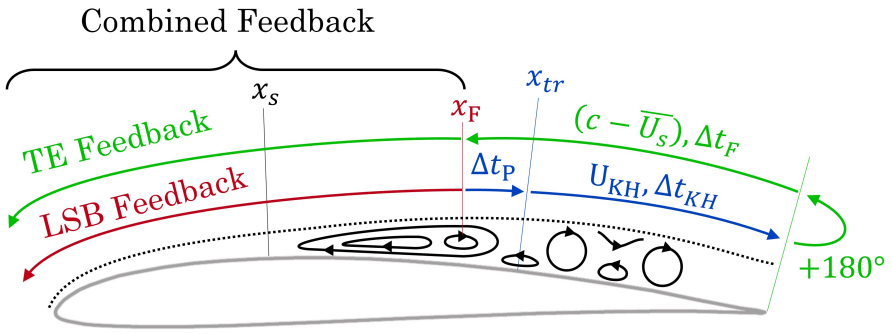


Figure 6.7: Diagram for interference calculation of LSB feedback and TE feedback

When calculating the phase difference between the LSB feedback and the TE feedback, the TE feedback loop begins at x_F with the downstream propagation of pressure fluctuations shown in blue in Figure 6.7. These downstream propagating behaviours include the K-H roll pinch-off from the reverse flow region of the LSB, which was explained for 1° AOA in Section 5.3.1, and the downstream propagation of the fully formed K-H rolls. At the TE, the K-H roll produces tonal noise, as was described in Section 6.1.2, and the pressure wave propagates upstream at $c - \bar{U}_s$ to x_F to complete the feedback loop which is shown in green in Figure 6.7.

The final effect to consider in the TE acoustic feedback loop is that the generation of tonal noise at the TE converts the negative aerodynamic pressure fluctuation in the BL to a positive acoustic pressure fluctuation, and vice versa. This sign change of the pressure fluctuation is represented in Figure 6.7 as a 180° phase change, which is the method for applying pressure conversion in theoretical feedback calculations [67]. The change of the sign of the pressure fluctuation at the TE is due to the dipole source that develops due to the interaction of the aerodynamic forces with the airfoil surface. In reaction to the pressure fluctuations of the coherent flow structures passing the TE, the dipole causes opposing acoustic pressure fluctuations on the suction side and pressure side of the TE. The details of the dipole source, also called loading noise, are described in Section 2.4.2. For the 1° AOA simulation, receiver locations were added above and below the airfoil at a distance of $1c$ and the FW-H acoustic analogy was applied to confirm the phase change of the acoustic wave on the suction side of the airfoil (i.e. the orientation of the dipole). When the aerodynamic pressure at the TE had a negative fluctuation associated with the K-H roll core passing the TE, the generated acoustic wave on the suction side of the airfoil had a positive fluctuation. This confirms the 180° phase change between the pressure fluctuations at the TE and the pressure fluctuation of the acoustic wave travelling upstream on the suction side of the airfoil.

Now that the acoustic feedback loop has been established, the necessary values for determining the total phase difference between the LSB feedback and acoustic feedback are determined using the simulated results from Chapter 5. The values of these feedback related parameters, which are labelled in Figure 6.7, are summarized for each AOA in Table 6.2 and were determined from the analysis of Figures 5.10, 5.13 and 5.14 in Section 5.4. The first variable is the average propagation time, Δt_P, of the K-H roll during the K-H roll pinch off process between x_F and the time-averaged BL transition location, x_{tr}. The x_F and x_{tr} values were rounded to the nearest $0.05c$ because the x/c spacing of the pressure and U_s signals in Figures 5.10, 5.13 and 5.14 limited the calculation of the propagation times and velocities to those chordwise locations. At each chordwise location, the temporal resolution is equivalent to the simulation time step size, which is 2×10^{-6} s for 1° AOA and 4×10^{-6} s for 3° and 5° AOA, as is included in Table 3.2. After x_{tr}, the fully-formed K-H rolls propagate downstream with a velocity of U_{KH} and a time to propagate to the airfoil TE of Δt_{KH}.

For each AOA, the $\bar{U_s}$ was calculated by averaging the local U_s between x_F and the TE using the U_s signals at the wall-normal height of $4 \times 10^{-3}c$ described in Section 5.4. These values are reported in Table 6.2 with the corresponding propagation time of the acoustic wave, Δt_F. The total time of the feedback loop, Δt, is also reported in Table 6.2, and is the summation of Δt_P, Δt_{KH} and Δt_F.

Feedback Variable	Angle of Attack		
	1°	3°	5°
x_F/c	0.85	0.70	0.50
Δt_P [s]	2.6×10^{-4}	4.4×10^{-4}	2.3×10^{-4}
x_{tr}/c	0.95	0.85	0.65
U_{KH} [m/s]	13.0	10.9	11.9
Δt_{KH} [s]	9.9×10^{-5}	3.6×10^{-4}	7.6×10^{-4}
U_s [m/s]	-1.4	-2.0	-0.5
Δt_F [s]	1.1×10^{-5}	2.2×10^{-5}	3.8×10^{-5}
Δt [s]	3.7×10^{-4}	8.2×10^{-4}	1.0×10^{-3}

Table 6.2: Summary of the parameters used for the pressure feedback calculation. Variables defined in Figure 6.7

6.3.2 Simulated Feedback Interference

The first estimation of the interference between the LSB feedback and the TE acoustic feedback replicates the feedback interference that would occur if the LES simulations were completed in a compressible form to resolve the propagation of sound waves from the TE. The downstream propagation behaviours shown in blue in Figure 6.7 are simulated by the LES model and the feedback process shown in green in Figure 6.7 is estimated through the upstream propagation of the BL pressure fluctuations at the TE. The pressure fluctuations at the TE were collected at $x/c = 0.99$ at the wall-normal height of $4 \times 10^{-3}c$ (0.1 mm) and had a bandpass filter applied from 1 kHz to 10 kHz to approximate the P' fluctuation as described in Section 5.4. The phase change of 180° is applied by multiplying the pressure signal by -1 and the propagation time from the TE to x_F is accounted for by adding a time lag of Δt_F specified for each AOA in Table 6.2.

The interference between the LSB pressure feedback and the TE acoustic feedback is shown in Figure 6.8 where the level of constructive or destructive interference is determined by the phase difference between these signals at x_F. The LSB feedback signal is the BL pressure collected at x_F at the wall-normal height of $4 \times 10^{-3}c$ in the LES simulation and shows the pressure fluctuation of the LSB feedback, and the calculated TE feedback signal is plotted on the secondary y-axis. The amplitude of the pressure feedback from the TE is not altered to adjust for the conversion to acoustic pressure, but it can be assumed that the pressure amplitude of the two feedback signals will be of a similar order of magnitude since both originate from the same source of the K-H rolls.

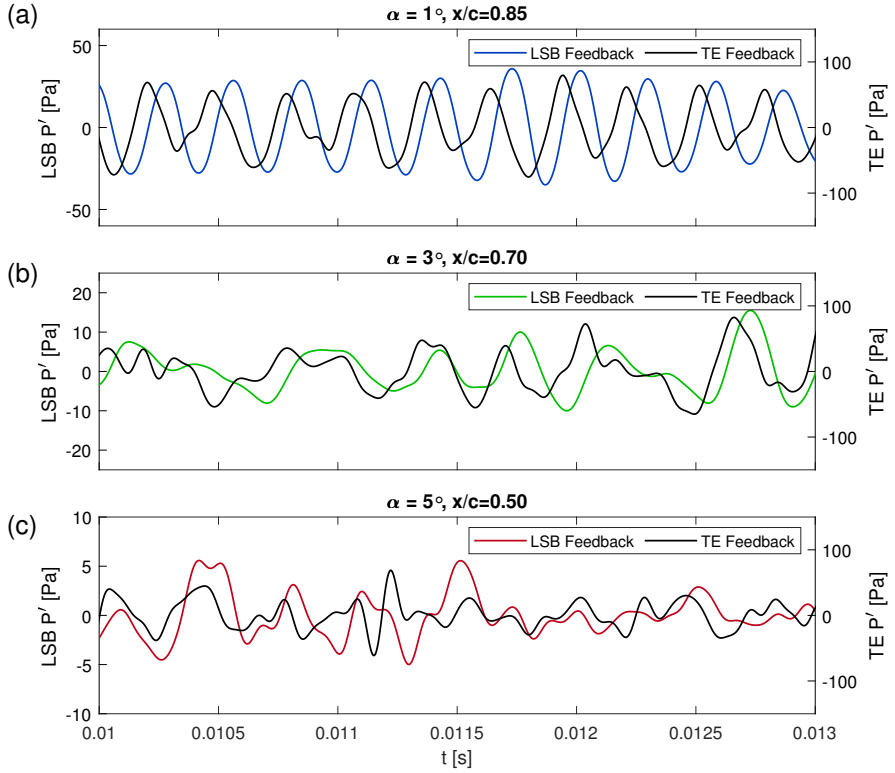


Figure 6.8: LSB feedback pressure signal with estimated TE acoustic pressure feedback for (a) 1° AOA at $x/c = 0.85$ (b) 3° AOA at $x/c = 0.70$ (c) 5° AOA at $x/c = 0.50$

For the 1° AOA interference in Figure 6.8(a), the time difference between the peaks of the pressure signals is an average of 7.6×10^{-5} s and is a phase shift of -26% of the period at the dominant tone frequency of 3.47 kHz (see Table 6.1). This results in a predicted constructive interference at 1° AOA and therefore the inclusion of the TE acoustic feedback would be expected to increase the SPL of the tonal noise. The experimental acoustic measurements for the SD 7037 airfoil [49] found that the highest SPL tone occurs at 1° AOA, with a significant increase in SPL in comparison to the tones at 0° and 2° AOA. From 0° to 2° AOA there is similar placement of the LSB relative to the TE [4] and therefore similar magnitude K-H rolls should be present at the TE with a similar amount of LSB pressure feedback. If only the TE acoustic feedback was present in the experiments, it would be expected that 0° to 2° AOA would all have a similar amplification of the dominant tone SPL due to the similarities of the K-H roll development at the TE. However, the amplification of the tonal noise SPL at 1° AOA in comparison to 0° and 2°

AOA indicates that the 1° AOA has a stronger feedback effect occurring. This trend in tonal noise SPL over a narrow range of AOAs is evidence of the interference of two separate feedback mechanisms and is also consistent with the predicted constructive interference of the LSB pressure feedback and the TE acoustic feedback for the simulated results at 1° AOA shown in Figure 6.8(a).

It is difficult to determine the feedback interference for the 3° and 5° AOA results shown in Figure 6.8(b) and (c) due to the inconsistent frequency behaviour in the BL, as was shown in Section 5.4. Further investigation of the feedback interference at all simulated AOAs is completed in the next section using an idealized calculation of the acoustic feedback loop at a single frequency.

6.3.3 Interference at Experimental Frequencies

In Section 6.2, the free-stream flow applied in the simulations was found to cause different trends in the frequencies of the dominant tone with changing AOA in comparison to the experimental acoustic spectra collected in the hard-walled wind tunnel test section. The frequency of the tonal noise is relevant to the interference of the LSB feedback and the TE acoustic feedback since it changes the period of the fluctuation for the LSB feedback at x_F, while the total travel time, $\Delta t = \Delta t_P + \Delta t_{KH} + \Delta t_F$, of the TE acoustic feedback process remains constant. This can alter whether the interference at x_F is constructive or destructive and therefore to be able to validate the expected feedback interference against the tonal noise SPL trends in experimental data for 3° and 5° AOA, the interference must be calculated at the experimental tone frequencies in Table 6.1.

For each AOA, a simple sinusoidal pressure fluctuation is created at the experimental tonal noise frequency to represent fluctuation of the LSB pressure feedback at x_F. Then the total phase change of the acoustic feedback signal at x_F is estimated using the process shown in Figure 6.7 by including the travel time of the downstream propagation shown in blue, the 180° phase change at the TE and the upstream propagation shown in green. The travel time values and the total Δt used for each AOA are summarized in Table 6.2. The resulting idealized interference of the feedback sources at the experimental frequency is shown in Figure 6.9 where the delay in the start time of the TE feedback signal shows the Δt of the combined downstream propagation of the K-H rolls and the upstream propagation of the acoustic pressure fluctuation. The resulting phase shift between the peaks of the LSB feedback and the acoustic TE feedback is -24% of the signal period for 1° AOA, +25% for 3° AOA and -7% for 5° AOA. The 1° AOA phase shift of -25% is in agreement with the -26% shift seen in Figure 6.8(a) due to the similarity of the simulated and experimental tone frequencies.

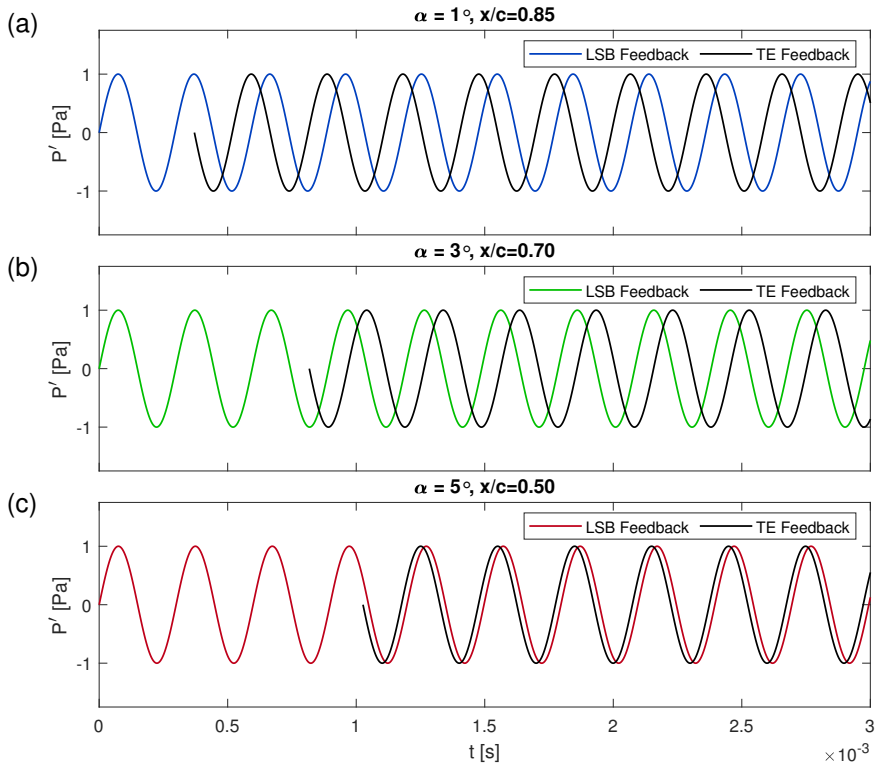


Figure 6.9: Idealized calculation of the LSB feedback pressure signal with the estimated phase change and time delay of the acoustic feedback from the TE for (a) 1° AOA at $x/c = 0.85$ (b) 3° AOA at $x/c = 0.70$ (c) 5° AOA at $x/c = 0.50$

At 3° AOA, there is a similar phase shift of 25% however the phase shift is positive rather than negative and Δt is over double that of 1° AOA. This shows how sensitive the feedback process is to the positioning of the LSB relative to the TE, since at 3° AOA the x_{tr} is $0.1c$ upstream of the 1° AOA location and x_F has a similar $0.15c$ upstream shift in location. Since there is inconsistency in the frequency of the 3° AOA simulation, as is shown in Figure 6.8(b), there is uncertainty in the downstream propagation times Δt_P and Δt_{KH} which were determined from the average behaviour in Figure 5.14. Small changes in either propagation time could easily change the feedback interference from constructive to destructive due to the high frequency of the dominant tone. The same uncertainty in the propagation times is present for the 5° interference in Figure 6.9(c), which predicts nearly complete constructive interference of the feedback sources.

The trends in the SPL of the experimental tones with AOA show evidence of destruc-

tive interference since the dominant tones at 1°, 3° and 5° AOA were 122.2 dB, 71.2 dB and 94.6 dB, respectively, as is shown in Figure 6.6(b) and Table 6.1. In the absence of destructive feedback, it would be expected that the dominant tone associated with the K-H roll frequency would decrease in SPL with increasing AOA due to the increased breakdown of the K-H rolls at the TE. This was the trend identified in the tonal noise SPL for the simulated results shown in Figure 6.6(a) and Table 6.1, where the simulations were only capturing the effect of the LSB pressure feedback and therefore there was no feedback interference to alter the tonal noise SPL trend. The destructive interference of the two pressure feedback sources at the experimental tone frequency provides a clear explanation for the low SPL of the experimental 3° AOA tone. The presence of the LSB pressure feedback and its interference with the TE acoustic feedback requires future investigation which will be outlined in Section 8.2.

6.4 Summary

This chapter presented the validation and analysis of the tonal aeroacoustic noise generated by the TE of the SD 7037 airfoil at a modest Re of 4.1×10^4. The application of the FW-H acoustic analogy to the incompressible wall-resolved LES simulation results from Chapter 5 resulted in a successful prediction of the tonal noise generated by a cambered low Re airfoil with an elongated LSB. Prior simulations to predict tonal aeroacoustic noise for low Re airfoils have been completed with a short LSB located near the LE or with a LSB that reattaches a short distance upstream of the TE. In the simulations in this chapter, there is a transitional separated BL at the TE for 1° and 3° AOA and an elongated LSB is in close proximity to the TE at 5° AOA. The elongated LSB length and direct interaction of the K-H rolls with the TE was complex to simulate and required the detailed mesh refinements of Mesh 2 and Mesh 3 in Section 3.2.6 in order to simulate the correct transient development of the transition structures in the BL.

The prediction of the tonal airfoil self-noise for the SD 7037 airfoil at 1° AOA was found to be in excellent agreement with the validating experimental acoustic spectra, with accurate prediction of the dominant tone frequency, the broadband hump around the dominant tone and broadband noise SPL. The source of the tonal noise was confirmed to be the interaction of the K-H rolls with the pressure side BL at the airfoil TE through a comparison with the detailed transient analysis of the K-H roll formation in Section 5.3.1. Analysis of short segments of the predicted acoustic signal also proved the presence of an intermittent secondary tone that was found to occur during the early spanwise breakdown of the K-H rolls. The 1° AOA simulation was therefore able to predict and identify the source of both

dominant tones measured in the validating experimental data. This showed the effectiveness of the chosen LES and FW-H method in identifying problematic aeroacoustic tonal noise and the aerodynamic source of the tonal noise which could then be used to inform design improvements for the low Re operation of a SWT.

The simulations at 3° and 5° AOA were able to predict weak tonal noise behaviour that was at a frequency near to the experimentally identified tonal noise. The analysis of the trends in the tonal noise frequency in comparison with the trends in the experimental measurements highlights the importance of considering the effect of the experimental wind tunnel setup on the acoustic measurements. In the case of the SD 7037 airfoil, the experimental tonal noise frequency remained constant with AOA while the simulations in a free-stream flow condition had a changing dominant tone frequency with AOA. This is important to keep in mind when validating the tonal noise prediction from the FW-H acoustic analogy while also recognizing that the transient behaviour in the LES simulation has been found to be sensitive to the filter length in the airfoil BL, as described in Section 3.2.6.

The amplification of tonal noise SPL was investigated through calculation of the interference between the LSB pressure feedback identified in Section 5.4 and an estimation of the TE acoustic feedback. A prediction of the interference between the simulated LSB pressure feedback and the calculated TE acoustic feedback showed that the 1° and 5° AOA have constructive interference of the feedback sources and that 3° AOA likely has destructive interference at the experimental tonal noise frequency. The analysis of the simulated LSB pressure feedback and estimated TE acoustic feedback shows that the interference of these two feedback mechanisms could have a significant impact on the tonal noise produced by an airfoil. The possible future investigation of this behaviour is discussed in Section 8.2.

This chapter completes the aerodynamic and aeroacoustic analysis of the LES and FW-H simulation of the SD 7037 airfoil at modest Re to study the role of the LSB in the generation of tonal aeroacoustic noise. The analysis fulfils objectives #2, #3 and #5 by accurately predicting the tonal noise generated by the SD 7037 airfoil and identifying the source of the tonal noise as the interaction of the K-H rolls with the pressure side BL at the airfoil TE. The interference between the LSB pressure feedback identified in Chapter 5 and the estimation of the TE acoustic feedback clearly illustrates the importance of the LSB in the amplification of the tonal noise SPL. The improved understanding of the complex role of the LSB in tonal TE noise generation provides invaluable information for the future aerodynamic and aeroacoustic design of low Re airfoils used for SWTs.

Chapter 7

Dynamic Stall Results[1]

This chapter presents the validated results of the unsteady Reynolds-averaged Navier-Stokes (URANS) simulations of dynamic stall for the SD 7037 and S833 airfoils operating at low Re with a laminar separation bubble (LSB) on the suction side of the airfoil. The approach and numerical method of the simulations is described in Sections 3.3 and 3.4 where a sinusoidal pitching motion is applied to replicate the dynamic stall process of small wind turbine (SWT) blades using the theory summarized in Section 2.5. The range of angles of attack (AOA) of the simulated pitching cycle is selected to produce deep dynamic stall behaviour which causes significant unsteady fluctuation of the aerodynamic loading and can lead to early fatigue failure of SWT blades. The SD 7037 airfoil is simulated at a pitching reduced frequency of $k = 0.08$ at a modest Reynolds number of $Re = 4.1 \times 10^4$, which is identical to the large eddy simulations (LES) results presented in Chapters 4 and 5. The S833 airfoil is simulated at a low Re of $Re = 1.7 \times 10^5$ and $k = 0.06$ and the simulation details for each airfoil are summarized in Table 3.3.

In this chapter, the validation and analysis of the deep dynamic stall simulations is focused on the role of the LSB in the prediction of the correct dynamic stall AOA and the aerodynamic load fluctuations at stall. The results and analysis reported in this chapter address the research objectives #4, #5 and #6 in Section 1.3 for the numerical prediction of dynamic stall for SWT blades operating at low Re with a LSB. The contents of this chapter have also been published in the peer-reviewed *AIAA Journal*[1].

[1]Published by Zilstra, A. and Johnson, D.A. (2024) Validated Dynamic Stall Simulation of Pitching Low Reynolds Number Airfoils. AIAA Journal, Vol. 62, No. 10, pp. 3700-3712, https://doi.org/10.2514/1.J063884

7.1 Static Validation

The simulation method described in Section 3.4 was first validated for a range of static AOAs to determine the ability of the $\gamma - Re_{\theta t}$ SST $k - \omega$ URANS model to predict the low Re BL and LSB. The theory of the BL transition process and the formation of the LSB due to the airfoil curvature is summarized in Section 2.1 and the theory of URANS methods is included in Section 2.2.2. The overall aerodynamic behaviour was assessed through the comparison of the simulated lift coefficient, C_L, and pressure coefficient, C_p, with experimental data from the studies summarized in Section 3.3. The SD 7037 static results are presented in Figure 7.1 and the validating experimental data was collected using particle image velocimetry (PIV) at the Re of 4.1×10^4 by Ghorbanishohrat [4] and Gharali and Johnson [103].

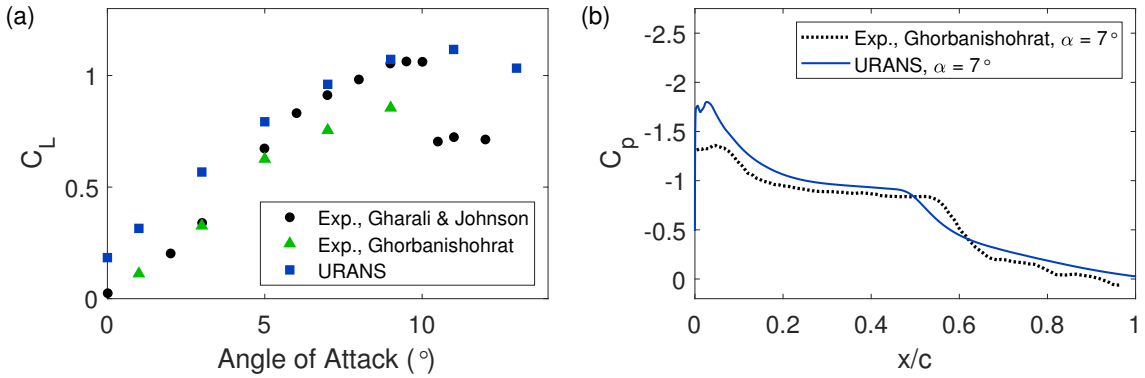


Figure 7.1: Static results for SD 7037 at $Re = 4.1 \times 10^4$ for (a) C_L plotted against experimental data by Gharali and Johnson [103] and Ghorbanishohrat [4] and (b) suction side pressure coefficient at AOA= 7° plotted against experimental data [4]

The average difference between the simulated and experimental [103] C_L results presented in Figure 7.1(a) is 0.16 ± 0.13, with better agreement at the high AOAs where the deep dynamic stall behaviour will occur in the dynamic case. Above 10° AOA, there is a discrepancy in the severity of stall with Gharali and Johnson measuring a greater loss in C_L than is predicted by the URANS model. For the Ghorbanishohrat data, the slope in the linear region of the C_L curve is in agreement with simulated results.

The pressure coefficient, C_p, is used to validate the accuracy of the BL simulation along the airfoil surface, including the prediction of a LSB. This is a particularly important parameter when it comes to investigating the behaviour leading to the deep dynamic stall

as the LSB bursting has been identified as a precursor to the LEV that causes stall at low Re [89,105]. As is described in Section 2.1.4, a C_p plot with a fully formed LSB will feature an indicative transition ramp [12], which begins with the levelling off of the C_p curve at the location of laminar separation followed by a sharp pressure recovery at reattachment. The C_p plot for the suction side (top) of the SD 7037 airfoil at 7° AOA in Figure 7.1(b) shows the successful simulation of the LSB identified experimentally by Ghorbanishohrat [4]. The selected URANS model is able to correctly predict the location of laminar BL separation, as seen by the agreement of the C_p gradient in the early stages of the transition ramp. In the selected AOA, the location of reattachment is at approximately 61% of the airfoil chord, c, which is earlier than the experimental location at approximately $0.67c$.

This difference in reattachment location is likely to occur since the separated BL is more sensitive to simulation parameters such as the inflow turbulence [119], where it is shown in Section 2.2.4 that a higher inflow turbulence will lead to earlier BL reattachment [9, 22, 32, 33]. In Section 5.2, the analysis of the LES simulations at 5° AOA found that early BL reattachment can also occur due to marginally insufficient sub-grid filter length in the separated BL which altered the prediction of the BL transition in the LSB and therefore a small numerical error in the prediction of the complex transient LSB formation can also lead to early BL reattachment. These errors will be accentuated in cases with an elongated LSB, which is the case for the SD 7037 airfoil at this modest Re. It should also be noted that the experimental suction peak measurements for the SD 7037 case are expected to be a lower magnitude than the simulated values due to the experimental method of C_p calculation [4], which has reduced accuracy near the LE due to low PIV resolution in comparison to the local BL thickness. The difference in the predicted C_p suction peak is discussed in Section 4.2 for the LES simulations of the SD 7037 airfoil. Even though there is a difference in magnitude for the first $0.1c$ in Figure 7.1(b), the average difference in C_p is 0.12 with a standard deviation of 0.08 and the maximum difference occurring at the LE with a value of 0.47.

The S833 C_L and C_p results are presented in Figure 7.2 and are validated against experimental data published by Samara and Johnson [113]. These experiments used differential pressure taps, meaning the C_p at each x/c location is a difference between a tap on the pressure side (bottom) and the suction side (top) of the airfoil. A comparison with the simulated results at a static AOA of 7° is shown in Figure 7.2(b) where the average difference in ΔC_p with the simulated values is 0.1 ± 0.06. During the validation process, it was found that the excellent agreement in ΔC_p did not lead to the same agreement with the experimental C_L results [113] shown as open circles in Figure 7.2(a). Since the validation of the dynamic cycle is heavily dependent on the C_L values, the decision was made to recalculate the C_L using the available ΔC_p data. This is presented as filled circles

in Figure 7.2(a), and results in an average C_L difference of 0.05 ± 0.03 compared to the simulated values, which is more consistent with the difference in the ΔC_p data. The S833 experimental C_L values used for the remainder of this chapter, including the dynamic case, are the recalculated values using the ΔC_p data [113].

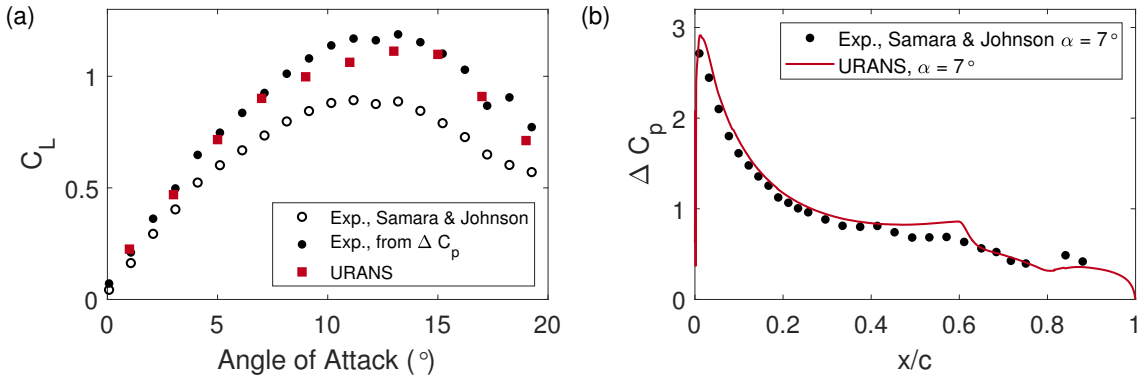


Figure 7.2: Static results for S833 at $Re = 1.7 \times 10^5$ for (a) C_L plotted against experimental data by Samara and Johnson [113] and C_L calculated from published ΔC_p data [113] and (b) ΔC_p at AOA= 7° plotted against experimental data [113]

The use of ΔC_p leads to difficulty in separating the development of the pressure side and suction side BLs. Examination of the simulated results identified a LSB on both the suction and pressure sides of the airfoil, with the location of the LSB on the suction side at x/c from 0.29 to 0.63 and at x/c from 0.58 to 0.88 for the pressure side. The location of the LSB on the suction side progresses upstream with increasing AOA whereas the pressure side LSB moves downstream with increasing AOA and is no longer present above 10° AOA. Therefore the pressure side LSB is not of concern during the high AOAs associated with dynamic stall for the S833 case, and focus will be placed on the suction side LSB for the remainder of this chapter.

Given the excellent agreement of the static results across a range of AOAs, particularly at the location of stall, there is confidence that the $\gamma - Re_{\theta t}$ SST $k-\omega$ model has sufficient accuracy in the prediction of the low Re BL and associated loading to proceed to the more complex dynamic simulation cases.

7.2 Deep Dynamic Stall

The dynamic stall simulation results are presented as C_L values throughout the sinusoidal pitching cycle, as is shown in Figure 2.12. The classic presentation of these results is to plot the C_L versus AOA, as this draws a direct comparison to the static C_L behaviour as a function of AOA in Figures 7.1(a) and 7.2(a). However, when examining deep dynamic stall, the stall behaviour is often compressed into a narrow range of AOA near the peak AOA of the pitching motion. This can obscure the stall behaviour and complicate the validation of the results, especially if the C_L during the pitch up and pitch down motions cross each other forming loops in the C_L versus AOA plot. Therefore, when examining deep dynamic stall, it is practical to also plot the C_L values with respect to time.

The results of the SD 7037 sinusoidal pitching case described in Section 3.4.1 are presented in Figure 7.3 and are validated against the experimental results [103] as well as previous URANS results by Gharali and Johnson [103]. The details of the sinusoidal pitching are summarized in Table 3.3. Figure 7.3(a) shows the C_L as a function of AOA and Figure 7.3(b) shows C_L as a function of non-dimensional time, t/T, where T is the period of the pitching cycle. The location of maximum pitching rate, ω_{max}, is labelled in both cycles, and Figure 7.3(b) has a vertical dashed line to indicate the maximum AOA of the cycle which corresponds to the initiation of the pitch down motion. In comparison to the static simulations, the dynamic C_L begins to exceed the static C_L at approximately 9° AOA. The average difference in C_L between the simulated results and the experimental data is 0.15 ± 0.09 and is similar to the C_L difference in the static results, showing that the dynamic motion is not adding additional error to the simulation. Overall the C_L trend throughout the pitching cycle is well replicated in the simulation, particularly the AOA of the lift peak that occurs before stall.

The lift peak at 18.6° AOA and subsequent drop in lift are associated with the formation and shedding of a large LEV, respectively [82], as is described in Section 2.5.2. After the bursting of the suction side LSB (labelled Burst in Figure 7.3), the BL is completely separated, leading to the roll up of the BL to form the LEV. The definition of the bursting of the LSB is provided in Section 2.5.3. The LEV resulted in a 79% increase in maximum C_L above the static value of 1.12 and a delay in the AOA of the maximum C_L by approximately 7° in comparison with the static results. After the LEV is shed, the C_L rapidly drops by 1.14 in comparison to the drop of 1.52 experimentally, confirming the presence of deep stall. Before reaching the maximum AOA in the pitching cycle, the C_L increases again due to the formation of a secondary LEV.

The accuracy of the prior URANS results by Gharali and Johnson [103] is high in comparison to URANS simulations by other researchers, and yet the current URANS

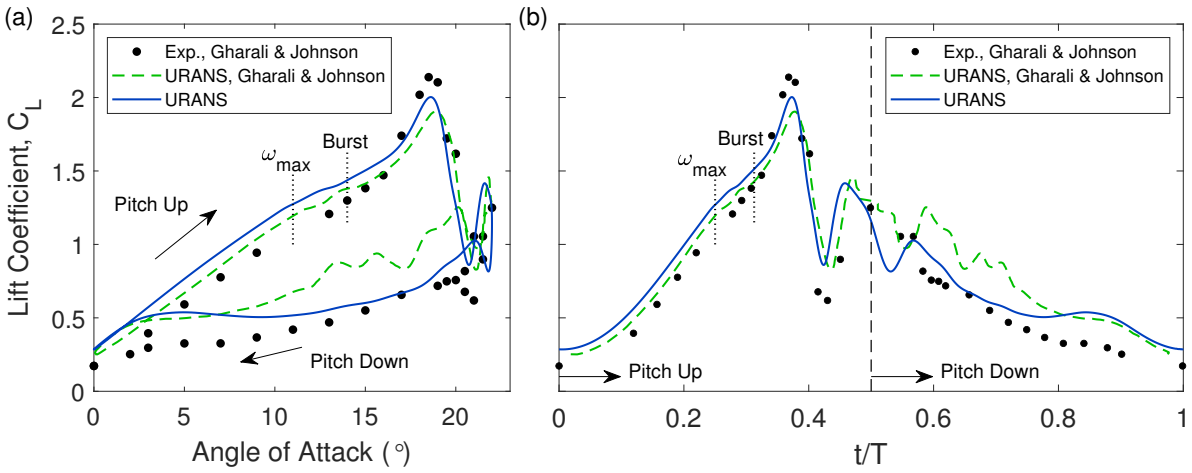


Figure 7.3: URANS predicted dynamic lift coefficient cycle for the SD 7037 airfoil at $Re = 4.1 \times 10^4$ and $k = 0.08$ compared with experimental [103] and URANS data [103] versus (a) AOA and (b) non-dimensional time t/T

results show some further improvements. Notably, the prediction of maximum C_L and its AOA is closer to the experimental results and the C_L magnitude through the pitch down motion is in better agreement. The simulation by Gharali and Johnson was completed using ANSYS Fluent, release 13, using the same numerical method as the current simulations and it is expected that improvements have been made in the software between release 13 and the release 19.2 used currently. A more likely factor for the improvement in the results is the mesh distribution in the airfoil BL. As is discussed in Section 3.4.2, the mesh distribution used for the current simulations was from a preliminary LES mesh that had the same near-wall distribution as Mesh 1 in Section 3.2.6 which was used to generate the LES results in Chapter 4. The near-wall distribution of Mesh 1 was refined using the attached BL criterion [17] where the mesh refinement extends further into the BL and produces a significant difference in the wall-normal mesh expansion in comparison to a traditional URANS mesh. This LES-quality mesh was shown to improve the accuracy of the simulation through the grid coarsening study presented in Section 3.4.3 where it was shown that the increased wall-normal density of the mesh in the laminar BL upstream of the LSB improved the prediction of the dynamic stall AOA. The effect of the LES-quality mesh on the prediction of the dynamic stall AOA is discussed further in Section 7.3.3.

The C_L results for the S833 dynamic pitching case are shown in comparison to the experimental results [113] in Figure 7.4(a) for C_L versus AOA and Figure 7.4(b) for C_L

versus t/T. As with the SD 7037 case, the location of ω_{max} and LSB bursting are labelled in both plots along with the vertical dashed line for location of maximum AOA in Figure 7.4(b). The experimental C_L values were calculated from the experimental ΔC_p [113] for the reasons explained in detail in Section 7.1. The simulated C_L values align well with the experimental results and the average difference in C_L is 0.24 ± 0.29, though the difference is increased when compared to the static simulation results. This pitching cycle causes deep dynamic stall to occur, with a LEV forming between the indicated burst location and the peak C_L followed by a rapid drop in C_L as the LEV is shed. For this cycle, the C_L begins to exceed the static lift at approximately 10° AOA, the maximum C_L is 84% higher than the static value of 1.0 and the delay in the peak C_L location is 6.2°.

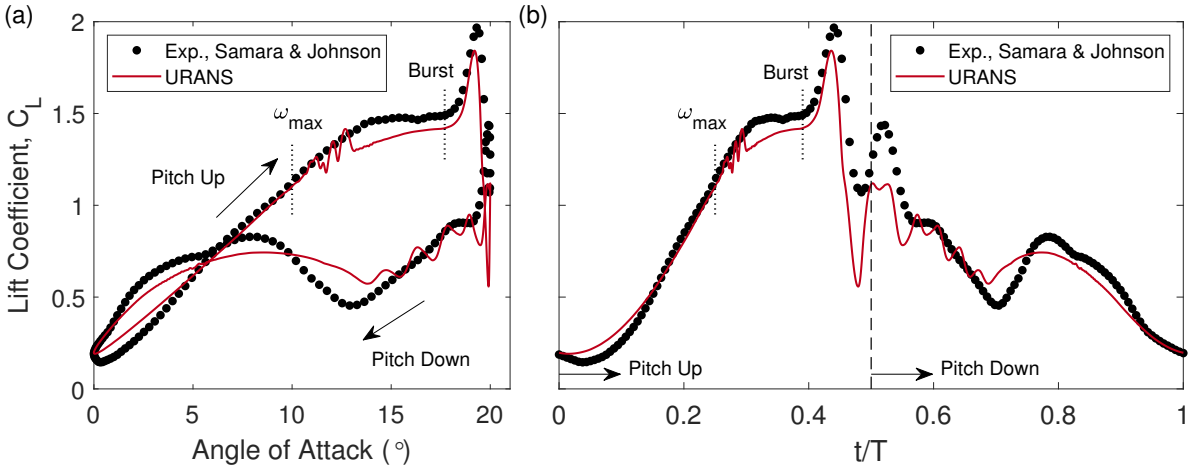


Figure 7.4: URANS predicted dynamic lift coefficient cycle for the S833 airfoil at $Re = 1.7 \times 10^5$ and $k = 0.06$ compared with experimental data [113] versus (a) AOA and (b) non-dimensional time t/T

The fluctuations in C_L during the pitch up motion from approximately 10° to 14° AOA are likely due to instability in the reattachment point of the suction side LSB, identified through the simulated C_p behaviour. A sample of the C_p behaviour is shown in Figure 7.5(a) comparing the ΔC_p to the experimental results [113]. The instability begins at the location of LSB reattachment ($x/c = 0.50$) but the overall trend is in agreement with the experimental pressure data with the average difference in ΔC_p being 0.16 ± 0.13. This BL instability was also observed by Visbal and Garmann [89] in their LES study, however in that case the fluctuations in C_p do not result in fluctuations in C_L during the pitch up motion. This is likely due to the LES method introducing additional randomization and spanwise variation in the turbulent structures in comparison to the 2D Reynolds-averaged

approach. For the URANS results, the fluctuations in C_L were identical in each simulated pitching cycle and therefore did not disappear when averaging the cycles. Tests of higher inflow turbulence as well as chordwise grid refinements were completed to determine if these fluctuations were a result of numerical errors. ANSYS Fluent specifically recommends a turbulent intensity greater than 0.1% around the airfoil, and while tests at $Tu = 0.7\%$ caused the damping of the C_p fluctuations, they were still present in the BL. It should be noted that these fluctuations begin immediately following the location of ω_{max} for the pitch up motion, giving further confidence in the assertion that the fluctuations are due to the flow physics and not due to numerical error. The impact of the location of maximum pitch up motion will be discussed in the next section.

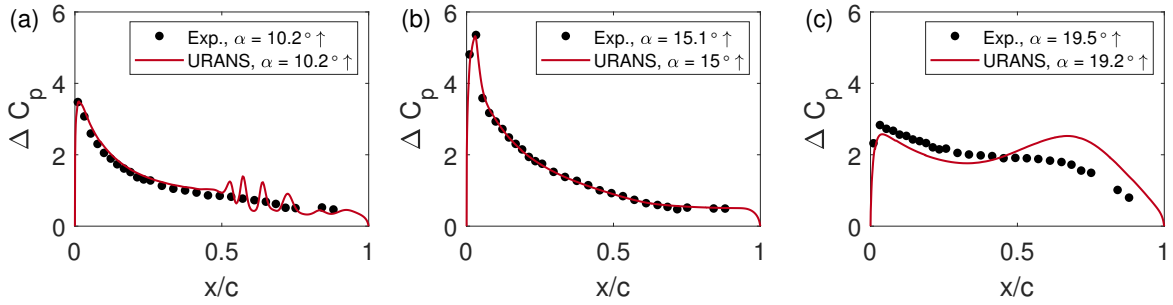


Figure 7.5: URANS predicted dynamic ΔC_p for the S833 airfoil at $Re = 1.7 \times 10^5$ and $k = 0.06$ compared with experimental data [113] for AOAs: (a) 10° ↑ (b) 15° ↑ (c) 19° ↑

The pressure behaviour was also validated for an AOA of 15° in the region of levelled off C_L before the LSB burst occurs (Figure 7.5(b)), and at the peak C_L (Figure 7.5(c)). At 15° the difference in ΔC_p is 0.05 ± 0.07 and at the peak C_L it is 0.39 ± 0.23. At the peak C_L location, the simulated LEV is located from approximately $x/c = 0.4$ to the TE, which can be seen due to the increase in suction pressure in that region. A similar increase in pressure can be seen in the experimental data, however it is not as strong as the simulated result. The AOAs associated with the downstream propagation of the LEV in the experimental data were reported to have a high standard deviation of ΔC_p [113]. Any differences in the pitching cycle due to experimental factors, such as cycle repeatability, could have resulted in small differences in the timing of the LEV shedding. Since the reported ΔC_p is averaged across all experimental cycles [113], the small variation in the location of the LEV would result in the lower ΔC_p magnitudes due to the wash out of the suction pressure during cycle averaging.

Previous researchers completing URANS [92, 96–99] and LES [88, 90–92] simulations of similar sinusoidal pitching low Re airfoils have had poor agreement with the location of peak

C_L, and consistently predict that the lift peak occurs before reference experimental data. In comparison, both presented cases are within 0.1° of the experimental peak lift AOAs. This indicates the timing of key behaviours in the dynamic stall cycle are simulated correctly using this URANS method and therefore a computationally expensive LES simulation is not required. These behaviours include the formation and bursting of the LSB and the formation and shedding of the LEV. The details of these behaviours are analysed in greater detail in the remaining results sections now that the simulation of the overall dynamic stall behaviour has been validated.

7.3 Dynamic LSB

7.3.1 SD 7037 LSB

The LSB formed on the suction side of the SD 7037 airfoil is inherent to the low Re BL and airfoil curvature, as described in Sections 2.1.3 and 2.1.4, and is therefore present in both the static and dynamic BLs. Due to the rapid pitching motion altering the velocity and pressure gradients in the BL, the development and movement of the LSB is delayed in comparison to the static behaviour. To quantify this delay, the movement of the LSB with AOA is tracked in the static and dynamic cases by plotting the locations of laminar BL separation, x_s, and reattachment, x_r, as well as the location of TE separation of the turbulent BL, $x_{s,TE}$. These values are determined using the skin friction coefficient, C_f, in the chordwise direction, as is described in Section 2.1.4, since this provides the exact locations of BL separation and reattachment and the same method was applied in Sections 4.5 and 5.2. The regions of the airfoil with an attached BL have a positive C_f, which means that regions of separation can be identified where $C_f \leq 0$. This method of BL development tracking has been previously used in the static experiments by Lee and Gerontakos [93] and the dynamic URANS simulations by Tseng *et al.* [105]. It is also possible to infer the location of the LSB from contour plots of C_p or C_f, such as in the LES work by Visbal and Garmann [89] and the experimental work by Samara and Johnson [113].

The results for the SD 7037 case are presented in Figure 7.6, with labels for the ω_{max} and LSB bursting locations included to align with the C_L cycles in Figure 7.3. The analysis of the dynamic LSB is split into the AOAs before and after ω_{max} as there is distinct behaviour that occurs depending on the AOA of the pitching up motion and whether the pitching motion is accelerating or decelerating (i.e. before or after ω_{max}, respectively). To draw conclusions about the impact of the sinusoidal pitching motion on the suction side BL, the

results are compared against the results from the static simulations presented in Section 7.1.

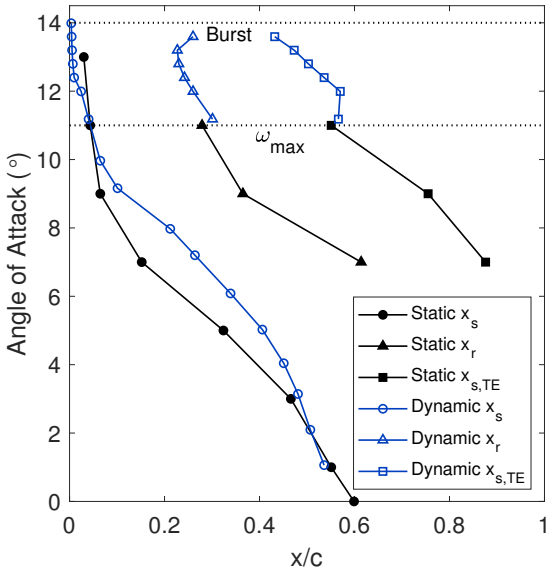


Figure 7.6: Comparison of BL development in the static and dynamic pitch up motion for the SD 7037 airfoil at $Re = 4.1{\times}10^4$. x/c locations of laminar separation (x_s), reattachment (x_r) and trailing edge separation ($x_{s,TE}$) with connecting lines for visualization only

The static SD 7037 results at low AOAs (shown in Figure 7.6) have a BL that undergoes laminar separation but does not reattach to form a LSB. The location of laminar separation moves upstream with increasing AOA, as expected, and reaches the LE as the AOA approaches the peak C_L AOA of 11°. The static LSB is first captured at the AOA of 7° with a length of $0.46c$ and the BL reattaches for a short distance before turbulent BL separation occurs at $x/c = 0.88$. The LSB x_r and TE separation move upstream at a similar pace to x_s, again until the peak C_L AOA of 11° is reached. By the next simulated AOA of 13° the LSB has burst due to the TE separation location meeting the LSB reattachment location, which results in a fully separated BL.

The dynamic SD 7037 results for the AOAs before the location of ω_{max} exhibit a minor delay in x_s in comparison to the static results, reaching a maximum of $0.11c$ at an AOA of 7°. A more significant difference between the static and dynamic results is that the dynamic case does not form a LSB before reaching the location of ω_{max}. This indicates that the acceleration of the rate of the pitch up motion is having a significant impact on

the development of the BL transition required to form the LSB. Immediately after reaching ω_{max}, the dynamic case forms a LSB and develops a region of turbulent BL separation at the TE. The LSB and TE separation locations are equal to the locations for the static case at the same AOA. This is assumed to be caused by the deceleration of the pitching motion that occurs after ω_{max}, which lessens the dynamic effect on the BL.

After reaching ω_{max}, the LSB length reduces from $0.26c$ to $0.22c$ and moves $0.04c$ upstream. At the same time, the TE separation location progresses upstream by $0.13c$ which is approximately 3 times the rate of the LSB motion. At 13.6° AOA , there is a slight expansion of the LSB towards the TE separation, with the x_r changing from 0.23 to 0.26, indicating the initiation of the type of LSB bursting seen in LE stall [86]. By 14° AOA, the LSB of the dynamic SD 7037 case has burst from the combination of the expanding LSB and the upstream progression of the TE separation. Visbal and Garmann [89] and Tseng *et al.* [105] both capture similar amounts of LSB expansion occurring before LSB burst in their dynamic simulations. Additionally, Tseng *et al.* [105] identified two regions during the pitch up motion with distinct BL behaviour, using the first appearance of TE separation as the division rather than the location of ω_{max} used in the current work. For their cycle, the TE separation begins 1.8° after the location of ω_{max}, and the location of ω_{max} marks initiation of a rapid reduction in the length of the long LSB that formed during the low AOAs of the cycle. The NACA 0015 case at $Re = 2 \times 10^5$ and $k = 0.1$ by Tseng *et al.* and the current SD 7037 case at $Re = 4.1 \times 10^4$ and $k = 0.08$ have a similar abrupt change in the LSB location after reaching the ω_{max} of the pitch up motion, showing that this LSB behaviour is likely inherent to the BL behaviour during sinusoidal pitching at low Re.

7.3.2 S833 LSB

The same analysis of the motion of the LSB can be completed for the S833 case to determine the role of the LSB in dynamic stall at low Re. The static S833 results shown in Figure 7.7 exhibit similar behaviour to the SD 7037 case, though with minor differences which can likely be attributed to the difference in Re. The S833 case has approximately 4 times the Re of the SD 7037 case, and a higher Re is known to result in shorter LSB lengths as well as reduced LSB wall-normal thickness [86]. The maximum static LSB length for the S833 case is $0.33c$ in comparison with the $0.46c$ of the SD 7037 case. The LSB also progresses towards the leading edge at a much higher rate with respect to AOA when compared to the SD 7037 case. This results in the S833 static LSB remaining stationary with a reattachment location of approximately $x/c = 0.05$ to 0.1 for AOAs ranging from 11° to 15°. The static LSB has burst by 17° AOA, which is several degrees after the peak

C_L AOA of 13°. In comparison to the SD 7037 static case, the S833 case has a longer delay in the bursting of the LSB after peak C_L. This is a result of the short LSB at the LE that forms at the higher Re, since that requires the TE separation point to progress further upstream to cause the LSB to burst.

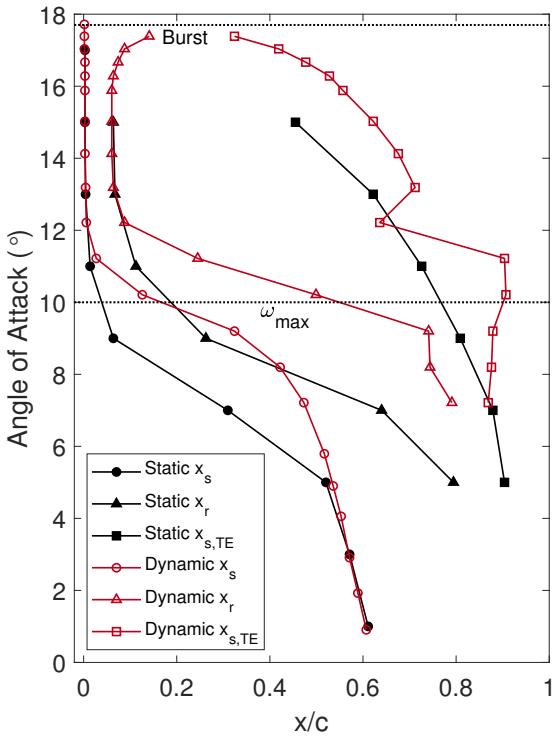


Figure 7.7: Comparison of BL development in the static and dynamic pitch up motion for the S833 airfoil at $Re = 1.7 \times 10^5$. x/c locations of laminar separation (x_s), reattachment (x_r) and trailing edge separation ($x_{s,TE}$) with connecting lines for visualization only

The dynamic S833 results before the location of ω_{max} show a delay in x_s in comparison to the static results. The maximum simulated delay is $0.26c$, which is over 2 times larger than the SD 7037 case. The reduced frequency, k, for the S833 case is 0.06 whereas the SD 7037 case is 0.08, so it would be expected that the higher reduced frequency of the pitching motion would result in a greater delay in the x_s for the SD 7037 case. However, it seems that the higher Re of the S833 case had a larger impact on the dynamic delay of x_s caused by the faster upstream progression of the LSB location seen in the static AOAs. Due to the shorter LSB present at higher Re, the LSB in the dynamic S833 case forms before

the location of ω_{max} at an AOA of 7.2°. The x_r remains relatively constant at a location of $x/c = 0.75$ until reaching ω_{max} and also has TE separation that remains constant at around $x/c = 0.88$. The formation of the LSB before ω_{max} was also seen in the URANS simulation at a similar Re of 2×10^5 by Tseng *et al.* [105].

On reaching ω_{max}, there is a rapid change in the BL behaviour associated with the deceleration of the pitching motion that was seen in the SD 7037 case and the work by Tseng *et al.* [105]. Both the x_s and x_r progress upstream to match with the LSB location for the S833 static simulations. This rapid change in x_r corresponds to the previously discussed fluctuations in C_L seen in Figure 7.4 during the pitch up motion from 10° to 14° AOA, indicating that the oscillations in C_p in Figure 7.5(a) are a result of the flow physics associated with this rapid motion of the x_r location. After 13°, the dynamic LSB remains stationary at a length of $0.06c$ until 16.3° where the LSB slowly expands to $0.14c$ before bursting. The AOAs of constant LSB length correspond to a region of approximately constant C_L in Figure 7.4(a). Due to the strong LE suction peak (Figure 7.5(b)) associated with the LE LSB, the upstream motion of the TE separation has little impact on the C_L between the locations of ω_{max} and LSB burst. During this time, the TE separation location progresses upstream from $x/c = 0.71$ to 0.32 before the LSB bursts at 17.7°.

7.3.3 Dynamic Bursting of the LSB

For the SD 7037 and S833 cases, the bursting of the LSB results in the complete separation of the suction side BL when the BL separation location changes from the TE separation location, $x_{s,TE}$, to the laminar separation location, x_s. This change in BL separation location is $0.43c$ for the SD 7037 case and $0.32c$ for the S833 case, as shown in Figures 7.6 and 7.7. The complete separation of the suction side BL is the driving force behind the LEV formation [84] and therefore having the URANS simulation predict the correct LSB bursting location is crucial in predicting the correct dynamic stall AOA. From previous test cases, it was determined that simulating the correct LSB size and location using URANS requires further grid refinement than is traditionally recommended. This is particularly important in the thin BL that forms close to the LE where higher Re airfoils, such as the S833 case, will have a short and thin LSB. The error introduced in the simulation of the LSB at the LE will lead to an incorrect prediction of the LSB bursting AOA, which is likely the reason that previous works [88, 90–92, 96–99] have consistently predicted early dynamic stall in comparison to experimental data. Therefore specific attention must be given to the LSB simulation for these dynamic stall cases in order to predict the correct dynamic stall AOA, regardless of whether the numerical method is LES or URANS.

As was previously stated in Section 3.4.2, the mesh used for the current simulations uses the same near-wall distribution as Mesh 1 used for the LES simulation of the SD 7037 airfoil presented in Chapter 4. The results of the grid coarsening study in Section 3.4.3, shown in Figure 3.9, indicated that the simulation is sensitive to the wall-normal grid resolution in the laminar BL at the LE and the reduction of the wall-normal resolution caused changes in the C_L cycle after the location of ω_{max} for each case. The early formation of the C_L peak in the WNN and CWN simulations indicates that the coarse mesh in the wall-normal direction is numerically causing the early bursting of the LSB and is leading to premature LEV formation in comparison to the experimental data. The use of the LES-quality BL refined mesh is therefore critical to the URANS simulation of the correct dynamic stall location, and is considered the main factor in the successful simulation of the dynamic stall location for both cases.

7.4 LEV Formation

The LEV formation occurs for AOAs between the location of LSB bursting and the peak C_L for each cycle (shown in Figures 7.3 and 7.4), and it is the growth and shedding of this LEV that is the source of the extreme load fluctuations that occur during deep dynamic stall. The formation of the LEV is shown in Figure 7.8 and Figure 7.9 through a combination of chordwise C_f and the non-dimensional z-vorticity, $\omega_z c/U_\infty$, where the z-direction is aligned with the spanwise direction. The chordwise C_f is used to identify the location of the LSB before bursting and identify the regions of strong reverse flow that occur between the LEV and the airfoil surface. The non-dimensional z-vorticity is used to visualize the formation and growth of the LEV. The locations chosen for analysis were selected from each case to highlight the same key moments in the LEV formation and therefore comparisons can be drawn between the two cases.

Location (a) shows the behaviour immediately before the bursting of the LSB, and location (b) shows the fully separated BL after the burst occurs. At location (a) the LSB reattachment location, x_r, is moving downstream as shown in Figures 7.6 and 7.7. From the negative C_f at location (b) for both cases, it is clear that the remnants of the LSB continue to expand in the downstream direction once the BL is fully separated. This effect is more pronounced for the S833 case, where the reverse flow for $x/c > 0.5$ remains relatively unchanged between location (a) and (b), but the region of negative C_f associated with the LSB has expanded from $x/c = 0.14$ to approximately $x/c = 0.25$.

The separation of the BL results in an unstable shear layer that begins to roll up to form the LEV in location (c), which is visualized for both cases in the thickening of the

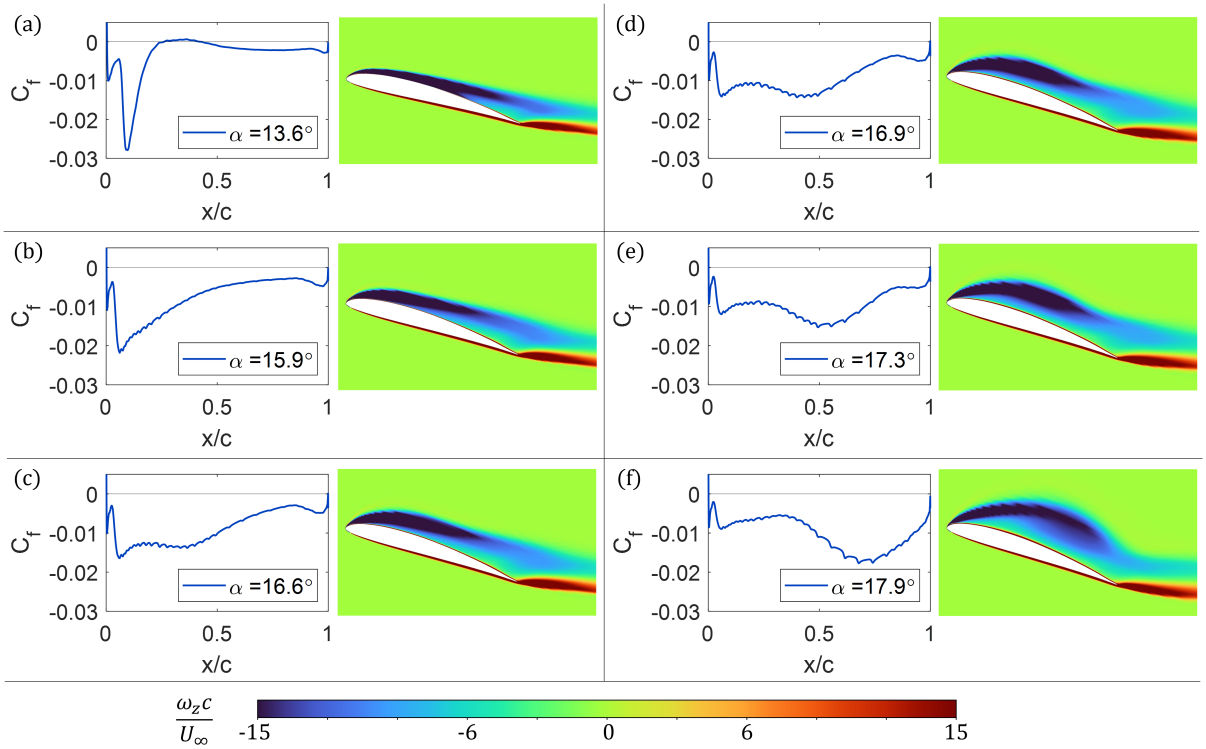


Figure 7.8: URANS dynamic C_f and non-dimensional z-vorticity contours of the LEV formation of the SD 7037 airfoil at $Re = 4.1 \times 10^4$ and $k = 0.08$ for AOAs: (a) 13.6° (b) 15.9° (c) 16.6° (d) 16.9° (e) 17.3° and (f) 17.9°

LE region of negative z-vorticity as well as the bump of increasing reverse flow seen in the range of $x/c = 0.2$ to 0.5 in the C_f plot. Since the LEV first appears from the region of negative C_f associated with the downstream expansion of the bursting LSB, this further highlights the need to take great care in simulating the LSB in these dynamic stall cases. Not only does the LSB bursting generate the separated BL that rolls up into the LEV, but it also determines the chordwise location where the LEV first appears.

Locations (d) to (f) show the chordwise progression of the LEV as both cases approach the peak C_L in the pitching cycle. For the S833 case, the negative C_f peak at the wall in Figure 7.9(f) at 19.1° AOA corresponds to the suction peak shown in the ΔC_p in Figure 7.5(c) at 19.2° AOA. The LEV motion can be tracked through either a peak in negative chordwise C_f or a suction peak in the C_p, and is often shown through contour plots [89,113] to condense the full pitching cycle into a single image.

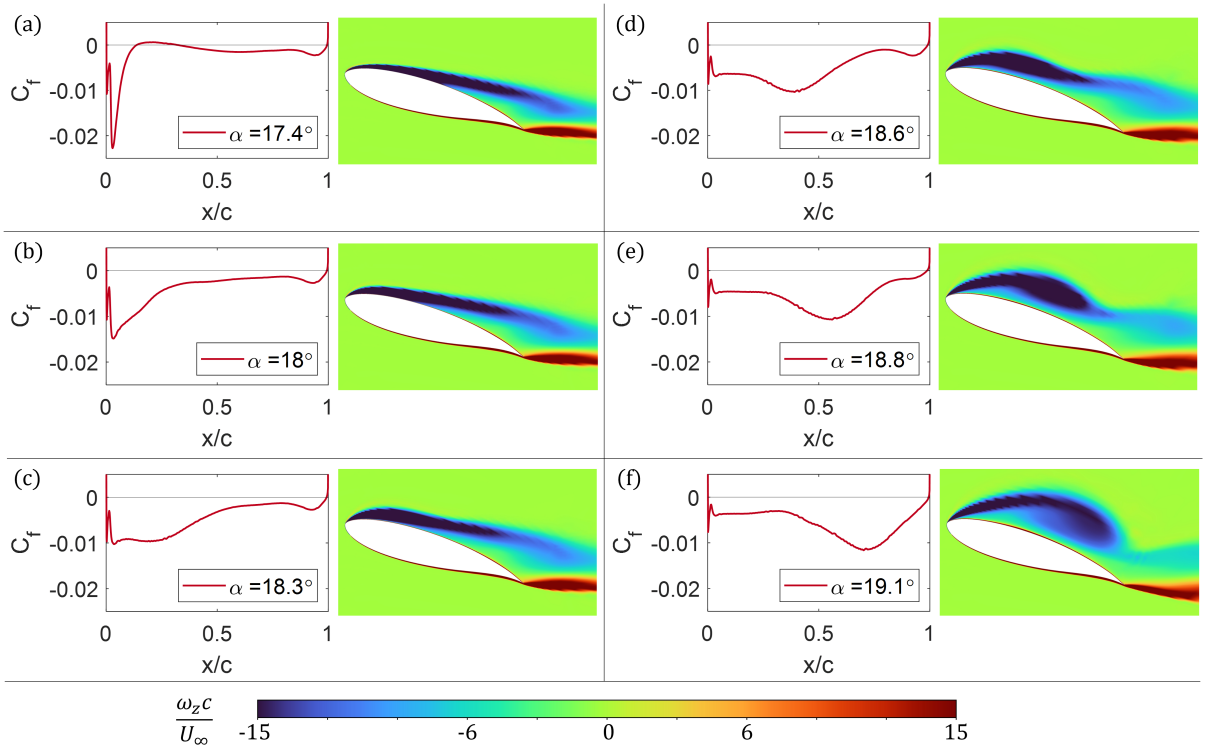


Figure 7.9: URANS dynamic C_f and non-dimensional z-vorticity contours of the LEV formation of the S833 airfoil at $Re = 1.7 \times 10^5$ and $k = 0.06$ for AOAs: (a) 17.4° (b) 18.0° (c) 18.3° (d) 18.6° (e) 18.8° and (f) 19.1°

The C_f trends and the z-vorticity magnitudes are very similar for the two cases except that the Z-vorticity visualization of the SD 7037 case shows less growth of the LEV in the wall-normal direction. This is best visualized in the z-vorticity contours of Figure 7.8 and Figure 7.9 at locations (e) and (f). There are several factors that could have an impact on the growth of the LEV that results in differences in the size of the LEV in the wall-normal direction between the two cases. One difference between the cases is that the peak C_L occurs closer to the ω_{max} for the SD 7037 cycle than it does for the S833 cycle, with the SD 7037 peak C_L occurring when $\omega = 0.7\omega_{max}$ and the S833 peak C_L when $\omega = 0.4\omega_{max}$. The higher percentage of ω_{max} at peak C_L for the SD 7037 case will result in a larger dynamic effect on the LEV formation, and is a factor in the reduction of the growth of the LEV in the wall-normal direction. Also, the reduced frequency for the SD 7037 case is higher than the S833 case, and therefore the expectation is that even if the LEV formation

occurred at the same location within the pitching cycle, that the SD 7037 case would have a thinner LEV due to increased dynamic effects. Additionally, the lower Re results in a lower momentum BL in comparison to the S833 case which has a short LSB and a longer chordwise distance for the turbulent BL to develop. Since the separated shear layer roll-up is the driving force in the LEV growth [84], the higher momentum in the S833 BL leads to a higher energy and therefore a LEV with greater wall-normal growth.

The SD 7037 and S833 cases have differing parameters (Re, k) and slight differences in the growth of the LEV, however the overall behaviour of the LEV is similar. The cycle location and the growth of the LEV are clearly simulated accurately using the URANS method, since the C_L results in Figures 7.3 and 7.4 agree with the experimental location and magnitude of the dynamic C_L peak that forms after the bursting of the LSB.

7.5 Summary

This chapter presented the validation and analysis of the URANS simulation of two low Re airfoils with an applied sinusoidal pitching motion to analyze the deep dynamic stall process that can occur on SWT blades. The chosen SD 7307 and S833 airfoils are designed for use in the Re range in which SWTs operate and the applied sinusoidal pitching cycle parameters were selected to replicate the change in effective AOA of a SWT in unsteady wind conditions. Previous URANS and LES simulations of similar low Re pitching airfoils have struggled to predict the correct dynamic stall AOA, which limits the usage of the simulations as a design tool for mitigation of the unsteady aerodynamic forces that occur during deep dynamic stall. There is also contradicting findings on the importance of the LSB to the initiation of the LEV and the subsequent dynamic stall, therefore extra attention was given to the LSB simulation especially since it is a complex behaviour to predict using URANS methods.

The $\gamma - Re_{\theta t}$ SST $k - \omega$ model, also known as transition SST, was selected after verification of the LSB simulation and lift coefficient for a range of static AOAs. The dynamic pitching simulation for the SD 7037 airfoil was run at a Re of 4.1×10^4 with a k of 0.08 and an AOA range from 0° to 22°. The S833 pitching simulation was run at a higher Re of 1.7×10^5 with a k of 0.06 and an AOA range from 0° to 20°. The simulated C_L through both the pitching cycles agreed with the experimental values and the location of the peak C_L AOA was within 0.1° of the experimental location. The agreement of the stall location is often obscured by the method of plotting the C_L versus AOA, and the results in this chapter were specifically plotted versus cycle time to highlight the excellent agreement throughout the whole dynamic stall process. This is a significant

improvement over previously published LES and URANS simulations, which consistently predicted early dynamic stall in comparison with experimental data. A grid coarsening study was completed that showed a similar erroneous prediction of early dynamic stall occurred when the mesh in the BL was coarsened in the wall-normal direction, and that a minimum of 8 nodes in the laminar BL at the airfoil LE are required to predict the correct peak C_L AOA.

Analysis was completed of the BL and LSB leading up to the complete separation of the BL that results in the formation of the large LEV that causes the peak C_L and dynamic stall. The location of the LSB during the pitch up motion was compared with the static LSB location through the tracking of its separation and reattachment locations as well as the TE turbulent BL separation location. It was found that for the SD 7037 and S833 airfoils in the static and dynamic cases, the complete BL separation occurs when the TE separation point meets the LSB reattachment point, causing the bursting of the LSB. In the dynamic cases, the LSB had a slight expansion in length before bursting due to the LSB reattachment location moving downstream in a similar manner to the bursting that occurs in LE stall. These findings show that any errors in the simulation of the LSB length and its expansion before bursting will result in incorrect timing of the LSB bursting and complete BL separation. Incorrect prediction of the BL separation in the pitching cycle will result in errors in the prediction of the LEV and the AOA of dynamic stall.

While examining the dynamic LSB motion, it was also found that during the pitch up motion there is a distinction in the behaviour of the LSB and BL depending on if the pitch rate is accelerating or decelerating. In the accelerating region that occurs before reaching the maximum pitch rate, ω_{max}, the LSB and BL development was delayed in comparison to the equivalent static AOA. In the SD 7037 case, this prevented the formation of the LSB and in the S833 case the LSB formation was delayed, with the reattachment location remaining relatively constant with increasing AOA. After reaching ω_{max}, the deceleration of the pitching rate caused rapid motion of the LSB to the LE of the airfoil, and also resulted in the location of the TE separation quickly approaching the reattachment location of the LSB. This abrupt shift in behaviour is seen in both the SD 7037 and S833 cases, regardless of the differences in airfoil shape, Re, or k, indicating that the acceleration and deceleration of the pitching motion is the driving force behind this phenomenon.

Analysis was also completed on the formation of the LEV after the LSB bursts and the BL separates for both simulated cases. It was found through the examination of the simulated C_f in the chordwise direction that the region of strong reverse flow associated with the LSB was still present after the LSB had burst. The remnants of the LSB continued to expand downstream in the same manner as the motion of the LSB reattachment location preceding the bursting of the LSB. It is from the downstream end of the remnants of the

bursting LSB that the first evidence of LEV is detected. This yet again highlights the importance of the correct LSB simulation during dynamic stall, since the length of the LSB at the time of bursting must be correct in order to result in the correct chordwise location of LEV formation.

Once the LEV formed, the S833 case predicted greater growth of the LEV in the wall-normal direction in comparison with the SD 7037 case. This was attributed to the lessened dynamic effect due to the lower k and because the shedding of the LEV occurred later in the pitching cycle, meaning the pitch rate was at a lower magnitude relative to ω_{max}.

The presented analysis thoroughly validated the ability of the $\gamma - Re_{\theta t}$ $k - \omega$ URANS model to simulate deep dynamic stall of low Re airfoils with a LSB and fulfils objectives #4, #5 and #6. The success is attributed to the use of a LES-quality mesh, as this was crucial to the simulation of the LSB formation, motion and bursting. A new requirement of a minimum wall-normal mesh resolution of 8 nodes in the laminar BL at the airfoil LE was established for the prediction of the correct dynamic stall AOA, since the bursting of the small LSB in the thin LE BL initiates the LEV that causes the peak C_L and deep dynamic stall. The accurate simulation of the LSB eliminated the issue of early prediction of dynamic stall and further strengthens the viability of this low-cost simulation as a design tool for methods to mitigate the variation in the aerodynamic loading of SWT blades under challenging unsteady wind conditions.

Chapter 8

Conclusion

This chapter provides a summary of the research contributions from the presented numerical studies on the role of the laminar separation bubble (LSB) in small wind turbine (SWT) tonal aeroacoustic noise and deep dynamic stall. The detailed conclusions from the aerodynamic and aeroacoustic analysis of the LSB that forms on the suction side of the SD 7037 airfoil at modest Re are summarized at the end of Chapters 4, 5 and 6. Similarly, the conclusions of the role of the LSB in the deep dynamic stall process for the SD 7037 and S833 airfoils at low Re are summarized at the end of Chapter 7. The full list of publications and conferences resulting from the work presented in this thesis to date are provided in Appendix A.

In the following sections, the objectives outlined in Section 1.3 are revisited and the major conclusions for each topic are summarized. The recommended future work for each topic is also provided.

8.1 Objectives Achieved and Contributions

8.1.1 Aeroacoustic Noise

The tonal noise produced by SWT blades is caused by the interaction of the flow structures within the low Re boundary layer (BL) and LSB with the sharp trailing edge (TE) of the blade. The ability to numerically predict the tonal noise generated by a SWT blade is beneficial to the aeroacoustic design of SWT as well as to other low Re applications of

airfoils. The analysis of the computational fluid dynamic (CFD) and computational aeroacoustic (CAA) simulations can be used to determine the exact mechanisms of tonal noise generation which can then be used to develop methods that reduce or prevent problematic tonal noise. Additionally, these simulations can be incorporated into the early phases of the design process for SWT blades such that the aerodynamic and aeroacoustic performance of the blade can be optimized simultaneously.

The simulation of the SD 7037 airfoil at modest Re and low AOA was completed using an incompressible wall-resolved large eddy simulation (LES) with the Ffowcs-Williams and Hawkings (FW-H) acoustic analogy. The prediction of tonal aeroacoustic noise using this method fulfilled the following objectives:

1. **Apply CFD methods to low Re airfoils under static conditions to accurately predict the transient behaviours in the transitional BL and LSB**

   The simulations accurately predicted the BL transition process and detailed analysis was completed of the Kelvin-Helmholtz (K-H) roll formation in the LSB. This analysis led to the discovery of a pressure feedback loop that exists between the K-H roll touchdown location in the LSB and the laminar BL upstream of the LSB. The presented results are a significant advancement to the understanding of the transient aerodynamic behaviour in the elongated LSBs that form on airfoils operating at modest Re.

2. **Predict the tonal airfoil self-noise generated by a low Re airfoil using CAA and the input data from the CFD simulation**

   The simulations successfully generated a prediction of the tonal airfoil self-noise with the accuracy of the acoustic spectra predicted for 1° AOA exceeding expectations, especially considering the complex interaction of the K-H rolls in the transitional separated BL with the pressure side BL at the airfoil TE. Prior CAA studies have not attempted the prediction of tonal noise at such modest Re or with a transitional separated BL at the TE and therefore the aeroacoustic analysis presented here expands the applicability of CAA methods to increasingly complex flow conditions.

3. **Determine the structures in the transitional BL and LSB that are responsible for the tonal airfoil self-noise at low Re**

   The K-H rolls in the LSB were identified as the source of tonal noise and the LSB pressure feedback process was found to increase the acoustic source strength. Interference between the simulated LSB pressure feedback and an estimation of the expected acoustic feedback from the TE noise showed that the combination of the feedback effects can result in further amplification of the tonal noise or destructive interference

that reduces the tonal noise. The identification of pressure feedback originating in the LSB represents a missing part of the overall acoustic feedback process which can be incorporated into future design and analysis for SWT blades and other low Re airfoil applications.

5. **Validate the simulated results against available experimental data to quantify the accuracy of each simulation method**

   The validation of the LSB simulation against time-averaged aerodynamic data confirmed the accurate prediction of the locations of BL separation, transition and reattachment. The validation against the aeroacoustic data showed the accurate prediction of tonal noise and also showed that the transient development of the K-H rolls occurred at the correct frequency. A major challenge faced by prior simulations of the formation of a LSB and the prediction of tonal aeroacoustic noise for low Re airfoils was the absence of sufficient validating data. This comprehensive validation of the LES and FW-H simulations enabled the strong conclusions on the formation of the LSB and the role it plays in the tonal aeroacoustic noise generated by low Re airfoils.

6. **Reduce computational cost through the selection of appropriate CFD methods and the optimization of the simulation parameters**

   The simulations were completed using incompressible wall-resolved LES to reduce the computational cost of the simulation while maintaining the accuracy required for the prediction of tonal noise using the FW-H acoustic analogy. This success was achieved through the careful application of mesh criteria to the attached and separated regions of the BL and through the optimization of the simulation domain size. The simulation of tonal airfoil self-noise is often assumed to require the use of compressible CFD methods due to the TE acoustic feedback, however it was clearly shown in the presented results that an incompressible simulation is sufficient for the prediction of problematic tonal noise and determining the source of the tonal noise.

8.1.2 Dynamic Stall

The deep dynamic stall process causes extreme load fluctuations on SWT blades due to unsteady wind conditions and the low Re flow over the blades complicates the stall process due to the presence of a LSB. The numerical prediction of the deep dynamic stall process at low Re can be used to determine the role of the LSB in these load fluctuations and can also be used to design technologies and techniques to reduce the unsteady loading on SWT blades.

The $\gamma - Re_{\theta t}$ SST $k - \omega$ URANS model was used to predict the deep dynamic stall of the SD 7037 airfoil at a modest Re and S833 airfoil at a low Re. The simulation of deep dynamic stall using this method fulfilled the following objectives:

4. **Predict the dynamic stall of low Re airfoils with a LSB using unsteady CFD methods**

   The load fluctuations that occurred during the deep dynamic stall cycle were accurately predicted with particular accuracy in the timing and magnitude of the unsteady loading at stall. Analysis of both simulations found that the deep stall process is initiated by the expansion and bursting of the LSB at the airfoil leading edge (LE) and is in contrast to prior experimental and simulated works which have disregarded the effect of the LSB in the stall process. The presented results are a significant advancement to the understanding of the deep dynamic stall process at low Re and outlines the appropriate URANS method which can be incorporated into the design of SWT blades with a high degree of confidence.

5. **Validate the simulated results against available experimental data to quantify the accuracy of each simulation method**

   The validation of the URANS method confirmed the accurate prediction of the timing of dynamic stall for two different airfoil profiles operating at drastically different Re values within the low Re range. Previous numerical studies predicted the early initiation of the dynamic stall process however, the analysis of the simulation mesh showed that the prediction of early stall is a result of the early bursting of the LSB due to insufficient wall-normal mesh resolution at the airfoil LE. The confirmation of the cause of this early stall behaviour at a modest Re with an elongated LE LSB and a low Re with a short LE LSB fully validated the role of the LSB in the deep dynamic stall process.

6. **Reduce computational cost through the selection of appropriate CFD methods and the optimization of the simulation parameters**

   The URANS method was successfully used to predict the positioning and bursting of the LSB in the low Re BL during the dynamic stall process. This method required the use of a LES-quality mesh in the airfoil BL to be able to accurately predict the LSB behaviour. This eliminated the need of using higher computational cost simulations such as LES to predict the dynamic stall process. The presented URANS method can be accurately used to predict the dynamic stall process of low Re airfoils and is a significant step towards the use of these CFD methods to improve the design of SWT blades to reduce the dynamic loading experienced in unsteady wind conditions.

8.2 Future Work

The following are the recommendations for future work to further investigate the role of the LSB in tonal aeroacoustic noise generation and the dynamic stall process for low Re airfoils:

LES of the LSB

- The effect of the sub-grid filter length on the transient formation and breakdown of the K-H rolls requires further investigation.

Acoustic Feedback Interference

- Confirmation is required that the LSB pressure feedback occurs upstream of the LSB for other low Re airfoils.
- The effect of the interference with the TE acoustic feedback needs to be quantified. This requires the further study of low Re airfoils operating under conditions where the LSB is in close proximity to the TE or where there is a transitional separated BL at the TE.

Dynamic Stall

- The further study of dynamic stall at low Re and the role of the LSB in the stall process requires the application of the URANS method to cycles with a wide range of different Re, pitching reduced frequencies and AOA ranges.

The analysis of the airfoil self-noise and deep dynamic stall simulations resulted in several new conclusions about the role of the LSB in these processes. The simulation methods required to accurately simulate the transient behaviour of the LSB were also established. The continuation of this analysis in the recommended future work will undeniably contribute to the improved aerodynamic and aeroacoustic design of applications operating at low Re.

References

[1] I. H. Abbott and A. E. Von Doenhoff, *Theory of Wing Sections, Including a Summary of Airfoil Data*. Mineola, NY: Dover Publications, 1959.

[2] H. Schlichting and K. Gersten, *Boundary-Layer Theory*. Springer-Verlag Berlin Heidelberg, 9th ed., 2017.

[3] F. M. White, *Viscous Fluid Flow*. New York: McGraw Hill, 2nd ed., 1991.

[4] F. Ghorbanishohrat, *Study of a low Re airfoil considering laminar separation bubbles in static and pitching motion*. PhD thesis, University of Waterloo, 2019. http://hdl.handle.net/10012/14428.

[5] P. Ziadé, M. A. Feero, P. Lavoie, and P. E. Sullivan, "Shear Layer Development, Separation, and Stability Over a Low-Reynolds Number Airfoil," *Journal of Fluids Engineering*, vol. 140, no. 7, pp. 1–12, 2018. https://doi.org/10.1115/1.4039233.

[6] J. R. Brinkerhoff and M. I. Yaras, "Interaction of viscous and inviscid instability modes in separation-bubble transition," *Physics of Fluids*, vol. 23, no. 12, 2011. https://doi.org/10.1063/1.3666844.

[7] W. Yuan, M. Khalid, J. Windte, U. Scholz, and R. Radespiel, "An investigation of Low-Reynolds-number flows past airfoils," *AIAA Applied Aerodynamics Conference*, vol. 1, pp. 102–120, 2005. https://doi.org/10.2514/6.2005-4607.

[8] H. J. Li and Z. Yang, "Separated boundary layer transition under pressure gradient in the presence of free-stream turbulence," *Physics of Fluids*, vol. 31, no. 10, 2019. https://doi.org/10.1063/1.5122889.

[9] J. G. Wissink and W. Rodi, "Direct Numerical Simulations of Transitional Flow in Turbomachinery," *Journal of Turbomachinery*, vol. 128, no. 4, pp. 668–678, 2006. https://doi.org/10.1115/1.2218517.

[10] R. Hain, C. J. Kahler, and R. Radespiel, "Dynamics of laminar separation bubbles at low-reynolds-number aerofoils," *Journal of Fluid Mechanics*, vol. 630, p. 129–153, 2009. https://doi.org/10.1017/S0022112009006661.

[11] G. J. Walker, "Transitional flow on axial turbomachine blading," *AIAA Journal*, vol. 27, no. 5, pp. 595–602, 1989. https://doi.org/10.2514/3.10150.

[12] J. M. Russell, *Length and Bursting of Separation Bubbles: A Physical Interpretation*. NASA. Langley Res. Center The Sci. and Technol. of Low Speed and Motorless Flight, Pt. 1, 1979. https://ntrs.nasa.gov/citations/19790015727.

[13] M. Lang, U. Rist, and S. Wagner, "Investigations on controlled transition development in a laminar separation bubble by means of LDA and PIV," *Experiments in Fluids*, vol. 36, no. 1, pp. 43–52, 2004. https://doi.org/10.1007/s00348-003-0625-x.

[14] B. R. McAuliffe and M. I. Yaras, "Separation-Bubble-Transition Measurements on a Low-Re Airfoil Using Particle Image Velocimetry," in *Volume 3: Turbo Expo 2005, Parts A and B*, vol. 3, pp. 1029–1038, ASME, 2005. https://doi.org/10.1115/GT2005-68663.

[15] H. Versteeg, W. Malalasekera, G. Orsi, J. H. Ferziger, A. W. Date, and J. D. Anderson, *An Introduction to Computational Fluid Dynamics - The Finite Volume Method*. Harlow: Pearson Education Limited, 2nd ed., 1995.

[16] L. F. Richardson, *Weather Prediction by Numerical Process*. Cambridge Mathematical Library, Cambridge: Cambridge University Press, 2 ed., 2007.

[17] S. B. Pope, *Turbulent Flows*. Cambridge University Press, 2000.

[18] A. N. Kolmogorov, "The local structure of turbulence in incompressible viscous fluid for very large reynolds numbers," *Proceedings: Mathematical and Physical Sciences*, vol. 434, no. 1890, pp. 9–13, 1991. https://doi.org/10.1098/rspa.1991.0075.

[19] J. Smagorinsky, "General circulation experiments with the primitive equations: The basic experiment," *Monthly Weather Review*, vol. 91, no. 3, pp. 99 – 164, 1963. https://doi.org/10.1175/1520-0493(1963)091<0099:GCEWTP>2.3.CO;2.

[20] M. Germano, U. Piomelli, P. Moin, and W. H. Cabot, "A dynamic subgrid-scale eddy viscosity model," *Physics of Fluids A: Fluid Dynamics*, vol. 3, no. 7, pp. 1760–1765, 1991. https://doi.org/10.1063/1.857955.

[21] D. K. Lilly, "A proposed modification of the Germano subgrid-scale closure method," *Physics of Fluids A: Fluid Dynamics*, vol. 4, no. 3, pp. 633–635, 1992. https://doi.org/10.1063/1.858280.

[22] S. Lardeau, M. Leschziner, and T. Zaki, "Large Eddy Simulation of Transitional Separated Flow over a Flat Plate and a Compressor Blade," *Flow, Turbulence and Combustion*, vol. 88, no. 1-2, pp. 19–44, 2012. https://doi.org/10.1007/s10494-011-9353-0.

[23] S. K. Roberts and M. I. Yaras, "Large-Eddy Simulation of Transition in a Separation Bubble," *Journal of Fluids Engineering*, vol. 128, no. 2, pp. 232–238, 2006. https://doi.org/10.1115/1.2170123.

[24] S. Burgmann, J. Dannemann, and W. Schröder, "Time-resolved and volumetric PIV measurements of a transitional separation bubble on an SD7003 airfoil," *Experiments in Fluids*, vol. 44, no. 4, pp. 609–622, 2008. https://doi.org/10.1007/s00348-007-0421-0.

[25] T. A. Smith and Y. Ventikos, "Boundary layer transition over a foil using direct numerical simulation and large eddy simulation," *Physics of Fluids*, vol. 31, no. 12, 2019. https://doi.org/10.1063/1.5126663.

[26] N. Thomareis and G. Papadakis, "Effect of trailing edge shape on the separated flow characteristics around an airfoil at low Reynolds number A numerical study," *Physics of Fluids*, vol. 29, no. 1, 2017. https://doi.org/10.1063/1.4973811.

[27] L. E. Jones, R. D. Sandberg, and N. D. Sandham, "Direct numerical simulations of forced and unforced separation bubbles on an airfoil at incidence," *Journal of Fluid Mechanics*, vol. 602, pp. 175–207, 2008. https://doi.org/10.1017/S0022112008000864.

[28] L. E. Jones and R. D. Sandberg, "Numerical analysis of tonal airfoil self-noise and acoustic feedback-loops," *Journal of Sound and Vibration*, vol. 330, no. 25, pp. 6137–6152, 2011. https://doi.org/10.1016/j.jsv.2011.07.009.

[29] Y. Hoarau, M. Braza, Y. Ventikos, and D. Faghani, "First stages of the transition to turbulence and control in the incompressible detached flow around a NACA0012 wing," *International Journal of Heat and Fluid Flow*, vol. 27, no. 5, pp. 878–886, 2006. https://doi.org/10.1016/j.ijheatfluidflow.2006.03.026.

[30] H.-J. Kim, S. Lee, and N. Fujisawa, "Computation of unsteady flow and aerodynamic noise of NACA0018 airfoil using large-eddy simulation," *International Journal of Heat and Fluid Flow*, vol. 27, no. 2, pp. 229–242, 2006. https://doi.org/10.1016/j.ijheatfluidflow.2005.08.007.

[31] M. C. Galbraith and M. R. Visbal, "Implicit large eddy simulation of low-Reynolds-number transitional flow past the SD7003 airfoil," *46th AIAA Aerospace Sciences Meeting and Exhibit*, 2008. https://doi.org/10.2514/6.2010-4737.

[32] M. Breuer, "Effect of Inflow Turbulence on an Airfoil Flow with Laminar Separation Bubble: An LES Study," *Flow, Turbulence and Combustion*, vol. 101, no. 2, pp. 433–456, 2018. https://doi.org/10.1007/s10494-017-9890-2.

[33] B. A. Lobo, A. P. Schaffarczyk, and M. Breuer, "Investigation into boundary layer transition using wall-resolved large-eddy simulations and modeled inflow turbulence," *Wind Energy Science*, vol. 7, no. 3, pp. 967–990, 2022. https://doi.org/10.5194/wes-7-967-2022.

[34] N. S. Dhamankar, G. A. Blaisdell, and A. S. Lyrintzis, "Overview of turbulent inflow boundary conditions for large-eddy simulations," *AIAA Journal*, vol. 56, no. 4, pp. 1317–1334, 2018. https://doi.org/10.2514/1.J055528.

[35] J. Christophe, J. Anthoine, and S. Moreau, "Trailing edge noise of a controlled-diffusion airfoil at moderate and high angle of attack," *15th AIAA/CEAS Aeroacoustics Conference*, no. May, pp. 11–13, 2009. https://doi.org/10.2514/6.2009-3196.

[36] D. P. Lockard, M. M. Choudhari, and P. G. Buning, "Influence of spanwise boundary conditions on slat noise simulations," *21st AIAA/CEAS Aeroacoustics Conference*, 2015. https://doi.org/10.2514/6.2015-3136.

[37] J. P. V. Doormaal and G. D. Raithby, "Enhancements of the simple method for predicting incompressible fluid flows," *Numerical Heat Transfer*, vol. 7, no. 2, pp. 147–163, 1984. https://doi.org/10.1080/01495728408961817.

[38] R. Issa, "Solution of the implicitly discretised fluid flow equations by operator-splitting," *Journal of Computational Physics*, vol. 62, no. 1, pp. 40–65, 1986. https://doi.org/10.1016/0021-9991(86)90099-9.

[39] B. P. Leonard and S. Mokhtari, "ULTRA-SHARP nonoscillatory convection schemes for high-speed steady multidimensional flow," Tech. Rep. NASA-TM-102568, NASA Reference Publication, 1990. https://ntrs.nasa.gov/citations/19900012254.

[40] S. Lee, L. Ayton, F. Bertagnolio, S. Moreau, T. P. Chong, and P. Joseph, "Turbulent boundary layer trailing-edge noise: Theory, computation, experiment, and application," *Progress in Aerospace Sciences*, vol. 126, p. 100737, 2021. https://doi.org/10.1016/j.paerosci.2021.100737.

[41] S. Oerlemans, "Primary Noise Sources," in *Wind Turbine Noise*, ch. 2, pp. 13–45, Multi-Science Publishing Co. Ltd., 2011.

[42] P. Moriarty and P. Migliore, "Semi-Empirical Aeroacoustic Noise Prediction Code for Wind Turbines," Tech. Rep. NREL/TP-500-34478, 2003. https://doi.org/10.2172/15006098.

[43] P. Moriarty, "NAFNoise User's Guide," tech. rep., National Renewable Energy Laboratory, 2005.

[44] R. K. Amiet, "Acoustic radiation from an airfoil in a turbulent stream," *Journal of Sound and Vibration*, vol. 41, no. 4, pp. 407–420, 1975. https://doi.org/10.1016/S0022-460X(75)80105-2.

[45] T. F. Brooks, D. S. Pope, and M. A. Marcolini, "Airfoil self-noise and prediction," Tech. Rep. NASA-RP-1218, NASA Reference Publication, 1989. http://ntrs.nasa.gov/archive/nasa/casi.ntrs.nasa.gov/19890016302.pdf.

[46] S. Wagner, R. Bareiss, and G. Guidata, *Wind Turbine Noise*. Berlin: Springer-Verlag Berlin Heidelberg, 1996.

[47] G. Leventhall, "Basic Acoustics," in *Wind Turbine Noise*, ch. 1, pp. 1–11, Essex: Multi-Science Publishing Co. Ltd., 2011.

[48] J. E. F. Williams and L. H. Hall, "Aerodynamic sound generation by turbulent flow in the vicinity of a scattering half plane," *Journal of Fluid Mechanics*, vol. 40, no. 4, p. 657–670, 1970. https://doi.org/10.1017/S0022112070000368.

[49] N. Tam, "An Aeroacoustic Study of Airfoil Self-Noise for Wind Turbine Applications," Master's thesis, University of Waterloo, 2017. http://hdl.handle.net/10012/11736.

[50] N. Curle, "The influence of solid boundaries upon aerodynamic sound," *Proc. R. Soc. Lond. A*, no. 231, pp. 505–514, 1955. https://doi.org/10.1098/rspa.1955.0191.

[51] D. Wood, *Small wind turbines: Analysis, Design, and Application*. London: Springer-Verlag, 2011.

[52] S. Pröbsting, J. Serpieri, and F. Scarano, "Experimental investigation of aerofoil tonal noise generation," *Journal of Fluid Mechanics*, vol. 747, pp. 656–687, 2014. https://doi.org/10.1017/jfm.2014.156.

[53] S. Pröbsting and S. Yarusevych, "Experimental investigation of aerofoil tonal noise generation," *Journal of Fluid Mechanics*, vol. 780, pp. 167–191, 2015. https://doi.org/10.1017/jfm.2015.427.

[54] S. Pröbsting, F. Scarano, and S. C. Morris, "Regimes of tonal noise on an airfoil at moderate Reynolds number," *Journal of Fluid Mechanics*, vol. 780, pp. 407–438, 2015. https://doi.org/10.1017/jfm.2015.475.

[55] P. Jaiswal, Y. Pasco, G. Yakhina, and S. Moreau, "Experimental investigation of aerofoil tonal noise at low Mach number," *Journal of Fluid Mechanics*, vol. 932, pp. 1–31, 2022. https://doi.org/10.1017/jfm.2021.1018.

[56] G. Yakhina, M. Roger, S. Moreau, L. Nguyen, and V. Golubev, "Experimental and analytical investigation of the tonal trailing-edge noise radiated by low reynolds number aerofoils," *Acoustics*, vol. 2, no. 2, pp. 293–329, 2020. https://doi.org/10.3390/acoustics2020018.

[57] S. Yarusevych, P. E. Sullivan, and J. G. Kawall, "On vortex shedding from an airfoil in low-Reynolds-number flows," *Journal of Fluid Mechanics*, vol. 632, pp. 245–271, 2009. https://doi.org/10.1017/S0022112009007058.

[58] M. Sanjose, A. Towne, P. Jaiswal, S. Moreau, S. Lele, and A. Mann, "Modal analysis of the laminar boundary layer instability and tonal noise of an airfoil at Reynolds number 150,000," *International Journal of Aeroacoustics*, vol. 18, no. 2-3, pp. 317–350, 2019. https://doi.org/10.1177/1475472X18812798.

[59] J. Winkler, H. Wu, S. Moreau, T. Carolus, and R. D. Sandberg, "Trailing-edge broadband noise prediction of an airfoil with boundary-layer tripping," *Journal of Sound and Vibration*, vol. 482, pp. 1–25, 2020. https://doi.org/10.1016/j.jsv.2020.115450.

[60] R. W. Paterson, P. G. Vogt, M. R. Fink, and C. L. Munch, "Vortex noise of isolated airfoils," *Journal of Aircraft*, vol. 10, no. 5, pp. 296–302, 1973. https://doi.org/10.2514/3.60229.

[61] C. K. Tam, "Discrete tones of isolated airfoils," *Journal of the Acoustical Society of America*, vol. 55, no. 6, pp. 1173–1177, 1974. https://doi.org/10.1121/1.1914682.

[62] M. R. Fink, "Prediction of airfoil tone frequencies," *Journal of Aircraft*, vol. 12, no. 2, pp. 118–120, 1975. https://doi.org/10.2514/3.44421.

[63] R. E. Longhouse, "Vortex shedding noise of low tip speed, axial flow fans," *Journal of Sound and Vibration*, vol. 53, no. 1, pp. 25–46, 1977. https://doi.org/10.1016/0022-460X(77)90092-X.

[64] H. Arbey and J. Bataille, "Noise generated by airfoil profiles placed in a uniform laminar flow," *Journal of Fluid Mechanics*, vol. 134, pp. 33–47, 1983. https://doi.org/10.1017/S0022112083003201.

[65] G. Desquesnes, M. Terracol, and P. Sagaut, "Numerical investigation of the tone noise mechanism over laminar airfoils," *Journal of Fluid Mechanics*, vol. 591, pp. 155–182, 2007. https://doi.org/10.1017/S0022112007007896.

[66] T. P. Chong and P. Joseph, ""Ladder" structure in tonal noise generated by laminar flow around an airfoil," *The Journal of the Acoustical Society of America*, vol. 131, no. 6, 2012. https://doi.org/10.1121/1.4710952.

[67] M. J. Kingan and J. R. Pearse, "Laminar boundary layer instability noise produced by an aerofoil," *Journal of Sound and Vibration*, vol. 322, no. 4, pp. 808–828, 2009. https://doi.org/10.1016/j.jsv.2008.11.043.

[68] F. Farassat, "The Acoustic Analogy as a Tool of Computational Aeroacoustics," in *Computational Aeroacoustics*, ch. Mathematical Aspects of Acoustics, pp. 133–155, Springer-Verlag New York, 1993. https://doi.org/10.1007/978-1-4613-8342-0_7.

[69] M. Deuse and R. D. Sandberg, "Different noise generation mechanisms of a controlled diffusion aerofoil and their dependence on Mach number," *Journal of Sound and Vibration*, vol. 476, 2020. https://doi.org/10.1016/j.jsv.2020.115317.

[70] C. K. Tam, "Computational aeroacoustics: An overview of computational challenges and applications," *International Journal of Computational Fluid Dynamics*, vol. 18, no. 6, pp. 547–567, 2004. https://doi.org/10.1080/10618560410001673551.

[71] M. Lighthill, "On sound generated aerodynamically I. General theory," *Philosophical Transactions of the Royal Society of London. Series A*, vol. 211, no. 1107, pp. 564–587, 1952. https://doi.org/10.1098/rspa.1952.0060.

[72] D. G. Crighton, "Computational Aeroacoustics for Low Mach Number Flows," in *Computational Aeroacoustics*, ch. Classical, pp. 50–68, New York: Springer-Verlag New York, 1993. https://doi.org/10.1007/978-1-4613-8342-0_3.

[73] K. S. Brentner and F. Farassat, "Analytical comparison of the acoustic analogy and kirchhoff formulation for moving surfaces," *AIAA Journal*, vol. 36, no. 8, pp. 1379–1386, 1998. https://doi.org/10.2514/2.558.

[74] M. Lighthill, "On sound generated aerodynamically II. Turbulence as a source of sound," *Philosophical Transactions of the Royal Society of London. Series A*, vol. 222, no. 1148, pp. 1–32, 1954. https://doi.org/10.1098/rspa.1954.0049.

[75] J. Ffowcs Williams and D. Hawkings, "Sound Generation by Turbulence and Surfaces in Arbitrary Motion," *Philosophical Transactions of the Royal Society of London. Series A*, vol. 264, no. 1151, pp. 321–342, 1969. https://doi.org/10.1098/rsta.1969.0031.

[76] K. S. Brentner, "An Efficient and Robust Method for Predicting Helicopter High-Speed Impulsive Noise," *Journal of Sound and Vibration*, vol. 203, no. 1, pp. 87–100, 1997. https://doi.org/10.1006/jsvi.1996.0834.

[77] H. Wu, S. Moreau, and R. D. Sandberg, "On the noise generated by a controlled-diffusion aerofoil at Rec=1.5 $\times$ 10^5," *Journal of Sound and Vibration*, vol. 487, p. 115620, 2020. https://doi.org/10.1016/j.jsv.2020.115620.

[78] S. Moreau, "The third golden age of aeroacoustics," *Physics of Fluids*, vol. 34, no. 3, 2022. https://doi.org/10.1063/5.0084060.

[79] T. Burton, N. Jenkins, D. Sharpe, and E. Bossanyi, *Wind Energy Handbook*. Wiley, 2011. https://doi.org/10.1002/9781119992714.

[80] A. C. Hansen, "Yaw Dynamics of Horizontal Axis Wind turbines: Final Report," Tech. Rep. NREL/TP-442-4482, National Renewable Energy Laboratory, 1992. https://www.nrel.gov/docs/legosti/old/4822.pdf.

[81] K. Gharali, *Pitching airfoil study and freestream effects for wind turbine applications*. PhD thesis, University of Waterloo, 2013. http://hdl.handle.net/10012/7833.

[82] W. J. McCroskey, "Unsteady Airfoils," *Annual Review of Fluid Mechanics*, vol. 14, no. 1, pp. 285–311, 1982. https://doi.org/10.1146/annurev.fl.14.010182.001441.

[83] J. G. Leishman, *Principles of Helicopter Aerodynamics*. Cambridge University Press, 2nd ed., 2006.

[84] J. D. Eldredge and A. R. Jones, "Leading-Edge Vortices: Mechanics and Modeling," *Annual Review of Fluid Mechanics*, vol. 51, no. 1, pp. 75–104, 2019. https://doi.org/10.1146/annurev-fluid-010518-040334.

[85] T. C. Corke and F. O. Thomas, "Dynamic Stall in Pitching Airfoils: Aerodynamic Damping and Compressibility Effects," *Annual Review of Fluid Mechanics*, vol. 47, no. 1, pp. 479–505, 2015. https://doi.org/10.1146/annurev-fluid-010814-013632.

[86] I. Tani, "Low-speed flows involving bubble separations," *Progress in Aerospace Sciences*, vol. 5, no. C, pp. 70–103, 1964. https://doi.org/10.1016/0376-0421(64)90004-1.

[87] G. B. McCullough and D. E. Gault, "Examples of Three Representative Types of Airfoil-section Stall at Low Speed," Tech. Rep. NACA-TN-2502, National Advisory Committee for Aeronautics, 1951. https://ntrs.nasa.gov/citations/19930083422.

[88] Y. Kim and Z.-T. Xie, "Modelling the effect of freestream turbulence on dynamic stall of wind turbine blades," *Computers and Fluids*, vol. 129, pp. 53–66, 2016. https://doi.org/10.1016/j.compfluid.2016.02.004.

[89] M. R. Visbal and D. J. Garmann, "Analysis of Dynamic Stall on a Pitching Airfoil Using High-Fidelity Large-Eddy Simulations," *AIAA Journal*, vol. 56, pp. 46–63, 2018. https://doi.org/10.2514/1.J056108.

[90] X. Huang, M. Albers, P. Meysonnat, M. Meinke, and W. Schröder, "Analysis of the effect of freestream turbulence on dynamic stall of wind turbine blades," *International Journal of Heat and Fluid Flow*, vol. 85, p. 108668, 2020. https://doi.org/10.1016/j.ijheatfluidflow.2020.108668.

[91] T. Boye and Z. Xie, "Aerodynamics of a pitching wind turbine blade at high reduced frequencies," *Journal of Wind Engineering and Industrial Aerodynamics*, vol. 223, p. 104935, 2022. https://doi.org/10.1016/j.jweia.2022.104935.

[92] F. Geng, I. Kalkman, A. Suiker, and B. Blocken, "Sensitivity analysis of airfoil aerodynamics during pitching motion at a Reynolds number of 1.35×10^5," *Journal of Wind Engineering and Industrial Aerodynamics*, vol. 183, pp. 315–332, 2018. https://doi.org/10.1016/j.jweia.2018.11.009.

[93] T. Lee and P. Gerontakos, "Investigation of flow over an oscillating airfoil," *Journal of Fluid Mechanics*, vol. 512, pp. 313–341, 2004. https://doi.org/10.1017/S0022112004009851.

[94] S. I. Benton and M. R. Visbal, "The onset of dynamic stall at a high, transitional Reynolds number," *Journal of Fluid Mechanics*, vol. 861, pp. 860–885, 2019. https://doi.org/10.1017/jfm.2018.939.

[95] J. Batther and S. Lee, "Numerical investigation of a pitching airfoil undergoing dynamic stall using Delayed Detached Eddy Simulations," *Computers and Fluids*, vol. 249, p. 105691, 2022. https://doi.org/10.1016/j.compfluid.2022.105691.

[96] K. Gharali and D. A. Johnson, "Dynamic stall simulation of a pitching airfoil under unsteady freestream velocity," *Journal of Fluids and Structures*, vol. 42, pp. 228–244, 2013. https://doi.org/10.1016/j.jfluidstructs.2013.05.005.

[97] M. Honarmand, M. H. Djavareshkian, B. F. Feshalami, and E. Esmaeilifar, "Numerical simulation of a pitching airfoil under dynamic stall of low reynolds number flow," *Journal of Aerospace Technology and Management*, vol. 11, pp. 1–14, 2019. https://doi.org/10.5028/jatm.v11.1076.

[98] Y. Wu, Y. Dai, and C. Yang, "Time-Delayed Active Control of Stall Flutter for an Airfoil via Camber Morphing," *AIAA Journal*, vol. 60, pp. 5723–5734, 2022. https://doi.org/10.2514/1.J061947.

[99] Y. Li, Y. Dai, J. Hu, and C. Yang, "Numerical investigation on stall flutter of an airfoil with split drag rudder," *Journal of Fluids and Structures*, vol. 114, p. 103718, 2022. https://doi.org/10.1016/j.jfluidstructs.2022.103718.

[100] Z. Xu, B. Wu, C. Gao, and N. Wang, "Numerical simulation of dynamic stall flow control using a multi-dielectric barrier discharge plasma actuation strategy," *Physics of Plasmas*, vol. 29, 2022. https://doi.org/10.1063/5.0107530.

[101] F. R. Menter, R. B. Langtry, S. R. Likki, Y. B. Suzen, P. G. Huang, and S. Volker, "A Correlation-Based Transition Model Using Local Variables—Part I: Model Formulation," *Journal of Turbomachinery*, vol. 128, no. 3, p. 413, 2006. https://doi.org/10.1115/1.2184352.

[102] Y. Liu, P. Li, and K. Jiang, "Comparative assessment of transitional turbulence models for airfoil aerodynamics in the low Reynolds number range," *Journal of Wind Engineering and Industrial Aerodynamics*, vol. 217, p. 104726, 2021. https://doi.org/10.1016/j.jweia.2021.104726.

[103] K. Gharali and D. A. Johnson, "PIV-based load investigation in dynamic stall for different reduced frequencies," *Experiments in Fluids*, vol. 55, no. 8, p. 1803, 2014. https://doi.org/10.1007/s00348-014-1803-8.

[104] C.-C. Tseng and Y.-E. Cheng, "Numerical investigations of the vortex interactions for a flow over a pitching foil at different stages," *Journal of Fluids and Structures*, vol. 58, pp. 291–318, 2015. https://doi.org/10.1016/j.jfluidstructs.2015.08.002.

[105] C.-C. Tseng, P.-B. Liu, and S.-Y. Hsu, "Numerical investigations of dynamic stall characteristics with laminar-to-turbulence transition," *Journal of Mechanical Science and Technology*, vol. 35, no. 8, pp. 3455–3468, 2021. https://doi.org/10.1007/s12206-021-0718-6.

[106] P. Giguère and M. S. Selig, "Low Reynolds number airfoils for small horizontal axis wind turbines," *Wind Engineering*, vol. 21, no. 6, pp. 367–380, 1997. https://www.jstor.org/stable/43749658.

[107] S. M. Orlando, "Laser Doppler Anemometry and Acoustic Measurements of an S822 Airfoil at Low Reynolds Numbers," Master's thesis, University of Waterloo, 2011. http://hdl.handle.net/10012/5864.

[108] A. Zilstra, "Computational Aeroacoustic Prediction of Airfoil Self-Noise at Static Angles of Attack," Master's thesis, University of Waterloo, 2019. http://hdl.handle.net/10012/14532.

[109] ANSYS Academic Research, Release 20.2, "ANSYS Fluent Theory Guide," in *ANSYS Help System*, ANSYS Inc., 20th ed., Release 20.2.

[110] Graham, "Digital Research Alliance of Canada," 2024. https://alliancecan.ca/en.

[111] F. Farassat, "Derivation of Formulations 1 and 1A of Farassat," Tech. Rep. NASA-TM-214853, NASA Reference Publication, 2007. https://ntrs.nasa.gov/citations/20070010579.

[112] M. S. Selig, C. A. Lyon, P. Giguere, C. P. Ninham, and J. Guglielmo, *Summary of low-speed airfoil data, Vol. 2*. VA: SoarTech Publications, 1996. https://m-selig.ae.illinois.edu/uiuc_lsat/Low-Speed-Airfoil-Data-V2.pdf.

[113] F. Samara and D. A. Johnson, "Dynamic Stall on Pitching Cambered Airfoil with Phase Offset Trailing Edge Flap," *AIAA Journal*, vol. 58, pp. 2844–2856, 2020. https://doi.org/10.2514/1.J059115.

[114] D. M. Somers, "S833, S834, and S835 Airfoils," Tech. Rep. NREL/SR-500-36340, 2005. https://doi.org/10.2172/15020040.

[115] F. R. Menter, R. B. Langtry, S. R. Likki, Y. B. Suzen, P. G. Huang, and S. Volker, "A Correlation-Based Transition Model Using Local Variables: Part I — Model Formulation," in *Turbo Expo: Power for Land, Sea, and Air*, vol. 4, pp. 57–67, 2004. https://doi.org/10.1115/GT2004-53452.

[116] F. R. Menter, "Two-equation eddy-viscosity turbulence models for engineering applications," *AIAA Journal*, vol. 32, no. 8, pp. 1598–1605, 1994. https://doi.org/10.2514/3.12149.

[117] J. C. R. Hunt, A. A. Wray, and P. Moin, "Eddies, streams, and convergence zones in turbulent flows," in *Proceedings of the Summer Program*, no. CTR-S88, pp. 193–208, Center for Turbulence Research, 1988. https://ntrs.nasa.gov/citations/19890015184.

[118] E. C. Nash, M. V. Lowson, and A. McAlpine, "Boundary-layer instability noise on aerofoils," *Journal of Fluid Mechanics*, vol. 382, pp. 27–61, 1999. https://doi.org/10.1017/S002211209800367X.

[119] S. Hosseinverdi and H. F. Fasel, "Numerical investigation of laminar–turbulent transition in laminar separation bubbles: the effect of free-stream turbulence," *Journal of Fluid Mechanics*, vol. 858, p. 714–759, 2019. https://doi.org/10.1017/jfm.2018.809.

APPENDICES

Appendix A

Publications and Conferences

The research presented in this thesis has resulted in the publication of numerous peer-reviewed journal articles and peer-reviewed conference proceedings for international aeroacoustics and wind energy conferences. The results and analysis presented in Chapter 4 have been published in the *ASME Journal of Fluids Engineering* and the contents of Chapter 7 have been published in the *AIAA Journal*. Preliminary results were presented and were well-received at the following international conferences: AIAA/CEAS Aeroacoustics Conference, TORQUE Conference, Wind Energy Science Conference. The complete list of publications and presentations is included below.

Peer-Reviewed Journal Articles

Zilstra, A. and Johnson, D.A. (2024) Validated Dynamic Stall Simulation of Pitching Low Reynolds Number Airfoils. *AIAA Journal*. doi: 10.2514/1.J063884.

Zilstra, A. and Johnson, D. A. (2022) Large eddy simulation of transitional separated flow over a low Reynolds number cambered airfoil. *ASME J. Fluids Eng.*, doi:10.1115/1.4056280.

Peer-Reviewed Conference Proceedings

Zilstra, A. and Johnson, D.A. (2024) Computational Aeroacoustic Prediction of Tonal Noise for Low Reynolds Number Airfoils. *30th AIAA/CEAS Aeroacoustics Conference*. doi:10.2514/6.2024-3362.

Zilstra, A. and Johnson, D.A. (2024) Numerical Prediction of Tonal Aeroacoustic Noise Produced by Small Wind Turbines. *J. Phys.: Conf. Ser.*, doi:10.1088/1742-6596/2767/7/072022.

Zilstra, A. and Johnson, D.A. (2020) Computational aeroacoustic prediction of trailing edge noise for small wind turbines. *J. Phys.: Conf. Ser.*, doi:10.1088/1742-6596/1618/4/042010.

Zilstra, A. and Johnson, D.A. (2019) LES and FW-H Prediction of Aeroacoustic Noise for a SD 7037 Airfoil for Wind Turbine Applications. *25th AIAA/CEAS Aeroacoustics Conference*. doi: 10.2514/6.2019-2537.

Peer-Reviewed Conference Presentations

Oral Presentations

Zilstra, A. and Johnson, D.A. (2024) Computational Aeroacoustic Prediction of Tonal Noise for Low Reynolds Number Airfoils. *30th AIAA/CEAS Aeroacoustics Conference*, Rome, IT.

Zilstra, A. and Johnson, D.A. (2020) Computational aeroacoustic prediction of trailing edge noise for small wind turbines. *TORQUE 2020*, Online - Delft, NL.

Zilstra, A. and Johnson, D.A. (2019) LES and FW-H Prediction of Aeroacoustic Noise for a SD 7037 Airfoil for Wind Turbine Applications. *25th AIAA/CEAS Aeroacoustics Conference*, Delft, NL.

Poster Presentations

Zilstra, A. and Johnson, D.A. (2024) Numerical Prediction of Tonal Aeroacoustic Noise Produced by Small Wind Turbines. *TORQUE 2024*, Florence, IT.

Non-Peer-Reviewed Conference Presentations

Oral Presentations

Zilstra, A. and Johnson, D.A. (2023) Validated URANS Simulation of the Boundary Layer Separation and Associated Blade Loading During Dynamic Stall. *Wind Energy Science Conference (WESC) 2023*, Glasgow, UK.

Zilstra, A. and Johnson, D.A. (2019) CFD and CAA Analysis of the SD 7037 Airfoil for Low Reynolds Number Flow. *CSME-CFDSC Congress 2019*, London, CA.

Research Seminars

Zilstra, A. (2023) CFD and CAA of Low Reynolds Airfoils, Wind Energy Research Group. *École Centrale Nantes*, July 2023, Nantes, FR.